Ocean Sensors

--for marine environmental monitoring

By

Weidong Gong

A Thesis Submitted for the degree of Doctor of Philosophy

Project Supervisor: Prof. Hywel Morgan

Prof. Michael Kraft

Dr. Matt Mowlem

UNIVERSITY OF SOUTHAMPTON

ABSTRACT

FACULTY OF ENGINEERING SCIENCE AND MATHEMATICS

SCHOOL OF ELECTRONICS AND COMPUTER SCIENCE

DOCTOR OF PHILOSOPHY

OCEAN SENSOR FOR MARINE ENVIROMENTAL MONITORING

By Weidong Gong

Various sensors and instruments were developed to measure the chemical and physical properties of sea water, but many are expensive and too large to be used on mass deployed vehicles such as the Argo float and submersed gliders. Marine mammal and fish tags require further sensor miniaturisation. This thesis describes the development of new in-situ micro sensor technology for marine environmental monitoring.

Nitrite and nitrate are two forms of dissolved inorganic nitrogen in sea water and their availability is a key factor in the regulation of primary productivity in the sea. The in-situ determination of nitrite and nitrate in sea water presents a significant analytical challenge. In this thesis, a simple, low cost double beam spectrophotometer for use in a nitrite sensor for sea water analysis is presented. The sensor uses a colorimetric method to determinate nitrite concentration in sea water, based on Greiss reaction that forms as Azo dye whose absorbance is measured at a wave length of 540nm. The design incorporates a green LED and integrated photo-detectors to make the nitrite sensor compact, with low-cost and low-power consumption.

A Conductivity, Temperature, Depth (CTD) sensor is the primary tool for determining the physical properties of sea water. A new CT (Conductivity and Temperature) micro sensor is presented in this thesis. The temperature sensor uses a thermistor, and the conductivity sensor uses a novel design of four planar electrodes built in an insulated channel. Conductivity sensors built of planar electrodes can be easily mass-produced on PCB boards, thus significantly reducing cost.

This thesis includes the background of the measurement of conductivity, temperature and nitrite concentration in sea water. It also presents a comprehensive analysis of conductivity cells with two, four and five electrodes, together with the detailed multi-sensor interface design. The design and construction of the prototype sensors are described in detail, the key issues and test results are also presented.

Contents

List of Figures

List of Tables

DECLARATION OF AUTHORSHIP

I, Weidong Gong, declare that the thesis entitled

OCEAN SENSORS FOR MARINE ENVIROMENTAL MONITORING

and the work presented in the thesis are both my own, and have been generated by me as the result of my own original research. I confirm that:

- this work was done wholly or mainly while in candidature for a research degree at this University;
- where any part of this thesis has previously been submitted for a degree or any other qualification at this University or any other institution, this has been clearly stated;
- where I have consulted the published work of others, this is always clearly attributed;
- where I have quoted from the work of others, the source is always given. With the exception of such quotations, this thesis is entirely my own work;
- I have acknowledged all main sources of help;
- where the thesis is based on work done by myself jointly with others, I have made clear exactly what was done by others and what I have contributed myself;
- parts of this work have been published as:

1. Weidong G., Mowlem, M., Kraft, M. and Morgan, H., "Oceanographic Sensor for in-situ temperature and conductivity monitoring", OCEANS 2008 - MTS/IEEE Kobe Techno-Ocean.
2. Weidong G., Mowlem, M., Kraft, M. and Morgan, H., "A Simple, Low Cost Double Beam Spectrophotometer for Colorimetric Detection of Nitrite in Seawater", IEEE Sensor Journal, Volume 9, Issue 7, July 2009, Pages: 862-869.

Signed: ……..

Date:…….

Acknowledgements

I would like to thank all the people who have given their help and support to this work. Special thanks go to Prof. Hywel Morgan, Prof. Michael Kraft and Dr. Matt Mowlem for their invaluable time and guidance through out this project. I would like to thank Dr. Tao Sun who gave me some papers on conformal mapping and also provided a Matlab script for two-dimension cell constant. I would like to thank Gareth Lewis who helped me to electroplate conductivity cells with gold. I would like to thank Stephen Harrison and David Childs who helped me during my experiments in National Oceanography Centre (NOC), Southampton. I also like to thank Dr. David Holmes, Daniele Malleo, Giuseppe Benazzi and Alan Taberham for their help and advice. Support for this project by the administration and faculty of Electronic & Computer Science School and National Oceanography Centre, Southampton are gratefully acknowledged. Finally, I would like to thank my family for their love and support.

Definitions and Abbreviations Used

FIA	*Flow Injection Analysis*
LOAC	*Lab On A Chip*
µTAS	*Micro Total Analysis System*
µFIA	*Micro Flow Injection Analysis*
SFA	*Segmented Flow Analysis*
SIA	*Sequential Injection Analysis*
LOV	*Lab-On-Valve®*
MEMS	*Microelectromechanical system*
SNR	*Signal-to-Noise Ratio*
LOD	*Limit Of Detection*
VIS	*Visible light*
UV	*Ultra Violet*
ISUS	In Situ Ultraviolet Spectrophotometer
NIR	*Near Infrared*
AU	*Absorbance Unit*
LPAS	*Long path length absorbance spectroscopy*
LCW	*Liquid Core Waveguide*
QTH	*Quartz-Tungsten-Halogen*
CMRR	*Common Mode Rejection Ration*
SPD	*Sample Photo-Detector*
RPD	*Reference Photo Detector*
PSD	*Phase Sensitive Detector*
LPF	*Low Pass Filter*
PLL	*Phase Locked Loop*
VCO	*Voltage-Controlled Oscillator*
PD	*Phase Detector*
PCB	*Printed Circuit Board*
TH	*Through Hole*
ESR	*Equivalent Series Resistance*
SMT	*Surface Mount Technology*
FWHM	*Full width at Half Maximum*
NED	*N*-(1-napthyl)ethylenediamine dihydrochloride

PVA *Polyvinyl alcohol*

PSU Practical Salinity Unit

CTD *Conductivity, Temperature and Depth*

MEMS *Micro-Electro-Mechanical Systems*

AC *Alternate Current*

DC *Direct Current*

C4D *Capacitively Coupled Contactless Conductivity Detection*

CCD *Contactless Conductivity Detection*

CE *Capillary Electrophoresis*

RTD *Resistance Temperature Device*

TC *Thermal Couple*

PRT *Platinum Resistance Temperature sensor*

DVM *Digital Voltage Multi-meter*

PTC *Positive Temperature Coefficient*

NTC *Negative Temperature Coefficient*

OHP *Outer Helmholtz Plane*

IHP *Inner Helmholtz Plane*

PZC *Potential of Zero Charge*

CPE *Constant Phase angle Element*

RMS *Root Mean Square*

FEM *Finite Element Methods*

SCM *Schwarz-Christoffel Mapping*

RF *Radio Frequency*

LP *Low Pass*

HP *High Pass*

BP *Band Pass*

FET *Field Effect Transistor*

JFET *Junction Field Effect Transistor*

CMOS *Complementary Metal Oxide Semiconductor*

F.S. *Full Scale*

ASIC *Application Specific Integrated Circuit*

CT *Conductivity and Temperature*

IHP *Inner Helmholtz Plane*

OHP *Outer Helmholtz Plane*

Chapter 1 Introduction

1.1 Overview of Research

The oceans cover almost 75% of the planet and affect the lives of every plant and animal on earth. With the global climate changing rapidly, the importance of studying the oceans has increased dramatically since they play a crucial role in global climate regulation. Various oceanographic sensors are designed to measure different properties of sea water, they are classified as: chemical oceanographic sensors and physical oceanographic sensors. This thesis reports development of miniaturised low-power chemical and physical oceanographic sensor technology. A sensor for the in situ determination of nitrite concentration is presented as an example of reagent based colourimetric chemical oceanographic sensor technology. Physical oceanographic sensors for in situ measurement of seawater temperature and conductivity are also presented.

1.1.1 Nitrite sensor

Nutrients are chemical elements and compounds necessary for, or contributing to an organism's metabolism, growth, and other functions. Nitrite (NO_2^-), nitrate (NO_3^-), ammonium (NH_4^+), and orthophosphates (PO_4^{-3}) are the main nutrient compounds in the ocean and rivers. Too much nutrient in the water can lead to algal blooms, which in turn causes oxygen depletion, and fish mortality; excess nitrogen is the prime cause of such problems. The determination of nitrite and nitrate concentrations in natural water is important for biological and also environmental concerns. Water pollution from high levels of nitrogen can be a serious sanitation problem; and the toxicity of nitrite is harmful to public health.

Numerous analytical techniques have been proposed for the determination of nitrite and nitrate levels. Conventional Flow Injection Analysis (FIA) methods to determine nitrite are well known [1-4], however, these systems are laboratory based and samples have to be collected from remote sites and then brought back to the laboratory. This can be expensive and labour intensive. Furthermore there is a significant risk that sample integrity will not be maintained as a result of biological activity and contamination if rigorous sample handling protocols are not followed. Although conventional FIA systems can be adapted for shipboard and remote analysis [5-8], their applications are limited since they require frequent replenishment and have high reagent consumption, large sample volume, and considerable maintenance. In both process studies and routine monitoring, in-situ chemical measurement capabilities offer a variety of substantial advantages relative to shipboard and laboratory analysis. Prompt in-situ analyses without human intervention considerably reduce sample contamination possibilities, improve rates of sample throughput, increase observational endurance, and more over, substantially reduce overall measurement cost due to automation of the analysis. A few in-situ analyzers built from traditional instruments are available for oceanographic application, but they are not suitable for mass deployment due to their big size and high cost. The development of low cost and miniaturized in-situ instruments able to measure nitrite and nitrate represents a real need in the oceanographic community for the study of marine nitrogen cycles.

In-situ analysis of nitrogen in seawater can become a challenge when both accuracy and small size are required. This demand has led to the miniaturization of analytical instruments; an area of much interest over the last few years. The ‘‘miniaturized total analysis system’’ (μTAS) concept was first introduced in the 1990s by Manz et al. [9], whereby sample pre-treatment, separation and detection were miniaturized and incorporated within a micro fluidic device. This led to a revolution in the miniaturization of analytical instruments on chips, so called ‘LOAC’ (lab on a chip)’’. Conventional FIA systems can be miniaturized to μFIA systems by using modern ‘LOAC’ technology. The advantages of miniaturization include low reagent consumption and thus less waste production; robust and small sample size due to the smaller flow rates, increased speed of analysis, portability and in-situ operation.

1.1.2 Temperature and conductivity sensor

Temperature, pressure, and salinity are the three basic parameters used for marine environmental study. The determination of salinity is extremely important in many aspects of marine technology. Before the 1970's, the classical method of determining salinity was to analyze sea water in a laboratory by chlorinity titration. Another way to determine salinity is using a refractometer, based on the fact that the refractive index of water is a function of salinity. Since these methods are usually quite sensitive to shock and vibration, they are not suitable for in-situ operation in oceans. It was not until 1978 that the measurement of electrical conductivity of sea water was formally established as a standard method to define the salinity of sea water by the Joint Panel of the United Nations Educational, Scientific and cultural Organization (UNESCO). Salinity is now defined as the ratio of the electrical conductivity of sea water sample (at 15°C and 1 standard atmospheric pressure) to that of a standard solution of potassium chloride (KCl) containing 32.4356g KCl in 1 kg of solution at the same temperature and pressure [10-12]. Since salinity is derived from a ratio, it has no units but is normally written in the unit "*psu*" (Practical Salinity Unit). A ratio of 1 is equivalent to a practical salinity of 35, written as 35*psu*.

The conductivity of seawater is directly related to temperature and pressure; the data must be compensated for the temperature and pressure to determine accurate salinity levels. The requirement of oceanographic instruments to combine conductivity, temperature and pressure sensors into a single package directly led to the CTD (Conductivity, Temperature and Depth) system. CTDs have become the standard oceanographic instruments for in-situ seawater measurement. CTD sensors are precision instruments designed with very high accuracy in order to get accurate sea water profiles. Although highly accurate CTD probes are available from commercial companies such as Seabird (e.g. Seabird Alace CTD which has an accuracy of 0.005 psu, 0.002 ^{o}C, and 2.4 deciBar, with a length of ~25cm) and FSI, they are usually quite big, and very expensive with most at the time of writing costing over £10,000. A new generation CTD for ocean monitoring is required to study global climate change. The ideal CTD should be miniaturized with low cost, low power consumption, suitable for mass deployment and long term ocean monitoring.

1.2 Contributions

Oceanographic sensors are important tools for surveying and monitoring the ocean. These sensors need to be very accurate, reliable and also highly robust since they are used in harsh environments. This work has developed sensor technology for nitrite, temperature and conductivity sensors suitable for in-situ operation. The sensor design is focused on accuracy, small size, low cost and low power consumption.

In this project, an in-situ nitrite analyzer based on a colorimetric detection method was developed. The proposed method is suitable for automated and continuous analysis, and was successively applied to the determination of nitrite in sea water. The goal of the work was to design a nitrite analyzer which is accurate (limit of nitrite detection 0.1μM as shown in table1-1), reliable, robust, cheap and simple. By using modern 'LOAC' technology, a single flow system can be miniaturized in a micro fluidic chip incorporating all the necessary elements such as micro pumps, fluid channels, mixers, chemical reaction chambers and an optical detection unit. The contribution to the nitrite sensor described here is successful development of a double beam spectrophotometer. With appropriate LEDs and spectral filters, it can be used to measure the absorbance of colourimetric reaction products for a number of analytes.

An in-situ combined conductivity and temperature sensor was also developed for long term ocean monitoring. The target was to design a high performance sensor which is accurate (0.01 ^{o}C for temperature and 0.1mS/cm for conductivity, see table 1-1), cheap, compact, robust, with low power consumption and suitable for mass deployment in the ocean. A new micro sensor was designed in this work using thermistors and planar electrodes. The main contribution of this work is the design of a small conductivity sensor with four planar electrodes and an integrated temperature sensor, and the development of integrated signal conditioning circuits for these sensors.

Table 1-1 Target Sensor Specifications

Sensor Type	**Nitrite**	**Conductivity**	**Temperature**
Measurement Range	0 ~ 50 μM	15 ~ 55 mS/cm	0 ~ 30 ^{o}C
Target Accuracy	±0.1 μM	±0.1 mS/cm	±0.01 ^{o}C

1.3 Document Structure

This thesis describes an in-situ nitrite analyzer and a CT (conductivity & temperature) sensor designed for marine environment monitoring. The thesis reviews the history and latest development of ocean sensors, describes the new CT and nitrite sensor system design including the detailed circuit design, and presents test results and discussion. The thesis also includes the relevant theory and background. The structure is shown as below:

Chapter 2 presents the background, theory and related literature for nitrite, conductivity and temperature sensor technology.

Chapter 3 describes the double beam spectrophotometer design for nitrite detection in sea water.

Chapter 4 presents test results for nitrite measurement, key issues and discussions are also presented.

Chapter 5 presents the theory for the electrode-electrolyte interface

Chapter 6 describes the conductivity cell design

Chapter 7 describes the electronic circuit design for multi-sensor application

Chapter 8 presents discussion and test results of the conductivity sensor and temperature sensor

Chapter 9 draws conclusion and makes recommendations for future work

Chapter 2 Background

Various ocean sensors have been developed to measure the chemical and physical properties of seawater. This chapter presents the background knowledge as well as the latest sensors development for ocean monitoring.

2.1 Nitrite and Nitrate Detection

Electrochemical and optical detection methods are usually used for the determination of nitrite and nitrate. Comparatively, optical sensors are more attractive since they do not suffer from the drawback of electrochemical sensors such as poor selectivity, aging and electrode fouling [13-17]. The most frequently used method to measure nitrite in aqueous samples is the reagent based colourimetric protocol based on the Griess reaction, in which nitrite (NO_2^-) is diazotized with sulfanilamide and then reacted with N-(1-naphthyl)ethylenediamine dihydrochloride (NED) to form a pink-colored Azo dye [18-20]. The chemical reaction for the formation of the pink-coloured Azo dye is given in figure 2-1 and figure 2-2.

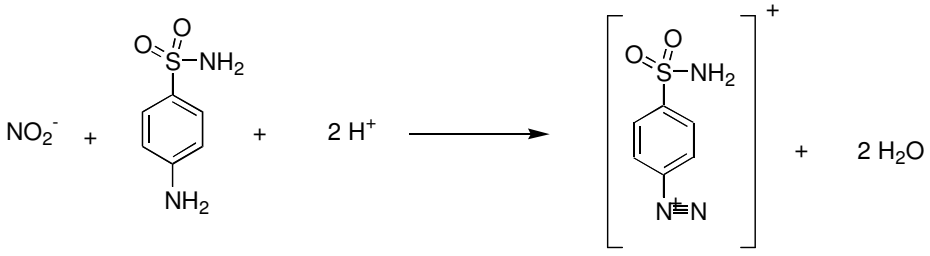

Figure 2-1 NO_2^- reacts with sulphanilamide to form diazonium ion [213]

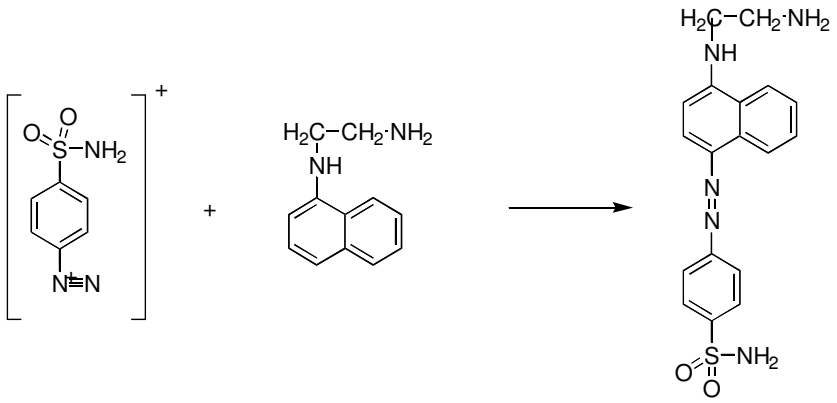

Figure 2-2 Diazonium ion reacts with NED to form Azo dye [213]

The first chemical reaction is shown in figure 2-1, in which the acidic reagent sulphanilamide is added to a sample containing nitrite to form a diazonium compound. Figure 2-2 shows how the diazonium compound reacts with the second reagent NED to form a pink Azo dye which can be measured at 540nm by spectrophotometer. This is a sensitive and reliable method for the measurement of nitrite in water. The colour intensity of the Azo dye is proportional to the nitrite concentration present in the aqueous sample.

In natural water, nitrite (NO_2^-) and nitrate (NO_3^-) often co-exist; they and other compounds containing nitrogen form the nitrogen cycle in the natural world. Therefore, the simultaneous determination of nitrite and nitrate is of great importance for both environmental and biological aspects. Most of the methods for simultaneous determination of nitrite and nitrate are based on the reduction of nitrate to nitrite and subsequent colorimetric determination of the nitrite with Greiss reaction [26-36]. The total amount of NO_2^-/NO_3^- can be measured by passing the sample through a copper-coated cadmium column in which the nitrate ion (NO_3^-) is heterogeneously reduced to nitrite ion (NO_2^-).

$$NO_3^- + Cd(s) + 2H^+ \rightarrow NO_2^- + Cd^{+2} + H_2O \qquad [2\text{-}1]$$

In order to determine nitrate, nitrite is first measured by the Greiss reaction, then nitrate is reduced to nitrite to give the total concentration of nitrogen. Nitrate concentration is then calculated as the difference between the total inorganic nitrogen and nitrite.

Ultra violet (UV) spectrophotometry is an alternative method for nitrite and nitrate detection [21-25]. The direct UV absorption measurement is a simple method since no chemical manipulations are required. An in situ ultraviolet spectrophotometer (ISUS) with a limit of nitrate detection of ~ 1.5μM is reported in [25]. A significant problem associated with UV analysis of nitrate is the interference caused by UV light absorbed by variant chemicals in seawater such as bromides and dissolved organic compounds [23]. Furthermore, UV spectrophotometers are usually large and power hungry. As far as the analysis of nutrients is concerned, the colorimetric methods are still the easiest and most reliable, providing adequate sensitivity and reliability, and unaffected by the other constituents usually found in sea water.

2.2 Spectrophotometry

Spectrophotometry is a quantitative method used to measure the light transmission of a material as a function of wavelength. Spectrophotometry involves the use of spectrophotometers which can measure light intensity as a function of the wavelength of light. In chemical analysis, spectrophotometers are widely used to measure absorbance in order to identify materials. The limit of detection (LOD) for absorbance made with current research-grade commercial spectrophotometers is about (5-6) $\times$ 10^{-5} AU (Absorbance Unit). By using electronic noise cancellation methodology, the performance can be improved to reach the theoretical shot noise limit, and the absorbance baseline noise can be reduced to a range from $1x10^{-6}$ to $4.2x10^{-8}$AU [50-51].

A spectrophotometer consists of two units: a light source for producing light, and a photometer for measuring light intensity. Spectral information is typically recorded by using one or more monochromators, spectral filters, interferometers or diffractive elements between the source and the sample or between the sample and the detector. There are two major classes of spectrophotometers; namely single beam and double beam. A single beam spectrophotometer measures the absolute light intensity while a double beam spectrophotometer measures the light intensity ratio of two separated light beams representing a reference and a sample respectively. Double beam instruments became quite popular in the early days of spectrophotometry due to the instability of

light sources, detectors, and the associated electronics. Generally speaking, a double beam spectrophotometer is more stable, which makes measurement easier since differential or ratio measurements in a double beam system reduce common mode noise in the light source, and in detectors and relevant electronics. A typical double beam spectrophotometer is shown in figure 2-3.

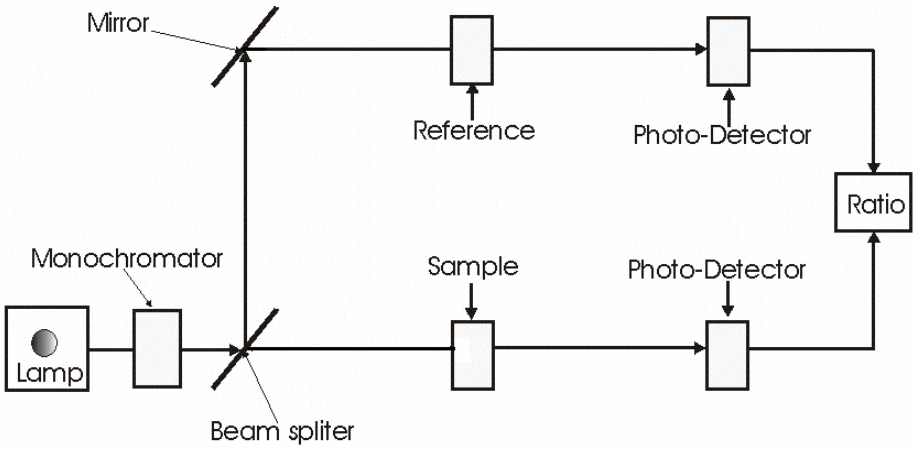

Figure 2-3 Block diagram of a double beam spectrophotometer, adapted from [72]

In a double beam configuration, a lamp is used to provide white light radiation which then passes through a monochromator to produce mono-coloured light. The monochromator is either a prism or a diffraction grating which separates the light into the coloured components and allows only the light of a particular wavelength to strike the sample. The mono-chromatic light is then split into two beams by a beam splitter. One beam illuminates the reference and the other illuminates the sample solution.

Spectrophotometers are available in the Visible light (VIS), Ultra Violet (UV), and Near Infrared (NIR) spectral regions. VIS spectrophotometers are more frequently used in chemical analysis based on colorimetric detection. Colourimetric protocols are available for a number of analytes such as nitrite/nitrate [214], phosphate [215], silicate [216], iron [217] and manganese [218]. Each uses specific reagents, that transform the analyte concentration into an intensity of a coloured product. This coloured product has an absorption maximum at a specific wavelength, and the absorbance at this wavelength is directly proportional to the concentration of the sample. The amount of light absorbed by a solution is governed by the Beer Lambert law:

$$A = \varepsilon(\lambda)*L*C \qquad [2\text{-}2]$$

where A is the measured absorbance, L is the path length in centimetres, C is the sample concentration (molarity), and $\varepsilon(\lambda)$ is a wavelength-dependant molar absorptivity with unit of $M^{-1}cm^{-1}$. For a given analyte at a specified wavelength (λ), $\varepsilon(\lambda)$ is a constant ε and the *Beer Lambert* law can be rewritten as:

$$A = \varepsilon * L * C \qquad [2\text{-}3]$$

VIS spectrophotometric detection has a wide range of applications, and is often used in flow injection analysis (FIA) systems for environmental monitoring. The development of a wide range of intense light-emitting diodes (LEDs) that can be coupled to fibre optics has enabled the miniaturisation of spectrophotometers, which can be integrated with microfluidic devices to provide on-chip detection [219, 220]. However, there are some limitations in the application of spectrophotometers in microfluidic devices due to reduction in path length within the micro device, which decreases the sensitivity of the method [221]. Long path length absorbance spectroscopy (LPAS) and Liquid Core Waveguide (LCW) can be use to extend the sensitivity of conventional colorimetric determination of nitrite and nitrate. It was reported in [52] that a LPAS absorbance spectroscopy with a 4.5 m path length LCW made of Teflon AF-2400 provided detection limits for NO_2^- and NO_3^- equal to 0.5 and 1.5 nM respectively. Optical elements are often difficult to miniaturize and separate optical devices also have alignment problems and shock stability in terms of packaging. Planar optical waveguides, monolithically integrated with microfluidic channels may offer a viable solution to these problems [53-55]. Alternatively, insertion of optical fibers in etched grooves provides another solution [56-58].

2.3 Flow Injection Analysis

Flow analysis methods were introduced in the field of chemical analysis in the middle of the last century [37]. The aim was to try to mechanize the process of chemical analysis. Until the end of the 1950's, the first practical application of flow measurements was carried out by a fluid stream segmentation technique with air segments, named segmented flow analysis (SFA) [38]. In the mid 1970's, a new flow

analysis technique called flow injection analysis (FIA) was developed to automate wet chemistry assays [39]. Automation is achieved by carrying out analysis in a flow system where a pump is used to continuously draw sample and reagent solutions into different lines or segments of plastic tubing, as well as push them forward through the system. Figure 2-4 shows a simple FIA system.

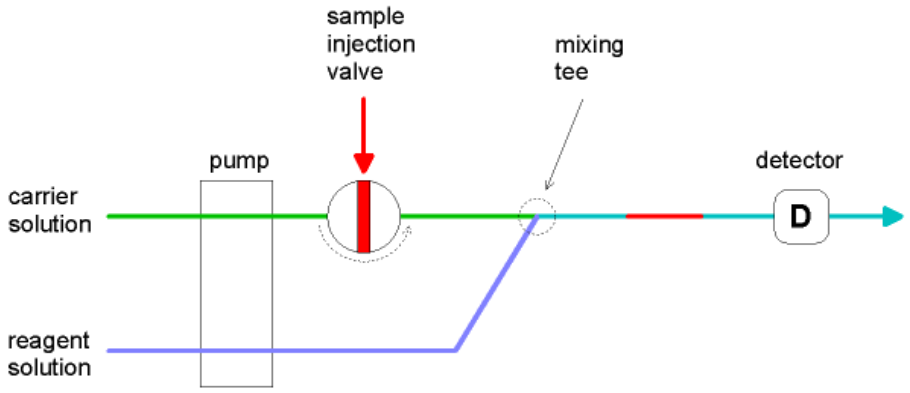

Figure 2-4 Schematic diagram of a simple FIA system [40]

In the simple FIA system shown in figure 2-4, the sample is injected into a carrier stream and the volume of injected sample is precisely controlled by an injection valve. Solutions from different lines are brought together in a mixing tee, where the reagent is automatically merged with a stream of sample. By connecting a detector at the end of the flow path, an automatic detection of the processed sample is achieved. A more advanced FIA system usually consists of a high quality multi-channel peristaltic pump, an injection valve, a coiled reactor, a detector such as a photometric flow cell, and an auto-sampler. Additional components may include a flow through heater to increase the speed of chemical reactions, columns for sample reduction, debubblers, and filters for particle removal.

Sequential Injection Analysis (SIA) is the second generation of FIA and was introduced in the early 1990s' [41]. SIA usually consists of a single-channel high precision bi-directional pump, a holding coil, a selection valve, a reactor and a flow through detector. A typical SIA system is shown in figure 2-5.

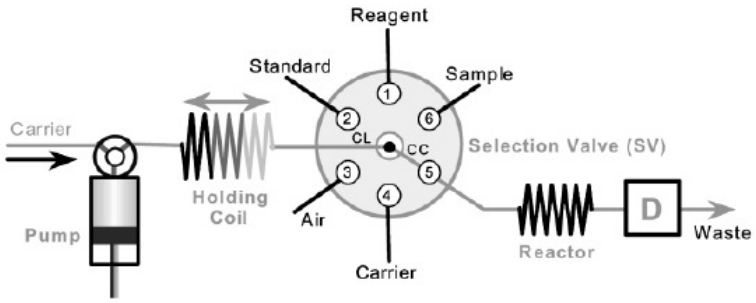

Figure 2-5 Schematic Diagram of a typical SIA system [42]

In a SIA system, a carrier stream, a sample and regent are sequentially aspirated into a holding coil, and stacked there in individual zones. The zones gradually overlap due to the parabolic profile induced by the differences between flow velocities of adjacent streamlines. Flow reversal and flow acceleration further promote mixing. When the selection valve is switched to the detector position, the flow direction is reversed, and the sample/reagent zones are propelled forward through the flow path. The advantage of SIA over traditional FIA is that SIA typically consumes less than one-tenth the reagent and produces far less waste – an important feature when dealing with expensive chemicals, hazardous reagents, or online/remote site applications. One disadvantage of SIA is that it tends to run slower than FIA.

Lab-On-Valve® is the third generation of FIA introduced at the end of 1990s', named LOV. LOV integrates all the manifold components into a single unit mounted on a multi-positioned selection valve. The single unit is potentially designed to handle all the necessary operations demanded for a given assay, even incorporates flow cell coupled with optical detector for optical assay (e.g., UV/VIS or fluorometry), acting as a mini-lab, hence the named Lab-On-Valve®. A schematic diagram of LOV system is shown in figure 2-6.

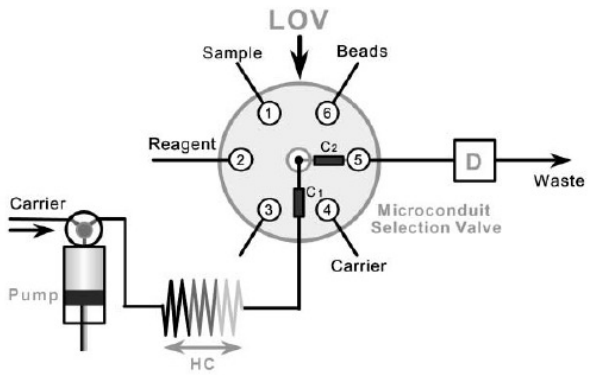

Figure 2-6 Schematic diagram of a LOV system [42]

2.4 Micro Total Analytical Systems (μTAS)

The concept of "Micro Total chemical Analytical Systems (μTAS)" was first proposed by Manz et al. in 1990 [9]. Nowadays, other terminologies such as "Microfluidics" and "Lab-On-A-Chip (or LOAC)" are increasingly used in place of μTAS as general terms. The μTAS concept is an extension of the Total Chemical Analysis System (TAS), where the aim is to simplify and automate chemical analysis by fully incorporating all analytical procedures into a flowing system [43]. A small scale TAS dramatically reduces solution consumption, meaning that lower sample volumes are required and less waste is generated. The trend toward miniaturized chemical assays led to the development of the Micro Total Analysis Systems (μTAS) [44, 45].

The fabrication of microstructures for μTAS (or microfluidics) relies essentially on the methods developed by the planar microelectronics industry. These are generally known as thin-layer techniques including deposition, photolithography and selective etching etc. The application of micromachining techniques (Microelectromechanical systems, also known as MEMS) has impacted on the fabrication of microfluidic devices. Unlike microelectronic chips based on silicon, other materials such as glass or plastics have been used to fabricate microfluidics devices. The excellent chemical and optical properties of glass and plastics are the main advantages for microfluidics. The fabrication techniques used for microfuluidics are developing rapidly and include micromachining, photolithography, replica moulding, embossing, and injection moulding [46]. Improved fabrication techniques and the use of new materials have helped microfluidics move toward the ultimate goal of producing small size, low-cost, disposable instrumentation.

As the dimensions of microfluidics shrink, surface area to volume ratios increase and a number of effects change significantly as size is decreased. One example is that laminar flow dominates since the Reynolds numbers are small. Inertial effects are reduced and turbulence prevented. As a consequence, intermixing of different solutions in a microfluidic device is by means of diffusion which is very slow. Numerous mixing strategies have been proposed to solve the problem since mixing is absolutely central to

Flow injection analysis (FIA) is a well-established technique for carrying out wet chemical assays that has great potential for miniaturization [47, 48]. In a micro flow injection analysis (μFIA) system, an entire FIA laboratory system is integrated onto a single microfluidic chip. Figure 2-7 shows an example of μFIA used for ammonium detection. A sample solution is injected by a micro pump into carrier stream in the main channel, and mixed with 2 reagents before they reach a reaction chamber. After the chemical reaction take place in the reactor, the reacted mixture passes a detection cell in which light absorption is measured to calculate the original amount of ammonium. In [49], two different approaches have been used to miniaturize the FIA system, namely hybrid modular system and planar monolithic integration. The planar monolithic integration approach has achieved the most degree of miniaturization, reduces solution consumption to a minimum while the hybrid modular approach is more flexible and provides easy replacement of components with either different functions or a malfunction.

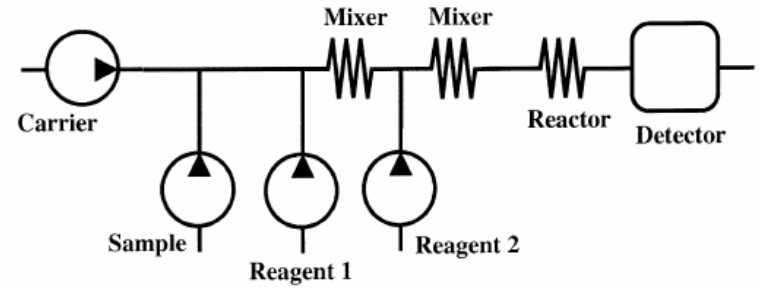

Figure 2-7 μFIA layout for the detection of ammonia [49]

2.5 Autonomous measurement of optical absorption

Colorimetric analytical methods are widely used to analyze chemicals in water because it is reliable, sensitive and accurate. With the advancement of portable and miniaturized spectrophotometers, various autonomous measurement instruments have been developed to measure nutrients in natural waters. Phosphate-Cycle sensor is an autonomous, in situ dissolved inorganic phosphate analyzer, jointly developed by SubChem Systems Inc. and WET Labs Inc.. It incorporates a novel electro-fluidic design and unique sampling regime with standard spectrophotometric methods for the determination of dissolved inorganic phosphate in natural waters.

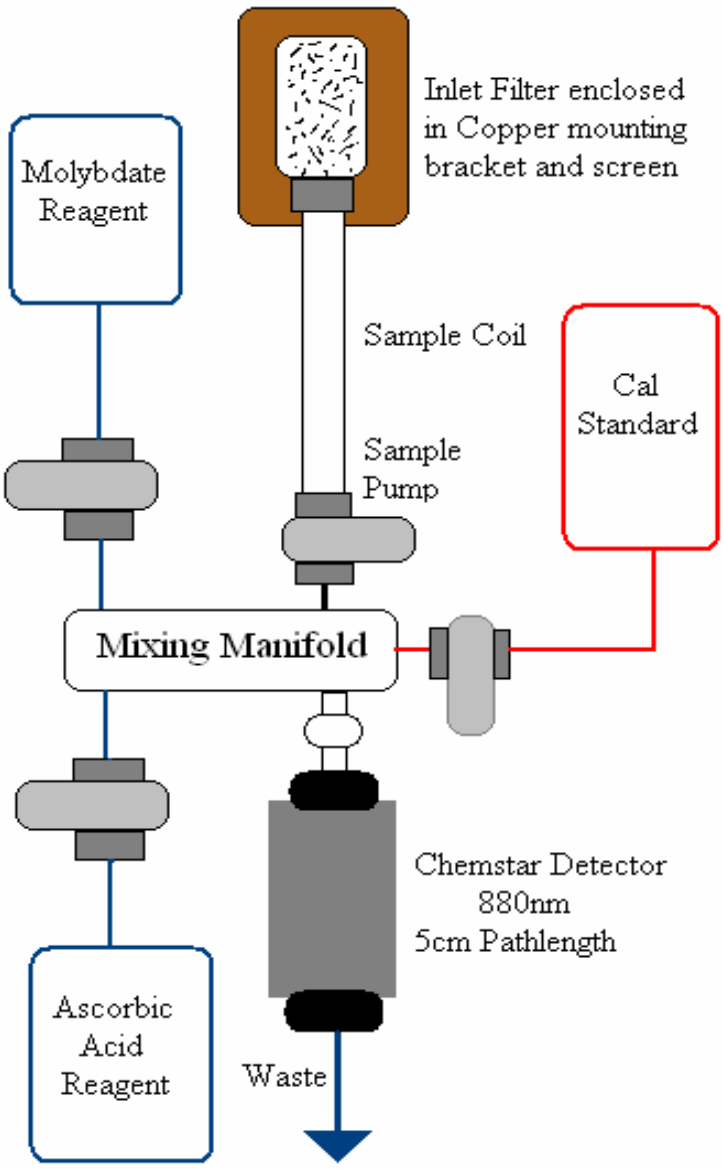

Figure 2-8 WETLabs Inc. Phosphate-Cycle sensor flow Schematic, reproduced from [227]

In figure 2-8, the sample is fed in through an inlet filter in order to impede biofouling. Samples and reagents are pumped into a mixer, and the product is analyzed by an optical detector at 880nm with 5cm path length. The unique sampling regime includes four baseline determinations, two sample determinations, and one standard addition calibration over a 20-minute sampling cycle. The phosphate detection limit is ~50 to100nM in the range from 50nM to 30µM. Power consumption is 520mW-hr per cycle, and the total reagent usage per cycle is 240uL.

Spectrophotometric elemental analysis system (SEAS) is a complete, compact, in-situ spectrophotometric developed by Robert H. Byrne's research group in the College of Marine Science, University of South Florida. This in situ spectral analysis system is capable of fully autonomous observations. SEAS makes use of the liquid core waveguide (LCW) technology that provides nanomolar to subnanomolar detection limits for a wide variety of laboratory-based spectral analyses including ferrous and ferric iron, nitrate and nitrite, chromate and molybdate, copper, hydrogen sulphide and pH measurement. A picture and block diagram of SEAS are shown in figure2-9 and figure 2-10.

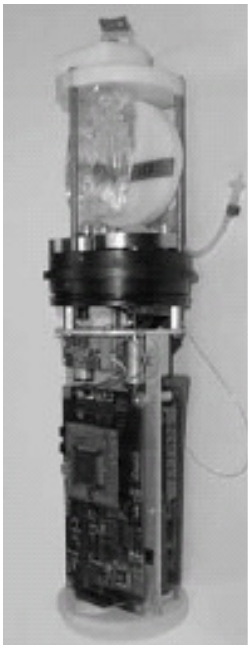

Figure 2-9 SEAS picture [228]

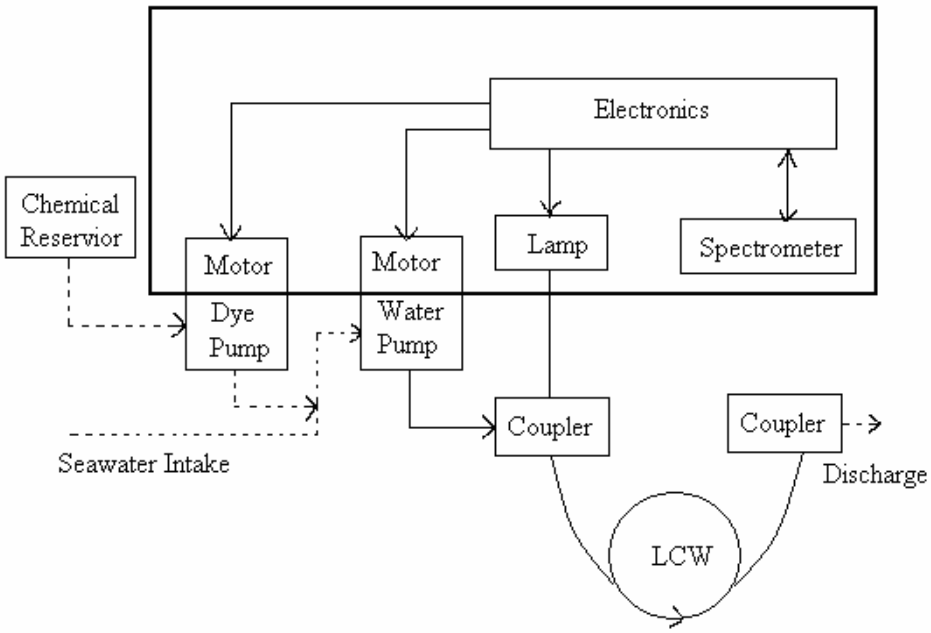

Figure 2-10 A block diagram of SEAS, reproduced from [228]

The entire analysis system of SEAS in figure 2-9 is contained in a housing that is 11.5 cm in diameter and 50-cm long. This pressure housing encloses the spectrometer, a light source and the pump motors. The LCW, pump heads, and reagent reservoirs are mounted outside the pressure housing as shown in figure 2-10. Since the optical path (LCW), reagents, and pumps are exposed to ambient conditions, the pressure in the sample/reagent pumping system does not change as depth changes. All operations of the instrument such as selecting system parameters (pump speed, sampling mode, etc.) are controlled by a microprocessor. The incandescent light source and spectrometer

used in SEAS provide absorbance observations throughout visible spectrum. This offers SEAS an important advantage by enabling it to be used for a variety of types of colorimetric analyses with only a change in reagent type. For conventional colorimetric method, the sensitivity of nitrite detection is limited principally by optical pathlength. A liquid core waveguide (LCW) can provide a long optical pathlength by constraining light propagation within a liquid medium that has a higher refractive index than the surrounding solid tubing such as AF-2400 (Dupont). The flexibility of Teflon AF-2400 allows long pathlengths to be coiled within small volumes. With 1-m pathlength LCW, SEAS was reported to have a power consumption of 6W and a detection limit of nitrite on the order of 1.2 to 2.5 nM [228].

With the development of modern optoelectronics, various light emitting diodes (LED) and photodetectors are available from commercial companies. LEDs, as a light source, are compact, inexpensive, energy-efficient, and available over a broad spectral range. The combination of LEDs with photodetectors is attractive for incorporating colorimetric analytical methods into in situ micro sensors. LEDs used as sunlight detector was first proposed by Mims III [229]. The photocurrent obtained by a reverse biased LED exposed to sunlight was converted to voltage by a transimpedance amplifier.

The use of a paired LED as both light emitter and detector for optical sensing has been developed by Dermot Diamond's research group [230]. The emitter LED is forward biased while the detector LED is reverse biased. Instead of directly measuring photocurrent, a simple timer circuit is used to measure the time taken for the photocurrent generated by the emitter LED to discharge the detector LED from 5 V to 1.7 V to give digital output directly without using an A/D converter or operation amplifier. Since the electric charge (Q) on the inherent capacitance of the diode is a constant, the time taken to discharge the capacitor is inversely proportional to the intensity of the incident light. This novel designed paired emitter-detector diode (PEDD) was used in a flow injection system to determine nitrite concentration [231]. The integrated PEDD cell was fabricated using two LEDs bonded on an optical flow cell. The detector was a red LED (λmax at 623 nm) and a green LED (λmax at 530 nm) was used as the emitter. The schematic of an integrated PEDD flow analysis device used for colorimetric detection is shown in figure 2-11.

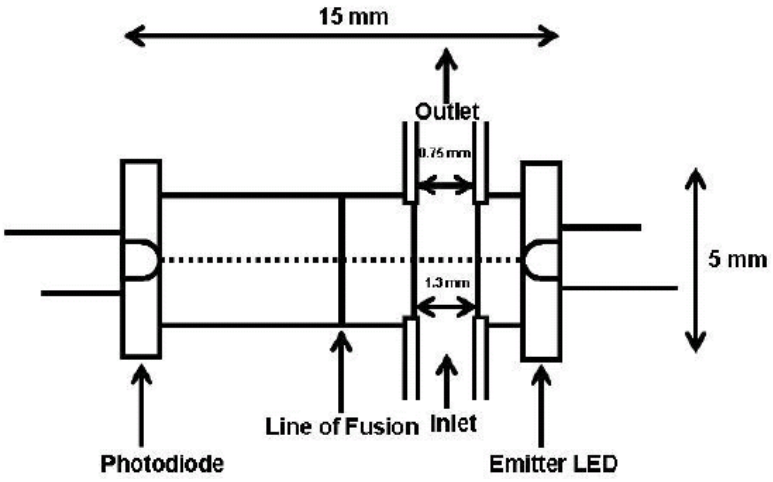

Figure 2-11 A schematic of the integrated PEDD [231]

The PEDD flow analysis system is highly sensitive for the detection of nitrite employing the Griess reaction method. It was reported that the PEDD flow device shown in figure 2-11 achieved a linear range of 0.2–100 μM and a limit of detection of 70 nM in the measurement of nitrite concentration [231]. The novel, low cost, miniaturized PEDD flow device has very low power consumption and can be directly operated by 9V battery, which is suitable to apply in an autonomous remote sensing system for in situ nitrite detection.

2.6 Conductivity of Sea Water

Conductivity measurements of sea water are accurate and reliable, and suitable for in-situ operation even in a harsh environment. The conductivity of sea water is related closely to the sea salt concentration. For this reason conductivity measurement based approaches are now almost exclusively used to determine the salinity of sea water. Electrical conductance of sea water is a property which describes its ability to conduct an electric current. The electrical conductance (G) is the reciprocal of electrical resistance which is given by the ratio of electrical current (I) and voltage (V):

$$G = \frac{1}{R} = \frac{I}{V} \qquad [2\text{-}4]$$

Figure 2-12 shows a cylindrical volume of electrolyte with length *L*, cross-sectional area *A*, with electrical conductance *G*. The specific conductivity (σ) is given by:

$$\sigma = \frac{L}{A} * \frac{1}{R} = \frac{L}{A} * G = \kappa * G \qquad [2\text{-}5]$$

where κ, the cell constant (m^{-1}), is the ratio of the length and cross-section of the cylinder. The specific conductivity (σ) is normalized by the geometry with a unit of Siemens/per meter (Sm^{-1}), and is a property of the measured material only.

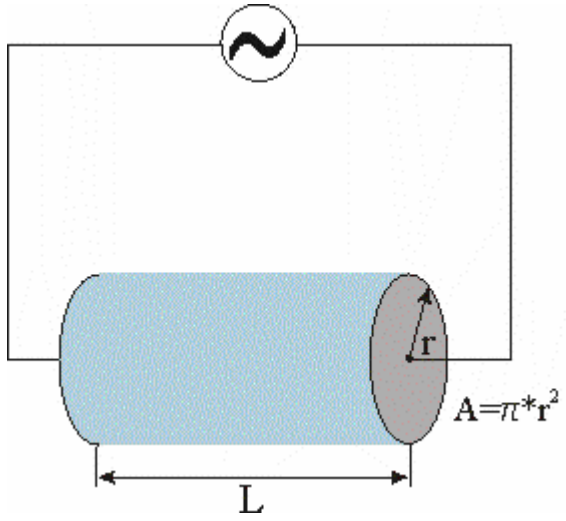

Figure 2-12 Cylindrical volume of electrolyte

2.6.1 Ions in sea water

Sea water is a complex mixture of dissolved salts. The dissolved salts constitute positive and negative ions which become the main electric conductors in sea water. Table 2-1 summarise major ions in the sea water.

Table 2-1 Major Ion in Sea Water

Positive Ions	Na^{+}	Ca^{+2}	K^{+}	Mg^{+2}
Negative Ions	Cl^{-}	SO_4^{-2}	CO_3^{-2}	HCO_3^{-}

Other ions such as ammonium (NH_4^+), nitrates (NO_3^-) and phosphates (PO_4^{-3}) are minor contributors to the conductivity of sea water, although they are very important biologically. For each ion of type n, the ionic conductivity (λ_n) is defined as [77]:

$$\lambda_n = z_n F \mu_n \qquad [2\text{-}6]$$

where z_n is the valence and μ_n is the mobility of the ion, F is the Faraday constant ($9.6487 \times 10^4 Cmol^{-1}$). The conductivity of water (σ) is given by the sum of the concentrations of each ion:

$$\sigma = \sum_n \lambda_n C_n \qquad [2\text{-}7]$$

where C_n is the molar concentration of the ion. Since the composition of sea salts is relatively constant, the measured conductivity is mainly determined by the concentration of the sea salts. For an individual salt (such as NaCl or KCl) with ionic conductivities λ_+ and λ_-, the conductivity (σ) is given by:

$$\sigma = (\lambda_+ + \lambda_-)C = \Lambda C \qquad [2\text{-}8]$$

where C is the molar concentration and Λ is the molar conductivity (S/m*mol) of the salt. The molar conductivity (Λ) tends to a constant value when the concentration is low. At high concentration, the ions interact with each other and the molar conductivity is not proportional to the concentration anymore because of higher order effects [75].

2.6.2 Temperature dependence of conductivity

The electrical conductivity of sea water is a function of both temperature and dissolved solids. The electrical conductivity as a function of salinity varies with temperature. In a laboratory, the sea water is placed in a temperature bath at a standard temperature to get accurate measurement. Alternatively, a ratio conductivity meter with a dual inductive cell system can be used to remove the temperature variation without the need for a highly stable temperature bath [76]. For in-situ application, since the temperature of sea water always changes, the use of conductivity as a measure of

salinity must be adjusted for temperature effects. A common practice to compensate the conductivity is to adjust the measured value to a standard temperature (normally 25°C or 20°C), with the temperature compensated conductivity given by:

$$\sigma_r = \frac{\sigma_t}{1 + \frac{\alpha}{100} * (t - r)} \qquad [2\text{-}9]$$

where σ_r is the compensated conductivity (Sm^{-1}), σ_t is the measured conductivity at sample temperature t (°C), α is the temperature coefficient at the reference temperature r (e.g. 25°C) and is often given in the unit of %/ °C.

For sea water, the temperature coefficient (α) is about 2.5%/ °C [77]. Using equation 2-9, removes the temperature effects from the data. However, this process may introduce errors because of the uncertainties of the temperature coefficient (α). Practically, a temperature coefficient can be obtained by tests with a sample of the sea water from the sampling site. The sample temperature is varied through the expected temperature range, the uncompensated conductivity and temperature are measured and the actual temperature coefficient is calculated as below:

$$\alpha = \frac{(\sigma_t - \sigma_r) * 100}{\sigma_r * (t - r)} \qquad [2\text{-}10]$$

An extensive study of the temperature and pressure influence on conductivity measurement was reported in [78-81]. For a high accuracy, an empirical equation with fourth degree polynomial is used to compensate for temperature effects, details can be found in [82, 83].

$$r_t = \sum_{n=0}^{4} C_n t^n \qquad [2\text{-}11]$$

where r_t is the ratio of the conductivity at temperature t to the conductivity at 15°C, and C_n are the four coefficients obtained from experiment.

2.6.3 History of Conductivity Sensor

The systematic study of the conductivity of electrolyte solutions owes much to the work of Friedrich Kohlrausch. He developed the basic techniques of the AC resistance bridge and recommended basic instrument designs and procedures to reduce the effects of electrode polarisation. These empirical measures are still of value today [84]. Figure 2-13 shows a picture of a Kohlrausch Bridge which is used to measure the impedance of electrolytes. AC-power is obtained from a battery and an induction coil with Wagner's hammer. The bridge balance is detected by a galvanometer or a headphone.

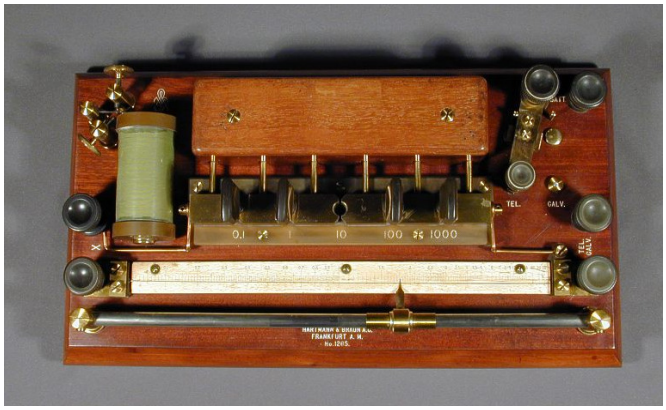

Figure 2-13 Kohlrausch Bridge [85]

In the development of conductivity sensors for marine application, various sensor designs are employed and a common factor is some form of AC system to avoid electrode polarization. Early designs were all based on the resistance bridge system, and later on replaced by the transformer bridge system. In 1961, Neil Brown and Bruce Hamon made the first inductive salinometer by using toroidal coils to measure the conductivity of sea water [86]. Inductive sensors are more resistant to fouling than the designs with exposed electrodes, and also have fewer polarisation problems. In 1974, Neil Brown designed a new miaturized conductivity sensor integrated in a precision CTD micro profiler [87]. This famous design has been known as the Neil Brown Mark III CTD system, which became the mainstay of physical oceanography, and Neil Brown quickly became a leading authority on the measurement of salinity in sea water.

To solve measurement problems caused by electrode polarisation, Schwan first proposed the use of a four electrodes technique to correct for the electrode polarisation

[88]. In 1975, Dauphinee developed a conductive salinometer using a four electrode (platinum) cell located in a temperature controlled bath [89]. The first commercial version of this type of conductivity salinometer was produced by Guildline Instruments Ltd., which has become a standard instrument and widely adopted in oceanographic laboratories around the world.

Sea-Bird Electronics is another important supplier of CTD instruments. Sea-Bird manufactures several conductivity instruments such as SBE 16plus and SBE 4 Conductivity Sensor using a three electrode cell as shown in figure 2-14. Unlike the inductive and other electrode cells, a three electrode cell has no external current flowing because the outer electrodes are connected together. The three electrode configuration is actually a two-terminal cell in which the cell resistance is equivalent to the parallel resistance of the two half cells. The cell is immune to proximity errors and also protected from fouling by anti-biology (toxic) gatekeepers installed at the ends of the cell.

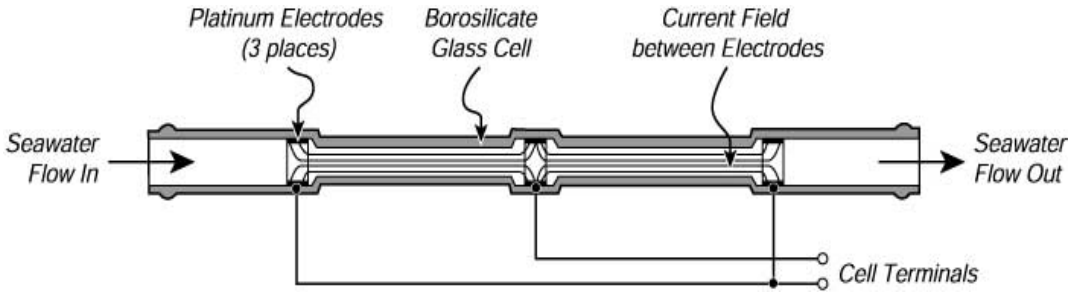

Figure 2-14 Three-electrode cell from Sea-Bird [90]

2.6.4 CCD sensor

The contact electrodes type is a simpler and some what cheaper type of cell than the inductive design, it is also more sensitive than any other sensor. However, electrode fouling causes uncertainties and problems in the measurement which limits its application. Alternatively, by coating electrodes with a thin film, bio fouling can be prevented but with the disadvantage of signal loss due to the insulation. This kind of conductivity sensor is called Capacitively Coupled Contactless Conductivity Detection (C4D) or Contactless Conductivity Detection (CCD), which is a particular type of conductivity based detector, where the electrodes are not in direct contact with the measured solution. This feature has advantages for capillary electrophoresis (CE): the

detection circuitry is isolated from the high separation voltage applied in CE (no direct dc coupling between the electronics and the liquid in the channel); the formation of gas bubbles and surface fouling at the metal electrodes is prevented; electrochemical modification or degradation of the electrode surface is prevented, thereby allowing a wide variety of electrode materials. It is for these reasons that CCD has become popular in electro-separation, after the work of Gas et al [91-102]. Figure 2-15 shows the CCD model for a two-electrode cell and a four-electrode cell.

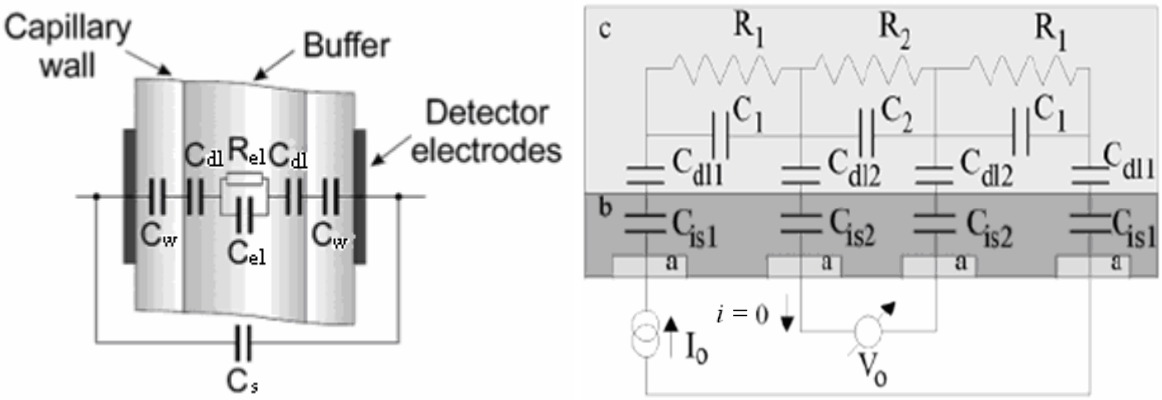

a. two-electrode model[103] b. four-electrode model[104]

Figure 2-15 Electric model of CCD with two and four electrodes (a,b)

It is clear from the models shown in figure 2-15 that a high frequency signal must be used to penetrate the capacitor formed by the insulation film in order to reduce the voltage loss. It is because of the reduced sensitivity due to voltage loss that CCD is mainly used for the detection of a solution with low concentration. Potentially, CCD can be used for the detection of a solution with high concentration such as sea water, but this will depend on development of a dielectric material with high permittivity.

2.6.5 Inductive Conductivity Sensor

The inductive conductivity sensor is electrodeless with no bare metal directly touching the water. For this reason, it is preferred over the electrode sensor for in-situ application in harsh environments. Corrosion and fouling are minimized by the nature of its design. The inductive cell consists of two transformers. The primary of the first transformer is an excitation toroid, a doughnut-shaped core wound with a coil and excited by an AC signal. The second transformer is a sensing toroid which is similar to the excitation toroid. The output of this coil is the signal. Coupling the two coils together is a loop of water that serves as the secondary of the first transformer and the

primary of the second transformer. In this manner, any electrical resistance in series with this loop causes a different amount of voltage to be coupled to the signal toroid. The resistance within the loop is simply determined by the conductivity of the sea water. The equivalent circuit and schematic diagram is shown in figure 2-16. The two coils are usually mounted together so that the common hole serves to provide the loop of sea water. Although commercial units have more elegant circuits, the basic principle is the same for all inductive conductivity sensors.

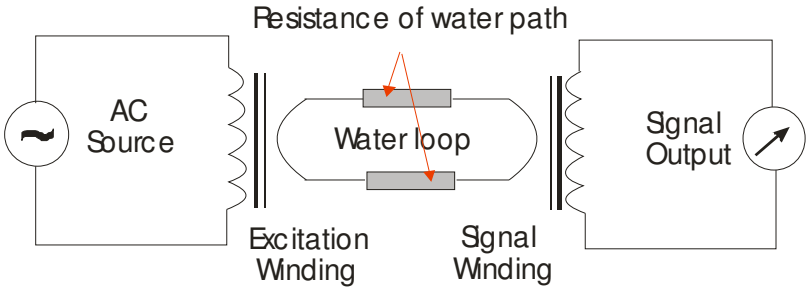

Figure 2-16 Toroidal coil conductivity sensor

The development of the inductive sensor, which permits a conductivity measurement without electrodes, is an important approach for the development of oceanographic instrumentation. These sensors are free from fouling and polarization effects, and exhibit high stability with time. However, they suffer from proximity effects which means the electric field around the toroidal transformer of the sensor is disturbed or distorted by nearby objects. Furthermore, because of the use of toridal transformer, the size of the sensor is usually too big to be integrated in a miniaturized sensor.

2.6.6 The contact electrodes sensor

The contact electrodes sensor has metal electrodes immersed in the sample; the electrical resistance between them is measured. There are two types of conductivity sensor used in common practice, namely two-electrode and four-electrode. The two-electrode conductivity sensors are most frequently used in conductivity measurement, where two electrodes are used for excitation current injection as well as voltage sensing. It is simple but suffers from electrode polarisation (see details in section 5.1), which mainly limits its application to the low conductivity range (<10mS/cm). Unlike the two-electrode conductivity sensor, the four-electrode conductivity sensors have two electrodes for current injection and another two electrodes for voltage sensing. If a high

input impedance amplifier is used, the bias current can be less than several picoamps, thus the voltage drop across the interface of the voltage sensing electrodes is very small and thus can be neglected. Therefore the four electrode configuration greatly reduces the problems of polarisation and fouling effects if the voltage sensing electrodes are connected to a high input impedance amplifier. Figure 2-17 shows the equivalent circuit for the two-electrode and four-electrode conductivity sensors.

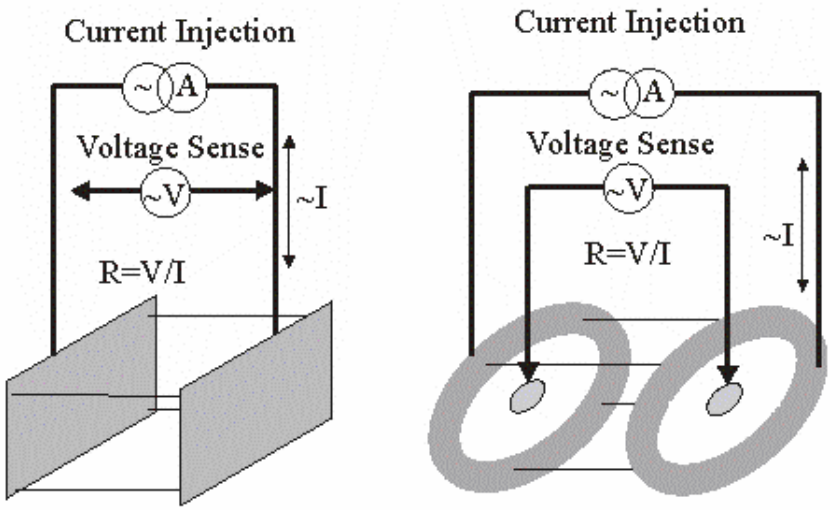

a. two-electrode cell b. four-electrode cell

Figure 2-17 Two and four electrode conductivity sensors (a,b)

2.6.7 Summary of Conductivity Sensors

The above described conductivity sensors have been used for various applications. Among them, three-electrode, four-electrode conductivity sensor and inductive conductivity sensor are the most frequently used to measure seawater; they are summarized in table 2-2.

Table 2-2 Conductivity Sensors used for seawater measurement

Sensor Type	**Three-electrode**	**Four-electrode**	**Inductive**
Example	SBE 4C	MK III CTD	AANDERAA 3211
Measuring Range	0 – 70mS/cm	1 – 65mS/cm	0 – 75mS/cm
Accuracy	0.003mS/cm	0.003mS/cm	0.3mS/cm

2.7 Temperature Measurement of Sea Water

The temperature of the ocean surface can be measured accurately from space by using infrared and microwave sensors. It is relatively easy to measure the temperature of the sea surface, but there is significant subsurface structure to deep sea temperature profiles and this requires an in situ measurement. The oceans have a relative small temperature range, generally between -2 and 30^{o}C. There are quite a few methods used to measure the in-situ temperature of seawater, such as mercury (or alcohol) glass tube thermometer, RTD (Resistance Temperature Device), TC (Thermal Couple), thermistors and Quartz Thermometers.

2.7.1 Mercury (or alcohol) Glass Tube Thermometer

These sensors rely on a glass tube with constant cross sectional area, attached to a reservoir of a fluid such as mercury which has a linear coefficient of expansion with temperature. As the temperature increases, the fluid expands and rises in the tube by a known volume so that the temperature is determined by measuring the volume of the fluid. For deep sea measurements, special thermometers are developed called reversing thermometers shown in figure 2-18, which can hold their reading until returned to the surface. These thermometers allow oceanographers to measure temperature at different depths; they have an accuracy of about 0.02^{o}C when used properly.

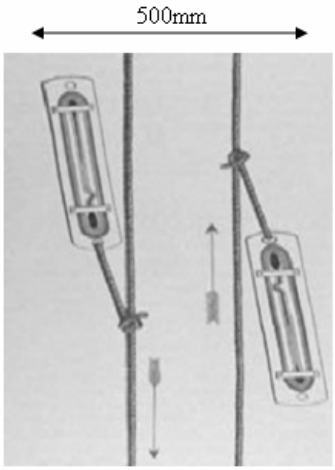

Figure 2-18 A reversing thermometer lowered into the sea [105]

2.7.2 Quartz thermometers

Quartz thermometers are made of a quartz crystal oscillator whose resonant frequency is temperature sensitive. The temperature dependence of frequency depends on the orientation of the piezoelement towards the crystallographic axis of quartz. For best sensitivity, the AT-cut quartz crystal should be used to achieve maximum temperature linearity. Quartz thermometers are capable of resolving micro degree C temperature fluctuations, and their sensitivities are constant with time. To obtain the accuracy of 0.001°C, a triple-point-of-water-cell is required for standardization to assure that no shift has occurred. Another advantage of quartz oscillators is that they consume low power (< 10mW).

Unfortunately, a quartz crystal is also sensitive to pressure, and shock which can cause crystal dislocations and measurement error. To prevent these pressure effects, quartz thermometers are often placed in strong metal cases which slow their thermal response due to the large mass. Another reason why Quartz thermometers are not widely used is that they are usually more expensive than any other thermometers.

2.7.3 Thermocouple (TC)

The thermocouple is one of most widely used temperature sensors in science and industry. A thermocouple usually consists of two dissimilar metals with one end joined together producing a very small voltage as a function of temperature. This thermoelectric voltage is known as Seebeck voltage, named after Thomas Seebeck, who discovered it in 1821. The Seebeck voltage is non-linear with respect to temperature. However, for small changes in temperature, the relationship between Seebeck voltage and temperature is approximately linear and given by [106,107]:

$$\Delta V = \alpha \Delta T \qquad [2\text{-}12]$$

where α is the Seebeck coefficient, ΔT is the temperature changes and ΔV is the Seebeck voltage. With an extra cold junction connected as a reference, the Seebeck voltage can be measured and interpreted by a thermocouple thermometer.

Thermocouples are inexpensive and very rugged, and can operate over a wide temperature range (−200 °C to +1750 °C). However, this type of sensor is not used

very often in oceanography because of relatively low sensitivity, a small output voltage of the order of a few micro volts per degree C.

2.7.4 Resistance Temperature Detectors (RTD)

RTD sensors use a sensing element whose resistance varies with temperature, usually with a positively temperature coefficient. RTDs are usually made of coils or films of metals such as platinum, gold, copper and nickel. The variation of resistance (R) with temperature (T) for most metallic materials can be represented by [108]:

$$R=R_0(1+a_1T+a_2T^2+\cdots+a_nT^n) \qquad [2\text{-}13]$$

where R_0 is the resistance at temperature $T = 0$, a_1 to a_n are the constants and the number of necessary terms depends on the material, the accuracy required, and the temperature range to be measured. Platinum requires three of the a constants for highly accurate representation; however in many application only a_1 is used since quite respectable linearity (0.3% FS) maybe achieved over limited ranges (-100 ~300 °F).

Platinum RTD, usually called PRT, is accurate (calibrated accuracy of ±0.003°C) and stable (Drift < 0.003 °C per year) with good repeatability (± 0.0015 °C or better); hence it is widely used as the laboratory standard for accurate temperature measurement. Frequently, PRT sensors are also used by oceanographers for precision measurements, i.e., they are quite often included in CTDs to measure the temperature of sea water. PRT sensors are available for a number of standard resistances. The dominant type has a resistance of 100Ω at the reference temperature and is named Pt-100. Figure 2-19 shows the four-wire method which is often used to measure the PRT resistance.

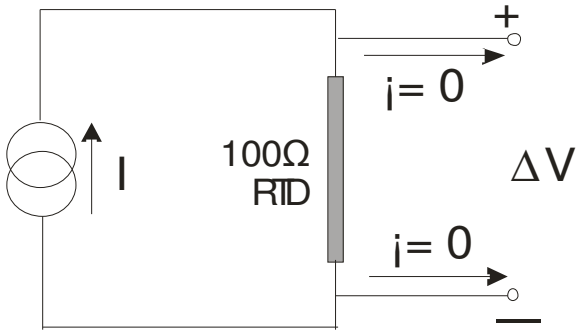

Figure 2-19 Four wire measurement for PRT

In figure 2-19, two wires are used to inject a constant current (I), and two wires are used to sense a voltage drop. To achieve high accuracy, a digital multi-meter (DVM) must have very high input impedance to prevent loading effects. Since the constant current (I) flow through the PRT sensor, this can cause I^2R heating which raises the temperature of the PRT, causing a self-heating error. The magnitude of this error depends on the injected current (I) and resistance (R) but also on heat-transfer conditions. To avoid self-heating problems, the injected constant current (I) must be small so that equilibrium is reached between the heat generation and dissipation.

To obtain high accuracy and resolution, a PRT with big resistance is preferred. Since the resistance per unit length of platinum wire is small, a long wire is needed to achieve a big resistance value. The platinum wire has a thermal mass and hence a time constant. The longer the platinum wire, the greater the resistance change per unit temperature change. Thus on one hand, it is preferred to use a long platinum wire as the sensing element in order to achieve greater accuracy and resolution; but on the other hand, a longer wire has a longer time constant which limit the sampling frequency. Old PRTs had a time constant near 1 second, but newer PRTs made in smaller stainless tubes have been improved to a time constants as fast as 100ms.

2.7.5 Thermistors

A thermistor has a resistance that changes with temperature. There are two types of thermistors, namely PTC and NTC. PTC has a positive temperature coefficient and is usually used in electrical circuits to limit current, and NTC has a negative temperature coefficient and is the most widely used as a temperature sensing element, e.g. automotive temperature sensors, oven temperature sensors, microprocessor controlled thermostats, and hospital and home thermometers. Unlike the PRT, the NTC is not a linear device and its resistance decrease with temperature in a non-linear fashion [108]:

$$R = R_0 e^{\beta(\frac{1}{T} - \frac{1}{T_0})} \qquad [2\text{-}14]$$

where T is temperature in Kelvin, R_0 is the resistance at a reference temperature T_0, and β is a constant (typically 3000-5000).

The NTC thermistor is constructed of ceramics composed of metal oxides. The most common used oxides are manganese, cobalt, iron, titanium, copper, and nickel. In the fabrication of NTC, a mixture of two or more metal oxide powders are combined with suitable binders and then pressed into the desired geometry, dried, and sintered at high temperature, and finally coated with epoxy or glass. By varying the types of oxides used, their relative proportions, the sintering atmosphere and temperature, different NTCs can be obtained with a wide range of resistance and temperature coefficient characteristics. The resistance value of a NTC is typically referenced at 25°C, which is usually abbreviated to "R_{25}". The most common NTC thermistors have R_{25} value between 1k and 100k ohms, and thermistors with other value can be produced. Since thermistors have nonlinear resistance-temperature relationship, they are commonly defined by using the Resistance/Temperature curve (*R/T* Curve). Figure 2-20 shows the *R/T* characteristics of some typical NTC thermistors in comparison with platinum RTD.

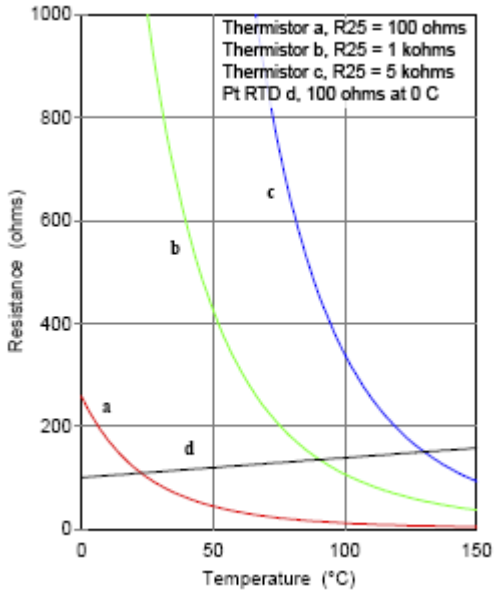

Figure 2-20 R/T characteristics of typical NTCs and a PRT [109]

Although PRTs offer the best stability and repeatability, they are less sensitive than thermistors. NTC thermistor exhibits a relative large change in resistance vs. temperature (~200 Ohm/°C), typically on the order of -3% to -6% per degree C, hence provides a much greater sensitivity or signal response to changes of temperature. Another major advantage of NTC is the wide range of relatively high resistance values. By using high resistance thermistors, a two-wire measurement becomes possible since the effects of sensor lead resistance are minimized. NTC has other important advantages over RTD in that it is cheap, available in smaller package size, with faster

response times, more rugged and with greater resistance to mechanical and thermal shock and vibration. It is because of these advantages that NTC has been increasingly used in oceanography; the thermistor strings [110] and the oceanographic temperature sensor SBE 3S [111] are just some examples. Although NTC thermistors have a limited temperature range (normally -5~300 °C), much narrower than TC (–200 ~ +1750 °C) and PRT (-200 ~ +1000°C), this does not hinder their application in oceanography.

2.7.6 Summary of Temperature Sensors

The temperature sensors described above are used for various applications depending on their characteristics. Among them, mercury thermometer, PRT and NTC thermistor are most frequently used to measure seawater temperature, and they are summarized in table 2-3.

Table 2-3 Temperature Sensors for Seawater Measurement

Sensor Type	**PRT**	**NTC**	**Mercury**
Example	MK3C/WOCE CTD	SBE 3*plus* Sensor	Reversing thermometer
Measuring range	-5 – 32°C	-5 – 35 °C	-2 – 40 °C
Accuracy	0.003°C	0.001°C	0.01°C

2.8 CTD system and Fish Tag

A CTD (Conductivity, Temperature, and Depth) system can produce profiles of ocean temperature, salinity, and density. It is the primary tool for determining essential physical properties of sea water. It gives scientists a precise and comprehensive measurement of the distribution and variation of water temperature, salinity, and density that helps to understand how the oceans affect all aspects of the earth system.

Because salinity and density are calculated from separate measurements of pressure, temperature, and conductivity, the separate measurements must be made at the same time and on the same sample of water. This has directly led to the development of CTD. It was in 1962 when Neil Brown developed the first widely used STD (Salinity/Temperature/Depth) measuring device, later called a CTD. In 1974, he developed the MK III CTD system with a very high accuracy and reliability. A MK III CTD includes a four-electrode conductivity sensor, a strain gauge pressure sensor and a

PRT thermometer to achieve a high accuracy as reported in [87]. Although the MK III CTD shown in figure 2-21 is very accurate and stable, the system is expensive, complicated and consumes about 4.5 watts power.

Figure 2-21 MK3C/WOCE CTD (with temperature accuracy: 0.003^{o}C in the range of -3 to +32^{o}C, conductivity accuracy: 0.003mS/cm from 1 to 65mS/cm, pressure accuracy: 0.03% at full scale (FS) of 6500m) [206]

Sea-birds Electronics is a leading manufactures of oceanographic CTD and water sampling systems. A typical Sea-bird's 9plus CTD shown in figure 2-22 is the primary oceanographic research tool chosen by the world's leading institutions. The SBE 9plus CTD incorporates certain key features to obtain the highest possible accuracy: an accurate and fast thermistor, a conductivity sensor with total internal field to avoid proximity effects, a pump controlled constant flow to provide constant rime response of temperature and conductivity sensors, a temperature and conductivity duct to ensure the temperature and conductivity sensor measure the same water, a precision quartz pressure sensor.

Figure 2-22 SBE 9plus CTD in cage with pump (with conductivity accuracy: 0.003mS/cm from 0 to 70mS/cm, temperature accuracy: 0.001^{o}C in the range of -5 to +35^{o}C, Pressure: 0.015% at full scale (FS) of 10500m.) [207]

Figure 2-23 shows a mini CTD probe developed by Valeport, which includes an inductive conductivity sensor, a PRT temperature sensor, and strain gauge pressure transducer. The sensor has a small size with a diameter of 54mm, and a length of 370mm. It weighs 1.8Kg with titanium housing. The sensor consumes a maximum power of 250mW, and can be supplied by an external 9 - 12 VDC, or an internal battery (1.5V alkaline or 3.6V lithium).

Figure 2-23 A mini CTD from Valeport (with conductivity accuracy of ±0.01mS/cm from 0 to 80mS/cm, temperature accuracy of ±0.01^{o}C in the range of -5 to 35 ^{o}C, and pressure accuracy of ± 0.05% at full scale (FS) of 600Bar.) [208]

Commercial CTD systems may have various designs. The conductivity sensor may either be made from four-electrode or inductive transformer; the temperature sensor may be a thermistor or PRT; the pressure sensor may be a strain gauge or a quartz crystal resonator; and some CTD systems also include a pump to flush the conductivity cell. Most commercial CTD systems are encapsulated in metal cases in order to measure deep sea, and those with titanium housing can go down as deep as 10500 meters. Shipboard CTD systems can provide high quality data for the oceanography scientist since they are designed with the priority of high stability and accuracy. However they are limited to certain application due to their large size and power consumption. Buoyancy-driven gliders and propeller-driven AUVs (Autonomous Underwater Vehicle) are increasingly used for environmental monitoring, search and surveillance missions. Due to the limited space for batteries on such vehicles, it is important that sensors have low power consumption. Also, small sensors with low drag are desirable in order to minimize impact on vehicle flight performance and endurance.

A new GCTD designed for gliders and other AUVs was reported in [180]. It uses a four-electrode conductivity cell, a NTC thermistor, a strain gauge bridge-type pressure sensor (Druck) with internal temperature sensor to achieve excellent dynamic response and high spatial resolution. The conductivity cell features a unique design with plastic side walls and a centre ceramic fin with small thermal mass as shown in figure 2-24. The cell has low flow drag and requires no pump, and is rugged and shaped to avoid fouling by seaweed and other flotsam. The fast response thermistor is positioned within the conductivity cell in order to achieve optimal time constant correction to minimize salinity spiking. The complete sensor includes electronics to interface to the conductivity, temperature and pressure sensor, a reference circuit to provide self calibration, and serial port to transmit data. It was reported that the new GCTD had better spatial resolution and superior dynamic performance over the unpumped SBE-41-CP CTD. The GCTD has modest power consumption and draws about 35mA when supplied by 12 VDC. Thus it is suitable for the application of mounting on modern gliders and AUVs.

Figure 2-24 Fin-cell mounted to the hull of a Webb Slocum Glider [180]

Recently, a small, low cost conductivity, temperature and depth (CTD) system for measurements of salinity in coastal waters was presented in [205]. The system incorporated three low cost expendable sensors: a planar, four-electrode cell; a resistive temperature device (RTD) and a piezoresistive pressure sensor. The conductivity cell and the resistive temperature device were fabricated using printed circuit board (PCB) microelectromechanical (MEMS) techniques combined with a new thin-film material, liquid crystal polymer (LCP). Figure 2-25 shows the CTD system with individual sensors.

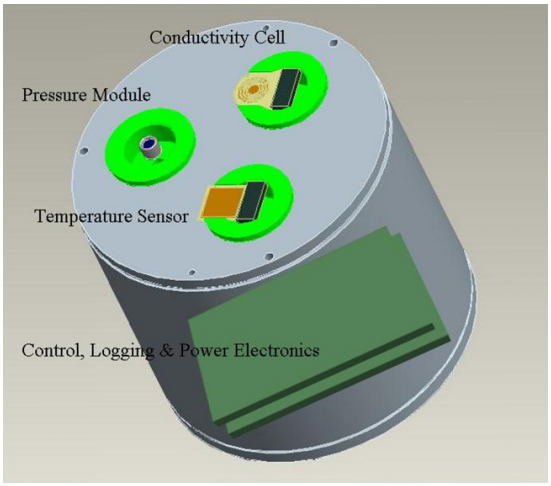

Figure 2-25 PCB MEMS-based CTD with expendable sensors [205]

In Figure 2-25, the three distinct sensors are packaged in independent plugs, and can be quickly replaced if bio-fouled or damaged. The sensor plugs are fitted with an O-ring and mounted in the top end cap of the underwater housing of the system. The watertight acrylic canister houses the circuit boards and internal battery. The bottom end cap contains an underwater connector for communications and external power. The overall dimension of the CTD system is approximately 10 cm in diameter and 10 cm in length. The accuracies for the conductivity, temperature and pressure sensors are

±1.47% from 0 to 60mS/cm, ±0.546°C in the range of 0-50°C and ±0.02 Bar, respectively. The whole CTD system consumes 22 mA when sampling water at 70 mS/cm and can be operated by a 9-volt alkaline battery.

The CTD systems described above can meet the most demands of the oceanographic research, but they are too big to use in special applications such as tagging small fish. Data Storage Tag (DST) is specially designed as an archival fish tag to analyse fish migration, distribution, feeding behaviour, and vertical and horizontal movements. A DST CTD tag measures conductivity, temperature and depth in the fish surroundings and stores the data in an internal memory which can be retrieved after return. A typical DST comprises of a sensor part, interface electronics, a non-volatile memory and an energy source. State of the art tags, such as the Cefas G5 tag and Star-Oddi DST CTD tag are shown in figure 2-26.

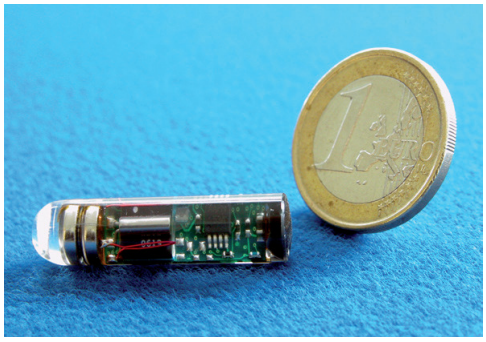

a. Cefas G5 Data Storage Tag [209] b. Star-Oddi DST CTD [210]

Figure 2-26 Commercial DST tags (a, b)

The Cefas G5 Data Storage Tag (DST) shown in figure 2-26a is a tiny temperature and pressure (depth) data logger, which is ideal for tagging small fish and animals. The overall size of the tag is only 8x31mm(diameter x length), and weighs as little as 2.7 gram in air with 10 or 24 month battery life option and up to 1 million readings. The accuracy achieved is moderate with pressure of ±1% at full scale of 2000m, and temperature of ±0.1°C in the range from 2 °C to 34°C. The Star-Oddi DST CTD tag shown in figure 2-26b is the smallest salinity logger current available on the world market, with a total dimension of 17x46mm and weight of 19 gram in air. The

typical battery life of the tag is about 4 year for maximum 87,000 measurements per sensor. The accuracies of conductivity, temperature and depth sensor are ±0.8mS/cm from 10 to 50mS/cm, ±0.1^{o}C in the range of -1 to 40 ^{o}C and ± 0.4% at full scale (FS) of 2000m respectively.

The detailed design of the commercial fish tags are not clear since very few papers have been published for the DST CTD tag due to commercial reasons. Recently, Hyldgard, A., et al. has developed a micro-fabricated multi-sensor chip (4mmx4mm) that can be exposed directly to the sea [232]. The sensor chip based on silicon substrate contains a piezo-resistive pressure sensor, a thermistor, four electrodes conductivity sensor and a pn-junction light sensor. The pressure sensor centred on the chip is made of piezo-resistors (30kΩ) configured as a Wheatstone bridge; the temperature sensor is made of a titanium disilicide ($TiSi_2$) thermistor (1kΩ); the conductivity sensor is made of four platinum electrodes placed in pairs on two sides of the pressure sensor and light sensor. The sensor chip is packaged using an epoxy potted tube to protect vulnerable parts while leaving the sensor area directly exposed to seawater. A low resistance $TiSi_2$ wiring system connects the sensors to contacts in the other end of the chip. The electrodes, the thermistor and the wiring system are isolated from the chip substrate by a silicon dioxide film and protected from the seawater by a silicon nitride (Si_3N_4) film. The photograph and the detailed layout of the chip are shown in figure 2-27.

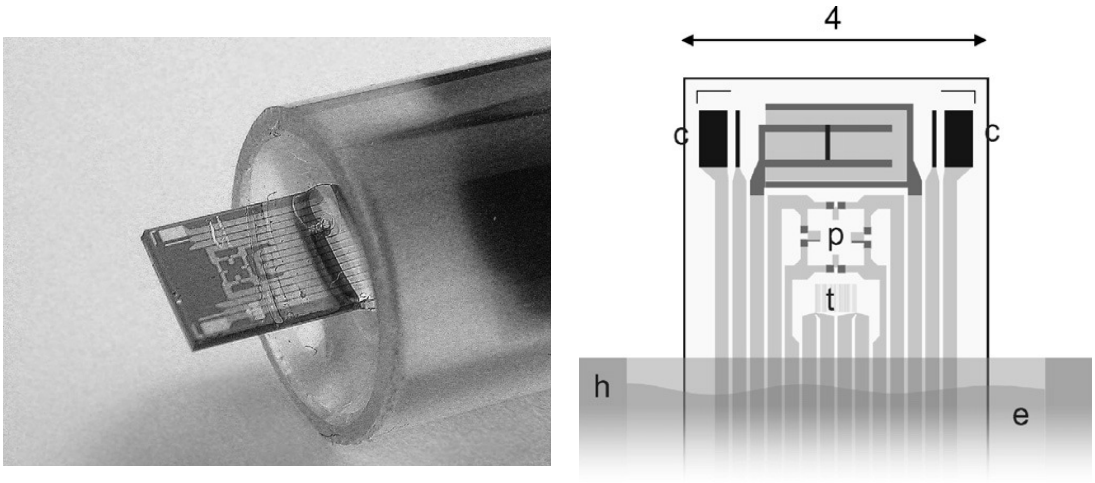

a. Photograph of sensor chip b. Chip (4mmx4mm) layout

Figure 2-27 A micro-fabricated multi-sensor chip including Pressure sensor (P), temperature sensor (T), pn-junction light sensor (L), four conductivity electrodes (C), polystyrene housing (H) and Epoxy (E) [232]

It was reported that the micro-fabricated multi-sensor chip, shown in figure 2-27, had measured conductivity, temperature, pressure accuracies of ±0.6mS/cm, ±0.13°C and ±0.05 bar, respectively. In their study, the temperature effects on conductivity measurement were also investigated, and the result is shown in figure 2-28.

.

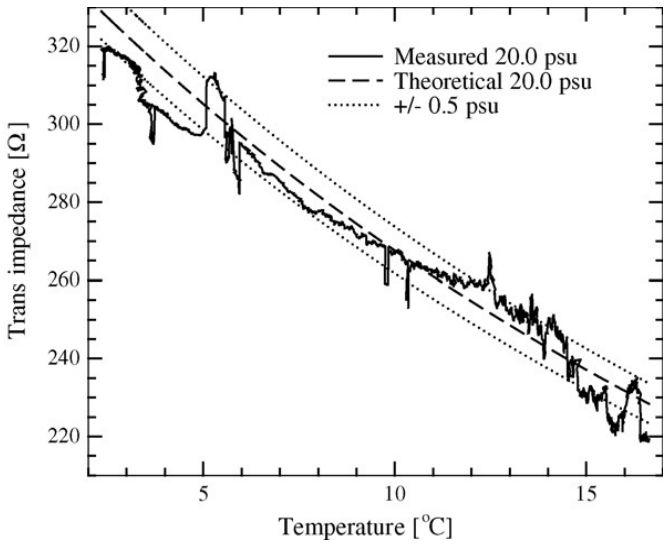

Figure 2-28 Temperature effects on salinity measurement [232]

Figure 2-28 shows that temperature had very strong effects on the conductivity measurement. The trans-impedance of the four electrodes changed from 300 Ω (@ 5 °C) to 230 Ω (@15 °C), which is almost 2.6% per degree. Figure 2-28 also shows the declared the accuracy of ±0.5 psu was achieved in the measurement of a sample with 20psu salinity, which indicates the measurement error is approximately ± 2.5%. Compared with macro-size CTDs (0.5psu vs. 0.005psu), the accuracy of the micro-fabricated multi-sensor is much lower. The possibly reason could be changes in the conditions of the water-electrode interface, caused by air bubbles or residues of salt or organic debris [232]. For bigger electrodes, the average influence by the changes of surface condition is smaller, thus improving measurement accuracy.

To summarize the different CTD systems described above, table 2-4 is given to compare their performance and main characters. Although MK3C/WOCE and SBE 9plus CTDs are more accurate than Star-Oddi DST CTD and Multi-sensor chip (0.003mS/cm, 0.001oC, 0.015% @ FS of 10500m VS. ±0.8mS/cm, ±0.1oC , ± 0.4%

@ FS of 2000m), they are much bigger and consume more power (Power: 34W, Dimension: 952x330x305 mm vs. Power: 200mW, Dimension: 4x4mm). It is a big challenge to miniaturize CTD with reduced power consumption while maintain the high accuracy of precision CTDs such as SBE 9plus CTD. Another issue need to be addressed is the external proximity effect which could cause measurement error when the external electric fields of CTDs disturbed by approaching objects.

Table 2-4 CTD Systems Summary

CTD System	**Conductivity accuracy**	**Temperature accuracy**	**Pressure accuracy**	**Power, weight & dimension**
MK3C/WOCE CTD (figure 2-21)	0.003mS/cm (1~65mS/cm)	0.003°C (-3 ~ +32°C)	0.03% @ FS of 6500m	Power: 4.5W, Weight: 95lbs,
SBE 9plus CTD (figure 2-22)	0.003mS/cm (0~70mS/cm)	0.001°C (-5 ~ +35°C)	0.015% @ FS of 10500m	Power: 34W; Weight: 65lbs, Dimension: 952x330x305mm
MiniCTD Valeport (figure 2-23)	±0.01mS/cm (0~80mS/cm)	±0.01°C (-5 ~ +35 °C)	±0.05% @ FS of 600Bar	Power:250mW; Weight: 1.8Kg, Dimension: Ø54 x L370mm
PCB MEMS CTD (figure 2-25)	±1.47% (0~60mS/cm)	±0.546°C (0 ~50°C)	±0.02 Bar	Power:200mW, Dimension: Ø100 x L100mm
Star-Oddi DST CTD (figure 2-26 b)	±0.8mS/cm (10~50mS/cm)	±0.1°C (-1 ~ 40 °C)	± 0.4% @ FS of 2000m	Weight:19gram Dimension: Ø17 x L46mm
Multi-sensor chip (figure 2-27)	±0.6mS/cm	±0.13°C	±0.05 bar	Dimension: 4x4mm

2.9 Measurement and noise

Oceanographic measurements using sensor technology are affected by different types of noise such as instrument noise, drift and transducer degradation. Although many techniques can be used to improve signal-to-noise ratio (SNR) and to minimise long term drift, identifying and mitigating the causes and prime sources of error in a system is not a simple task.

2.9.1 Thermal Noise

Thermal Noise, also called Johnson noise, has a white frequency spectrum with Gaussian amplitude distribution. Thermal noise is caused by the random motion of charged carriers in any conductor due to ambient heat energy; this in turn creates voltage fluctuations which appear in the readout as noise. Thermal Noise is always presents in resistive elements even in the absence of current flow and it can be measured in terms of a noise voltage:

$$V_{rms} = \sqrt{4\kappa_B TR\Delta f} \qquad [2\text{-}15]$$

where *Vrms* is the root-mean-square of thermal noise voltage, k_B is Boltzmann constant (1.380×10-23J/K), R is resistance in Ohms, T is temperature in Kelvin and Δf is bandwidth in Hz. Equation 2-15 suggests that thermal noise disappears only when the absolute resistance (R) is zero and can be decreased by narrowing the bandwidth (Δf).

2.9.2 Shot Noise

Shot noise is caused by the random signal fluctuations when quantised entities carry information. For example the quantised signal could be derived from charge carriers flowing across a P-N junction, electrons in a transistor or photons in a photodiode. Shot noise has a white frequency spectrum with a Gaussian amplitude distribution. The strength of shot noise depends on the average magnitude of the current or intensity of the light, and it is only a problem when the magnitude of current or light intensity is small. Shot noise is a function of the bias current and the electron charge, the strength of shot noise is normally measured in terms of noise current which is governed by Poisson statistics and given by equation 2-16.

$$I_{rms} = \sqrt{2Ie\Delta f} \qquad [2\text{-}16]$$

where I is the mean current, e is electron charge (e=1.6×10-19), and Δf is the bandwidth in Hz. From equation 2-16, it is clear that shot noise can be minimized by reducing bandwidth (Δf).

2.9.3 Flicker Noise

Flicker noise occurs in all electronic devices at low frequencies and the reason is not well understood. Flicker noise has a magnitude that is inversely proportional to the frequency, thus also known as *1/f* noise. Flicker noise is ubiquitous and recognizable by its frequency dependence; it becomes significant at frequencies lower than 100Hz and even worse for 0Hz when long-term drift occurs at DC. In practical electronic circuits, Flicker noise can be reduced significantly by using wire-wound or metallic film resistors rather than carbon-composition type.

2.9.4 Environmental noise

Environmental noise is a composite of different forms of noise that arise from the surroundings. Electromagnetic radiation is one of the most significant noise sources in instruments; any inductor in an instrument is potentially an antenna capable of picking up electromagnetic radiation and converting it to an electrical signal. There are two regions that are relatively noise free, namely 3 Hz to 60 Hz (except 50 Hz in habited areas due to pick up from domestic AC power) and 1 kHz to 500 kHz, which are often preferred for the design of instruments. Ambient light is another big noise source in an optical detection system, and in the worst case photo-detectors will become saturated if ambient light is too strong.

2.9.5 Chemical Noise

Chemical noise arises from a host of uncontrollable variables that affect the chemistry of the system being analyzed. Examples include undetected variations in temperature or pressure that affect the position of chemical equilibrium, fluctuations in relative humidity that cause changes in the moisture content of samples, vibrations that leads to stratification of powdered solids, changes in light intensity that affect photo sensitivity materials, and laboratory chemical contamination such as fumes interacting with samples or reagents. In a conductivity measurement, electrodes corrosion, degradation, and chemical adsorption could change the surface condition of the electrolyte-electrode interface which will directly add noise to the measurement.

2.10 Lock-in Amplifier

In an electronic system, noise is a complex composite including Thermal Noise (or Johnson noise), Shot Noise, Flicker Noise (or *1/f* noise), Environmental Noise. Figure 2-29 shows the typical noise frequency distribution.

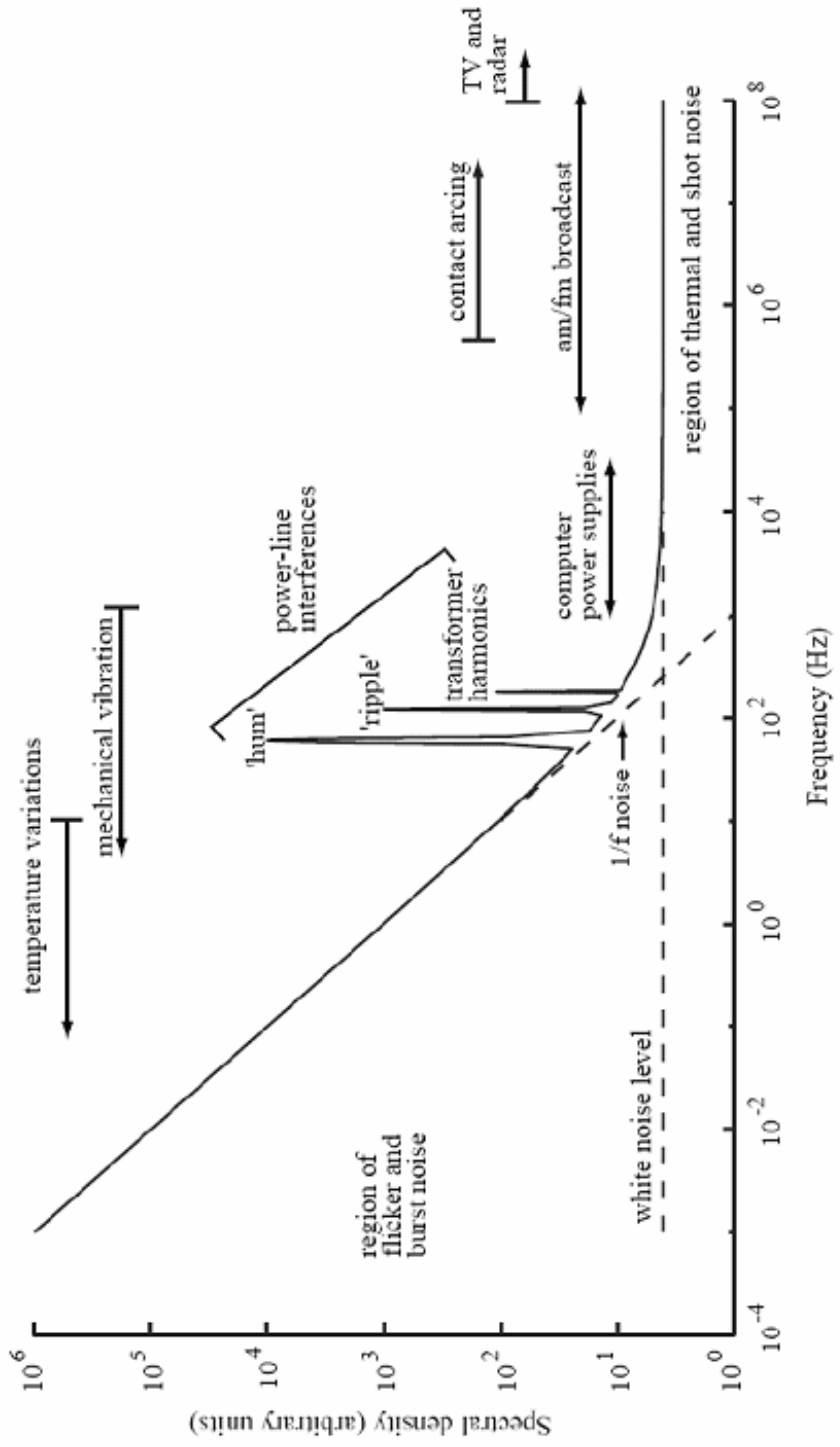

Figure 2-29 Noise Spectrum Diagram [66]

During initial testing of a measurement system, noise interference could be apparent. However, noise generated by electromagnetic radiation can be substantially reduced by shielding, grounding, using twisted wires, and minimizing the lengths of connection wires. Batteries provide very stable and pure voltage output, and are preferred to be used in a measurement system as a power supply. Low frequency (LF) filters are usually used to remove the radio high frequency interference, but the flicker noise (or *1/f* noise) still remains in the low frequency spectrum. Direct amplification of a low-frequency or DC signal is particularly troublesome when an instrument exhibits amplifier drift and flicker noise. Often, this flicker noise is several times larger than the types of noise that predominate at higher frequencies as shown in figure 2-29. One way to relieve this problem is to avoid this region and move the low frequency signal into a higher frequency region.

Modulation is the process which converts a low frequency or DC signal to a higher frequency where flicker noise is less troublesome. Once the signal is modulated, it can be amplified with much less noise and the original low frequency or DC signal can be recovered by demodulation and finally filtering with a low-pass filter. A lock-in amplifier also known as a phase sensitive detector (PSD) is a demodulator which works at a particular frequency. A lock-in amplifier measures an AC input voltage and gives an output in the form of a DC voltage proportional to the value of the AC signal being measured. Figure 2-30 shows the principle of a basic lock-in amplifier.

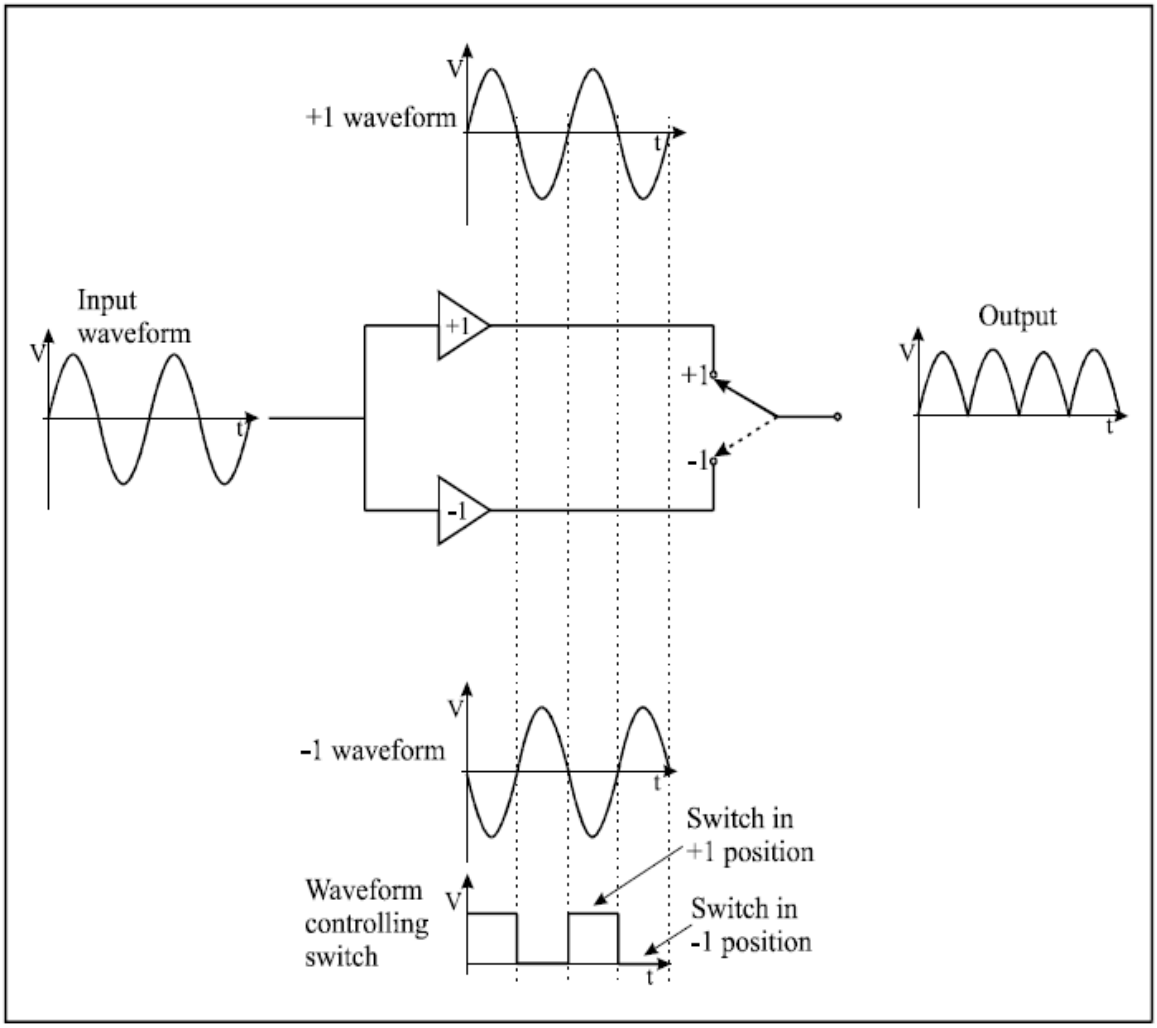

Figure 2-30 Principle of lock-in amplifier [67]

In figure 2-30, the input signal is fed to an inverting amplifier as well as a non-inverting amplifier with both amplifiers having unity gain. The outputs of these two amplifiers are selected by a switch position controlled by the polarity of a reference square wave. The final output signal is a rectified sine wave, thus lock-in amplifiers sometimes are also called synchronous rectifiers. Lock-in amplifiers are very powerful devices, used to recover a very small AC signal buried in noise. The essence of lock-in amplifiers is that it locks to and measures a particular frequency of interest while blocking and rejecting noise signals at frequencies other than the reference frequency. Lock-in amplifiers are widely used in different applications, particularly in optical detection systems to recover small optical signals. The lock-in amplifier can be considered as a multiplier, as in figure 2-31.

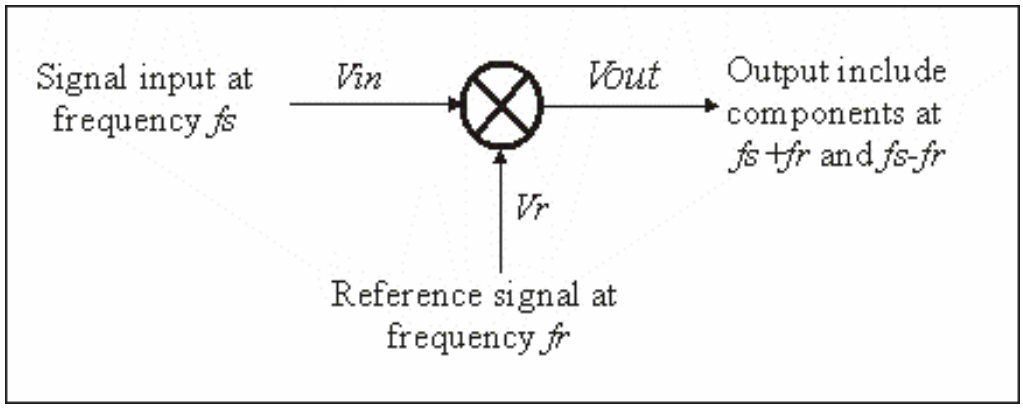

Figure 2-31 Multiplier model of lock-in amplifier

Assuming the input signal V_{in} is a sine wave with peak magnitude V_o and ω is the angular frequency, then the input signal can be represented as below.

$$V_{in} = V_o \sin(\omega t) \qquad [2\text{-}17]$$

If the reference signal V_r is a square wave with the same angular frequency ω but a different phase shift (θ), the analytical Fourier series for a square wave is given by:

$$V_r = \frac{4}{\pi}[\sin(\omega t + \theta) + \frac{1}{3}\sin(3\omega t + \theta) + \frac{1}{5}\sin(5\omega t + \theta) - \ldots] \qquad [2\text{-}18]$$

The output signal V_{out} of the lock-in amplifier is simply the multiplication product of V_r and V_{in}:

$$V_{out} = V_r \times V_{in} \qquad [2\text{-}19]$$

Insert equation 2-17 and 2-18 to equation 2-19, obtain equation 2-20

$$V_{out} = \frac{4}{\pi} V_o [\frac{1}{2}\cos(\theta) - \frac{1}{3}\cos(2\omega t + \theta) - \frac{1}{15}\cos(4\omega t\ \omega t + \theta)$$

$$- \frac{1}{35}\cos(6\omega t + \theta)\ldots] \qquad [2\text{-}20]$$

Equation 2-20 shows that the output has a DC level proportional to the input voltage. If the output signal V_{out} is passed through a low pass filter, the AC signals are removed, giving a DC output.

$$V_{out} = \frac{2}{\pi} V_o \cos(\theta) \qquad [2\text{-}21]$$

From equation 2-21, it is clear that the output voltage is not only related to the input voltage but also the phase shift (θ). A maximum output voltage can be obtained if the phase shift (θ) is eliminated. The output low pass filter is an essential part of the lock-in amplifier used to remove the high frequency AC from the DC output of lock-in amplifier. Often a low pass filter with narrow bandwidth is preferred to improve the output signal-to-noise ratio (SNR). The improvement factor is given by the ratio between the input bandwidth (B_I) and output bandwidth (B_O):

$$SNR_O = \frac{B_I}{B_O} \bullet SNR_I \qquad [2\text{-}22]$$

Where SNR_O and SNR_I are the output and input signal-to-noise ratio respectively. For a lock-in system with input bandwidth of 1kHz and a low pass filter with a 2 Hz cut off frequency, the output signal-to-noise ratio is improved by 500 times.

It is because the above mentioned merits, lock-in amplifiers are frequently used in a high precision measurement instruments to recover weak signal and improve SNR performance. In the application of optical sensors with strong interference from ambient light, light modulation together with lock-in amplifiers provide a good solution to remove the out of band noise.

2.11 Summary and conclusions

This chapter presents prior research and development of ocean sensors for marine application. Although there are various sensors to measure different properties of ocean, few of them are suitable for in-situ mass deployment applications due to their high cost, big dimension and power consumption.

It is a challenge to miniaturize various ocean sensors while maintaining their high accuracy. Modern technologies such as the latest advancement of microelectronics, LOAC and MEMs may provide viable solutions for the development of new generation micro sensor suitable for in-situ application.

Chapter 3 A Double Beam Spectrophotometer for Nitrite Detection

Lab spectrophotometers are widely used for chemical analysis in water, but they are not suitable for in-situ application where size and power consumption become the main consideration. This chapter presents a double beam spectrophotometer designed for in-situ nitrite detection in ocean.

3.1 System Design

The system design includes a microfluidic device and an electronic circuit. An optical sensor block was built to verify the electronic circuit since a microfluidic device was not available at that stage. The electronic circuit is based on the structure of a double beam spectrophotometer which includes one light source and two photo-detectors. The advantage of a double beam spectrophotometer is reduction of the common mode noise by using differential or division amplifier [64]. Common mode noise sources include turbidity or coloured dissolved matter in the sample, and variations in the light source. In order to improve the SNR, two lock-in amplifiers are also used in the design to reduce the effect of light source noise and the flicker noise (*1/f)* generated in the pre-amplifier. Figure 3-1 shows the block diagram of the system design.

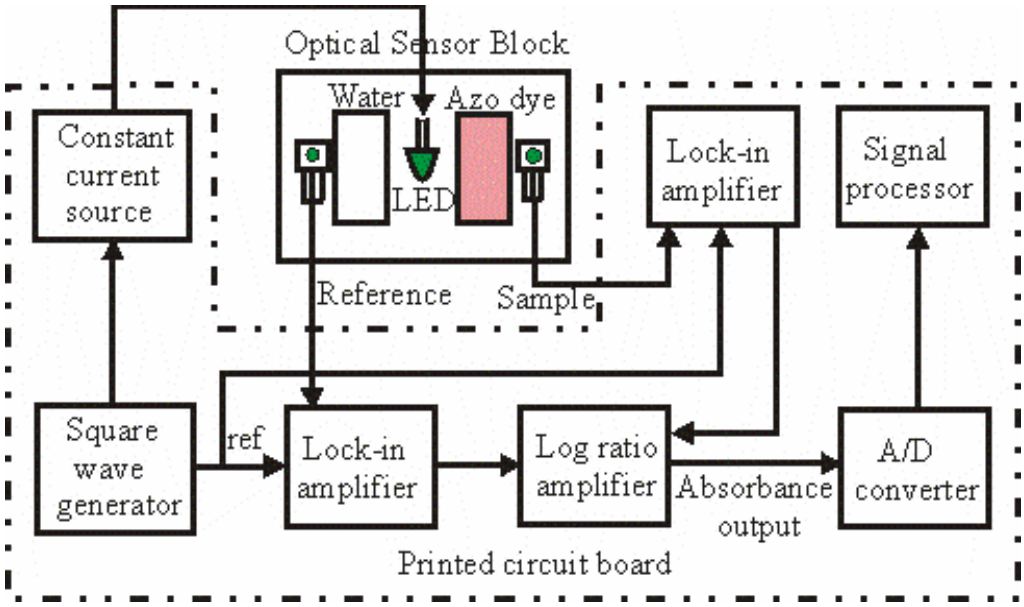

Figure 3-1 Block diagram of system design

In Figure 3-1, the green LED is driven by a constant current source modulated by a square wave. The two photo-detectors are integrated optical sensors which include a photodiode and a trans-impedance amplifier. After pre-amplification, the reference and sample are sent to two lock-in amplifiers. The modulated signals of reference and sample are demodulated by two lock-in amplifiers which are used to remove all out of band noise sources such as out of band shot noise and Johnson noise, the interference of ambient light and low frequency flicker noise of the pre-amplifier circuits. The lock-in amplifier recovers the modulated signal synchronously, and any frequency other than the modulated signal is removed. The DC output voltages from the two lock-in amplifiers are sent to a log ratio amplifier where a voltage directly proportional to the absorbance is obtained without further calculation.

3.2 Signal Processing

From equation 2-2, the relationship between absorbance and the concentration of a sample is governed by the Beer Lambert law. For a given analyte at a specified wavelength (λ), the molar extinction coefficient is a constant which means the absorbance is a linear relationship with concentration. The transmittance (T) is the ratio of radiant power transmitted (P) by a sample to the radiant power incident (P_o) on the sample:

$$T = P / P_o \qquad [3\text{-}1]$$

Absorbance (A) is defined as the logarithm (base 10) of the reciprocal of the transmittance:

$$A = log_{10} \frac{1}{T} = log_{10} \frac{P_o}{P} \qquad [3\text{-}2]$$

In instrumentation design, the measurement is usually made in transmittance (T) which is converted to absorbance (A). The photo-detector used in this design has a photo diode integrated with a trans-impedance amplifier with a linear relationship between the input light intensity (I) and output voltage (V_S), thus the transmittance (T) can be calculated as:

$$T = \frac{P}{P_o} = \frac{I}{I_o} = \frac{\alpha I}{\alpha I_o} = \frac{V_S}{V_{So}} \qquad [3\text{-}3]$$

I is the light intensity after passing through the sample and I_o is the initial light intensity before entering the sample, α is the coefficient due to light loss in background, V_{So} is the voltage output from the sample photo-detector (SPD) with blank solution, and V_S is the voltage output of the sample photo detector (SPD) when filled with sample liquid. Since we use the double beam structure in our design, the term of V_{So} can be replaced with V_R (the output voltage of the reference photo detector--RPD) if the double beam system is balanced with both channels filled with blank solution.

$$T' = \frac{V_S}{V_R} = \frac{V_S}{V_{So}} \qquad [3\text{-}4]$$

The absorbance is given by

$$A' = -log_{10} T' = -log_{10} \left(\frac{V_S}{V_R} \right) \qquad [3\text{-}5]$$

3.3 LED and Photo-detector

As mentioned previously, nitrite is measured using the Greiss action to form a coloured product. This Azo dye is a pink-coloured product with the peak absorption at a wavelength of about 540nm. Conventional spectrophotometers use quartz-tungsten-halogen (QTH) lamps as light sources and monochromators to select the 540nm wave length. The drawback of QTH lamps is that they are expensive and consume a lot of power (typical 100W); furthermore their size restricts their application in a miniaturized system. LEDs are efficient with low power consumption (30-60mW); the average commercial solid-state lighting (SSL) currently outputs 32 Lumens per Watt (Lm/W), and new technologies promise to deliver up to 80 Lm/W [59]. LEDs are attractive since more and more mono-coloured (though not mono-chromatic (typical FWHM ≈40nm)) high intensity LEDs are commercially available. Compared with incandescent light bulb, LEDs have a lot of advantages:

- LEDs emit light of an intended colour without the use of colour filters.
- The shape of the LED package allows light to be focused. Incandescent and fluorescent sources often require an external reflector to collect light and direct it in a useable manner.
- LEDs are insensitive to vibration and shock, unlike incandescent sources.
- LEDs are built inside solid cases that protect them, making them hard to break and extremely durable.
- LEDs have an extremely long life span: typically ten years, twice as long as the best fluorescent bulbs and twenty times longer than the best incandescent bulbs.
- LEDs give off less heat than incandescent light bulbs with similar light output.
- LEDs light up very quickly. An LED will achieve full brightness in approximately 0.01 seconds, 10 times faster than an incandescent light bulb (0.1 second).

In this design, a mono colour LED (E1L31-AG0A-02) from TOYODA GOSEI was chosen as the light source. The wave length characteristics of 4 different colour LEDs from TOYODA GOSEI are shown in figure 3-2. The green LED has a peak wave length of 525nm and 40nm FWHM.

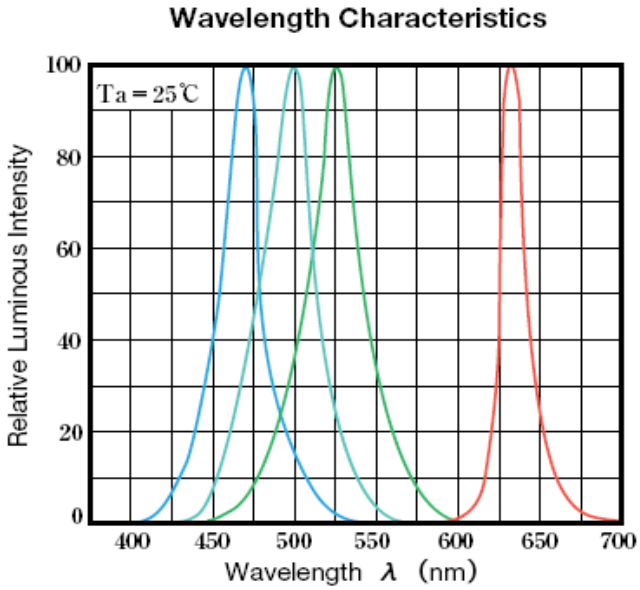

Figure 3-2 Wavelength characteristics of color LEDs [60]

The photo-detector (TSLG257) is a highly sensitive light-to-voltage optical converter and incorporates an integrated green optical filter (FWHM 47nm). The device combines a photodiode and transimpedance amplifier on a single monolithic CMOS integrated circuit. The output voltage of the device is directly proportional to light intensity (irradiance) on the photodiode. Each device has a transimpedance gain of 320 MΩ with improved offset voltage stability and low power consumption. The noise is low and the typical value is 200 µV RMS at 1 kHz bandwidth. Figure 3-3 shows the spectral response of the photo-detector.

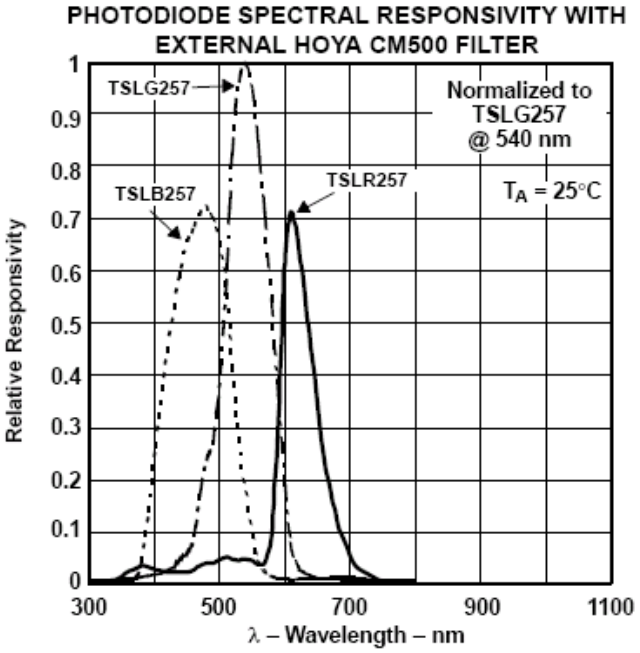

Figure 3-3 Spectral response of photo-detector TSLG257 [61]

3.4 Circuit design

To make the light source stable, a constant current source is used to drive the green LED. This constant current source is further modulated to a square wave in order to improve signal-to-noise ratio (SNR) using Lock-in amplifiers. The demodulated signals are further processed by a log ratio amplifier to obtain the absorbance.

3.4.1 Constant Current Drive

Light Emitting Diodes (LEDS) have a p-n junction and emit light when a forward current pass through the p-n junction. Equation 3-6 is the ideal diode equation used to approximate the p-n diode's I-V characteristic in the forward-bias region.

$$I = I_0 \left(Exp \{ \frac{eV}{kT} \} - 1\right) \qquad [3\text{-}6]$$

where I is the diode current, I_0 is the diode's saturation current, V is the voltage across the diode. The voltage versus current characteristics of LEDs is approximately exponential which means a small voltage change results in a big change of current. If a constant current is applied to a LED, the voltage across the p-n junction is stable over the LED operating range and the power can be considered to be almost proportional to the current. Therefore a constant current source is suitable for driving a LED in order to maintain a constant power across variations in supply.

In electro-optical systems, light chopping is the technique often used to modulate a light signal. A square wave modulated current source has the same function as mechanical light chopping but does not need any shutter and driving motor. The square wave generator used in this design is realized by a simple relaxation oscillator which has a square wave output directly controlling the constant current source.

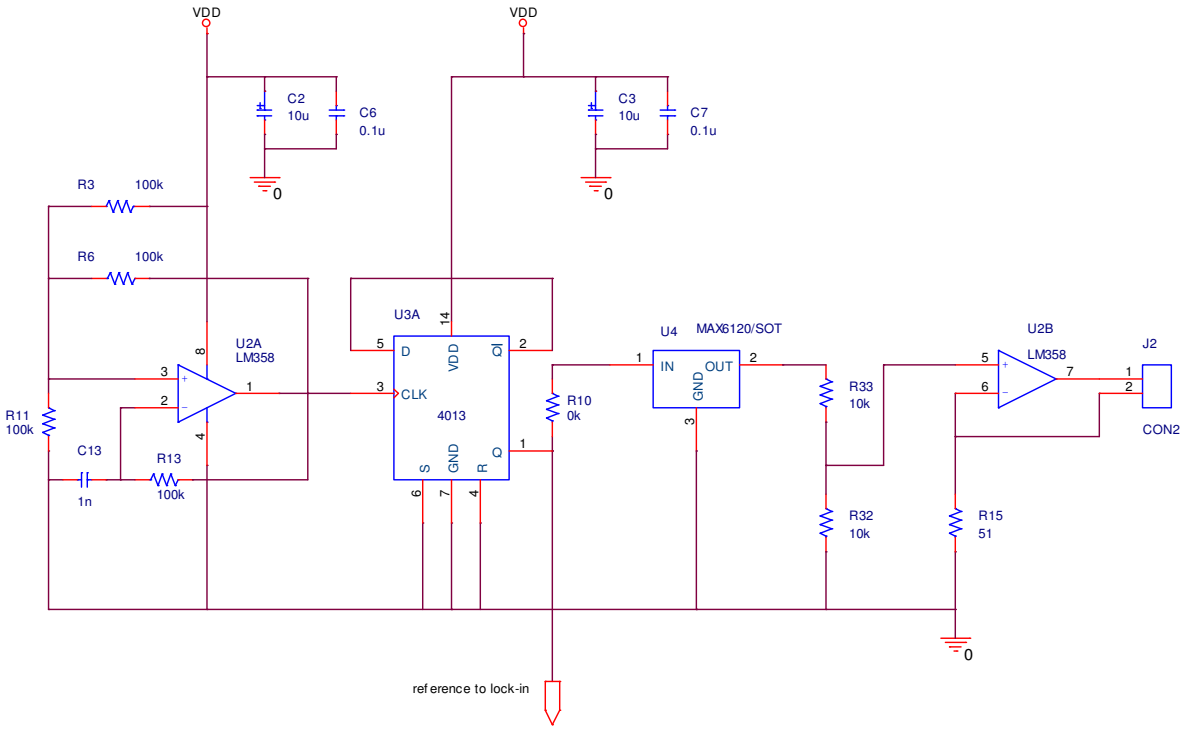

Figure 3-4 Square wave modulated constant current source

In figure 3-4, the relaxation oscillator consists of an opamp (*U2A*) and some resistors and capacitors; the frequency of the oscillator is set to 2 kHz and can be tuned by *R13* and *C13*. *U3* (HC4013) is a dual D-type flip flop which is configured as a two-divider in the design. The signal from the oscillator is divided by two to ensure the output square wave has a duty cycle of 50% which is essential for the lock-in amplifier. The output square wave from *U3* is then fed into a voltage reference *U4* (MAX6120) which outputs a well defined voltage with 1.2V amplitude and is further divided by a resistor network. *U2B* is configured as constant current controller and the current feed back is achieved through the resistor *R1*. The current is a constant value and given by:

$$I_{LED} = \frac{1.2V * (10K / 20K)}{R1} = \frac{0.6V}{51\Omega} \approx 11.8mA \qquad [3\text{-}7]$$

3.4.2 Lock-in amplifier design

Analog devices' AD630 is a balanced modulator/demodulator which is suitable as lock-in amplifier [68]. This device is attractive for its high performance and it can be used with only a small number of external components. To take advantage of low

environmental noise, the reference frequency for the lock-in amplifier is chosen around to be 1 kHz, which is also the upper frequency of the photo-detectors (TSLG257). Figure 3-5 shows a simple lock-in amplifier design using AD630.

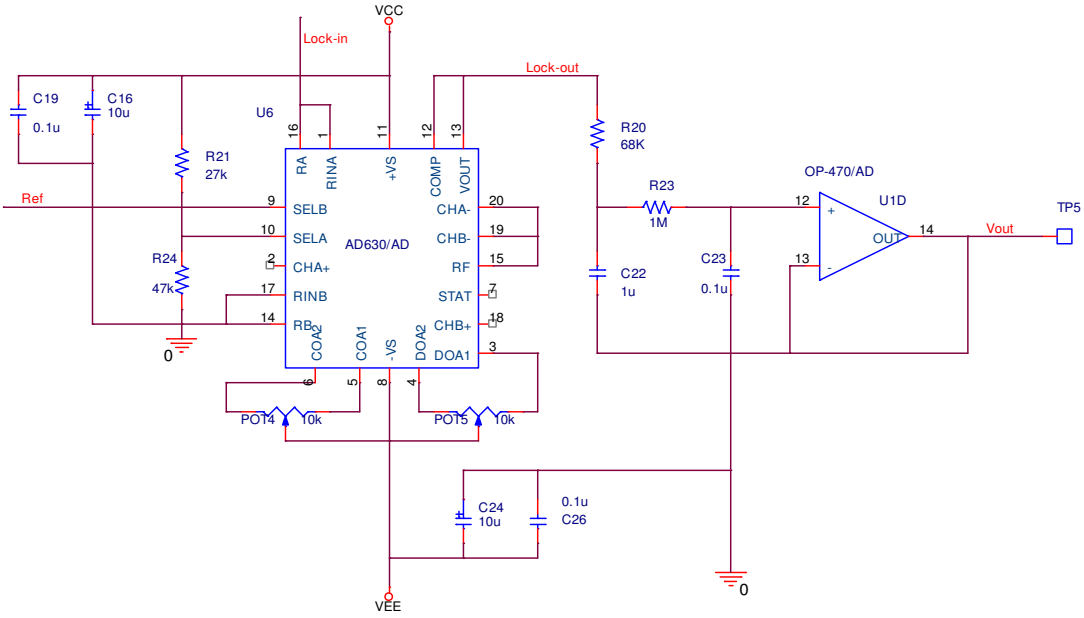

Figure 3-5 Schematic of Lock-in Amplifier

The input signal from the pre-amplifier is connected to pin 1 (*RINA*) and pin 15 (*RA*). The reference signal from the phase shifter is connected to pin 9 (*SELB*) which is an input of a comparator used to control an internal switch. Pin 13 (*VOUT*) is the output of AD630 connected to low pass filter (LPF). When the reference signal is low voltage, AD630 is switched to a non-inverter amplifier with a gain of +2; when the reference signal is high, AD630 is switched to an inverter amplifier with a gain of -2. In this way, the signal is demodulated by the reference signal and the flicker noise from the pre-amplifier is greatly reduced. Figure 3-6 shows the rectified output wave form of AD630 and the synchronous signal.

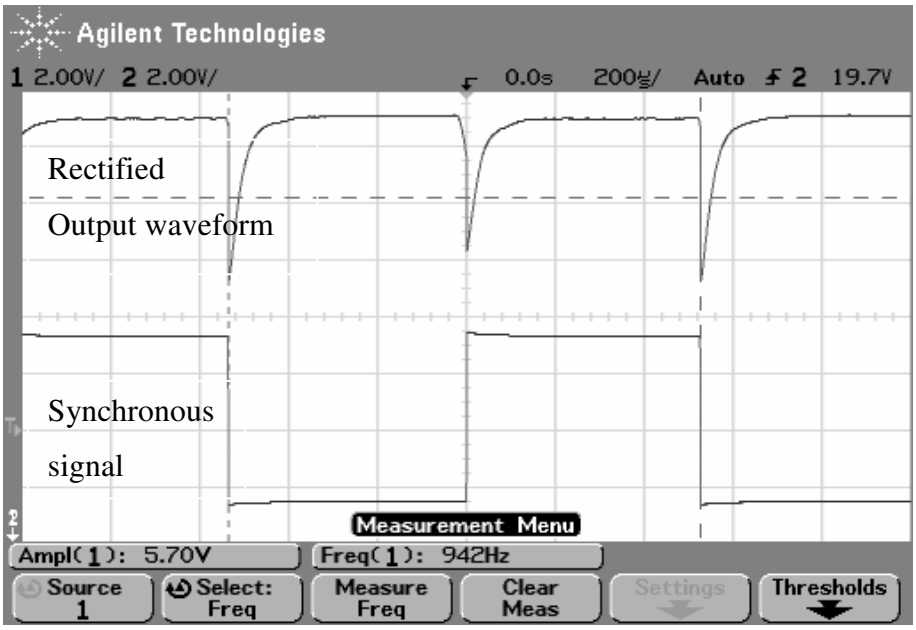

Figure 3-6 Output waveform of synchronous Rectifier

3.4.3 Low Pass Filter

A low pass filter is an essential part of a lock-in amplifier and is used to remove the high frequency AC from the DC output of lock-in amplifier. In this design, a two pole active filter is chosen as the low pass filter used in the output of the lock-in amplifier. The filter uses a Sallen-Key filter structure and is configured as a Butterworth low pass filter with unity gain. The circuit of the filter is shown in figure 3-7. The cut off frequency of the low pass filter is set to about 2.1 Hz and the detailed calculation is given below.

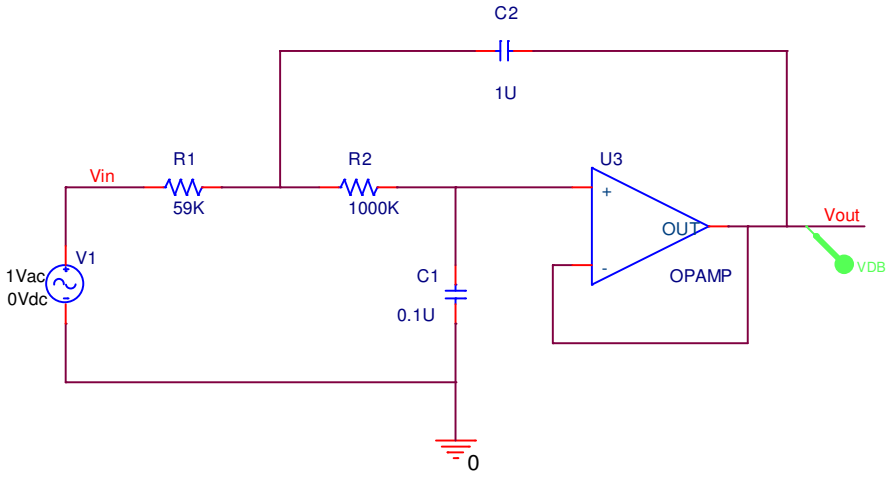

Figure 3-7 Second order low pass filter

The transfer function of the filter is given as:

$$A(s) = \frac{1}{1 + C_1(R_1 + R_2)s + R_1R_2C_1C_2s^2} \qquad [3\text{-}8]$$

Substitute $s = j\omega,$

Then $$A(f) = \frac{1}{1 + C_1(R_1 + R_2) * j2\pi f - R_1R_2C_1C_2 * (2\pi f)^2} \qquad [3\text{-}9]$$

Compare with the standard frequency domain of second order low pass filter given in equation 3-10:

$$H(f) = \frac{k}{-(\frac{f}{f_C})^2 + \frac{jf}{Qf_C} + 1} \qquad [3\text{-}10]$$

We have $$f_C = \frac{1}{2\pi\sqrt{R1R2C1C2}} \text{ , and } Q = \frac{\sqrt{R1R2C1C2}}{C1(R1 + R2)} \qquad [3\text{-}11]$$

Assume $R1 = mR, \quad R2 = R, C1 = C, C2 = nC$

Then $$f_C = \frac{1}{2\pi RC\sqrt{mn}} \quad , \quad \text{and } Q = \frac{\sqrt{mn}}{m+1} \qquad [3\text{-}12]$$

For Butterworth low pass filter, typically $Q = 0.707$,

If $R = 1M\Omega, \qquad C = 0.1uF,$

Then $f_C = 2.13Hz,$

And $$2.13 = \frac{1}{2\pi * 0.1 * \sqrt{mn}}, \quad \text{and } 0.707 = \frac{\sqrt{mn}}{m+1} \qquad [3\text{-}13]$$

Solve equation 3-13, we obtain:

$$m \approx 0.058, \ \ and \ \ n \approx 9.6$$

Choose the standard value for resistors and capacitors:

$$R1 = mR = 58K\Omega \approx 59\ K\Omega,$$

Thus $$C2 = 0.96uF \approx 1uF$$

Figure 3-8 shows the PSPICE simulation, showing that the -3dB corner frequency is around 2.12Hz, which is in good agreement with the calculation.

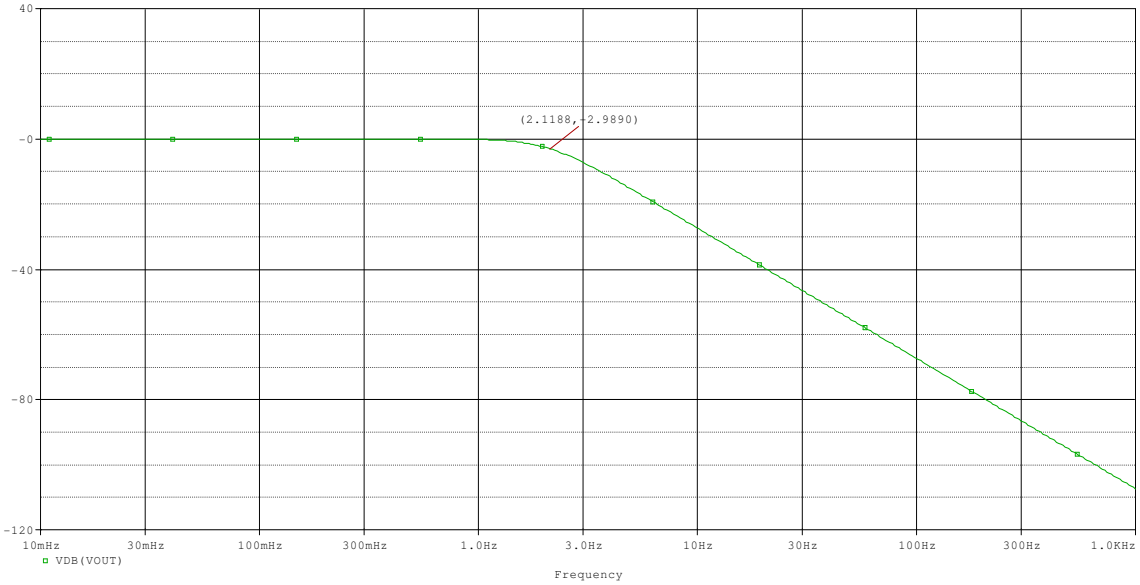

Figure 3-8 Frequency response of low pass filter

3.4.4 Phase shift

In addition to the input signal, a reference signal is also needed in a lock-in amplifier to give the specified reference frequency and phase. In electronic circuits, almost all of the signals have some time delay when they arrive at the input of the lock-in amplifier. Thus it is necessary to adjust the phase of a reference signal in order to get maximum output signals. A phase shifter is usually included which may be simply a RC circuit. One major issue of RC phase shifters is the nonlinearity between phase shift and component value, furthermore the precise value of the phase shifter depends on the stability of additional components such as comparators.

An alternative solution is the use of a phase sensitive detector which can be triggered by a phase-coupled input signal. LM565 is a general purpose Phase Locked Loop (PLL) which contains a phase detector, low pass filter and highly linear voltage-controlled oscillator (VCO) [69]. A block diagram of LM565 used as phase shifter is shown in figure 3-9.

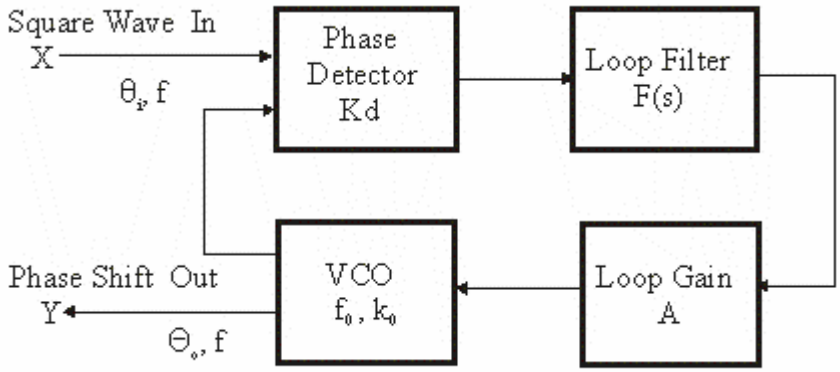

Figure 3-9 Block diagram of the phase-shift generator

When a signal with frequency f_{in} and phase θ_{in} is input to the *X* terminal, after the transient state, the VCO outputs a signal with the same frequency but different phase on the *Y* terminal. The actual phase shift between the input and output is directly related to the difference between the free running frequency (f_0) and input frequency (f_{in}) [70], and is given by equation 3-14.

$$\Delta\theta = \frac{\pi}{2} - \frac{(f_{in} - f_0)}{K_0 \cdot K_d \cdot A \cdot f_0} \qquad [3\text{-}14]$$

where $\Delta\theta$ is the phase difference between the input and the output signals of the VCO, K_0 is the conversion coefficient of VCO, K_d is the conversion coefficient of the phase detector (PD), and A is the gain of the loop amplifier. If K_0, K_d, f_{in}, and A remain constant during operation, then the appropriate phase shift $\Delta\theta$ can be produced by changing the free running frequency (f_0) of the PLL.

$$f_0 = \frac{0.3}{R_0 C_0} \qquad [3\text{-}15]$$

These calculations are only valid under the lock condition of the PLL. In the lock situation, the transfer function of the loop filter can be assumed to have a unity gain after the transient condition has been completed. The dynamic parameters of the loop filter determine the natural frequency of the PLL and its transient response. The natural frequency limits the maximum frequency where the PLL can be operated, and anything above the natural frequency will degrade the phase accuracy, caused by the excessive phase jitters of the VCO in the PLL. Figure 3-10 shows the design using LM565 as a phase shifter.

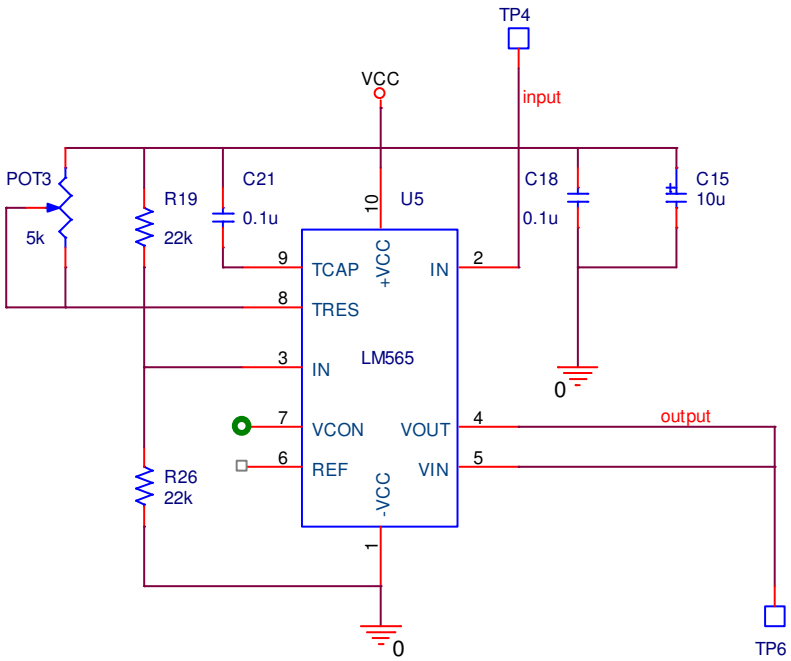

Figure 3-10 Schematic of phase shifter

3.4.5 Log ratio amplifier

The LOG100 is a log ratio amplifier from Burr-Brown which is a suitable for absorbance measurement. The circuit uses a specially designed thin film monolithic integrated circuit which contains amplifiers, logging transistors, and low drifting thin-film resistors. The resistors are laser-trimmed for maximum precision. FET input transistors are used for the amplifiers whose low bias currents (1pA typical) permit signal currents as low as 1nA while maintaining guaranteed total errors of 0.37% FSO maximum [71].

The LOG100 can achieve its guaranteed accuracy without any user trimming, and only simple adjustments of scale factor, offset voltage, and bias current is needed if enhanced performance is desired. Figure 3-11 shows the circuit for the log ratio amplifier configuration.

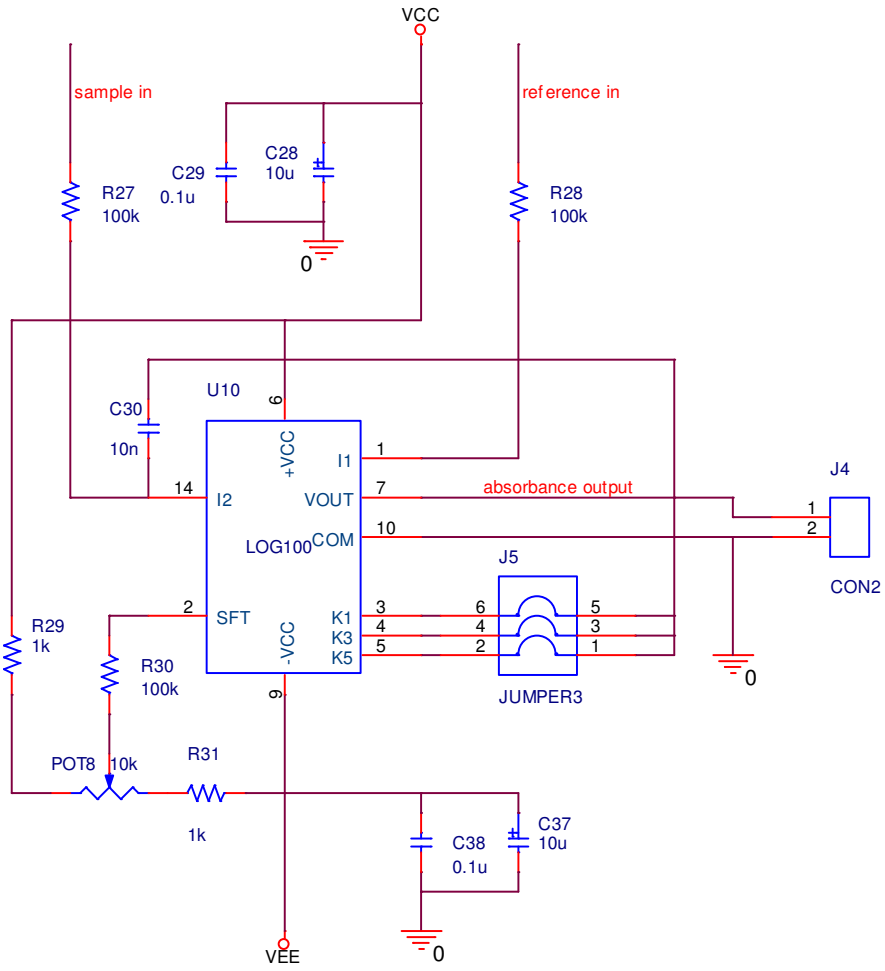

Figure 3-11 Schematic of log ratio amplifier

The sample and reference signals are connected to pin 14 and pin 1 respectively, *POT 8* is used for offset adjustment, and *J5* is used for scaling factor selection. The voltage output at pin7 is directly proportional to absorbance with no further calculation required. The outputs of photo-detectors (V_S and V_R) are permanently connected to the inputs of LOG100 which means the reference and sample signals are always collected at the same time, and a signal proportional to the absorbance is immediately obtained from the output signal without any calculation. Since the measurement of the two signals is simultaneous, the measurement errors inherited in a single beam system caused by measuring sample and reference at different time are avoided.

3.5 PCB layout

In this design, Orcad CAD was used to draw the schematic diagram as well as the PCB layout. The circuits were tested on breadboard before the prototype PCB was built. The components lists and schematic diagram are included in Appendix D and F, and the picture of the prototype PCB is shown in figure 3-12.

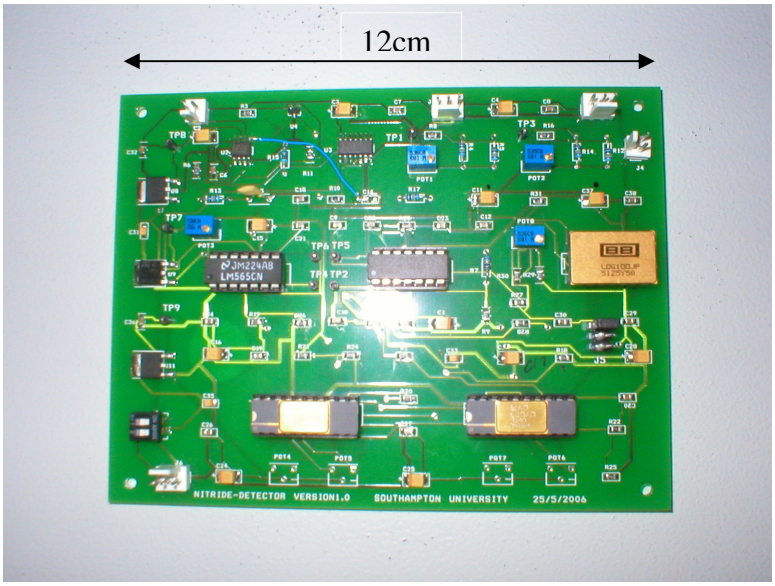

Figure 3-12 Prototype PCB of the double beam spectrophotometer

To make the PCB design compact, SMT (Surface Mount Technology) components were used. However the main IC chips are only available in TH (Through Hole) package, thus the PCB design is a hybrid approach. Since the PCB board includes a relaxation oscillator and a current source, the switching frequency and current pulse could be a source of noise. In order to reduce interference from the power

supply, decoupling capacitors are used for every IC and capacitors are mainly tantalum and ceramic with low ESR (Equivalent Series Resistance). In this design, linear voltage regulators are used to supply power. The power consumption is 1 Watt when the LED is driven by a 12 mA pulse current with a duty cycle of 50%. Compared with switching mode voltage regulators, the linear voltage regulators are less efficient but they have an advantage that there is no high frequency switching which could produce noise in the power supply. The width of power and ground tracks was increased to reduce the track resistance, thus reducing voltage drop and errors.

The PCB function was tested before nitrite measurement experiment. It worked as expected proving the circuit design is successful.

3.6 Conclusions

A successful prototype double beam spectrophotometer has been designed for absorbance measurement of nitride in seawater. Compared with the lab standard spectrophotometers, the designed double beam spectrophotometer is simple and compact with low power consumption (1W).

A new phase shifter using PLL technique was realized in the design which is used with lock-in amplifiers with square wave modulation. The signal noise ratio is improved by the lock-in amplifiers used in this design, removing the interference from ambient light as well as the flicker noise produced by the pre-amplifiers. The design also uses a log ratio amplifier to process the reference and sample signal simultaneously and a voltage proportional to the absorbance is the direct output.

Chapter 4 Double Beam Spectrophotometer Test and Discussion

This chapter presents the test results of the in-house made double beam spectrophotometer; main issues found in the experiments are also discussed.

4.1 Test and Instruments

A UV-Visible spectrophotometer (Cary 1Bio UV-Vis Spectrophotometer with wavelength range 190 - 900 nm, wavelength accuracy +/- 0.2nm, slit width/band width 0.2 to 4.0nm in 0.1nm steps, photometric range (ABS) 3.5A.) was used as a benchmarking system to obtain a calibration curve and to evaluate the in-house made double beam spectrophotometer operation. The output voltage of the in-house made spectrophotometer was measured by a true RMS multimeter (Fluke 187) and an oscilloscope (Agilent 54621D) in the average voltage mode. A temporary sensor block (consisting of the required optical elements and two standard cuvettes, see figure 4-2) was built for experiments. In the experiments, a food dye was placed in the sensing arm of the double beam spectrophotometer in the initial test, nitrite detection was subsequently evaluated by the formation of Azo dye. Figure 4-1 shows the experimental setup.

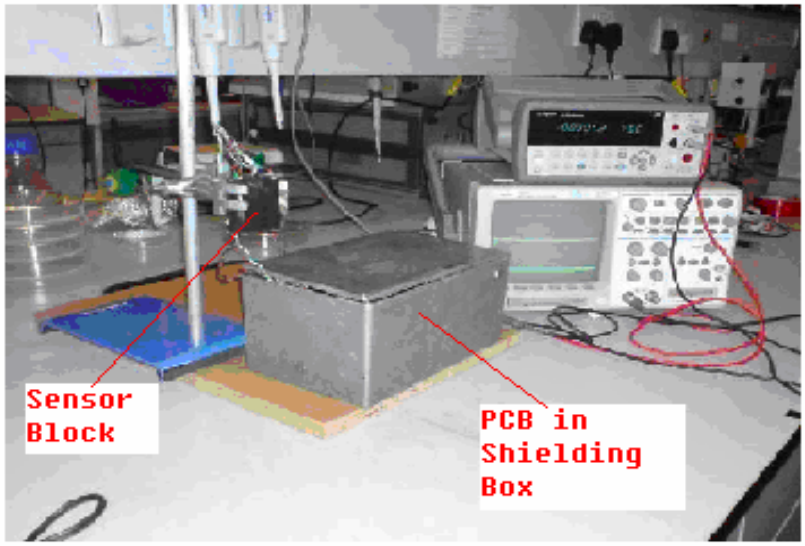

Figure 4-1 Spectrophotometer experiment setup

4.2 Sensor Block

The sensor block consists of two cuvettes, one green LED (E1L31-AG0A-02) and two photo-detectors (TLSG257). The structure of the sensor block is shown in figure 4-2. The LED is fixed in between two cuvettes by casting resin to prevent shock and vibration. Two black plastic boards with holes (Ø1mm) were used to separate the LED from cuvettes which formed apertures to limit the intensity and control the direction of the light. Two photo-detectors are mounted on the outsides of cuvettes with black plastic boards used to prevent stray light. The holes in the two plastic boards are covered by two interference filters (Filter INT 540NM, Edmund Optics λp 540nm, FWHM 10nm) to provide spectral filtering which improves the measurement linearity. The whole assembly of the sensor block is wrapped by black tape to prevent the interference from ambient light which may cause the photo-detectors to saturate.

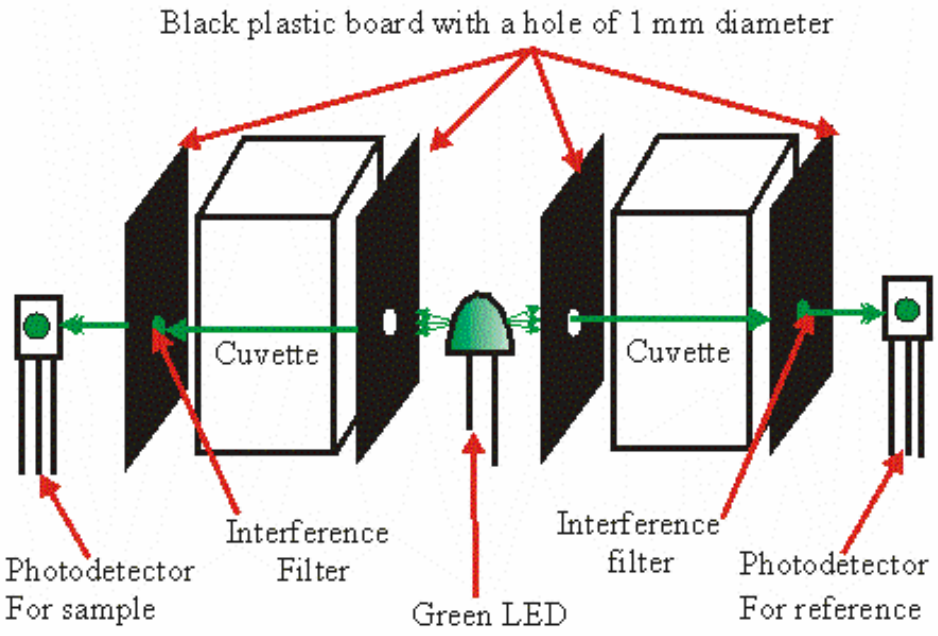

Figure 4-2 Diagram of temporary sensor block, using a green LED as light source and two photodetectors as sensors, the sample and reference solution are contained in two cuvettes

4.3 Experiment with Red dye

A red food dye was used with peak absorbance at 500nm and figure 4-3 shows a spectrum of the dye.

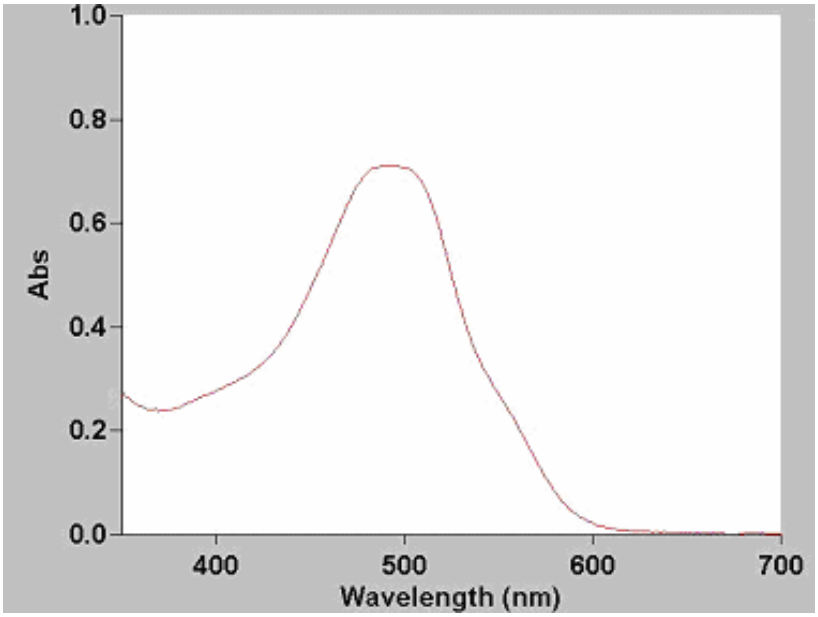

Figure 4-3 Red food dye absorbance spectrum

The dye absorbance was measured on the benchmarking (Cary 1Bio) and then again with the in-house made spectrophotometer. Pure water was used as a reference, and the red dye was diluted with tap water and then poured into the sample cuvette. The absorbance test result of the red dye is shown in figure 4-4.

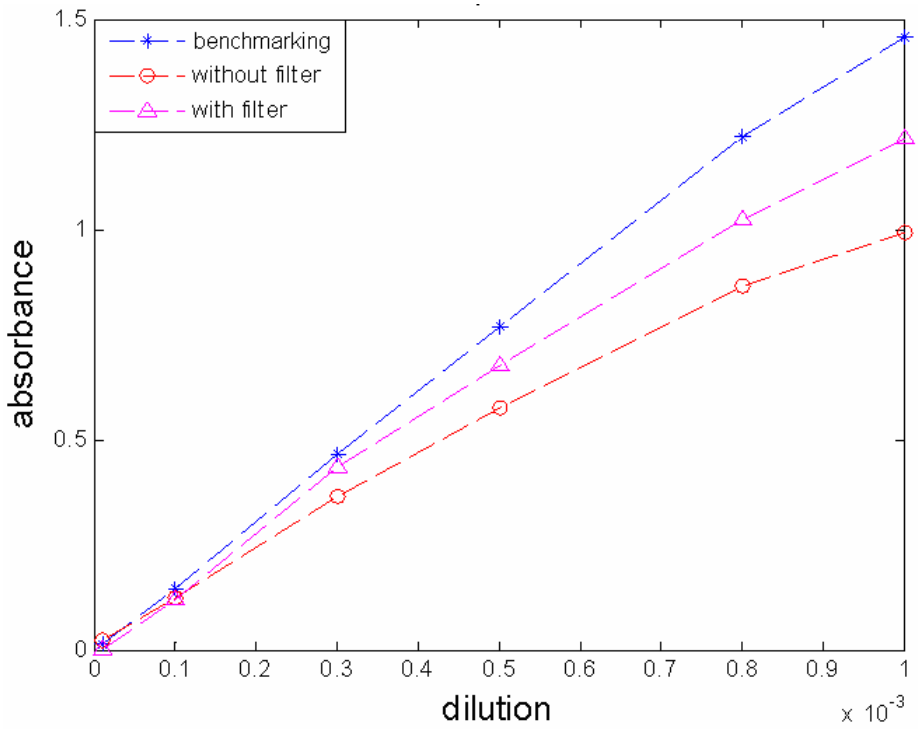

Figure 4-4 Absorbance measurement of red dye, a red food dye diluted with tap water used as samples measure by the benchmarking (blue dots), and then the in-house made spectrophotometer with (pink dots) and without (orange dots) interference filters.

In figure 4-4, the blue line is the calibration curve measured by the benchmarking; both the pink and orange lines are data from the in-house made spectrophotometer with and without interference filters. The calibration curve shows that the relationship between absorbance and dilution is linear at high dilution, but that deviation occurs at low dilution, particularly when the absorbance is above 1. This is because Beer's law is limited to relatively low analyte concentration [72]. At high concentration (usually >0.01M), the average distance between the molecules responsible for absorption is diminished to the point where each molecule affects the charge distribution of its neighbours. This interaction, in turn, can alter the ability of the molecules to absorb a given wavelength of radiation. Another limitation of Beer's law is that it is valid only when the incident light is monochromatic [72]. In practice, it is not easy to produce a pure single wavelength, but approximation can be achieved by

using light with very narrow bandwidth. For polychromatic radiation, deviation always occurs and the linearity of the curve can be improved by narrowing the bandwidth of the incident light. In figure 4-3, the red curve shows a bigger deviation without filters, whereas the pink curve shows improved linearity when using interference filters (with FWHM of 10nm) to reduce the bandwidth of the green LED (with FWHM of 40nm).

To explain the deviation effects of polychromatic radiation, assume an incident light consist of two wavelength λ' and λ''. Applying Beer's law to each of the individual wavelengths we have:

$$A' = \varepsilon(\lambda')*L*C \qquad [4\text{-}1]$$

Because $$A' = log\frac{1}{T'} = log\ \frac{P_0'}{P'} \qquad [4\text{-}2]$$

Thus $$P' = P_0'10^{-\varepsilon(\lambda')*L*C} \qquad [4\text{-}3]$$

Similarly, for λ'' $$P'' = P_0''10^{-\varepsilon(\lambda'')*L*C} \qquad [4\text{-}4]$$

When an absorbance measurement is made with radiation composed of the both wavelengths, the power of the light passing through the sample solution is given by $P'+P''$ and that of the light from the reference by $P_0'+P_0''$. Therefore, the measured absorbance A_m is given by

$$Am = log\ \frac{P_0'+P_0''}{P'+P''} \qquad [4\text{-}5]$$

Using equation 4-3 and 4-4 to substitute for P' and P'' yields

$$Am = log\frac{P_0'+P_0''}{P_0'10^{-\varepsilon(\lambda')LC} + P_0''10^{-\varepsilon(\lambda'')LC}} \qquad [4\text{-}6]$$

Equation 4-6 shows the relationship between Am and concentration C is no longer linear when the light consists of different wavelength components hence different molar extinction coefficient. Greater departures from linearity can be expected with increasing differences between $\varepsilon(\lambda')$ and $\varepsilon(\lambda'')$[72].

Stray light is another reason for non-linearity. To understand this, the stray light can be considered as a light with a zero molar extinction coefficient. In figure 4-4, the deviation could be caused by both polychromatic radiation and stray light.

The deviation effects of polychromatic radiation always reduced the measured absorbance as shown in figure 4-4. This is because the effective molar extinction coefficient is reduced by the light consisting of different wavelength compounds and so the wider bandwidth (without filter), the more reduction.

4.4 Experiment with Nitrite

Chapter 2 described the reaction of nitrite with *N*-(1-napthyl)ethylenediamine dihydrochloride (NED) and sulphanilamide to form a pink coloured Azo dye where the absorbance is proportional to the concentration of nitrite. Sodium citrate is premixed with the sample (nitrite in sea water) to reduce the precipitation of calcium, magnesium and other salts. Polyvinyl alcohol (PVA) mixed with the sulphanilamide reduces bubble formation and stabilizes the measurement. The detailed procedure is given below [73]:

1) Mix 2g sulphanilamide, 1g PVA and 35ml of concentrated HCl (12M). Make up to 100ml with MQ water (distilled water produced by Milli-Q system) to form reagent *R5a*.
2) Dissolve (will require stirring / agitation) 0.1g NED in 100ml MQ water to form *R5b*.
3) Dissolve 2.5g sodium citrate in 100ml MQ water to form *R1*.
4) Premix the sample with *R1* in 1:1 ratio.
5) Mix a small quantity of *R5a* and *R5b* to form *R5*.
6) Measure the same volume of *R5* as that used for sample and then mix with the sample and *R1* mixture.

To achieve the best results, many researchers report that the sample and citrate mixture should be mixed with the sulphanilamide before mixing with the NED. But in short duration experiments, the sulphanilamide and NED can be premixed before being mixed with the sample and citrate with few side effects. After all the reagents and sample are mixed together, the mixture requires agitation and stirring to aid the chemical reaction. The pink-coloured Azo dye is gradually formed in the reaction, normally taking about 10 minutes to fully develop the colour. The Azo dye has a peak absorbance at a wavelength 540nm. The spectrum of the Azo dye is shown in figure 4-5.

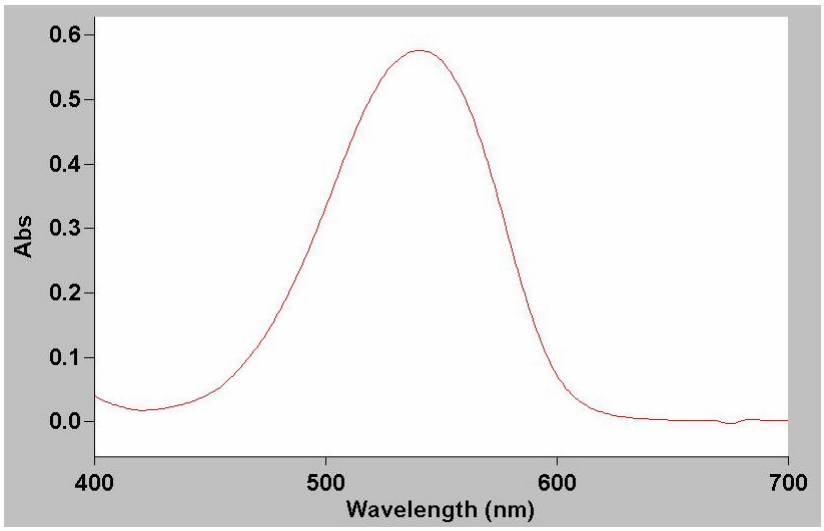

Figure 4-5 Spectrum of Azo dye

To calibrate the circuit, Azo dye solutions with various concentrations were measured using the benchmarking system, and then tested again on the in-house made spectrophotometer. A fresh batch of reagents and samples was produced at the beginning of the experiment and used throughout the tests. All the reagents, nitrite standard, sea water, MQ water used in the experiments are of analytical grade. The samples are made from nitrite standard (100μM) diluted with low nutrient seawater (standard stock sea water with salinity 35, nutrients < 1μM). A group of samples were made with various nitrite concentrations in the range of 0.1-50μM, as found in seawater. After the samples were mixed with *R1* and *R5*, these solutions were stored in light resistive bottles ready for the test. During tests, the reference cuvette of the sensor block was filled with pure sea water mixed with *R1*, *R5* in the ratio of 1:1:1, while the solutions with various concentration of Azo dye were injected by a pipette into the sample cuvette.

To test the absorbance of various solutions, the oscilloscope (Agilent 54621D with sampling rate of 200 MSa/s, set to average mode with 256 samples, accuracy of ± 3.78mV) was used to measure the voltage (directly representing absorbance) output from the in-house made spectrophotometer (with Log100 scale factor set to 1), and the result is compared with the benchmarking (Cary 1Bio). In figure 4-6, the blue dots were measured by the benchmarking and the pink dots were measured by the in-house made spectrophotometer. The trend lines shows the test results are very close. The pink dots deviate from the trend line of blue dots, especially at higher concentration. This can be explained by the polychromatic radiation and stray light.

The deviation between the reference spectrometer and the designed sensor is shown in figure 4-7.

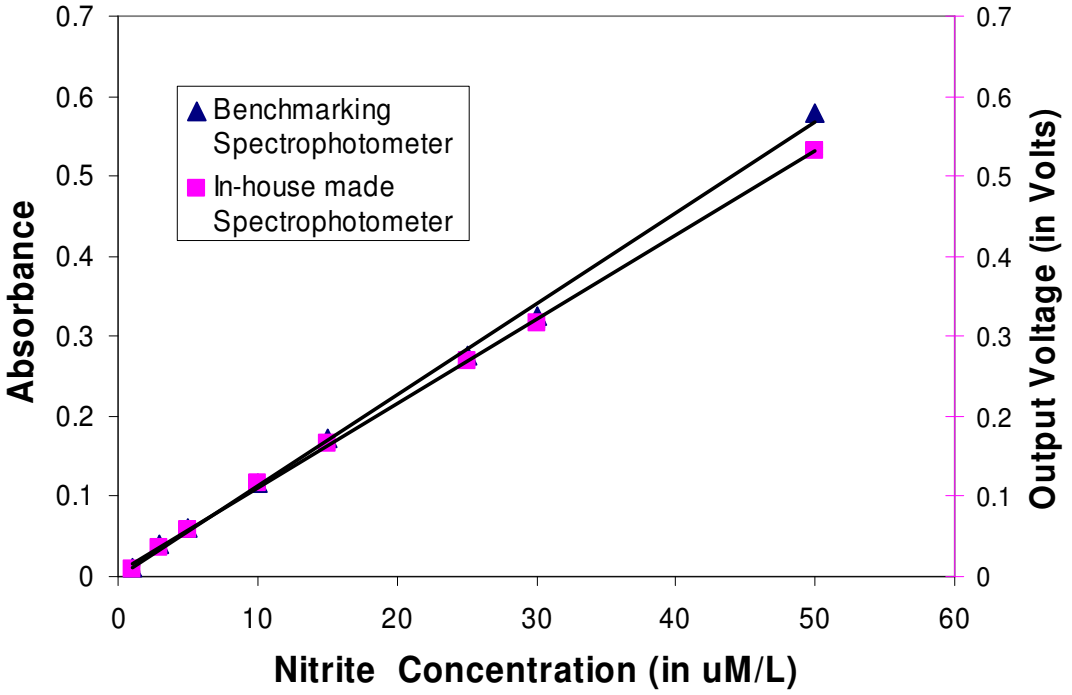

(a) Test in the concentration range of 1 - 50 µM

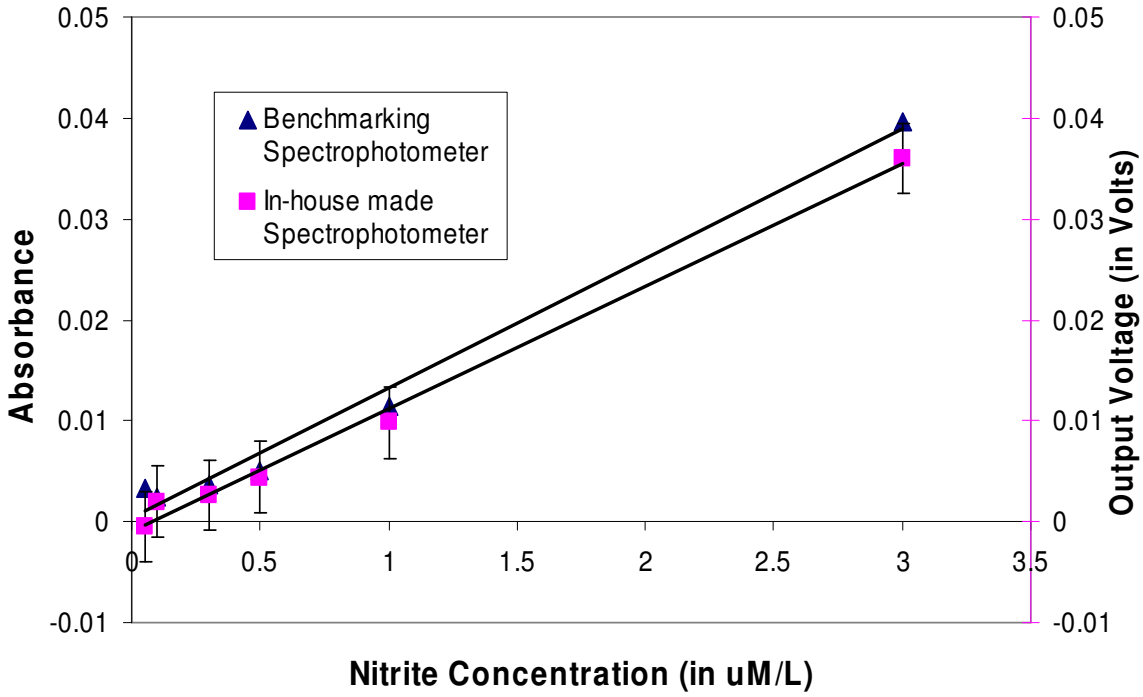

(b) Test in the concentration range of 0.05 - 3µM

Figure 4-6 Absorbance test comparison (a, b)

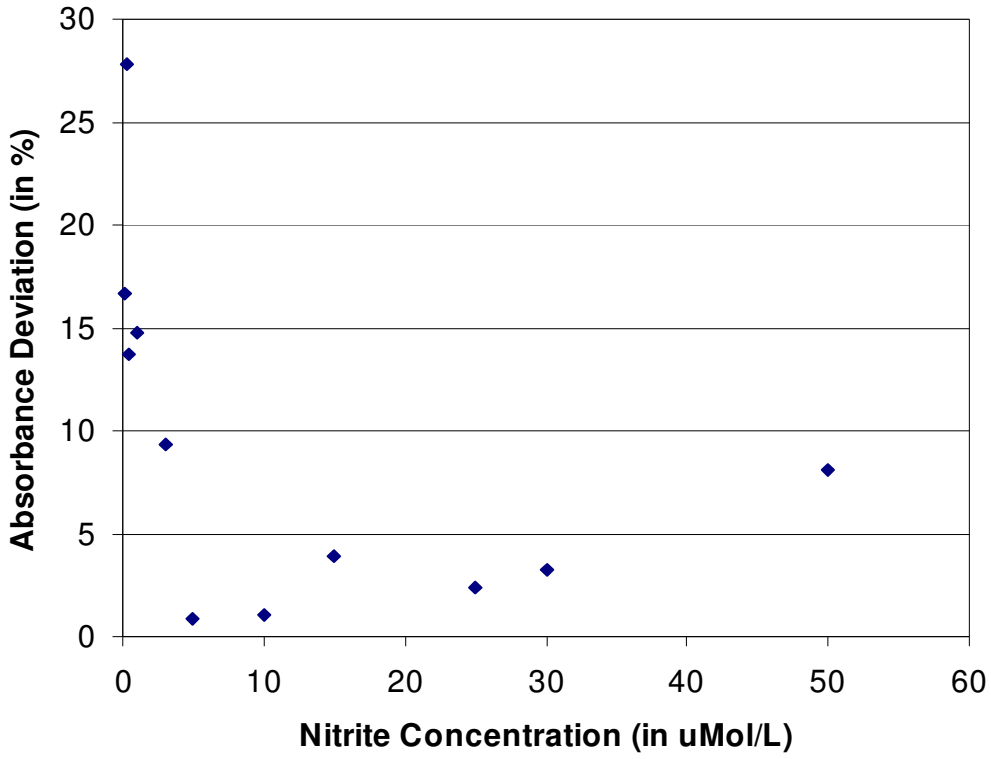

Figure 4-7 Absorbance test deviation

In figure 4-7, the deviation is within 5% in the concentration of 5-30μM, however the deviation is higher (7%) in the concentration of 50μM and especially higher (<27%) in the low concentration range (<0.5μM). Figure 4-6b also shows that the system has a limit of detection of 0.1μM, correspondent to a sensitivity of 2mVrms/ (0.1μM), almost 4 times of the noise floor standard deviation (0.55mV).

4.5 Discussion

Figure 4-7 shows that there is a good agreement between the benchmarking and the in-house made spectrophotometer. The deviation at high concentrations (5-50μM) is within 7%; this is mainly caused by the polychromatic radiation (Deviation about 6% for red dye test at absorbance of 0.467). However the deviation increases to 27% at low concentrations (<0.5μM), the reason for this is complicated. In figure 4-6b, the pink dots show deviations from the blue calibration curve, possibly due to chemical contamination, even though great care was taken. Only MQ water was used in the experiments. The solution was filtered to remove particles and the sample cuvette was rinsed several times with the new solution before testing. All the chemicals containing

NED were stored in light resistive bottle since it is a light sensitive material. Although these measures reduce chemical contamination, it can never be eliminated. At low concentrations, small chemical contamination could easily account for the large variance in the results. Another limitation was the uncertainty introduced by the low nutrient seawater which had a nutrients level of < 1μM.

Shock and vibration would make LED and photodetectors slightly shift, this could cause measurement error. The test circuit has noise (0.55mV), which also contribute to the measurement errors. To prevent radio frequency interference, twisted pairs were used for wire connections and a shielding can enclosed the circuit board. The instrument also contributes to the errors (Indicated by the error bar in figure 4-6 b) and the reading errors of the oscilloscope could be up to 3mV in the test (Oscilloscope performance: for 50mV signal, scope set to 10mV/div, accuracy = ±3.78mV). In order to evaluate the measurement error, a precision multi-meter (Fluke 187, 1μV resolution, set to DC average mode with 10Hz sampling rate) was used to measure the circuit output voltage. Three solutions with different nitride concentration were used to measure absorbance, and each solution measured 5 times in order to obtain the standard deviation, which was used to evaluate measurement errors and resolution. The standard deviation is calculated from equation 4-7 [74].

$$\sigma = \sqrt{\frac{(d_1^{\,2} + d_2^{\,2} + \cdots + d_n^{\,2})}{n-1}} \qquad [4\text{-}7]$$

where d_1 to d_n are deviations of the measurements from the average value, and n is the number of measurements. The calculated standard deviations and the data for absorbance are given in table 4-1.

Table 4-1 Standard deviation of absorbance measurement

Times	**30μM**	**$\sigma/\sqrt{Hz}$**	**1μM**	**$\sigma/\sqrt{Hz}$**	**0.5μM**	**$\sigma/\sqrt{Hz}$**
1	0.3154		0.0098		0.0040	
2	0.3145		0.0101		0.0044	
3	0.3163	$5.38\text{x}10^{-4}$	0.0125	$5.06\text{x}10^{-4}$	0.0038	$2.21\text{x}10^{-4}$
4	0.3175		0.0085		0.0052	
5	0.3151		0.0117		0.0035	

From table 4-1, the biggest standard deviation is 5.38×10^{-4} which indicates a resolution of 51nM at high concentration (30 μM). At low concentration (0.5μM), the calculated standard deviation is 2.21×10^{-4} which indicates a resolution of 26nM. Thus the calculated limit of detection is about 78nM. The possible reason for measured LOD limited to 0.1μM in the experiment is chemical contamination, instrument errors, interference and circuit noise.

Although the calculated limit of detection is about 78nM, this can be further improved by increasing the light path length. Assume a path length is increased by 10 times, the signal level of absorbance can be improved as given by equation 4-8:

$$A_{shortpath} = \varepsilon(\lambda)*(L)*C \Rightarrow A_{longpath} = \varepsilon(\lambda')*(10L)*C = 10A_{shortpath} \quad [4\text{-}8]$$

If a path length of 10cm (10 times of the 1cm of a standard cuvette) was used, the system could have achieved a LOD of 7.8nM, better than 70nM reported by M. OToole et al. [231].

4.6 Conclusions

Test results shows there is good agreement between the benchmarking and the in-house made double beam spectrometer which proved the double spectrophotometer system design is successful. During the test, a temporary sensor block with standard cuvette (1cm light path length) was used and the limit detection of nitride in seawater was 0.1μM, which is the desire target given in table1-1. The resolution can be further improved if a longer light path is used.

The interference filters used in the temporary sensor block narrow the bandwidth of the green LED radiation, improves the linearity of the absorbance-concentration curve and thus reduce the deviation from Beer's law.

Chapter 5 The Electrode-Electrolyte Interface

This chapter presents the theory and background knowledge to help understand the interface between the electrode and electrolyte, and the electrode polarisation effects in the application of contact electrode conductivity sensor.

5.1 Electrode Polarisation

The simplest method of measuring specific conductivity of sea water is with two electrodes. The two metal electrodes are used to inject AC current as well as sense the voltage. Since the current path in the measured sample is defined by the geometry of the cell, the conductivity can be obtained from equation 2-5. However, the results also depend on the injected signal. The conductivity measured by injecting a DC or a low-frequency is quite different from that measured by injecting a high-frequency. This phenomenon is due to electrode polarization. To understand this we need to study the different mechanisms of electrical conduction in metal electrodes and sea water, and also the interface between the metal-electrolyte phases.

When a metal electrode is immersed in a conducting medium, an electrochemical equilibrium is established. This complex system can be modelled using passive circuit elements as described and reviewed in numerous electrochemical texts [112-115]. At the instant when a metal is placed in an ionically conducting solution, the metal and the

solution are electrically neutral, an electrochemical equilibrium is established. Chemical reactions occur whereby electrons are transferred between the metal and the electrolyte ($M^+ + e^- \rightarrow M$). This results in the formation of an electric field between the electrode and the electrolyte which influences further chemical reactions. This induced electric field inhibits the reduction reaction ($M^+ + e^- \rightarrow M$) while accelerating the oxidation reaction ($M \rightarrow M^+ + e^-$). These two competing reactions eventually reach an equilibrium condition whereby the currents due to electron transfer to and from the metal are equal.

This equilibrium exchange current density flows across the interface in both directions resulting in a net current of zero. The electric field generated by these electron transfer reactions also has an impact on the electrolyte. Water dipoles orient themselves in the field to form a layer at the metal surface which is known as the hydration sheath. Just beyond the water dipoles are solvated ions (result of the electron transfer with the metal) which form another layer, the locus of which is known as the outer Helmholtz plane (OHP). There is also specific adsorption of ions (cations or anions) at the electrode surface interspersed with the orientated water dipoles. Since these ions are not counter ions, they are not bound to the electrode surface primarily by the Coulombic (van der Waals) forces due to the charge on the metal, but are absorbed by chemical bonds. It is possible to have anions specifically adsorb to the surface of a negatively charged metal. The locus of these ions is known as the inner Helmholtz plane (IHP) (although in some texts it is the locus of the orientated water dipoles which is termed the IHP) and can affect the overall charge density profile of the interface. The total result of these reactions, adsorptions and orientations is the creation of an electrified interface usually called the electrical double layer (or simply double layer) which describes the interphase region at the boundary of an electrolyte.

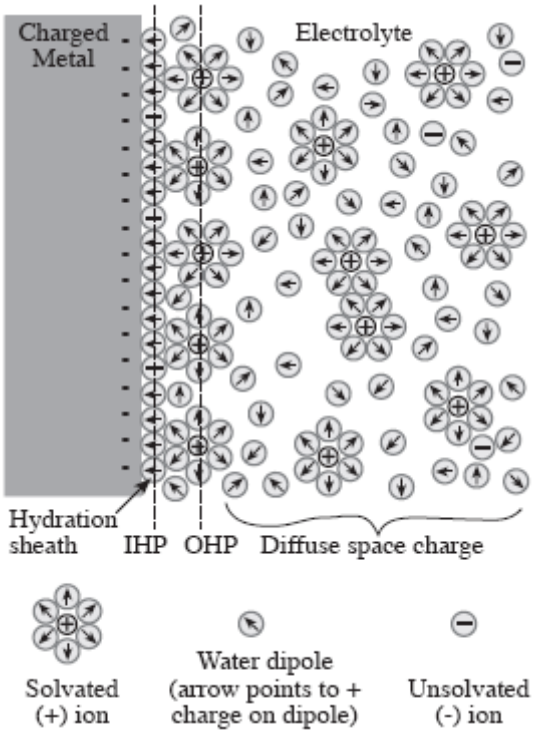

Figure 5-1 A schematic representation of a typical double layer showing the hydration sheath, inner and outer Helmholtz planes as well as the diffuse space charge layer [114]

This electrified interface is illustrated in figure 5-1 where the arbitrary case of positive ions at the OHP and electrons at the metal surface has been assumed. For specific absorption at the electrode surface, the assumption of unsolvated negative ions which is independent of the other charges in the system is also arbitrary. The space charge region shown in figure 5-1 has a graded profile with the strongest field at the interface, diminishing to zero in the bulk electrolyte.

5.2 The Double Layer Capacitance

As mentioned above, when a metal and electrolyte come into contact, a space charge region is formed in the electrolyte at the interface. However, the exact structure of this region is difficult to determine. Initial theories developed by Helmholtz assumed the charge of solvated ions was confined to a rigid sheet at the OHP, and was equal and opposite to that in the metal. With the orientated water dipole layer acting as a dielectric, the model predicted the interface would behave like a simple capacitor. This capacitance modelled by Helmholtz is determined by the dielectric permittivity of

electrolyte ($\varepsilon_o\varepsilon_r$), the area of the interface (A), and the distance of the OHP from the metal electrode (d_{OHP}):

$$C_H = \frac{\varepsilon_o \varepsilon_r * A}{d_{OHP}} \qquad [5\text{-}1]$$

where C_H is the capacitance (F), ε_o is the permittivity of free space (8.85419×10^{-12} F/m) and ε_r is the relative permittivity of the electrolyte. Assumptions of ε_r and d_{OHP} may be used to determine a Helmholtz capacitance per unit area. Assume ε_r is 5 for the Helmholtz layer at the interface of NaCl or KCl solution [116-117] and an outer Helmholtz plane distance of 3 Å [118-120], the Helmholtz capacitance per unit area (C_H/A) is approximately 15 $\mu F/cm^2$. This rough estimate is often useful and can be used for a general design guide, although numerous factors can affect both ε_r and d_{OHP}. This simple model of Helmholtz is not adequate and neglects the dependence of capacity on potential which has been observed experimentally.

Later, Gouy and Chapman modified the simple Helmholtz model (a rigid sheet of solvated ions) by considering mobile solvated ions at the electrode surface. In addition to the electrical forces, these mobile ions are also influenced by thermal forces. The result is an ion cloud near the interface where the combined effects of thermal and electrical forces finally reach equilibrium forming a diffuse double layer. In Gouy and Chapman's modified model, the distribution of the space charge is concentrated at the OHP, tending toward zero in the bulk solution (a linear potential drop across the hydration sheath was not assumed). Since the ion movement is controlled by an applied potential, consequently changing the applied potential will also change the equivalent capacitance of the diffusion layer. Detailed discussions have been reviewed in several texts [112-114], and will not be repeated here. However, it is useful to examine the resulting relationships of the potential distribution and capacitance. For relatively small applied voltages (<50mV) the voltage drop through the space charge region is exponential:

$$V(X) = V_0 * exp\left(-\frac{X}{\lambda}\right) \qquad [5\text{-}2]$$

where V_0 is the potential at the electrode (X=0), X is the distance from the electrode, and λ is the Debye length. The Debye length characterizes the spatial decay of potential and can be viewed as the characteristic thickness of the diffuse layer:

$$\lambda = \sqrt{\frac{\varepsilon_o \varepsilon_\gamma V_t}{2 n_0 z^2 q}} \qquad [5\text{-}3]$$

where V_t is the thermal voltage (kT/q), n_0 is the bulk number concentration of ions in the electrolyte (ions/dm^{-3}), z is the valence of the ions, and q is the charge on an electron (1.60219×10^{-19} C). For KCl solution, replacing the constants by numerical value, equation 5-3 can be simplified and the Debye length is given in terms of molar concentration C [75]:

$$\lambda = 1.764 x 10^{-11} \sqrt{\frac{T}{C}} \qquad [5\text{-}4]$$

A list of diffuse layers with different concentration is given in table 5-1. For any solutions with a concentration higher than 100 mM, the width of this diffuse layer is extremely small (< 10 Å) as shown by the table.

Table 5-1 Character thickness of the diffuse layer at 25°C [112]

Molar Concentration (mM)	**λ (Å)**
1000	3.0
100	9.6
10	30.4
1	96.2
0.1	304

The equivalent capacitance per unit area (F/m^2) of the diffuse double layer can be calculated as:

$$C_G = \frac{\varepsilon_o \varepsilon_r * A}{\lambda} \cosh\left(\frac{z V_o}{2 V_t}\right) \qquad [5\text{-}5]$$

where the first term ($\varepsilon_o\varepsilon_r$*$A/\lambda$) is simply the capacitance of two plates with an area A and separated by a distance λ , and the second term of the hyperbolic cosine is used to compensate the effects of mobile charges.

While the Gouy-Chapman model is an improvement over that of Helmholtz, it is still not complete and generally overestimates the interfacial capacitance compared to experimental values. Stern rectified this inconsistency by combining the Gouy-Chapman model with the Helmholtz model. In this combined model, the complete double layer consists of two layers: the Helmholtz layer is formed by the bound ions at the OHP, and beyond it, the Gouy-Chapman layer is formed by the diffused ion cloud. Thus, the total interfacial capacitance is the series combination:

$$\frac{1}{C_{DL}} = \frac{1}{C_H} + \frac{1}{C_G} \qquad [5\text{-}6]$$

where C_{DL} is the total interfacial capacitance (also called double layer capacitance), C_H is the Helmholtz capacitance and C_G is the Gouy-Chapman capacitance. When a potential is applied, the voltage drop across the interface is determined by the capacitance given by equation 5-6. The voltage drop across the Helmholtz layer is linear in the region between the electrode and the OHP. Beyond the OHP, the voltage drop across the Gouy-Chapman layer decays almost exponentially from the OHP to the bulk solution. This decay depends on the voltage at the interface and becomes sharper as the potential (V_o) is increased. The position of λ will also shift to the left as the ionic concentration of the electrolyte is increased, as it is shown in figure 5-2.

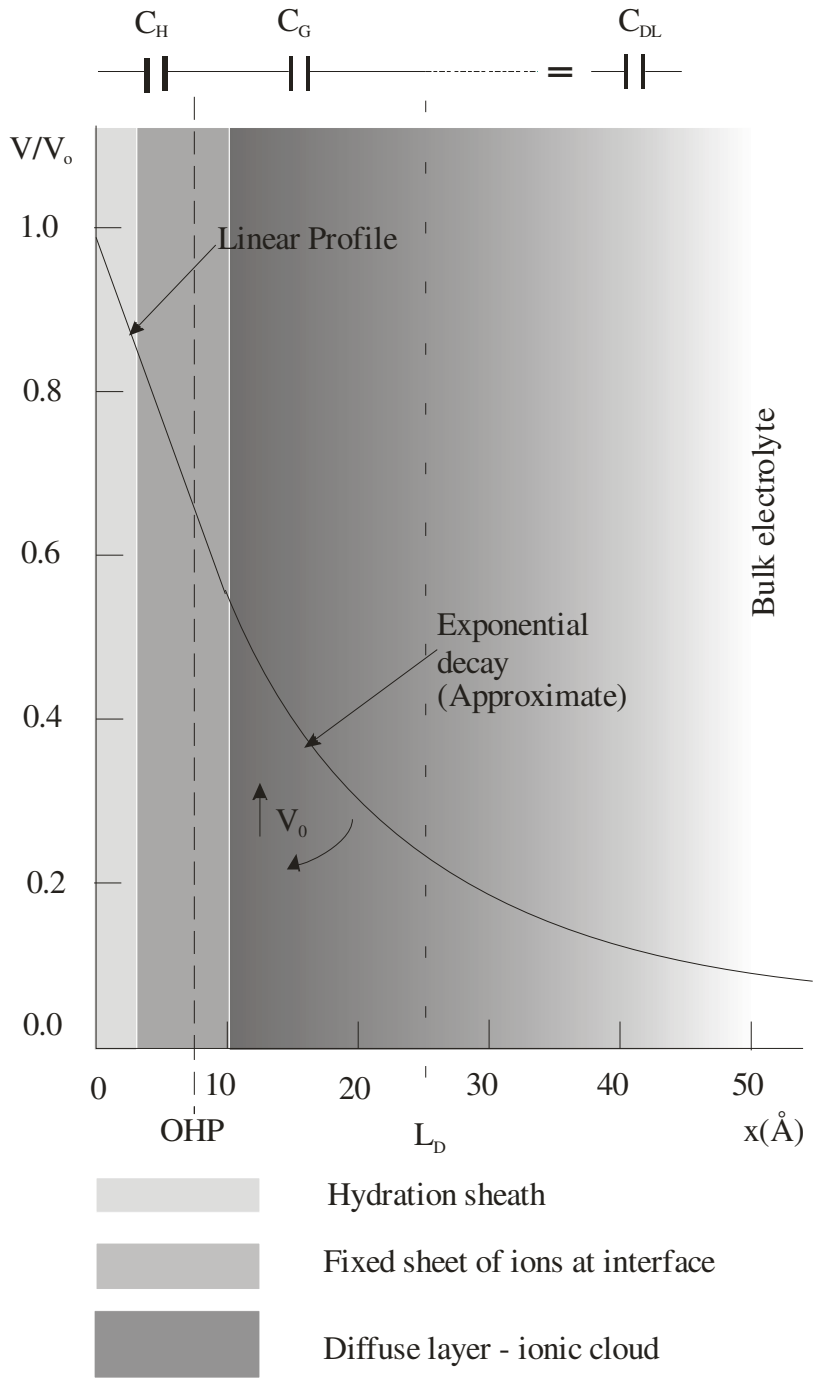

Figure 5-2 Potential profile representation of double layer, the total interfacial capacitance (C_{DL}) is the series combination of the Helmholts capacitance C_H and the Gouy-Chapman capacitance C_G, reproduced from [112]

When a bias is applied to the electrodes (as is the case in a conductivity measurement), the interfacial capacitance (C_{DL}) increases and is dominated by the Helmholtz capacitance (C_H). This can be explained by the first term of equation 5-6.

When the potential is applied to the electrode, the ions in the diffuse layer are pulled toward the electrode (electrical forces dominate over thermal) to reduce the effective Debye length (λ) of the diffusion layer which results in an increase in the Gouy-Chapman capacitance (C_G). As C_G is increased, the series combination of C_H and C_G is dominated by the smaller C_H term and the total interfacial capacitance (C_{DL}) approaches the Helmholtz capacitance (C_H) given by equation 5-1. Furthermore, the Gouy-Chapman capacitance (C_G) increases as the applied potential increases, which can be explained by the hyperbolic cosine term in equation 5-5. From equation 5-3, 5-4 and 5-5, it can be seen that the Gouy-Chapman capacitance is also dependent on the concentration of the electrolyte. As the molar concentration increases, the Debye length (λ) decreases which results in an increase in the diffusion layer capacitance (C_G). The consequence of increasing concentration is similar to that of increasing potential, which make the interfacial capacitance (C_{DL}) approach the fixed value of Helmholtz capacitance (C_H), as it is shown in figure 5-3.

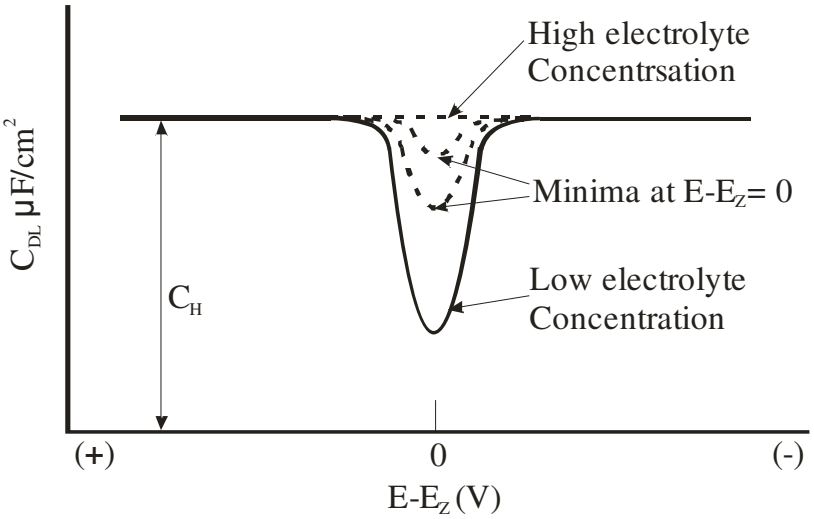

Figure 5-3 The interface capacitance (CDL) changes with electrolyte concentration and potential, reproduced from [112].

Figure 5-3 shows that, as the electrolyte concentration increases, the contribution of C_G to the total interfacial capacitance decreases and C_{DL} increases to a maximum value dictated by C_H (approximately 15µF/cm^2). Similarly, when the potential moves away from the potential of zero charge – PZC (potential where the charge on the electrode is zero) C_{DL} increases to C_H according to the hyperbolic cosine relation of Equation 5-5. With very low potential and dilute electrolyte solutions, the total interfacial capacitance is dominated by the Gouy-Chapman capacitance (C_G).

The basic models and concepts examined above are sufficient for understanding the double layer capacitance, and also can be used as general design guides. However, when consider the fractal nature of electrical double-layer impedance, due to the effect of specifically adsorbed ions and the surface roughness at the electrode, the impedance of the double layer is often represented by a constant phase angle element (CPE) [121-123], and is given by the empirical relation:

$$Z_{DL} = \frac{K}{(j\omega)^{\beta}} = \frac{K}{\omega^{\beta}}\left[\cos(\frac{\pi}{2}\beta) - j\sin(\frac{\pi}{2}\beta)\right] \qquad [5\text{-}7]$$

where K is a measure of the magnitude of Z_{DL} and has unit of $\Omega s^{-\beta}$ and β is a measure of the deviation from pure capacitive behaviour due to inhomogeneities on the electrode surface. For a pure capacitance, $\beta = 1$; for a perfect resistor, $\beta = 0$; for double layer impedance measured on solid electrodes, β typically is between 0.7 and 0.9 [112].

5.3 Faradaic Impedance

If a DC potential is applied across the interface, a current may flow under certain conditions. Thus, it is important to consider an additional resistive path in parallel to the double layer capacitance. Unfortunately, as with the double layer capacitance, this resistor can be non-linear with applied voltage. The flow of current through the electrode/electrolyte interface requires the net movement of charge in response to an electric field (due to an applied voltage). At equilibrium, there is a constant flow of charge across the interface, but the net flow is zero. Thus, the applied voltage (V) must push the total potential across the interface away from its equilibrium value (V_o). This potential difference ($V - V_o$) responsible for the net flow of charge is termed the over potential (η) and is thought to be the sum of four different over potentials:

$$\eta = V - V_o = \eta_t + \eta_d + \eta_r + \eta_c \qquad [5\text{-}8]$$

where η_t is due to the charge transfer through the double layer; η_d is due to the diffusion of reactants to and from the electrode; η_r is due to chemical reactions at the electrode; and η_c is due to exchange of metal atoms with corresponding ions in solution (crystallization) [124]. Thus equation 5-8 can be explained as follows. Given a potential in excess of the equilibrium condition, part of that potential will drive charge

transfer, diffusion, chemical reactions and crystallization. We can imagine there are three parallel currents in series with the diffusion current, each driven by a certain part of the total over potential. When the potential of an electrode nears its equilibrium point, the charge transfer over potential (η_t) tends to dominate the overall current. As the applied potential is further pushed away from the equilibrium point, the diffusion of reactants may become a limiting factor, making the diffusion over potential (η_d) more significant. For practical purposes, the over potentials due to chemical reactions (η_r) and crystallization (η_c) are not of significance [125].

The process by which electrochemical equilibrium is obtained when a metal is placed in an electrolyte has been discussed in detail in section 5.1. The equal but opposite oxidation and reduction currents balance each other, and the total net current is zero. The absolute value of this current density is known as the exchange current density (I_o). It is dependent on the electrolyte composition, the material properties of the electrode, as well as the resulting oxidation and reduction reactions. Since the exchange current is dominated by the electrochemical reaction, it is difficult to determine I_o from theory. However, I_o can be obtained through experiments, and it is often determined by measuring the charge transfer resistance around the equilibrium potential of the electrode in the electrolyte of interest. Table 5-2 summarizes some published value of I_o.

Table 5-2 Some published exchange current density (Io) Values

Material/Reaction	**Io (A/cm^2)**	**Reference**
Au in buffered saline	2.00×10^{-9}	[126]
Au, hydrogen reaction	3.98×10^{-6}	[114]
Pt, hydrogen reaction	7.94×10^{-4}	[127]
Ir, hydrogen reaction	2.00×10^{-4}	[127]

As long as the exchange current density (I_o) for the electrode/electrolyte interface is given, the data can be used to determine the current which flows as a result of an applied potential. If the applied potential is close to the equilibrium value, then the Butler-Volmer equation can be used to calculate the resulting current density (I):

$$I = Io\left[\exp\left(\frac{(1-\alpha)nF\eta}{RT}\right) - \exp\left(\frac{(-\alpha)nF\eta}{RT}\right)\right] \qquad [5\text{-}9]$$

where I_o is exchange current density (in A/cm^2), η is over potential, n is number of electrons, F is the faraday constant (= qN_A, where N_A is Avogadro's number), α is the symmetry factor that reflects the energy barrier differences for the oxidation and reduction reactions, R is the gas constant (= $N_A k_B$, k_B is the Boltzmann constant), T is the absolute temperature in Kelvin. Since the carriers for the charge transfer current are electrons and holes, they are much more likely to be transferred one at a time than in groups of two or more. Thus if we assume n = 1, equation 5-9 can be rewritten as:

$$I = Io\left[\exp\left(\frac{(1-\alpha)\eta}{V_t}\right) - \exp\left(\frac{(-\alpha)\eta}{V_t}\right)\right] \qquad [5\text{-}10]$$

where V_t is the thermal voltage, equal to RT/F. It can be seen that small changes in η can produce very large changes in the current density I. In addition, the exchange current density (I_o) has a direct impact on the overall current. Thus, the choice of electrode material can significantly impact the amount of current which flows in response to an applied voltage. Since electrochemical reactions and gas evolution at the interface (unwanted for conductivity measurement) often occur at higher voltages, it is desirable to limit the excursions from equilibrium as much as possible. Examination of equation 5-10 reveals that each exponential term resembles the exponential current, which can be considered as an ideal diode. Thus equation 5-10 can be further rewritten as:

$$I = I_1 + I_2$$

$$I_1 = Io\left[\exp\left(\frac{(1-\alpha)\eta}{V_t}\right) - 1\right]$$

$$I_2 = Io\left[1 - \exp\left(\frac{(-\alpha)\eta}{V_t}\right)\right] \qquad [5\text{-}11]$$

where I_o and η can be considered as the saturation current density and the forward bias voltage, α can be considered as a diode factor accounting for the difference between

the two diodes. Thus the charge transfer current of an electrode/electrolyte can be simplified to an equivalent model of two diodes assembled in an anti-parallel connection, as shown in figure 5-4. This first order model is very useful to simplify analysis when visualizing the current flows through the electrode/electrolyte interface in response to an applied potential. A detailed analysis of the rectification properties of electrodes in solution can be found in [128].

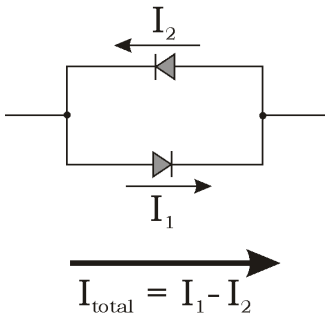

Figure 5-4 The diode model for the charge transfer current

5.3.1 Charge Transfer Resistance

A theoretical value for the charge transfer resistance (R_t) that appears in parallel with the interfacial capacitance can be determined from Butler-Volmer equation. Assuming a temperature of 300K, the I-η relationship is shown in figure 5-5a. As can be seen, the current voltage relationship is symmetrical around zero when α = 0.5; as the symmetrical factor (α) is adjusted towards 1 or 0, the I-η curve shifts to the right or left (indicating a preference for the oxidation or reduction reactions). Obviously, it is not possible to extract a linear resistance value for large variations in η. However, if we scale up the small-signal region as shown in figure 5-5b, we see there is a linear region between -50mV and 50mV. Thus it is possible to approximate a charge transfer resistance (R_t) in a small signal region, and the estimated value of R_t can be directly obtained by inversing the slope of the curve.

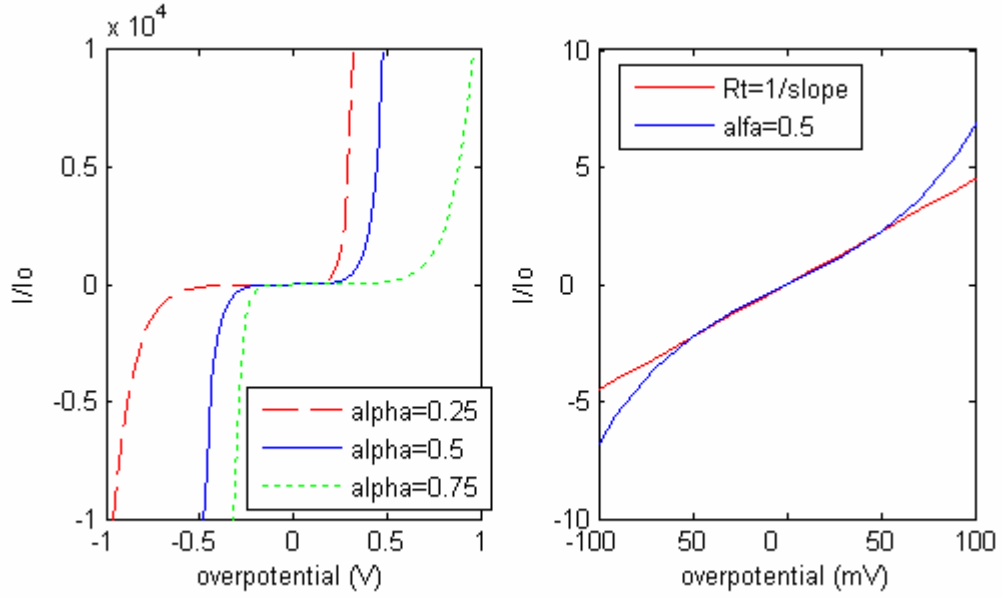

a. large signal b. small signal

Figure 5-5 I-η curve shows current and voltage relationship (a, b)

For the conditions (α= 0.5, T = 27^{o}C) given in figure 5-5b, it can be seen that this approximation for R_t holds for over potentials less than 50mV peak. The theoretical value for the charge transfer resistance under low field conditions with α= 0.5 (nonrectifying system) can be calculated as below [112]:

$$R_t = \frac{V_t}{I_o} = \frac{RT}{FI_o} \qquad [5\text{-}12]$$

in Ω•cm^2. Here the resulting current (I) is calculated directly from Ohm's law,

$$I = \frac{\eta}{R_t} = \frac{I_o \eta}{V_t} \qquad [5\text{-}13]$$

The above equation 5-13 is only valid for small current. For higher currents, it is no longer possible to define a pure resistance term. However, by assuming a non-rectifying system (α= 0.5), one exponential term of equation 5-10 tends toward zero while the other increases in magnitude, the total current may be estimated by

$$I = Io * exp\left(\frac{\eta}{2V_t}\right) \qquad [5\text{-}14]$$

Again, from figure 5-5 it is clear that the transition from the low field to high field approximations occurs around 50mV, and this limiting value will increase with increasing temperature. For a real system of interest, the point of non-linearity can easily be determined by excitation with a pure sinusoid and monitoring the onset of harmonics [129-130].

At this point the model of a metal electrode placed in an electrolyte is a voltage dependent capacitor (C_{DL}) determined from equation 5-6, in parallel with a charge transfer resistance (R_t) which can be determined from equation 5-12 when the applied potential is less than approximately 50 mV peak. For higher voltages or higher current density, the charge transfer resistance is no longer linear [121, 131-132] and the empirical data of the interfacial impedance can be found in Schwan's papers [129, 133]. The relative impedances of these two elements determine the basic characteristics of the electrode (neglecting diffusion limits, discussed in the next section). If the electrode has a very high exchange current density ($I_o \to \infty$), the slope of I versus η curve is infinite and the charge transfer resistance tends toward zero. Thus even though a significant current density flows across the interface, there is no substantial over potential developed. This is termed an ideally non-polarisable interface. The opposite situation ($I_o \to 0$) results in what is called an ideally polarisable interface. It behaves like a capacitor with no Faradic (charge transfer) processes. The charge in solution equals the charge on the electrode at all times. However, as noted above, this capacitance is not independent of potential.

Of course no material in practical applications is perfectly polarisable or non-polarisable, but rather somewhere in between. What is of importance is the magnitude of the resulting current relative to the exchange current density. If the resulting current is small with respect to I_o, then the interface should not be perturbed far from equilibrium. Thus non-polarisable behaviour would be observed. However, if the current is large compared to I_o, one can expect the interface to be far from equilibrium, resulting in polarisable behaviour.

5.3.2 Warburg Impedance

As mentioned above, in most cases the charge transfer over potential dominates the resistive part of the electrode interface impedance. But the situation changes when the current density (AC or DC) is so large that reactants are not able to diffuse from the bulk to the interface fast enough. The current becomes diffusion limited resulting in a diffusion over potential (η_d). This additional impedance is in series with the charge transfer resistance (R_t) since physically diffusion and charge transfer must occur as a serial process, i.e., reactants diffuse to the interface where they contribute to oxidation or reduction reactions. While there is a theoretical steady-state diffusion resistance for DC conditions [125], this discussion will focus on the AC case since it is representative of the situations encountered in this work.

For the case of sinusoidal signal acting on the ions at the metal-electrolyte interface, these charged particles will move in response to the applied electric field. This results in a spatial concentration of the ions that vary sinusoidally. As the frequency of excitation is increased, it becomes more difficult for the ions to follow the field. Thus, the effects of the diffuse ion cloud become less significant. At high enough frequencies, the ions are not able to follow the field at all, resulting in this diffusion impedance tending towards zero. In 1899, Warburg proposed a model for this frequency dependent diffusion impedance [134]:

$$\left|Z_W\right| = \frac{k}{\sqrt{f}} \qquad [5\text{-}15]$$

where k is a constant determined by the electrochemistry and mobility of the ions involved in the charge transfer reaction and f is the excitation frequency. This impedance can be represented by a series combination of a resistance and capacitance (both non-linear). The Warburg impedance elements may be theoretically determined by the following equations [112, 135-136], provided that the diffusion is dominated by a single ion species and the electrode is operated near equilibrium:

$$R_W = \frac{\beta}{\sqrt{\omega}} \qquad [5\text{-}16]$$

$$C_W = \frac{1}{\beta * \sqrt{\omega}} \qquad [5\text{-}17]$$

$$Z_W = \frac{\beta}{\sqrt{\omega}} - j\frac{\beta}{\sqrt{\omega}} \qquad [5\text{-}18]$$

$$\beta = \frac{\sqrt{2} * R * T}{n * F^2 * A * C * \sqrt{D}} \qquad [5\text{-}19]$$

where ω is the angular frequency, n is the number of electrons, D is the diffusion coefficient (cm^2 / sec) of the ion in question, C is the equilibrium concentration of the ion, and A is the active cross-section area of the electrode, R is the gas constant ($8.3143 JK^{-1}/mol$) and T is absolute temperature in Kelvin. Equation 5-18 shows that the Warburg impedance has a constant phase angle of -45^o, and the magnitude is also a constant which is given by

$$|Z_W| = \sqrt{\frac{2}{\omega}} * \beta \qquad [5\text{-}20]$$

The above model works well for systems where the electrode is operated near equilibrium using an AC sinusoidal excitation. Although it does not predict the DC behaviour well, this is of little concern where an AC excitation is used. When measuring the impedance of physical electrodes it is important to remember that the Warburg elements are not measured alone, but rather in concert with the charge transfer resistance (R_t) and the interfacial capacitance (C_{DL}).

5.4 Randle's Equivalent Circuit

For a small sinusoidal excitation, an electrochemical cell behaves as an impedance, and can be represented by an equivalent circuit of resistors and capacitors which pass current with the same amplitude and phase angle as that of the cell. Randle's equivalent circuit is frequently used to represent an electrochemical cell as shown in figure 5-6. The electrode-electrolyte interface impedance consists of parallel

elements because the total current through the working interface is the sum of distinct contributions from Faradaic process (i_f) and double-layer charging (i_c). C_{DL} is the double-layer capacitance which is modelled as a pure capacitance. Z_f is the Faradaic impedance due to Faradaic processes. Since the value of Faradaic impedance depends on frequency, it cannot be represented by simple linear elements. It is more effective to model the Faradaic impedance as a general impedance under AC condition, and this impedance can be further represented by the charge transfer resistance (R_t) in series with the Warburg impedance (Z_W). Finally, to complete the whole picture, a solution resistance (R_S) is also included in the equivalent circuit. Since all of the current must pass through the solution resistance, the solution resistance (R_S) is in series with the parallel elements.

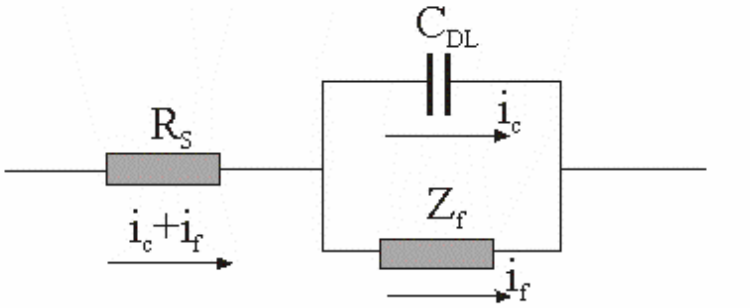

a. Equivalent circuit of an electrochemical cell

b. Subdivision of Z_f into R_t and Z_W

Figure 5-6 Randle's equivalent circuit

In the Randle's equivalent circuit, the solution resistance (R_S) and the double-layer capacitance (C_{DL}) are nearly ideal circuit elements. But the Faradaic impedance is not ideal, because they change with frequency (ω). Thus a given equivalent circuit can only represent cell performance at a specified frequency. Figure 5-7 shows a typical Nyquist plot for the Randle's equivalent circuit.

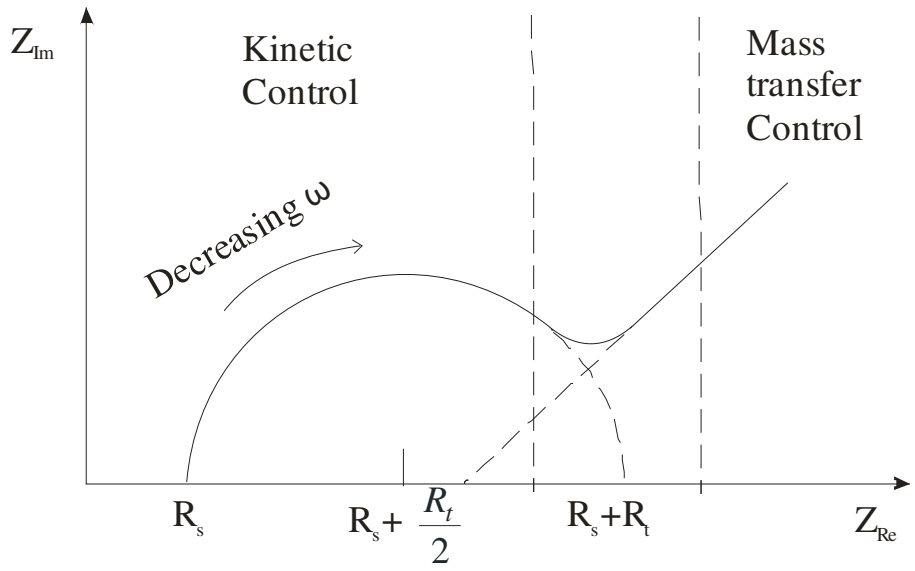

Figure 5-7 Nyquist plot for Randle's Equivalent Circuit, reproduced from [112]

As in figure 5-7, the total impedance is dominated by the solution resistance (*Rs*) at high frequency, since the double layer capacitance provides a path of negligible resistance to the current. It follows that at high frequency no electrolysis takes place and hence there is no contribution from Faradaic impedance. However, the situation changes as the frequency decreases. The effect of R_t in parallel with the C_{DL} gives rise to the characteristic semicircular part of the plot. At lower frequency, the impedance is reduced before it shows a large rise modelled by the Warburg impedance. As the frequency decrease again, the Warburg impedance increases and the impedance is dominated by the diffusion impedance.

5.5 Electrode Noise and Measurement Errors

For a conductivity sensor with noble metal electrodes, there is an intrinsic noise associated with the metal-electrolyte interface. This noise has been empirically shown to be thermal noise [137-138], following the standard Johnson noise equation for the RMS voltage noise of a resistor:

$$V_{RMS\,NOISE} = \sqrt{4k_B T R_N \Delta f} \qquad [5\text{-}21]$$

where R_N is the real part of the electrode impedance in ohms, and Δf is the bandwidth of interest. For reference, this theoretical thermal noise voltage is plotted versus R_N in figure 5-8. It is important to remember that R_N is the effective resistance of the electrode and will be attenuated by the electrode capacitance as the frequency is increased.

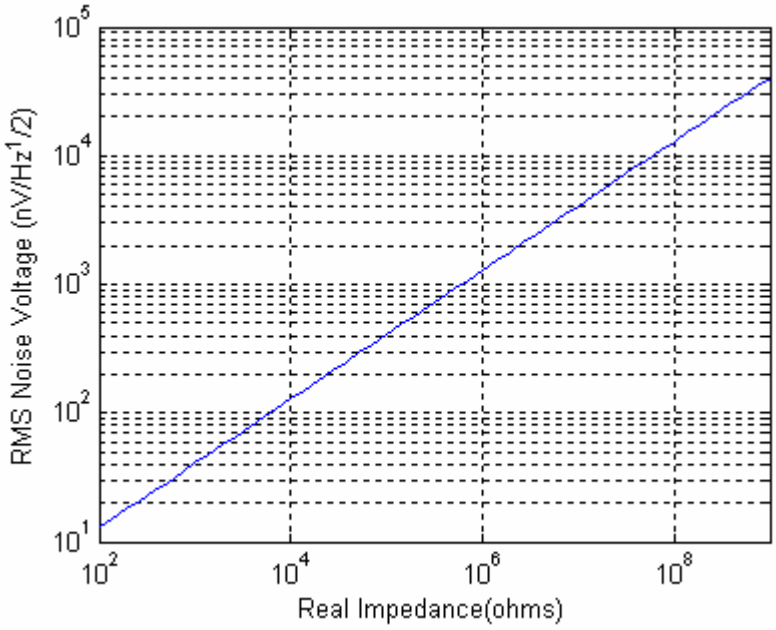

Figure 5-8 Theoretical noise voltage plotted versus the real part of the electrode impedance at 27°C.

For practical applications, the electrode impedance is measured in the bandwidth of interest and the obtained resistance is used in equation 5-21 to estimate the thermal noise. This noise can be compared to the anticipated signal levels to determine if it is necessary to reduce the electrode impedance. For impedance measurements where homodyne techniques are employed, the effective bandwidth of the measurement is significantly reduced making this thermal noise less significant. However, saturation of any amplification prior to the homodyne stage is possible, making this noise an issue for most practical systems.

In addition to noise considerations, another issue is the measurement error introduced by the recording circuit and the electrode-electrolyte interface impedance. Consider the example shown in figure 5-9 to measure the impedance of a conductivity cell, the two electrodes of the conductivity cell is excited by a sinusoidal source with constant voltage. As shown in figure 5-9, the bias current (I_B) of the preamplifier

introduces measurement errors since it reduces the injected current (I_{in}) to the current (I_f) that passes through the feed back resistor. Thus it is desirable to choose an amplifier with very small bias current. The electrode impedance also introduces measurement errors since there are voltage drops across the electrode interfaces. For an accurate measurement of solution conductivity, it is desirable for the electrode impedance to be significantly smaller than that of the solution resistance. One way to reduce the error caused by the electrode impedance is to increase the geometric size of the electrode or increase the surface area through the control of electrode roughness. Since electrode size is often limited by the dimensions of the cell, increasing surface area without altering the geometric area is preferred in many applications. One of the most frequently used methods is to deposit platinum-black on the electrodes [139-140]. The sponge-like nature can effectively increase the surface area of the electrodes and thus greatly reduce the electrode impedance by two orders of magnitude [137, 141]. There are other techniques that may be used to reduce the electrode impedance such as micro-patterning the surface, etching the surface of the metal to form pits, and chemical modifications (such as activation of iridium to form iridium oxide). Another way to reduce the measurement errors is to use the four-electrode configuration in which two electrodes are used to inject current and two electrodes are used to sense voltage sensing. As long as the input impedance of the voltage sense amplifier is high enough, the voltage drop across the electrode interface is very small and hence negligible.

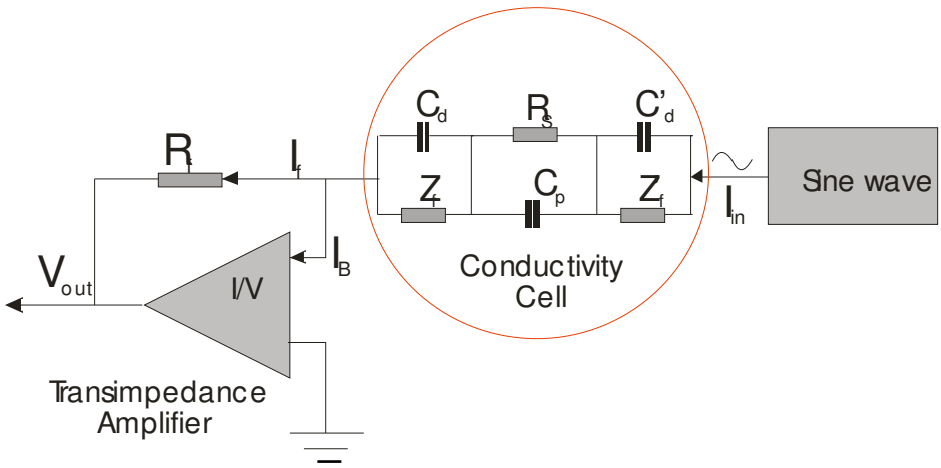

Figure 5-9 I/V converter for Impedance Measurement

Measurement errors are also introduced by the stray capacitance or parasitic capacitance (Cp) of the sensor as shown in figure 5-9. Since AC excitations are normally used to stimulate the conductivity cell, a small current will pass through stray capacitances. The higher the frequency, the more current will bypass the solution. Thus high frequency design is not desirable because of stray capacitances; this is particularly true when the solution conductivity is low.

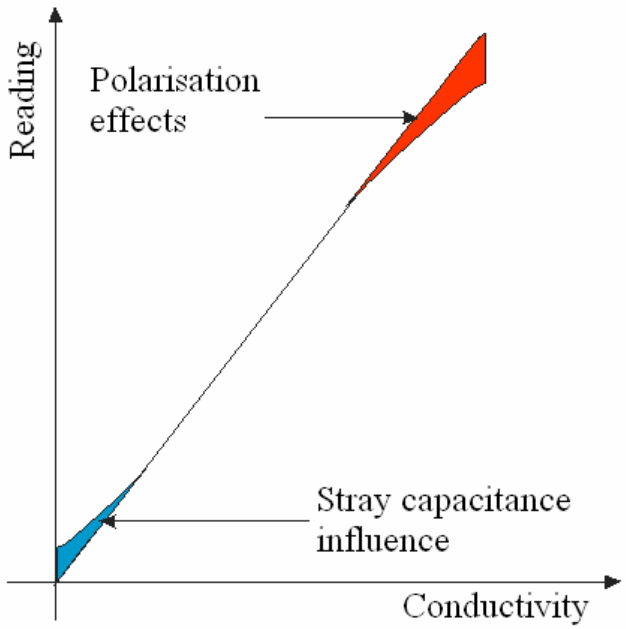

Figure 5-10 Measurement Errors vs. Conductivity

In figure 5-10, the measurement errors (in blue) are dominated by stray capacitance in the low conductivity region. The reason for this is more current bypasses the solution since the solution resistance is very high at low conductivities. The measurement errors (in red) are dominated by polarisation effects at high conductivities. This is because more voltage drops across the electrode interfaces when the solution resistance is very low at high conductivities.

5.6 Summary and conclusions

From the above study, we know the electrode-electrolyte interface impedance consists of parallel elements including a double layer capacitance and Faradaic impedance. The double layer capacitance (C_{DL}) is the series combination of Helmholtz capacitance (C_H) and Gouy-Chapman capacitance (C_G). The double layer capacitance

(C_{DL}) is dominated by the Helmholtz capacitance (C_H) when a bias is applied to the electrodes and the electrolyte concentration is high (>100mM) (as is the case in a seawater conductivity measurement). With very low potential and diluted electrolyte solutions, the total interfacial capacitance is dominated by the Gouy-Chapman capacitance (C_G). Faradaic impedance can be represented by the charge transfer resistance (R_t) in series with Warburg impedance (Z_W). In most cases the charge transfer resistance (R_t) dominates Faradaic impedance (Z_f). Warburg impedance (Z_W) decreases towards zero when the excitation frequency is high enough; it only becomes significant when the current density is too large and ions are not able to diffuse from the bulk to the interface fast enough.

For the conductivity measurement with contact electrode sensor, AC excitation is needed to penetrate the double layer generated between the electrodes and electrolyte. Big electrode and high frequency excitation reduce electrode polarisation effects, but stray capacitance influence will put limit on high frequency excitation. Polarisable electrode is preferred to be used in conductivity sensor since it behaves like a capacitor with no Faradic processes.

Chapter 6 Conductivity Cell Design

In this chapter, two-electrode, four-electrode and five-electrode conductivity cells are analyzed; the design and simulation of a four-electrode conductivity cell are also presented.

6.1 Cell Option

Because sea water is highly conductive, suitable sensors are two-electrode, four-electrode and inductive sensors. Potentially, it is possible to use a CCD (Contactless Conductivity Detection) sensor design, but this will depend on the development of the thin film dielectric materials with high permittivity (ε_r>1500). Like CCD, inductive sensors don't suffer from the effects of electrode polarisation and fouling, since they have no direct contact with seawater. This advantage makes them very popular in conductivity measurement in the ocean. However, the drawback of the inductive sensors is that they suffer from proximity effects [142] and are not very accurate in the low conductivity range. Furthermore, inductive sensors consist of a pair of co-axial toroidal transformers in which one is a voltage ratio transformer and another is a current ratio transformer. The ratio errors in transformer vary as the inverse square of the linear dimension, and unacceptable errors occur when the diameter of the transformer is scaled down [87]. It is for this particular reason that the inductive sensor is not considered for this work. Conventional two-electrode and four-electrode sensors are the most sensitive sensors used for conductivity measurement. These sensors, with planar structures are very attractive because they are easy to mass-produce and miniaturize. Although the conventional two and four electrode sensors suffer from

fouling effects and electrode polarisation, these problems can be controlled or reduced to a limited range by careful design.

The classic two-electrode sensor has the simplest structure, simplifying interface circuit design, making it more compact than the four-electrode sensor. With proper circuit design, the four-electrode sensor is not sensitive to electrode polarisation or fouling. The current feedback combined with high input impedance of the voltage amplifier ensures the four-electrode measurement is independent of electrode condition, resulting in higher accuracy over a wide range (see 2.6.6 and 6.5). The design started with the two-electrode analysis, and then four-electrode and five-electrode with planar electrode built on PCB. A complete conductivity sensor consists of two parts: the conductivity cell and the signal conditioning circuit. The best performance of the sensor can only be achieved by the optimum design of the both parts.

6.2 Two-electrodes Conductivity Cell

An equivalent circuit for the two electrode conductivity cell [77, 143-144] is given in figure 6-1. The model shown in figure 6-1 is actually Randle's equivalent circuit except there are two set of interface elements because there are two electrodes. From the previous chapter, it is clear that the interfacial capacitance of the electrodes is determined by the double layer capacitance (C_{DL}). The Faradaic impedance of the electrodes can be further divided to the charge transfer resistance (R_{CT}) and Warburg impedance (Z_W). Additionally, a stray capacitance (Cp) is included in the equivalent circuit which represent the parasitic capacitance between the two electrodes and the leads.

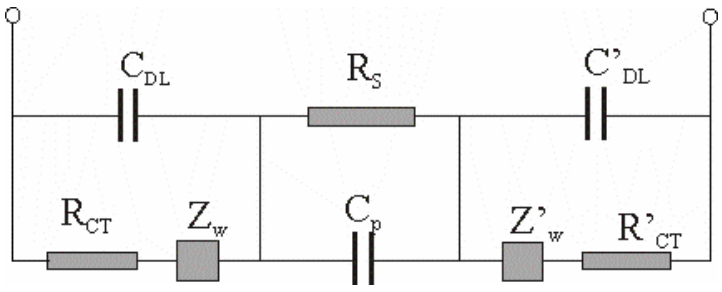

Figure 6-1 Equivalent circuit for two-electrode conductivity cell

For non-polarisable electrodes, like silver/silver chloride (Ag/AgCl) and mercury/mercurous chloride (Hg/Hg_2Cl_2), the charge carriers can be transferred freely over the electrode-electrolyte interface by means of Faradaic current. The potential of the electrode will not change significantly from its equilibrium potential with the application of even a large current density. These electrodes are usually used as reference electrodes to record the potential caused by electrochemical reactions. Although there are no perfect polarisable electrodes, electrodes made from noble metal such as platinum (Pt) are very close to polarisable electrodes under small signal excitation (<1V). They are inert to chemical reactions and no net charge transfer occurs over electrode-electrolyte interface. This means the Faradaic impedance of the platinum electrodes is negligible. Furthermore, the Faradaic impedance will be shorted by the double layer capacitance if a high frequency AC excitation is applied, as shown in figure 5-7. Therefore we ignore the Faradaic impedance of the polarisable electrodes when a small high frequency AC signal is used. Hence, the equivalent circuit for the two electrodes conductivity cell can be simplified as shown in figure 6-2.

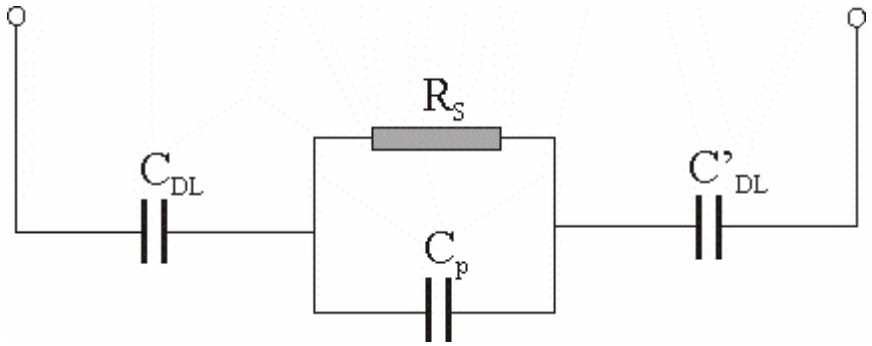

Figure 6-2 Simplified equivalent circuit for conductivity cells with two electrodes

6.3 Cell Size and Frequency Response

Since the double layer capacitances are connected in series to the solution resistance, there is always a voltage drop across the double layers. This phenomenon is called electrode polarisation which results from the accumulation of charge on electrode surfaces and the formation of electrical double layers. Unfortunately, it is

impossible to prevent electrode polarization. Various approaches are proposed for electrode polarization correction. Methods such as the use of four-electrode [88, 145-147], high surface area electrodes [90] and high current density [129] methods, allow the reduction of this harmful effect. Another method is to use the cells with movable electrodes. By adjusting the distance between the two electrodes, accurate conductivity is obtained after subtracting the interface impedance [88, 129 and 133]. For a simple two electrode sensor, there are two ways to reduce the voltage drop across the double layer. One way is to increase the double layer capacitance, and another way is to increase the frequency of the excitation.

To reduce the measurement error from electrode polarisation, a high frequency excitation is preferred. But there are limitations to the upper frequency. The first is the physical constraint of the components, i.e. opamps always have limited bandwidth. The second is the influence of stray capacitance. By checking the simplified model shown in figure 6-2, the measured impedance is given as:

$$Z = \frac{R_S}{j2\pi f * R_S * C_p + 1} + \frac{2}{j2\pi f * C_{DL}} \qquad [6\text{-}1]$$

In general, the reactance of the double layer capacitance should be very small while the reactance of the stray capacitance should be much higher than the solution resistance. To find out the appropriate frequency range, assume a cell constant of $\kappa = 10 cm^{-1}$, two cells with different electrode size were simulated using MATLAB.

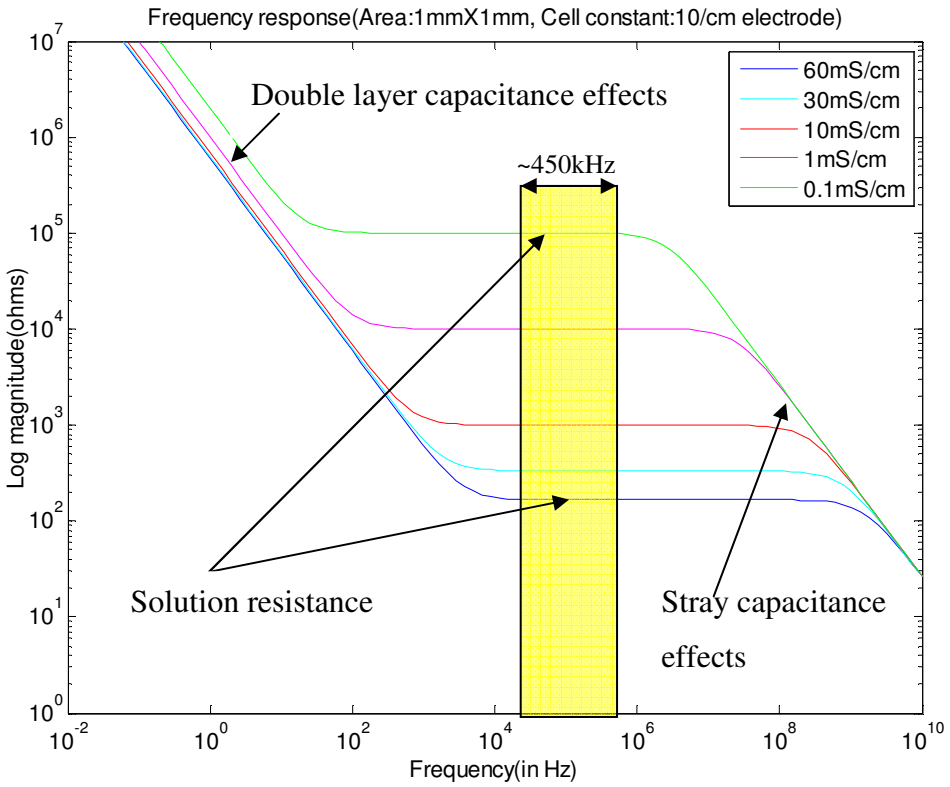

a. 1mm^2 electrode with 6pF stray capacitance

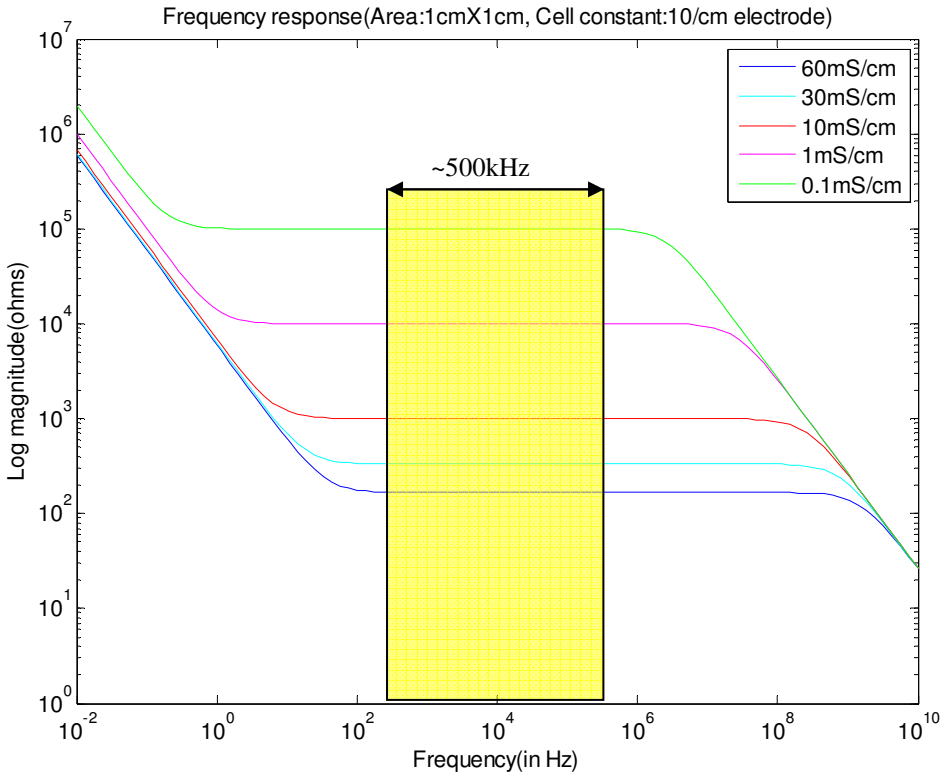

b. 1cm^2 electrode with 6pF stray capacitance

Figure 6-3 Two-electrode cells' frequency response (a, b)

The simulation results given in figure 6-3 show the frequency response for two cells with different electrode area, 1 mm^2 (in figure 6-3a) and 1 cm^2 (in figure 6-3b). Both cells are assumed to have a cell constant of $10cm^{-1}$ and a stray capacitance of 6 pF. In figure 6-3a, it is clear that that the impedance is dominated by the double layer capacitance when the frequency is below 50 kHz while the stray capacitance distorts the measurement when the frequency is above 500 kHz. The intermediate frequency range, there is a narrow plateau which is given by the resistance of solution. The yellow bar in the diagram shows the best frequency range for the cell ($1mm^2$) is somewhere around 200 kHz. Figure 6-3b shows that the double layer dominates the impedance below 200Hz while the stray capacitance dominates when the frequency is above 500 kHz. Obviously, the bigger electrode has wider bandwidth, hence more freedom for the instrument design.

6.4 The ratio of double layer reactance and solution resistance

Because sea water has a high conductivity, the measurement error is mainly from electrode polarisation. It is necessary to theoretically analyse the error caused by the voltage drop across the double layer. The double layer capacitance (C_{DL}) and reactance are given by:

$$\frac{1}{C_{DL}} = \frac{1}{C_H} + \frac{1}{C_G} \qquad [6\text{-}2]$$

$$C_H = \varepsilon_o \varepsilon_{\gamma 1} \frac{A}{d_1}, \quad C_G = \varepsilon_o \varepsilon_{\gamma 2} \frac{A}{d_2} \qquad [6\text{-}3]$$

$$Z = \frac{1}{j\omega C_{DL}} = \frac{1}{j2\pi f C_{DL}} \qquad [6\text{-}4]$$

where A is the electrode area; $\varepsilon_{\gamma 1}$, $d1$ are the permittivity and thickness of the outer Helmholtz plane; and $\varepsilon_{\gamma 2}$, $d2$ are the permittivity and thickness of diffusion layer respectively. Assume $C_G >> C_H$, the double layer capacitance (C_{DL}) can be approximately considered as a single layer capacitance—Helmholtz capacitance (C_H):

$$C_{DL} \approx C_H$$

$$C_{DL} \approx \varepsilon_o \varepsilon_{\gamma 1} \frac{A}{d_1} \qquad [6\text{-}5]$$

Assume the solution is contained in a cylinder with two electrodes. The cross section of the solution has the area (A_S), and the length of the column is L. The resistance of the solution is:

$$\sigma = \frac{L}{A_S} * \frac{1}{R_S} \qquad [6\text{-}6]$$

$$\kappa = \frac{L}{A_S} \qquad [6\text{-}7]$$

$$\sigma = \kappa * G_S \quad [S/m] \qquad [6\text{-}8]$$

$$R_S = \frac{L}{A_S} * \frac{1}{\sigma} \quad [S/m] \qquad [6\text{-}9]$$

To achieve the desired accuracy (0.1mS/cm^{-1}), the cell has to be designed to make the voltage drop across the double layer very small. For cells with two electrodes, the error voltage (ΔV) caused by the double layer capacitance (C_{DL}) is:

$$\Delta V = I * \frac{2}{j2\pi f C_{DL}}$$

$$\Delta V = \frac{Vin}{R_S + 2/j2\pi f C_{DL}} * \frac{2}{j2\pi f C_{DL}} \qquad [6\text{-}10]$$

Thus we have

$$\frac{\Delta V}{Vin} = \frac{2/j2\pi f C_{DL}}{R_S + 2/j2\pi C_{DL}} \qquad [6\text{-}11]$$

Equation 6-11 shows that the ratio between the error voltage (ΔV) and the input voltage (Vin) is controlled by the ratio between the reactance of the double layers and the solution resistance. It is obvious that the cell should be designed to make the solution resistance (R_S) much bigger than the reactance of the double layer capacitance (C_{DL}) to reduce the error voltage. To achieve the desired accuracy of 0.1mS/cm at the highest conductivity of 72mS/cm, the ratio has to be in the range:

$$\frac{\Delta V}{Vin} = \left| \frac{2/j2\pi fC_{DL}}{R_S + 2/j2\pi fC_{DL}} \right| < \left| \frac{\Delta R}{R} \right| \qquad [6\text{-}12]$$

Since
$$\left| \frac{\Delta R}{R} \right| = \left| \frac{\kappa(\frac{1}{\sigma} - \frac{1}{\sigma \pm 0.1})}{\kappa * \frac{1}{\sigma}} \right| \approx 1.39*10^{-3} \qquad [6\text{-}13]$$

Thus
$$\frac{\Delta V}{Vin} = \left| \frac{1/j\pi fC_{DL}}{R_S + 1/j\pi fC_{DL}} \right| < 1.39*10^{-3} \qquad [6\text{-}14]$$

Insert equation 6-5, equation 6-7 and 6-9 into equation 6-14:

$$\left| \frac{\frac{1}{j\pi f\varepsilon_o\varepsilon_{\gamma 1}\frac{A}{d_1}}}{\frac{1}{\sigma}*\frac{L}{A_S} + \frac{1}{j\pi f\varepsilon_o\varepsilon_{\gamma 1}\frac{A}{d_1}}} \right| < 1.39*10^{-3} \qquad [6\text{-}15]$$

$$\left| \frac{1}{j\pi f\varepsilon_o\varepsilon_{\gamma s}*\frac{A}{d_1}*\frac{1}{\sigma}*\frac{L}{A_S}+1} \right| < 1.39*10^{-3} \qquad [6\text{-}16]$$

$$\left| \frac{1}{j\pi f\varepsilon_o\varepsilon_{\gamma s}*\frac{A}{d_1}*\frac{1}{\sigma}*\kappa+1} \right| < 1.39*10^{-3} \qquad [6\text{-}17]$$

Equation 6-17 shows that the accuracy can be improved by increasing either the electrode surface area (A) or the cell constant (κ) or more effectively both. For cells where the electrode surface area (A) is equal to the cross section area of solution (A_S), equation 6-16 can be simplified to:

$$\left| \frac{1}{j\pi f \varepsilon_o \varepsilon_{rs} * \frac{1}{\sigma} * \frac{L}{d_1} + 1} \right| < 1.39*10^{-3} \qquad [6\text{-}18]$$

Equation 6-18 shows the accuracy now only depend on the cell length (L) when the area of the electrode (A) is effectively equal to the cross section area of solution (A_S). Assume the excitation frequency (f) is 200 kHz, the distance from the outer Helmholtz plane distance to the electrode (d_1) is 3 Å, and the relative permittivity (ε_{r1}) is 5, the ratio between the reactance of the double layer and the resistance of the solution changes with the cell length as it is shown in figure 6-4.

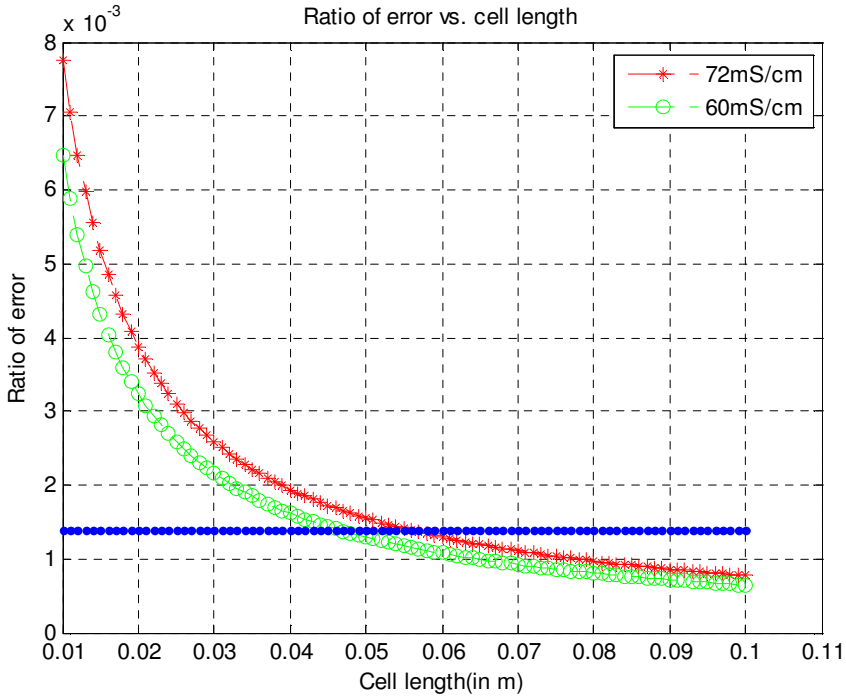

Figure 6-4 Cell length and error ratio

In figure 6-4, the blue line is the desired accuracy, the red and green curve are the simulation results for solutions with conductivity of 72mS/cm and 60mS/cm respectively. It is clear that the cell length has to be longer than 5.8cm for a 72mS/cm solution in order to achieve the required accuracy. Assume the cell length is 6cm, and the electrodes area of $1cm^2$, the cell constant is $6cm^{-1}$; for a cell with $1mm^2$ area electrodes, the cell constant is $600cm^{-1}$.

For smaller electrodes, the cell constant has to be much bigger than that of the cell with bigger electrodes in order to achieve the same accuracy. For a conventional conductivity cell, it is very difficult to achieve a design with very high cell constant, and the only way is to increase the distance of the electrodes which results in a large size and obviously is not desired. However, a microfluidics can be used to produce a high cell constant without excessively increasing the size. To restrict the area of the cross section of the solution, the fluidic channel can be made very narrow, confining the electric fields and the current stream lines. To increase the distance between the electrodes, a channel with a zigzag shape can effectively increase the length without excessively increasing the size of the cell. Another advantage of microfluidics is that the external proximity effect is avoided since the solution is totally enclosed inside the channel. The drawback of a sensors built in a microfluidics is possible blockage and more power consumption since the channel needs a pump for flushing.

6.5 Four-electrodes Conductivity Cell

From figure 6-4, we know that for a two-electrode cell, even when high frequency excitation (200k Hz) is used, the distance between the two electrodes still needs to be longer than 5.8 cm in order to achieve the desired accuracy. Therefore the two-electrode cell is not the best option when considering both size and accuracy. Four-electrode cells have some advantage when high accuracy is in demand. When the voltage sensing electrodes are connected to a high impedance amplifier, they suffer much less polarisation effects even with small electrode.

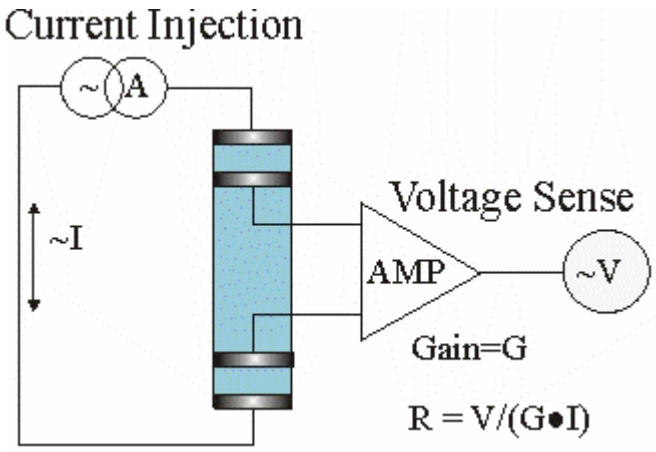

Figure 6-5 Four-electrode conductivity cell

In figure 6-5, an AC current source is connected to the outer two electrodes of the conductivity cell to inject excitation current (I). The inner two electrodes are connected to a high impedance amplifier (with gain of G); the resistance of the measured sample (R) is proportional to output voltage (V). The electrode polarization on the injecting electrodes doesn't affect the measurement, as long as the injecting electrodes are connected to a constant current source. Although the electrode polarization on the sensing electrodes does affect the measurement, but this effects can be minimized and ignored when an amplifier with high input impedance is used.

Figure 6-6 shows the equivalent circuit for a four-electrode conductivity cell. R_{S1} is the solution resistance between the inner electrodes, $Rs2$ and R'_{s2} are the solution resistance between the inner and outer electrodes; C_{DL1} and C'_{DL1} are the double layer capacitance of the inner electrodes, C_{DL2} and C'_{DL2} are the double layer capacitance of outer electrodes; C_{p1} is the stray capacitance of the inner pair electrodes, and C_{p2} is the stray capacitance of the outer pair electrodes. Assume the inner-electrode pair is connected to an amplifier with infinite input impedance, a constant AC current I is injected from the outer pair electrodes, the voltage between the outer electrodes is given by

$$V_{outer} = \mathrm{I} \times \left\{ \frac{(R_{s2} + R'_{s2})(1 + R_{s1}C_{p1}s) + R_{s1}}{(R_{s2} + R'_{s2})(1 + R_{s1}C_{p1}s)C_{p2}s + R_{s1}C_{p1}s + 1} + \frac{1}{C_{DL2}s} + \frac{1}{C'_{DL2}s} \right\} \qquad [6\text{-}19]$$

where s is the Laplace variable ($j\omega$).

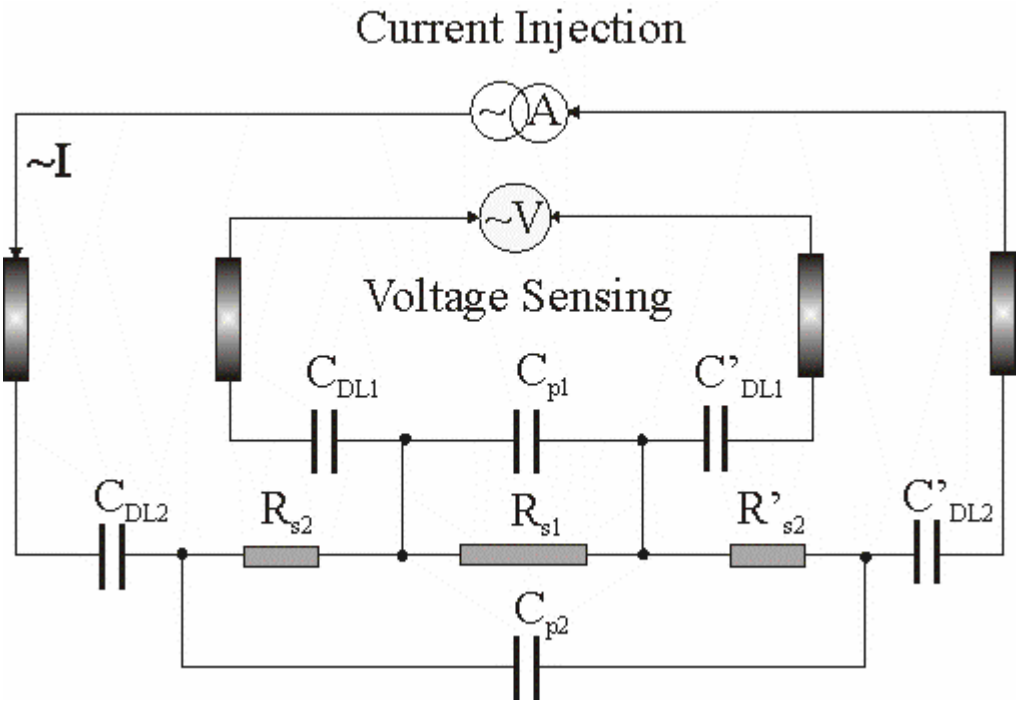

Figure 6-6 Equivalent circuit of four-electrode conductivity cell

For a conductivity cell with a cell constant of $10cm^{-1}$, the solution resistance between the electrodes is in the range of 10 kΩ to 200 Ω when the conductivity of the solution varies from 1mS/cm to 50mS/cm. Since the stray capacitance between a small pair electrode is normally less than 10pF, for AC current with 1 kHz, the maximum reactance of stray capacitance is given by

$$X < \frac{1}{j\omega C_{assume}} = \frac{1}{2\times 3.14\times 1000\times 10\times 10^{-12}} \approx 16\ M\Omega \qquad [6\text{-}20]$$

For a cell constant of $10cm^{-1}$, 16MΩ is equivalent to 0.625μS/cm.Therefore, it is reasonable to ignore the stray capacitances between the electrodes, and equation 6-19 can be further simplified:

$$V_{outer} = \mathrm{I}\times\left(R_{s2} + R'_{s2} + R_{s1} + \frac{1}{C_{DL2}s} + \frac{1}{C'_{DL2}s} \right) \qquad [6\text{-}21]$$

Equation 6-21 shows that the total voltage (V_{outer}) between the outer-electrode pair includes not only the voltage drop on the solution resistance (R_{s2}, R'_{s2} and R_{s1}), but also the voltage drop on the double layer capacitance (C_{DL2} and C'_{DL2}). As we are only

interested in the voltage drop on the solution resistance, two inner electrodes are placed close to the current injection electrodes to sense the voltage drop on the solution resistance (R_{s1}). As long as the input impedance of the amplifier connected to the inner electrodes is high enough, the voltage drop caused by the current flowing through the double layer capacitance (C_{DL1} and C'_{DL1}) can be ignored and hence minimize the electrode polarization effects. In figure 6-6, the sensitivity can be increased by reducing the solution resistances (R_{s2} and R'_{s2}). The maximum sensitivity can be achieved by minimizing the distance between the inner and outer electrode.

6.6 Planar Electrodes and Conformal Mapping

Most commercial conductivity meters use a two-electrode cell with electrodes are usually made of platinum, titanium, gold-plated nickel, or graphite. One simple design is the dual-needle sensor which simply uses two platinum wires as electrodes [150]. Concentric dual-ring sensor and coaxial cylinder electrodes [151-153] are also used. A special design with a movable electrode to adjust the electrodes distance is also reported [154]. Planar electrodes are widely used in the miniaturized sensors due to their simple structures which are easy to be fabricated and miniaturized. Among them, two-electrode and inter-digitated structure with rectangular shape [155-160] are the most common type of planar electrodes. One disadvantage of planar electrode is the electric field is not homogeneous and thus it is difficult to calculate the equivalent cell constant and cell geometry. Conformal mapping is an analytic method which can be used to map the inhomogeneous electric field. The fundamental principle behind conformal mapping is to reduce a three-dimensional problem to a two-dimensional problem, thus a simplified solution is obtained.

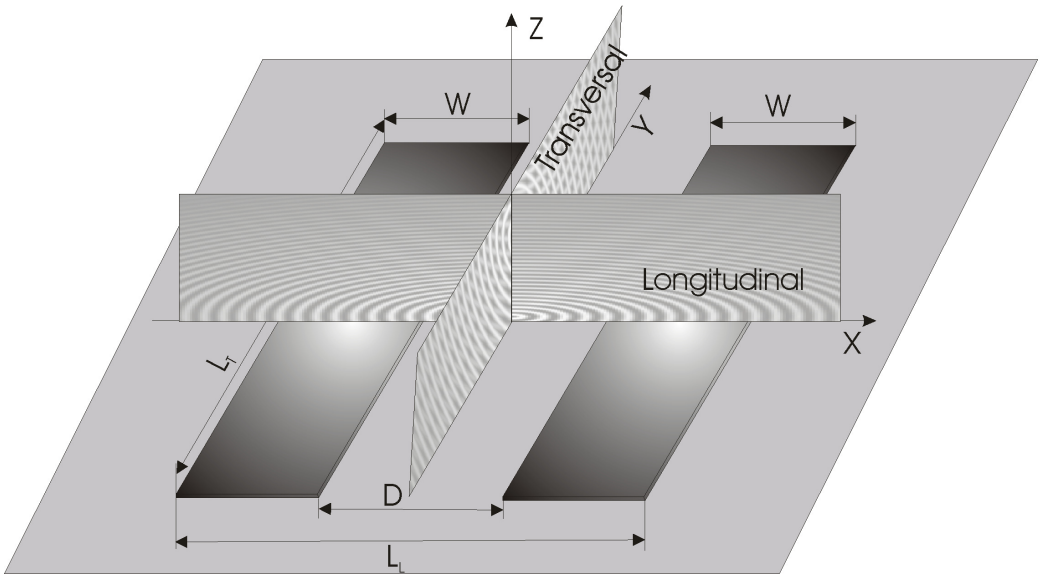

Figure 6-7 Two-electrode cell with planar structure

Figure 6-7 shows a typical structure of a rectangular planar two-electrode cell. The direction in parallel with the electric field or current lines is termed longitudinal. The planes perpendicular to the current lines form the transversal planes. The lines formed by the intersection of the transversal planes and the plane of electrode substrate define the transversal direction**.** Since the electric fields and current lines of the planar two electrodes are three-dimensional problems, they are quite complex and can be solved by the finite element methods (FEM). Commercial software such as COMSOL is available for these applications, but the drawback is the software need a big memory (RAM) to run a simulation; normally a work station is necessary for the better accuracy.

Alternatively, a three dimensional problem can be reduced to a two-dimensional approximation using conformal mapping. The approximation is based on the assumption that the edge effect in the transversal direction is negligible (as in the case of a channel with insulation side walls are used). The electric field and current lines are proportional to the dimension in the transversal direction, leading to a boundary value problem in the longitudinal plane, defined by the inter-electrode distance *D* and the electrode width *W*. As a consequence, all results obtained must be interpreted as normalised per unit length in the transversal direction, and the relation ship between the three dimensional cell constant and the two dimensional cell constant is given as [161]:

$$\kappa = \kappa_{2D} * \frac{1}{L_T} \qquad [6\text{-}22]$$

where κ is the normal cell constant in tree-dimension, κ_{2D} is the two dimensional cell constant and L_T is the electrode length in transversal direction. The two dimensional cell constant is a function of the electrode width W and gap D, and can be calculated by conformal mapping.

6.6.1 Schwarz-Christoffel Mapping (SCM)

The Schwarz-Christoffel Mapping (SCM) method is a subset of conformal mapping and has been widely used to analyze electromagnetic field problems in planar electrodes and coplanar-strip waveguides [156, 162-169]. SCM can be used to map the upper half of a complex t-plane into the interior of a polygon of another complex w-plane which has n sides and external angles (α_1, α_2 ... α_n).

$$w = C_1 \int_0^t \frac{dt}{(t-t_1)^{\alpha_1}(t-t_2)^{\alpha_2}\cdots(t-t_n)^{\alpha_n}} + C_2 \qquad [6\text{-}23]$$

where C_1 and C_2 are the integral coefficients, C_1 establishes the scale and orientation of the polygon and C_2 gives its position in the w-plane. By plugging the positions of the corresponding points in the both planes into equation 6-23, the coefficients of C_1 and C_2 can be determined.

For a two-electrode conductivity cell with planar structure, the inhomogeneous electric field is distributed above the insulated substrate which can consider as the upper half of the t-plane. Assume the solution is homogeneous, and the boundary conditions of the cell can be defined. For the metallic electrodes with constant potential, Dirichlet boundary condition is defined as:

$$\varphi = \text{constant}, \quad \frac{D}{2} \le \left| x \right| \le \frac{D}{2} + W \qquad [6\text{-}24]$$

For the boundary section between the solution and the substrate, since there is no flux lines crossing the limiting planes, Neumann boundary condition can be applied as:

$$\frac{\partial \varphi}{\partial n} = 0, \quad 0 \le |x| \le \frac{D}{2}, \ \frac{D}{2} + W < |x| < +\infty \qquad [6\text{-}25]$$

Where $\varphi$the applied potential, and n is the normal to the boundary section between the solution and the substrate. By apply SCM mapping, the inhomogeneous electric field in the t-plane is transformed into the homogenous electric field in the w-plane, as it is shown in figure 6-8.

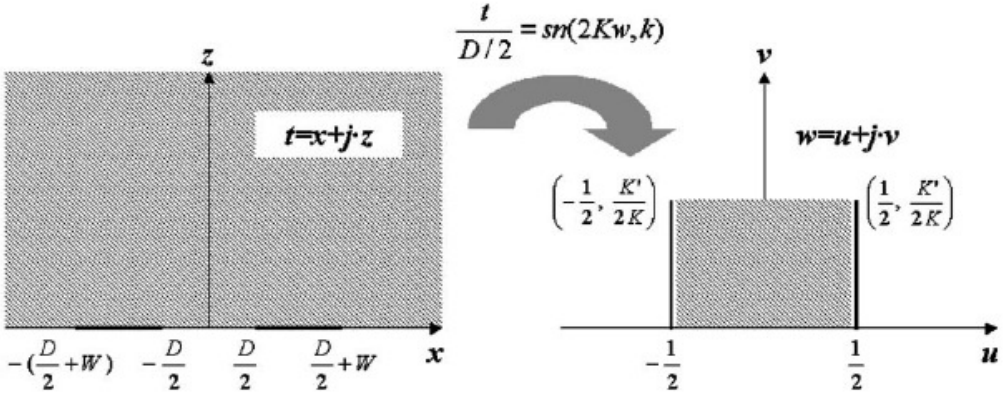

Figure 6-8 SCM used to transform semi-infinite half-plane into bonded rectangular region [161]

The solution of the potential distribution is also solved by SCM transformation from the semi-infinite t-plane into a rectangular region defined in the w-plane, which is determined by the function:

$$\frac{t}{D/2} = sn(2Kw, k) \qquad [6\text{-}26]$$

Where $sn(u,k)$ is the Jacobian elliptic function with modulus k, at the argument u. The modulus k is related to the electrode layout:

$$k = \frac{1}{1 + \frac{2W}{D}} \qquad [6\text{-}27]$$

Since the electric field in the rectangular region of w-plane is given by a uniform distribution, the solution for the two dimensional cell constant is easily obtained by checking figure 6-8.

$$\kappa_{2D} = \frac{2K(k)}{K'(k)} \qquad [6\text{-}28]$$

where *K(k)* is the complete integral of the first kind, defined as

$$K(k) = \int_0^1 \frac{dt}{\sqrt{(1-t^2)(1-k^2t^2)}} \qquad [6\text{-}29]$$

And *K'(k)* is the complete integral of the first kind taken in the complementary modulus *k'*, given by

$$K'(k) = K(k')$$

$$k' = \sqrt{1-k^2} \qquad [6\text{-}30]$$

6.6.2 Modified SCM for Finite Height

The above analysis is based on an open cell with infinite height (*z* direction). However, planar electrodes with open structure do not have a high cell constant. Furthermore the open structure also makes measurement unrepeatable due to the undetermined volume effects since the space for the electric field is not defined. In practice, the electrodes are always enclosed in a shroud in order to avoid the volume effects. To achieve a high cell constant, the solution volume and the current path must be confined in order to achieve a high resistance. Usually, planar electrodes need to be put in a tube or channel made from plastic or ceramic. Figure 6-9 shows an example of a cell with insulation to limit the cell height.

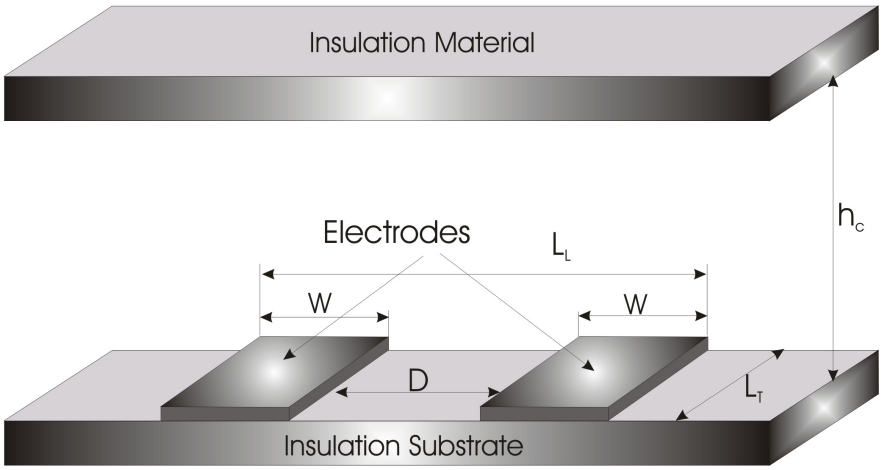

Figure 6-9 Planar two-electrode cell with limited height

In the case where the cell height is finite, equation 6-27 cannot be used. This problem has been solved by several papers [170-171], and the detailed analysis will not be discussed here. For a cell with limited height of h_c, as shown in figure 6-9, the modulus (k_h) is totally different from the modulus (k) of the cell with infinite height and is given by [172]:

$$k_h = \frac{\tanh(\frac{\pi D}{4h_c})}{\tanh(\frac{\pi(D+2W)}{4h_c})} \qquad [6\text{-}31]$$

Thus the modified equation for the cell constants with a finite height:

$$\kappa_{2h} = \frac{2K(k_h)}{K'(k_h)} \qquad [6\text{-}32]$$

$$\kappa_h = \kappa_{2h} * \frac{1}{L_T} \qquad [6\text{-}33]$$

where κ_{2h} is the modified two dimensional cell constant and κ_h is the modified three dimensional cell constant respectively. Elliptic functions are well documented and tabulated, and can be found in the commands of some commercial software such as MATLAB.

6.7 Four Electrode Cell Design

A novel four-electrode conductivity cell was designed and built on a PCB substrate with four electrodes fully enclosed in an insulated channel. The design is different with other reported conductivity cells built on a PCB which normally have open structure without any cover or lid [203, 204]. There are mainly two advantages to build a conductivity cell in a channel: increasing cell constant, and remove external proximity effects. An insulated channel can confine the electric field in a narrow space to increase the solution resistance between the electrodes, hence significantly increase the cell constant. Such a conductivity cell does not suffer external proximity effects if it is installed in a flow system where the inlet and outlet is separated and controlled by a pump. However there are also some drawbacks, the use of a pump will increase power consumption and also an extra filter is necessary since the narrow channel could be blocked by particles and bio fouling when they are deployed in the sea.

Figure 6-10 shows the structure of a four-electrode conductivity cell built in an insulated channel. The four electrodes are made from platinum foil glued on a PCB substrate, and electrodes are connected to copper tracks through via holes. Two plastic strips are glued on the PCB as side wall, and a plastic lid is glued on top of the side wall to complete the insulated channel.

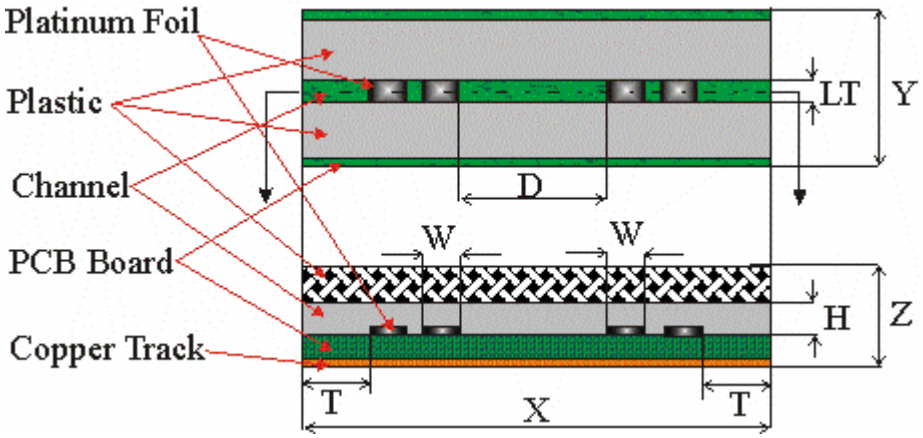

Figure 6-10 Four-electrode cell built on PCB (Dimension: Y= 30mm, X = 50mm, Z =12mm, LT=H=5mm, D=20mm, W= 2mm, T = 10mm)

The conformal mapping method is used to calculate the cell constant, the calculated cell constant of the conductivity cell in figure 6-10 is 10.74/cm. A MATLAB script used to calculate cell constant is included in Appendix A.

6.7.1 Four Electrode Cell Simulation

In order to verify the design of four-electrode conductivity cell, simulation was done using the commercial software Comsol.

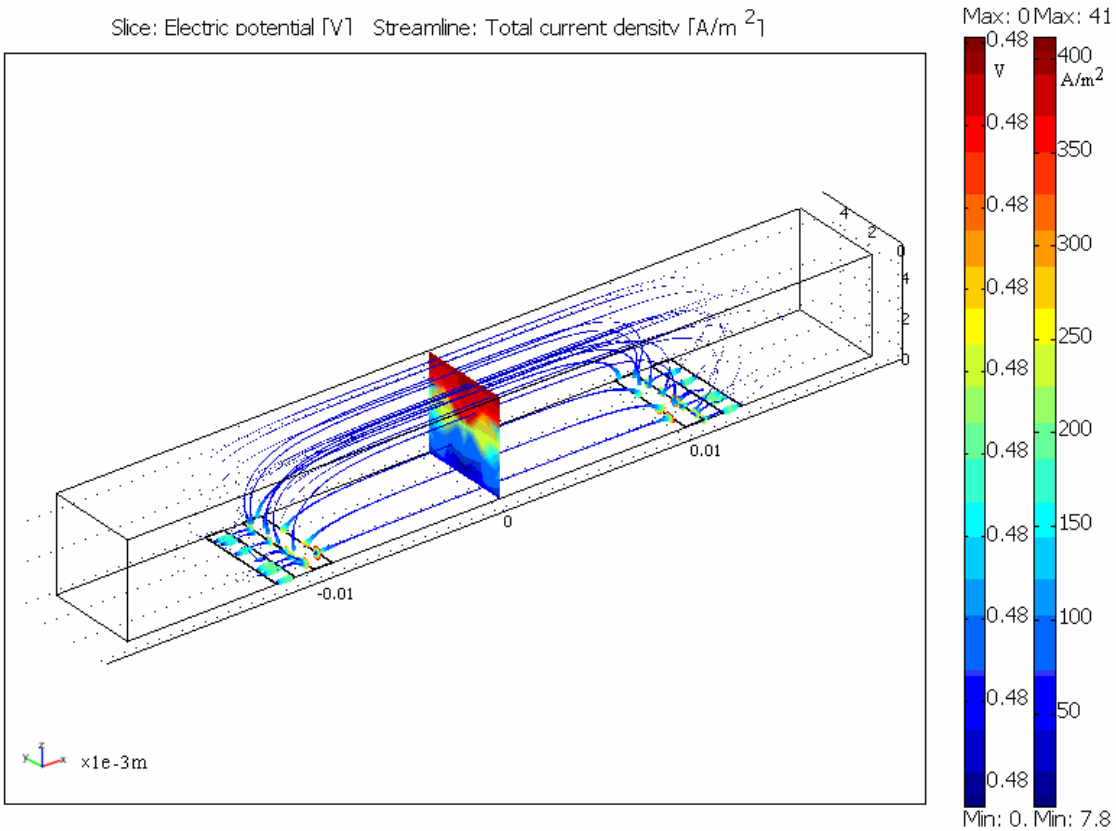

Figure 6-11 Comsol Simulation of a four-electrode conductivity cell, the cell dimension is in mm, the electric potential distribution of the channel centre cross section is indicated by the left colour-bar, the current density of streamline between the inner electrode is indicated by the right colour-bar.

Figure 6-11 shows the simulation of a four-electrode conductivity cell. In figure 6-11, the four-electrode cell is located in a channel where it is filled with conductivity solution. The electrode material was assumed as Cu, the conductivity of the medium was 10mS/cm and the whole cell was insulated by side and end wall. The blue lines in the channel are current stream lines and the potential distribution in cross section is represented by different colour. The inner two electrodes were used as the active electrodes and two outer electrodes were floated. As we can see there are few current stream lines passing through the two outer electrodes, therefore less voltage drop

between the inner and outer electrodes. This indicates that, for a four-electrode cell building in an insulation channel with no external current flow, a better sensitivity can be obtained if the outer electrodes are used to sense the voltage instead of the inner electrodes. To maximize the sensitivity, the outer electrodes should be located as close as possible to the inner current injection electrodes. However, for a four-electrode cell with external current flow, the inner electrodes are best to be used as sensing electrode in order to minimize the proximity effect. The equivalent impedance of the four-electrode conductivity cell given by the simulation is 1108 Ω. The cell constant can be calculated as:

$$\kappa = R^* \sigma = 1108*0.01/cm = 11.08/cm \qquad [6\text{-}34]$$

The simulation result shows the cell constant given by FEM simulation (11.08/cm) is close to the cell constant (10.74/cm) calculated using SCM. The small difference (about 3%) is caused by the difference between FEM and SCM algorithms used in the simulation.

6.7.2 Four-electrode Cell for Immersion Application

In the application where a pump is not used, the conductivity cell needs to be immersed in seawater, and the four-electrode conductivity cell can be modified to adapt to this situation. As it is shown in figure 6-12, the two end sections of the cell are defined as the half length of the gap between the outer electrodes, thus the total resistance between outer electrodes are given by

$$R_{total} = R_{in} \,||\, (R_{end} + R_{out} + R'_{end}) \qquad [6\text{-}35]$$

Where R_{in} is the internal resistance between the outer electrodes, R_{end} and R'_{end} are the resistances of the end sections of the channel and R_{out} is the sea water resistance outside the cell.

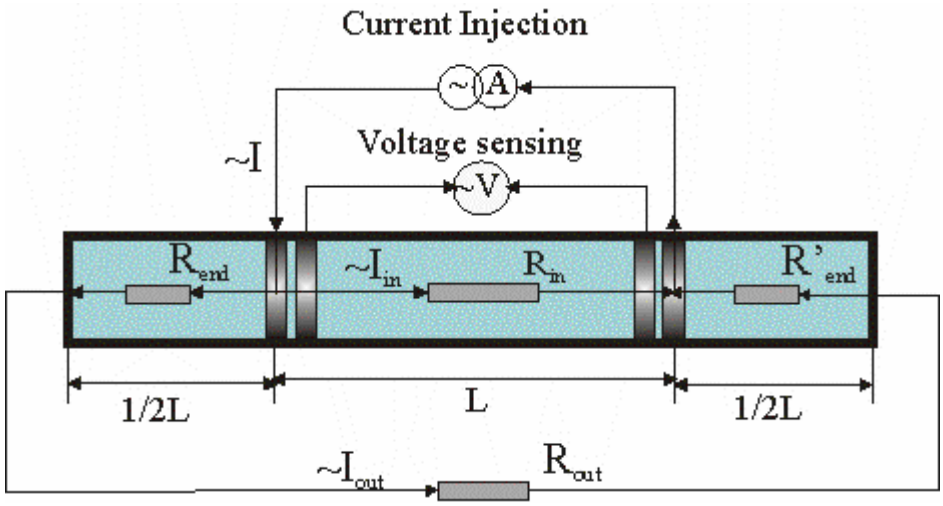

Figure 6-12 Four-electrode cell for immersion application

Assume the channel dimension and conductive medium are uniform, both end resistances (R_{end} and R'_{end}) are equivalent to half of the internal resistance (R_{in}) since the both ends have half length of the gap (L) between the outer electrodes. Thus equation 6-35 can be further simplified as

$$R_{total} = R_{in} \,||\, (R_{in} + R_{out}) \qquad [6\text{-}36]$$

The resistance (R_{out}) is determined by the seawater around the conductivity cell where current path cross section can be infinite; on the other hand, the end section resistance (R_{end}) can be well defined by the channel dimension and is given by

$$\mathrm{R_{out}} = \frac{l_{out}}{\sigma \bullet A_{out}} \qquad [6\text{-}37]$$

$$R_{in} = \frac{L}{\sigma \bullet A_{in}} \qquad [6\text{-}38]$$

where σ is the conductivity of the measured seawater, l_{out} and A_{out} are the equivalent current path length and cross section area outside of the cell, L and A_{in} are the equivalent current path length and cross section area inside the cell. The ratio of R_{in} and R_{out} is given by

$$\frac{R_{in}}{R_{out}} = \frac{L \bullet A_{out}}{l_{out} \bullet A_{in}} \qquad [6\text{-}39]$$

To reduce the external proximity effects, we need increase the ratio of R_{in} and R_{out}, and this can be achieved by increasing L and reducing A_{in}. Thus a long narrow channel is preferred to be used in an immersion application.

6.8 Five-electrodes Conductivity Cell

In figure 6-13, a shielding (fifth) electrode is added on an end of a four-electrode cell to remove the external proximity effects. Since the fifth electrode is directly connected with the first electrode by wire, they have equal potential and there is no current flowing outside of the cell. The biggest advantage of the five-electrode is that the external proximity effect is avoided, but the drawback is the increasing dimension. For a five-electrode conductivity cell shown in figure 6-13, the cell constant κ is given by equation 6-40.

$$\kappa = \frac{1}{2} \bullet \frac{L}{A} \qquad [6\text{-}40]$$

where L is the distance between the first (or fifth) and fourth electrode, and A is the equivalent cross section area of the channel inside the cell in figure 6-13.

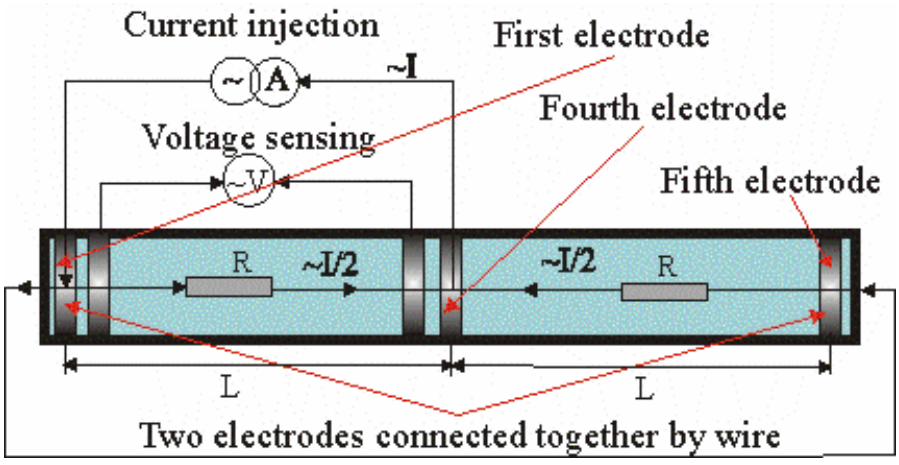

Figure 6-13 A five-electrode conductivity cell with fifth electrode as a shielding electrode

Compared with the five-electrode cell shown in figure 6-13, the five-electrode cell in figure 6-14 has the same dimension, but a doubled cell constant. This is because the excitation current of the cell in figure 6-14 only flows between the first and fourth electrode inside the channel, and the current from the shielding electrode to fourth electrode is supplied by an additional buffer. The cell constant κ of the cell in figure 6-14 is given by equation 6-41.

$$\kappa = \frac{L}{A} \qquad [6\text{-}41]$$

where L is the distance between the first and fourth electrode, and A is the equivalent cross section area of the channel inside the cell in figure 6-14.

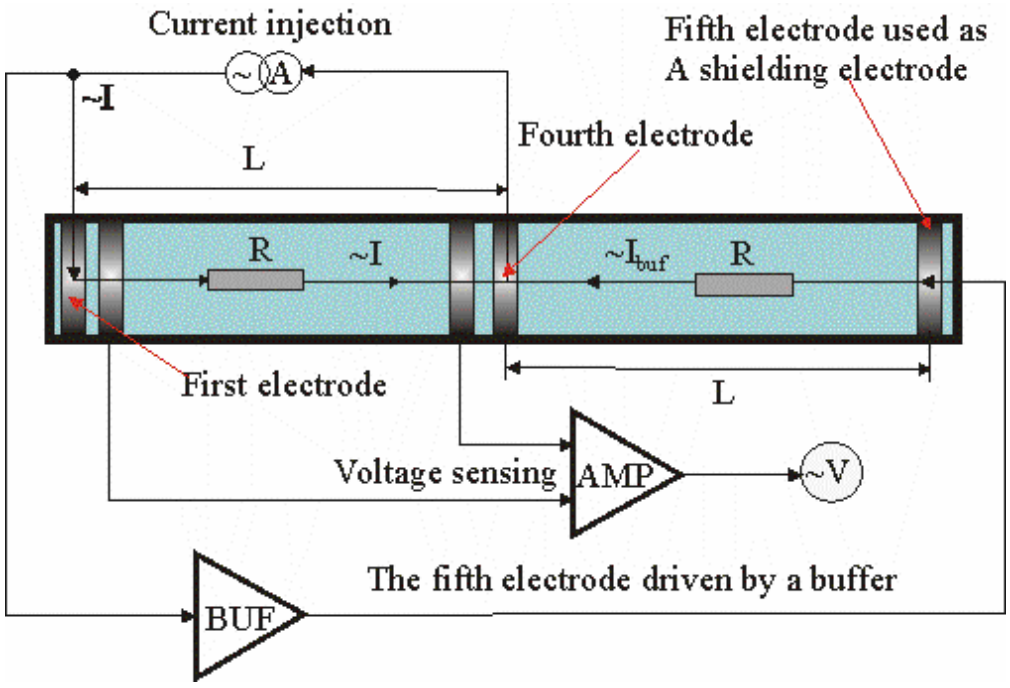

Figure 6-14 A modified five-electrode cell with a buffered shielding electrode

6.9 Summary and conclusions

For two-electrode conductivity cell, an excitation signal frequency need to be carefully chosen due to the double layer effects and stray capacitance influence. The distance between two electrodes should be longer than 5.8cm in order to achieve desired accuracy of 0.1mS/cm.

Four-electrode conductivity cell has advantage over two-electrode conductivity cell, because it uses two electrodes to inject excitation current and other two electrodes to sensing the voltage. As long as the sensing electrodes are connected to a high impedance amplifier, they suffer much less electrode polarisation effects.

Comformal mapping is a simple, useful analysis method suitable for conductivity cell with planar electrodes. The essence of conformal mapping is to convert a three dimension to two dimension problem, thus simplify the analysis. A four-electrode cell designed by using conformal mapping has a cell constant (10.74/cm) close to the Comsol simulation result (11.08/cm).

The four-electrode conductivity cell built in an insulated channel is best to be used as a flow cell with a pump and valve control to remove the external proximity effects. For immersion application, five-electrode conductivity cell is the best option since it has an addition shielding electrode to remove the external proximity effects.

Chapter 7 Signal Conditioning and Circuit Design

This chapter describe the signal conditioning and circuit design for the temperature and conductivity sensors. The key design issues and detailed circuit analysis are also presented.

7.1 Conductivity sensor design

Different circuits can be used to measure impedance. AC Bridge and active bridge circuits are very popular [173-174]; various oscillator techniques are also frequently used to convert the impedance to frequency signal [175-178]; a few more advanced designs even include a multiplexer to support multi-channel signal process with built-in test for self calibration [179-181]. With the rapid development of modern microelectronics, more and more opamps with high performance are available; consequently greatly simplify the circuit design.

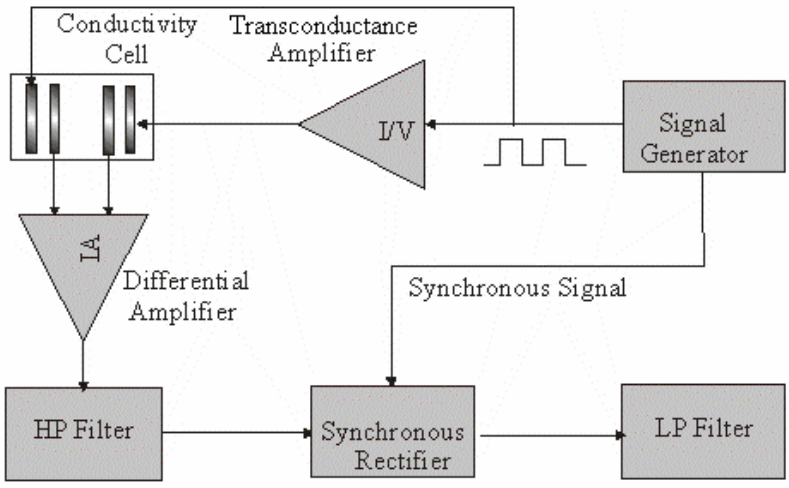

Figure 7-1 Block diagram of conductivity sensor design

Figure 7-1 shows the block diagram of the four electrode conductivity sensor circuit design. In this design, the various design techniques have been combined, and AC excitation with 1 kHz square wave is used to reduce the polarisation effects. The circuit consists of a signal generator, a trans-conductance amplifier, an instrumentation amplifier, a high pass filter, a synchronous rectifier and a low pass filter. A small current is injected into the trans-conductance amplifier, where it passes the four-electrode conductivity cell which is connected in the feedback loop. The output voltage of the four-electrode conductivity cell is sent to an instrument amplifier which has a high input impedance to minimize the polarization effects on the two voltage sensing electrodes. The high pass (HP) filter is used to block DC voltage caused by the bias current of the trans-conductance amplifier. The synchronous rectifier is used to demodulate the injection signal and the final DC voltage is measured after a low pass (LP) filter.

7.2 Temperature sensor design

A thermistor is used in the temperature sensor design, because thermistors are more sensitive than other temperature sensors. A small constant current is used as an excitation, and the voltage drop across the thermistor is measured to give the resistance. The temperature can be calculated using the Steinhart equation:

$$1/T = C1 + C2 * lnR + C3 * (lnR)^3 \qquad [7\text{-}1]$$

where T is the calculated temperature (Kelvin) and R is the thermistor resistance. $C1$, $C2$ and $C3$ are the Steinhart-Hart constants for a specified thermistor which are obtained by calibration.

Self heating is an issue need to be addressed in the temperature sensor design. When a current passes through a thermistor, it consumes power and produces heat; consequently, the resistance of the thermistor changes. An effect called self-heating need to be addressed in the temperature sensor design. In order to achieve an accurate measurement, the excitation current must be minimized so that the self generated heat is balanced by the dissipated heat. The thermal dissipation constant (D) of a thermistor

is defined as the power required to raise the thermistor's body temperature by 1°C in a particular measurement medium. The dissipation constant (D) is expressed as:

$$D = \frac{P}{\Delta T} \qquad [7\text{-}2]$$

where P is the consumed electrical power and ΔT is the resulting temperature rise in the thermistor as a result of self-heating, the unit of D is mW/°C. Equation 7-2 shows that the maximum allowable power can be calculated if the dissipation constant and required temperature accuracy are known. In this work, a thermistor (type: Betatherm 30K6A1B) from BetaTHERM Sensors is used with a dissipation constant of 8mW/ °C in a well stirred oil bath at 25 °C [189]. For an accuracy of 0.01 °C, the maximum allowable power to the thermistor is therefore

$$P = D*\Delta T = 8*10^{-3}* 1*10^{-2} = 80\,\mu W \qquad [7\text{-}3]$$

The thermistor has a nominal value of 30kΩ @ 25 °C, in extreme applications the thermistor has a value of 100kΩ @ 1 °C. Thus the maximum current passing the thermistor is calculated as

$$\mathrm{I} = \sqrt{P/R} = \sqrt{8*10^{-5}/100*10^{3}} = 28.3\,\mu A \qquad [7\text{-}4]$$

Therefore, to minimize the self-heating issue, the injected current has to be less than $28.3\,\mu A$.

Various circuit designs have been used in the temperature sensor, such as the Wheatstone bridge, Wien Bridge oscillator [111], AC ratiometric technique [87], and 4-wire measurement with self-calibration [188]. For resistance measurement, 4-wire method is preferred over 2-wire method for a better accuracy. It is especially true when the resistance value is low. However the thermistor used in this design has a relatively high resistance (30kΩ @ 25°C), thus a 2-wire method can be used which simplifies the circuit design. For a precision design, DC excitation is not preferred since it is hard to remove various noises such as offset and signal drift, the inherent flicker noise and

thermal noise. In this design, AC excitation combined with a lock-in amplifier is used, and the circuit is similar with that of the conductivity sensor in order to share and make system compact.

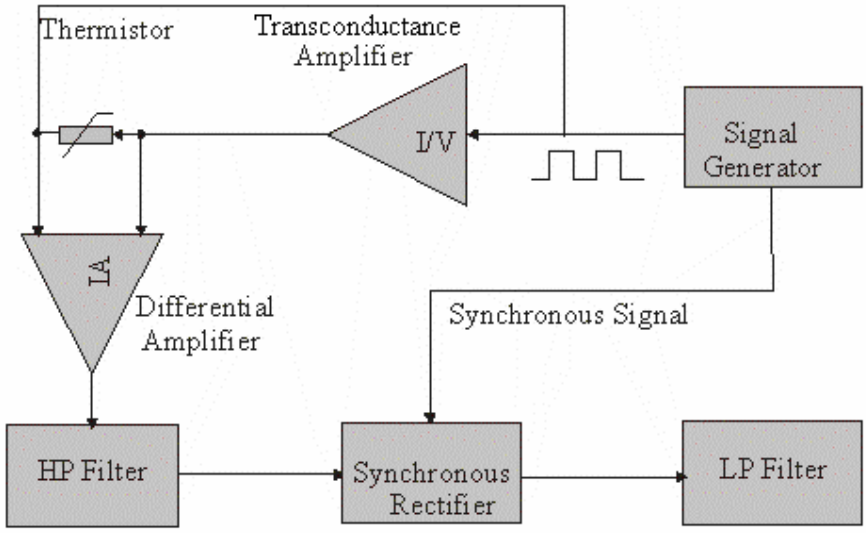

Figure 7-2 Block diagram of temperature sensor

Figure 7-2 shows the block diagram of the temperature sensor circuit design. The circuit consists of a signal generator, a trans-conductance amplifier, an instrumentation amplifier, a high-pass (HP) filter, a synchronous rectifier and a low-pass (LP) filter. A square wave is generated by the signal generator, and then converted to a current by the trans-conductance amplifier. This current flows through the thermistor which is then converted to a voltage signal. An instrumentation amplifier is used to amplify the differential voltage, and followed by a HP filter used to block DC voltage. The synchronous rectifier is used to demodulate and rectify signal and the LP filter is used to remove the ripple current of the rectified signal, and the finally the DC signal is obtained.

7.3 Multi-sensor System Design

To combine the temperature and conductivity sensor in a single system, both sensor and electronic circuit need to be compact and integrated. The main task of the circuit design is to obtain an accurate measurement with small size and low power consumption. One way to reduce both of the size and power consumption is to reduce the total components used in the circuit. This can be realized by reusing or sharing

amplifiers between the multi-sensors in the price of additional multiplexers and control circuits. In this design, the system uses a set of signal conditioning circuit which is shared by conductivity and temperature sensors, calibration resistors by switching multiplexers as it is shown in figure 7-3.

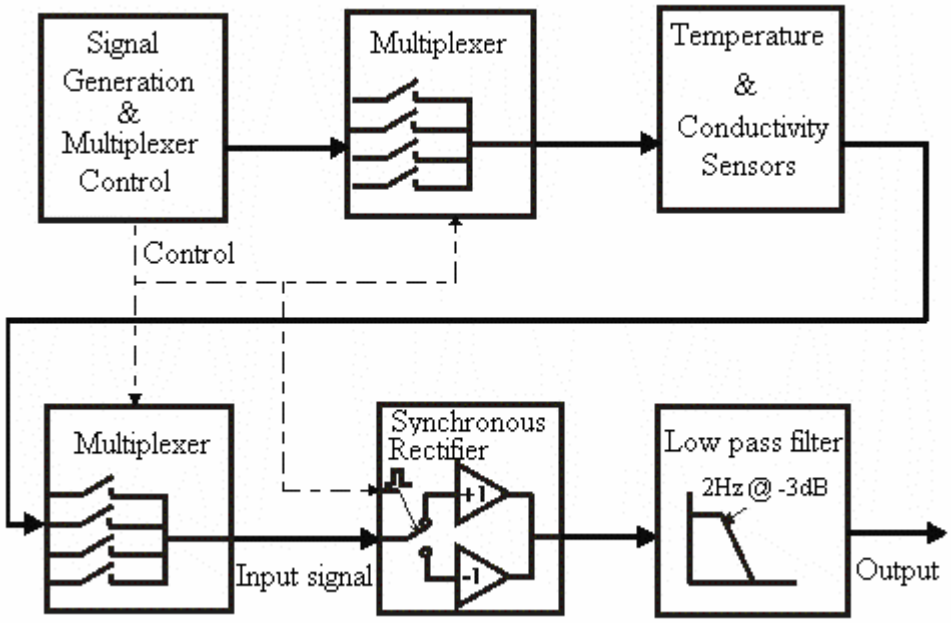

Figure 7-3 Block diagram for multi-sensor system design

7.3.1 Signal generation and multiplexer control

A microprocessor (PIC16C505) is a low cost, high-performance, 8-bit, fully static, EPROM / ROM-based CMOS microcontroller. It employs a RISC architecture with only 33 single word/single cycle instructions. Except for program branches, which take two cycles, all instructions are single cycle consists of four input clock cycles. The design uses a microprocessor to generate excitation signal for sensors as well as to control the multiplexers. Jumpers are used as the input to the microprocessor to select the measurement range and switch sensors. The microprocessor is driven by an external low frequency (32 kHz) crystal to reduce power consumption. The typical current is <2.0 mA @ 5V, and < 1.0 µA typical standby current @ 5V [200]. The microprocessor can be configured to work in either sleep or work mode depending on the jumper setting. The device was programmed in assembly language, the program flow chart is given in Appendix B and the assembly code is given in Appendix C.

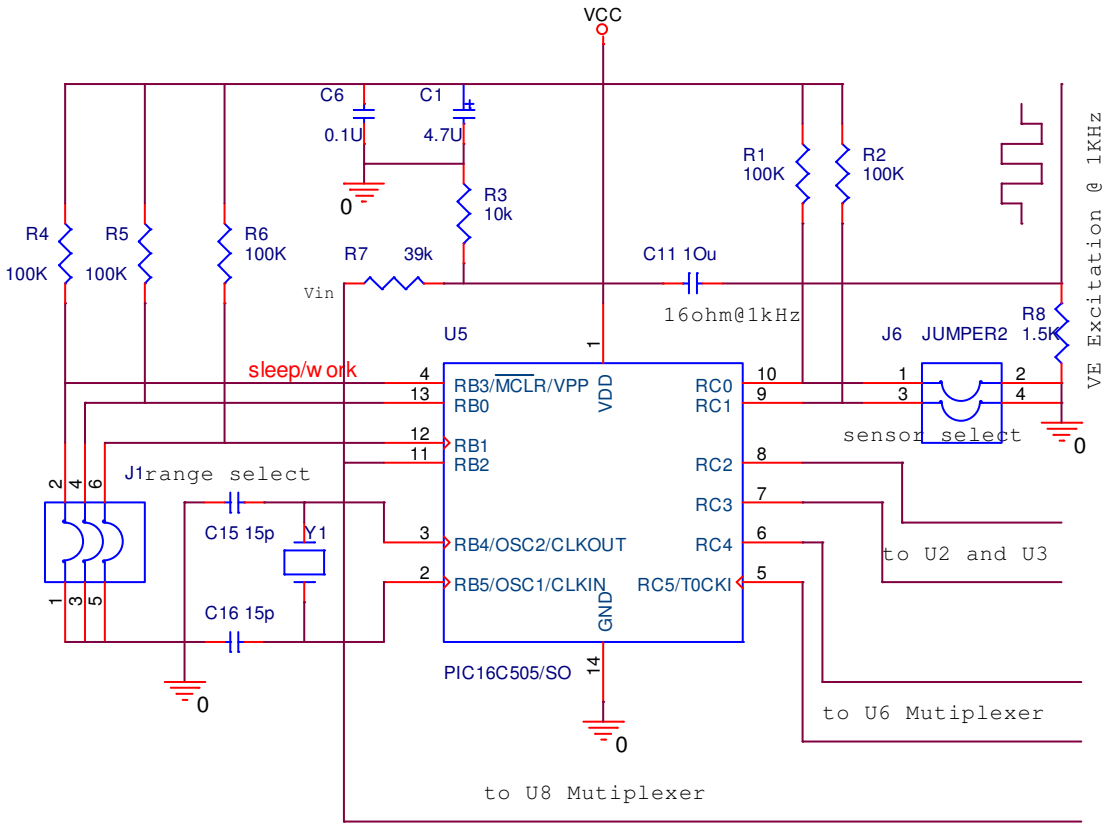

Figure 7-4 Signal generation and multiplexer control

In figure 7-4, the jumper *J1* is used to preset the measurement range (input pins: *RB0*, *RB1*; output pins: *RC4* and *RC5*) and also switch between sleep and work mode (input pin: *RB3*). The jumper *J6* is used to select sensors or calibration resistors (input pin: *RC0*, *RC1*; output pin: *RC2* and *RC3*). The inputs and output logic relationship is shown in table 7-1, where logic '1' represents high voltage and logic '0' represent low voltage.

Table 7-1 Input and output Logic relationship

Jumper	J1	S1	S2	S3	S4	J6	S1	S2	S3	S4
Input	RB1RB0	00	01	10	11	RC1 RC0	00	01	10	11
Output	RC5 RC4	00	01	10	11	RC3 RC2	00	01	10	11

Y1 is a crystal which provides 32 kHz time clock to the microprocessor, this input signal is divide by four to produce internal Q cycles. The programmed 1kHz clock signal is output from pin *RB2*, this clock is use to control a synchronous rectifier and

also further attenuated by resistor and capacitor network (*R7*, *R3* and *R8*) to produce an excitation AC signal (V_E) for sensors:

$$V_E = \frac{R_8 C_{11} s + R_3}{R_7 R_3 C_{11} s + R_7 R_8 C_{11} s + R_8 C_{11} s + R_3 + R_7} \bullet \frac{R_8 C_{11} s}{R_8 C_{11} s + 1} \bullet V_{in} \qquad [7\text{-}5]$$

Where *s* is Laplace variable and is given by $j\omega$. Assume the *Vin* is 5V, and the calculated voltage amplitude is 160mV and RMS value is about 80mV which is close to the test result as it is shown in figure 7-5.

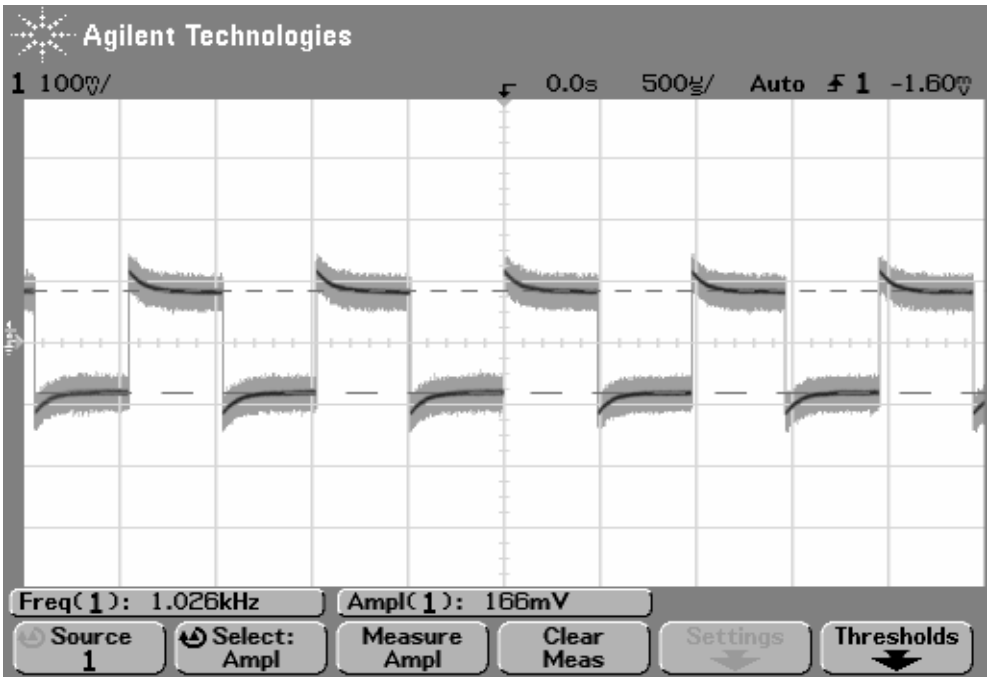

Figure 7-5 Square wave AC excitation Signal

7.3.2 Current injection

The excitation signal generated from the microprocessor need to be converted to a current signal by a trans-conductance amplifier before it can be feed into a conductivity sensor. This is simply realized by passing the excitation voltage signal through fixed value resistors to convert to current signals as it is shown in figure 7-6. *U1B* is a voltage follower to buffer the input voltage signal. *R21* (120 Ω), *R22* (1 kΩ), *R23* (10 kΩ) are the resistors used to convert voltage to current signal, and they are selected by a multiplexer *U6* according to the measurement range. Table 7-2 show the resistors and their measurement range.

Table 7-2 Injected current and measurement range

Resistor (Ω)	Produced current (RMS)	Measurement Range (Ω)
R21 (120)	670µA	125-1000
R22 (1 K)	80 µA	1k-10k
R23 (10 K)	8 µA	10k-100k

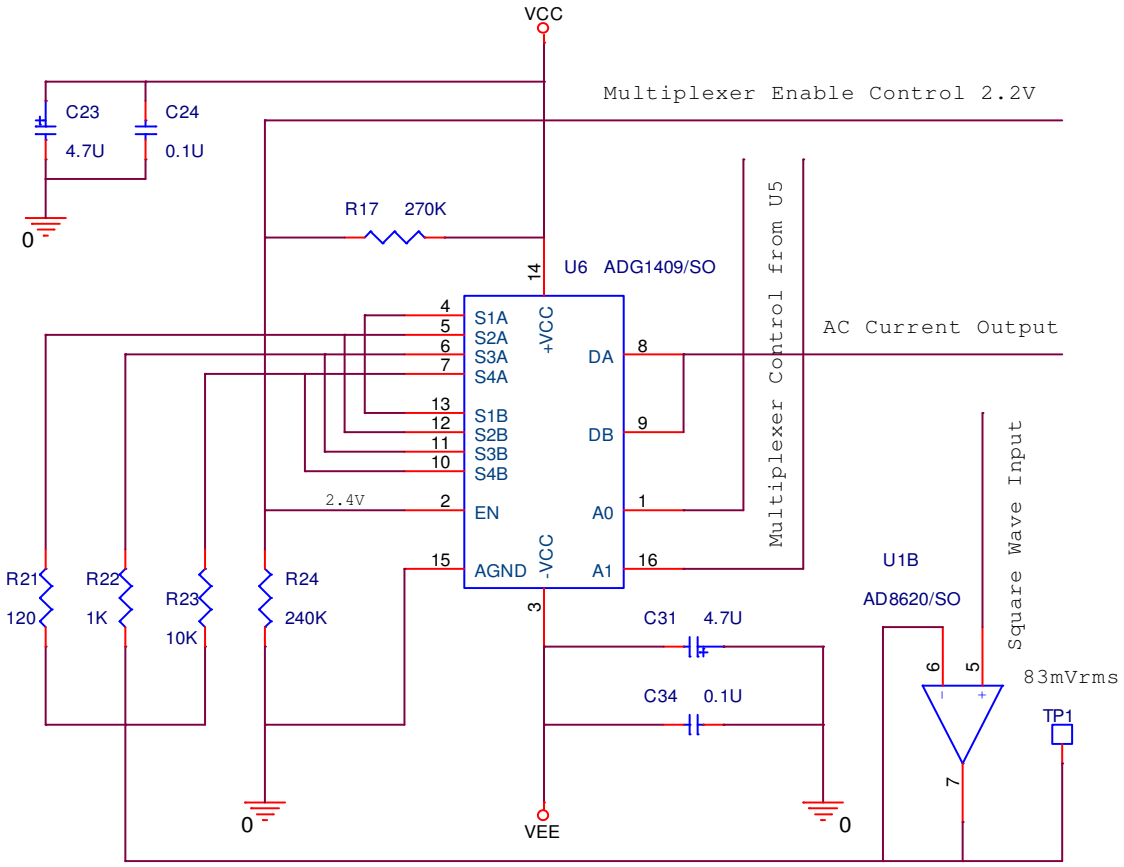

Figure 7-6 Current signal generation

7.3.3 Trans-conductance Amplifier

The output from the multiplexer *U6* is directly connected to the virtual ground of the trans-conductance amplifier, and thus the current signal is forced to flow through the feedback loop of the trans-conductance amplifier *U1A* as it is shown in figure 7-7.

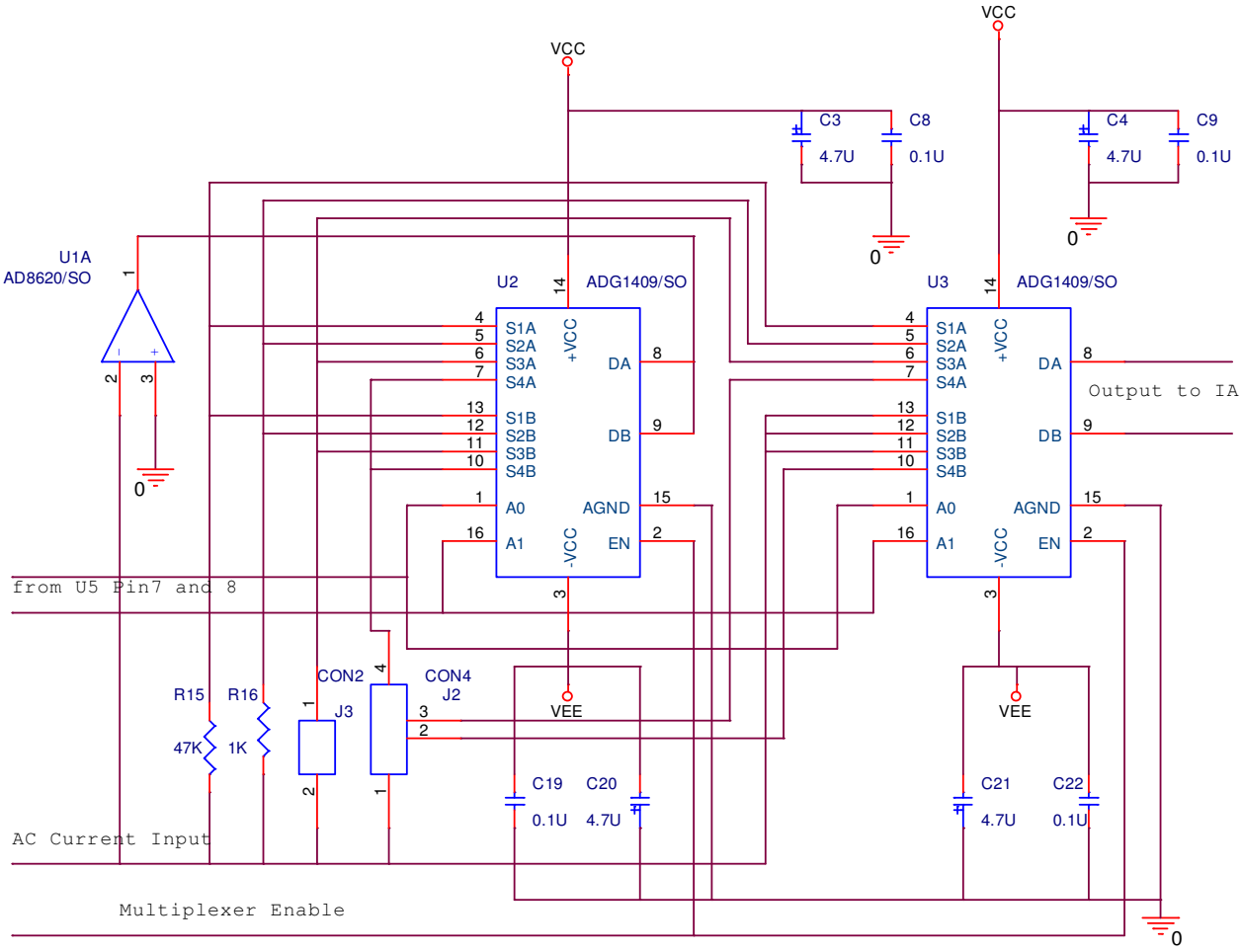

Figure 7-7 Tans-conductance amplifier with multiplexed sensors

In figure 7-7, *U1A* is the trans-conductance amplifier, *CON2* is a two way socket connected to a thermistor, *CON4* is a 4 way socket connected to a four-electrode conductivity cell, and *R15* and *R16* are calibration resistors. All the sensor and calibration resistors are in the feedback loop of the trans-conductance amplifier selected by the multiplexer *U2*; the output voltage of the selected sensor is further selected by another multiplexer *U3*.

7.3.4 Instrumentation Amplifier

The output voltage signal from the trans-conductance amplifier is sent to an instrumentation amplifier *U4* (AD8220) in figure 7-8. AD8220 is a JFET input instrumentation amplifier with a very high common-mode rejection ratio (minimum CMRR of 86 dB at dc and 80 dB at 5 kHz for G = 1). The input impedance (40 GΩ) is

extremely high with input bias current of 10 pA which typically remains below 300 pA over the entire industrial temperature range. The gain (G) of the instrumentation amplifier is about 5 and is given by equation 7-6:

$$G = 1 + \frac{49.4K\Omega}{R9} \qquad [7\text{-}6]$$

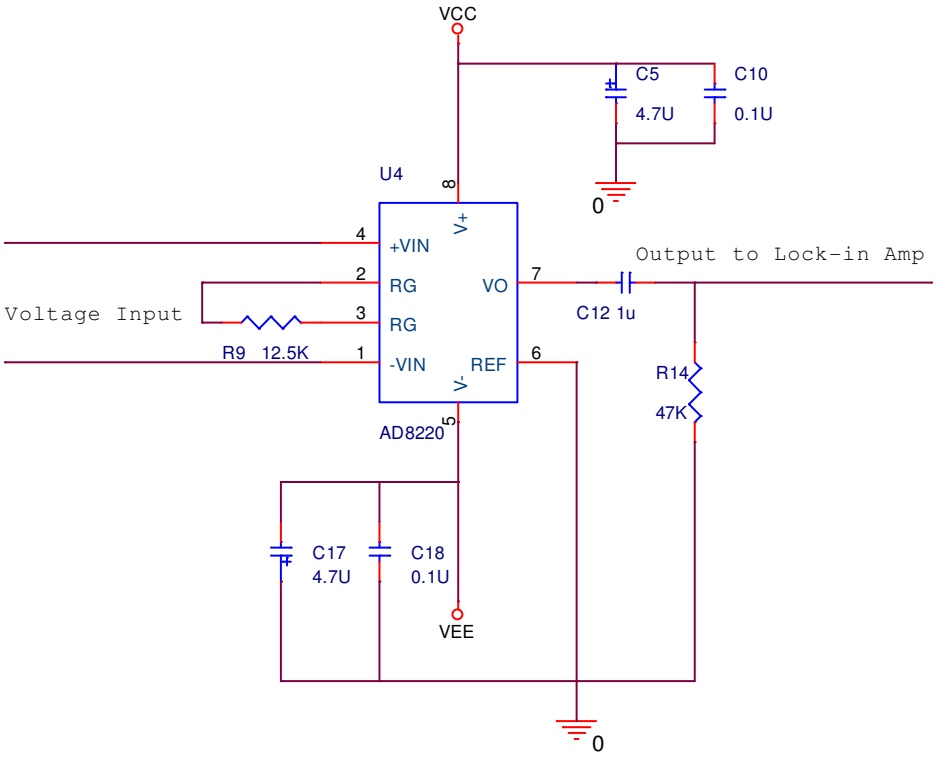

Figure 7-8 Instrumentation amplifier

The output of the instrumentation amplifier *U4* passes a high pass filter to remove any DC voltage offset, and the amplified square wave signal is shown in figure 7-9. The cutoff frequency (f_{-3dB}) of the filter is determined by the time constant (τ) of *R14* and *C12*.

$$f_{-3dB} = \frac{1}{2\pi\tau} = \frac{1}{2\pi \bullet R_{14}C_{12}} \approx 3.4 \text{ Hz} \qquad [7\text{-}7]$$

Where f is in hertz, τ is in seconds, R is in ohms, and C is in farads.

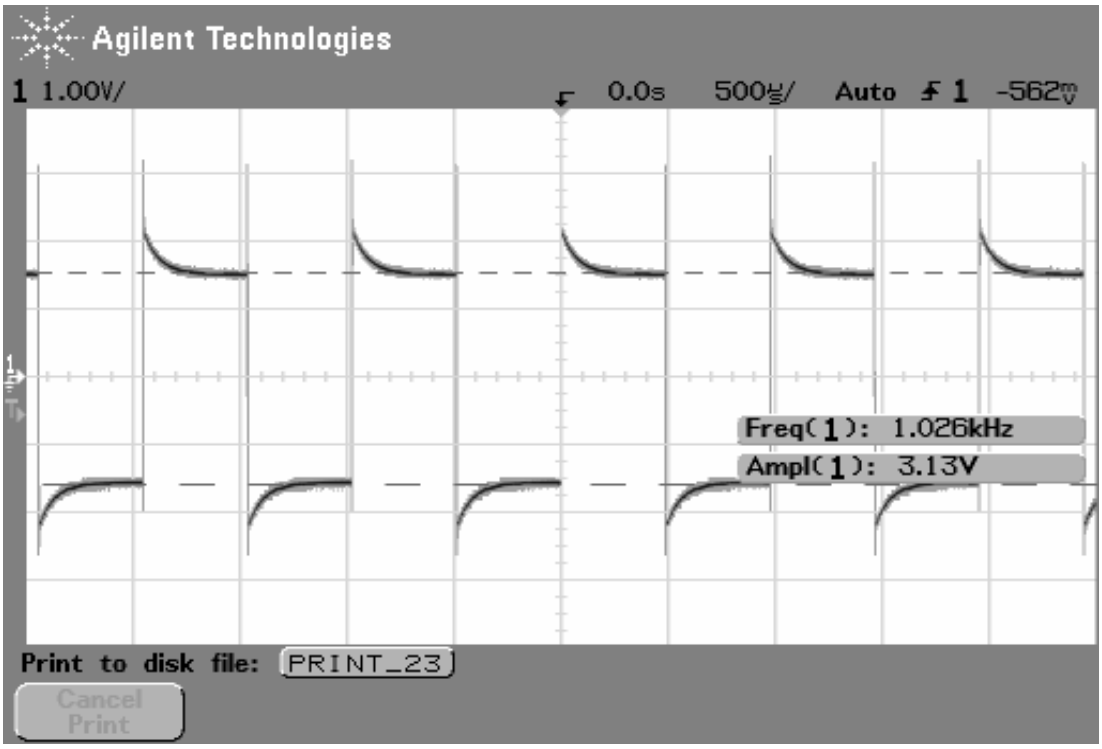

Figure 7-9 The output wave form of high pass filter

7.3.5 Synchronous Rectifier

A synchronous rectifier together with a low pass (LP) filter to form a lock-in amplifier which is used in the circuit to increase Signal to Noise Ratio (SNR) and improve the performance. The principle of a lock-in amplifier is described in chapter 2 and will not be repeated here.

In figure 7-10, *U7A* (AD8620) and *U8* (MAX4700) form a synchronous rectifier. AD8620 a very high precision JFET input amplifiers featuring ultralow offset voltage (100 µV Max) and drift , very low input voltage noise (6 nV/√Hz), very low input bias (10 pA Max) [201]. MAX4700 is a dual analogue switch which features a maximum on-resistance of 1.25 Ω [202]. The MAX4700 has one *NC* and one *NO* switch and features guaranteed break-before-make switching. When pins *COM1* and *COM2* of *U8* are connected together, this device works as a two-input multiplexer with one input signal directly coming from the high pass filter and another input coming from an invert amplifier (*U7A*). Since *U8* is controlled by a synchronous signal, the output gain is +1 when the synchronous control is high, and -1 when the synchronous control is low. The output waveform of the synchronous rectified signal is shown in figure 7-11. Although there are some spikes in the synchronous rectifier's output due to switching *U8*, these spikes can be easily removed by a low pass filter.

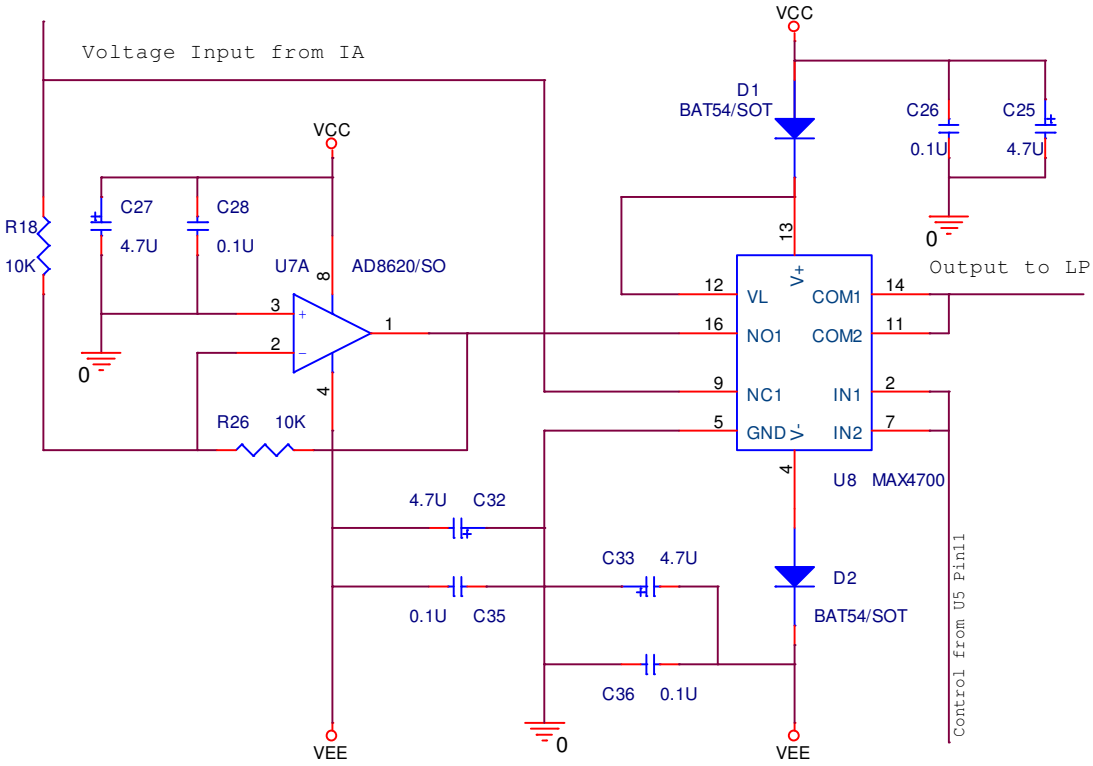

Figure 7-10 Synchronous rectifier

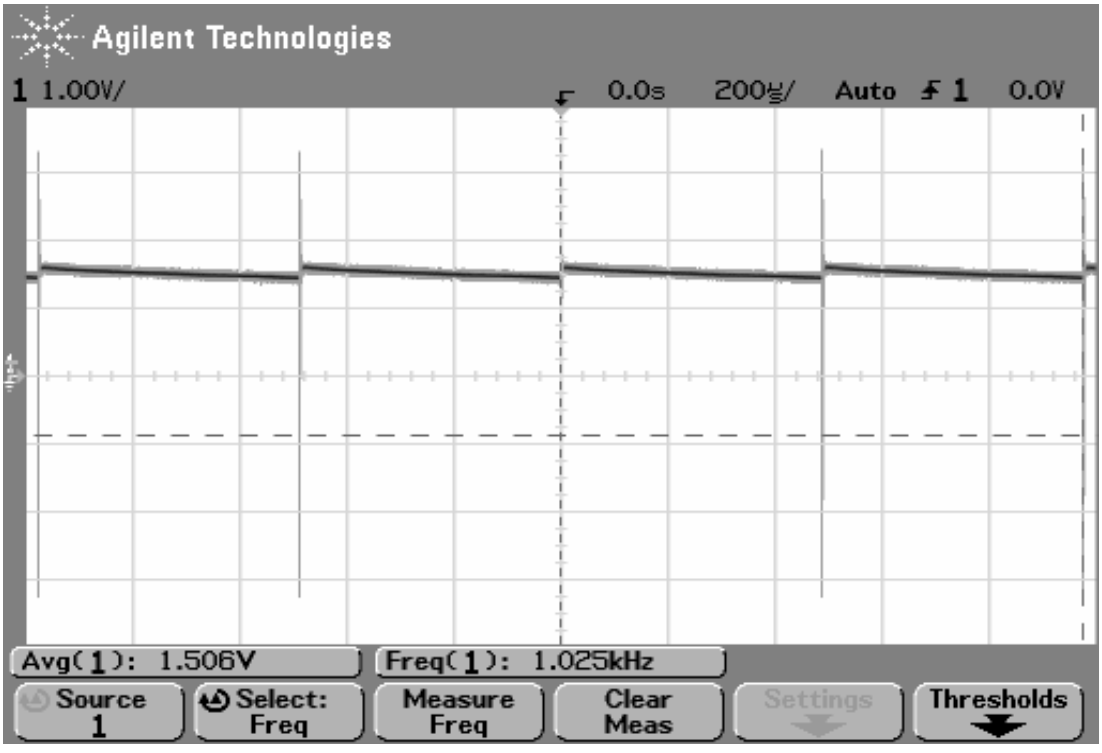

Figure 7-11 Output wave form of the synchronous rectifier

7.3.6 *Low Pass Filter and output buffer*

In order to obtain a DC output, a low-pass filter is needed to remove the spikes and ripple components of the output from the synchronous rectifier. In this design, a two pole active filter was chosen, using the Sallen-Key filter structure configured as a Butterworth low-pass filter as it is shown in figure 7-12.

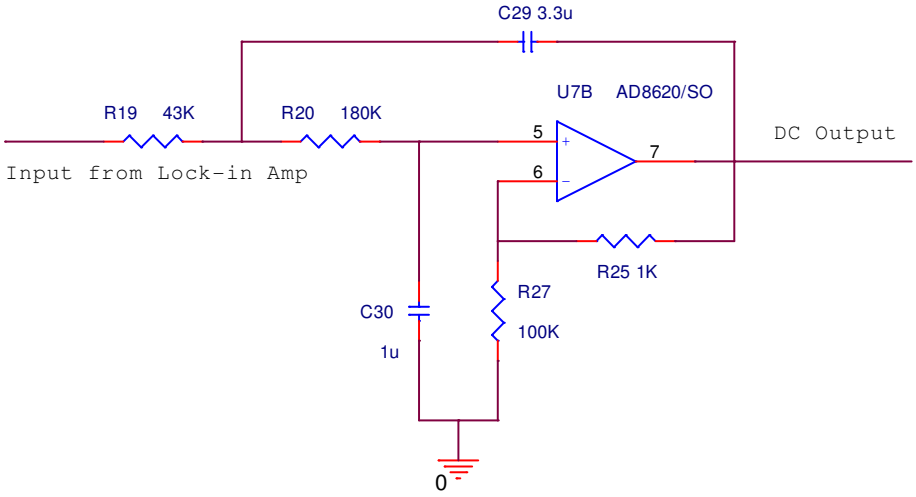

Figure 7-12 Low-pass (LP) filter

In figure 7-12, *U7B* is the op amp used for the active low-pass filter; and the gain of the filter is about 1; the cut off frequency of the low pass-filter is set to about 1Hz. The PSPICE simulation of the low pass filter is shown in figure 7-13.

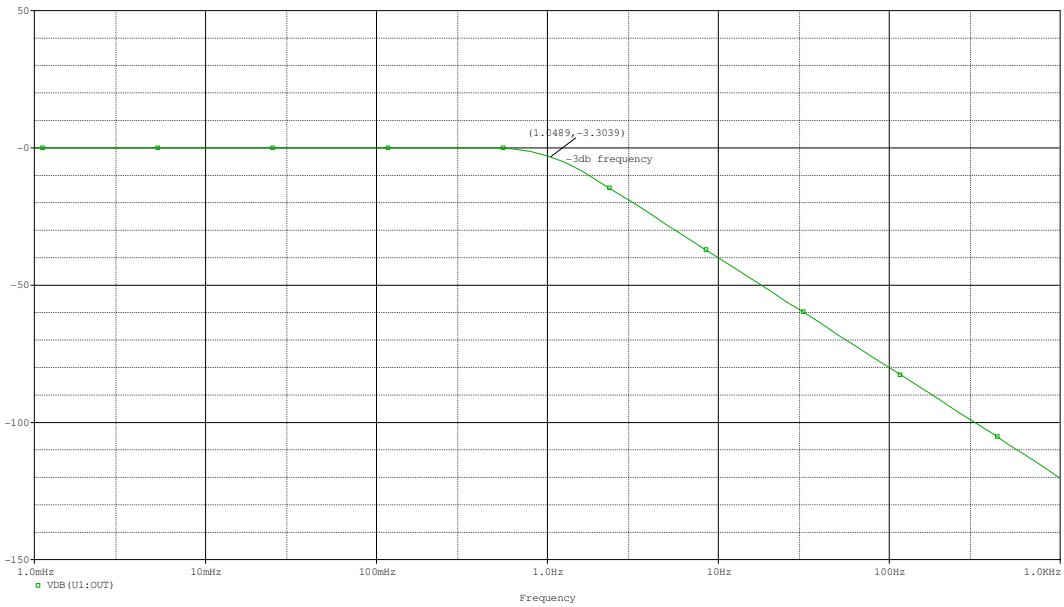

Figure 7-13 LP filter PSPICE simulation

The output low pass filter is an essential part of the lock-in amplifier used to remove the high frequency AC from the DC output of lock-in amplifier. Often a low pass filter with narrow bandwidth is preferred to improve the output signal-to-noise ratio (SNR). The improvement factor is given by the ratio between the input bandwidth (B_I) and output bandwidth (B_O):

$$SNR_O = \frac{B_I}{B_O} \bullet SNR_I \qquad [7\text{-}8]$$

where SNR_O and SNR_I are the output and input signal-to-noise ratio respectively. For a lock-in system with input bandwidth of 1 kHz and a low pass filter with 1 Hz cut off frequency, the output signal-to-noise ratio is improved by 1000 times.

7.4 PCB board fabrication

The schematic diagram and component list are attached in Appendix F and D respectively, and the prototype PCB is shown in figure 7-14.

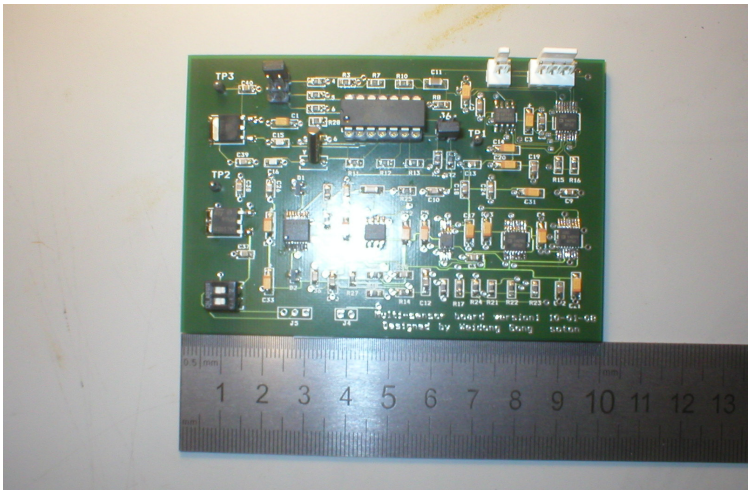

Figure 7-14 PCB board for the multi-sensor system (temperature, conductivity, potentially could extend to pressure) with a total dimension of 100x65mm and power consumption of 175mW

Since the conductivity sensor and temperature sensor need to be operated simultaneously, they were integrated and built on a single board. The PCB board use four layers and SMT components to make it compact. Among the four layers, one is

used for ground plane. The digital and analogue components were partitioned and separated into upper and lower location in order to avoid mutual coupling. To reduce the coupling effects from power supply, each IC was fitted with decoupling capacitors placed as close as possible to the power supply pins. Linear voltage regulators were used to supply the positive +5V and negative -5V. The whole board consumes approximately 0.175 Watt which is half of the power consumption of the CTD recently developed in Woods Hole Oceanography Center, USA [180]. Compared to commercial CTDs such as SBE 9plus CTD (18W), SBE 25 SEALOGGER CTD (5W), SBE 49 CTD (3.2W); SBE 52-MP (3W) [211] and FSI Micro CTD3 (600mW) [212], the designed multi-sensor system consumes much less power and the total dimension of the PCB is 100x65mm.

7.5 Conclusions

A multi-sensor signal conditioning circuit is successfully presented. The circuit design is small (100x65mm) with good performance (SNR improved by 1000) and low power consumption (175mW) and self-calibration function which is suitable to be used in a multi-sensor system for environmental monitoring.

Potentially, the multi-channel design could be extended to include a pressure sensor to make a complete CTD system.

Chapter 8 Test and Results

This chapter presents the test result of temperature and conductivity sensors, the experiment set up and calibration procedure are described, key issues are also discussed.

8.1 Conductivity Measurement and Calibration

Since the output of the sensor is a voltage signal, the conductance-voltage relationship has to be determined first of all, using testing resistors. The conductivity is calculated by using the measured solution conductance times the cell constant of the conductivity sensor, where the cell constant of the conductivity cell is obtained by calibration.

8.1.1 Resistance-voltage relationship

The conductivity sensor circuit measures the resistance of the conductivity cell, and output voltage. Thus calibration is needed to find the exact relationship between the input resistance and output voltage before any conductivity measurement. Calibration was carried with standard resistor ranging from 160Ω to 100k. The resistance values of the standard resistors and the output voltage from the conditioning circuit were measured using a precision multi-meter (Agilent 34410A, 6½ Digit High Performance Digital Multimeter). To measure conductivity, the Jumper *J6* is set to *S4* (refer to table 7-1). Since the measurement range is too wide, the circuit uses a jumper with three-positions (only use *S2*, *S3*, *S4*) to adapt the gain to different resistance ranges. The test result shows a linear relationship between the resistance and the output voltage, see figure 8-1.

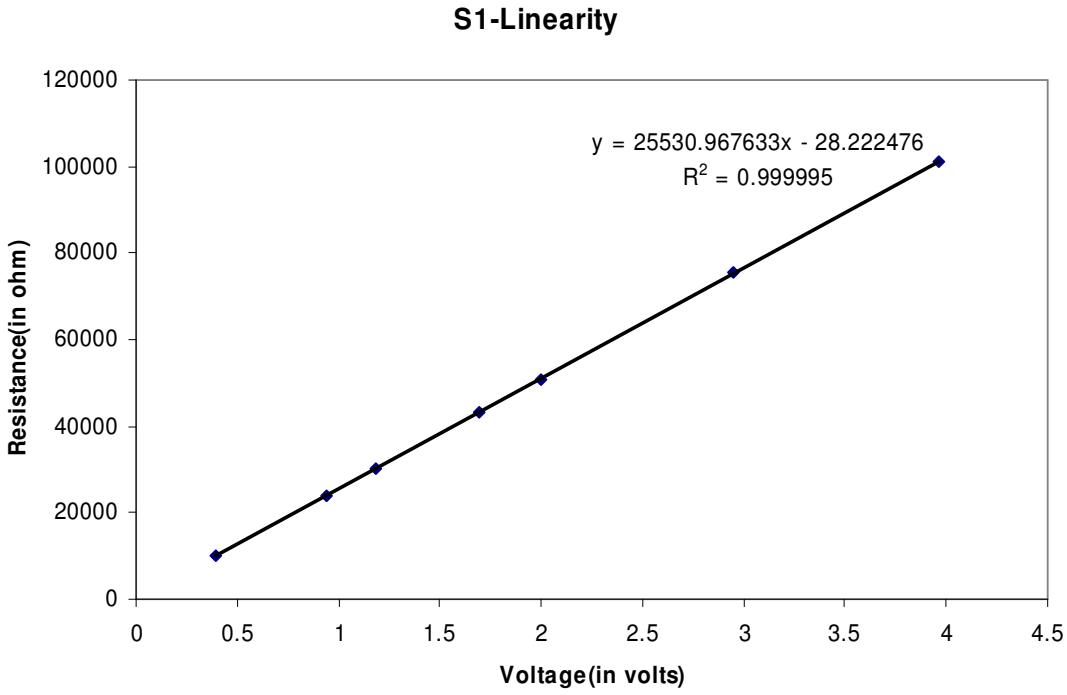

a. Jumper J1 set to S4 with 8 µA excitation

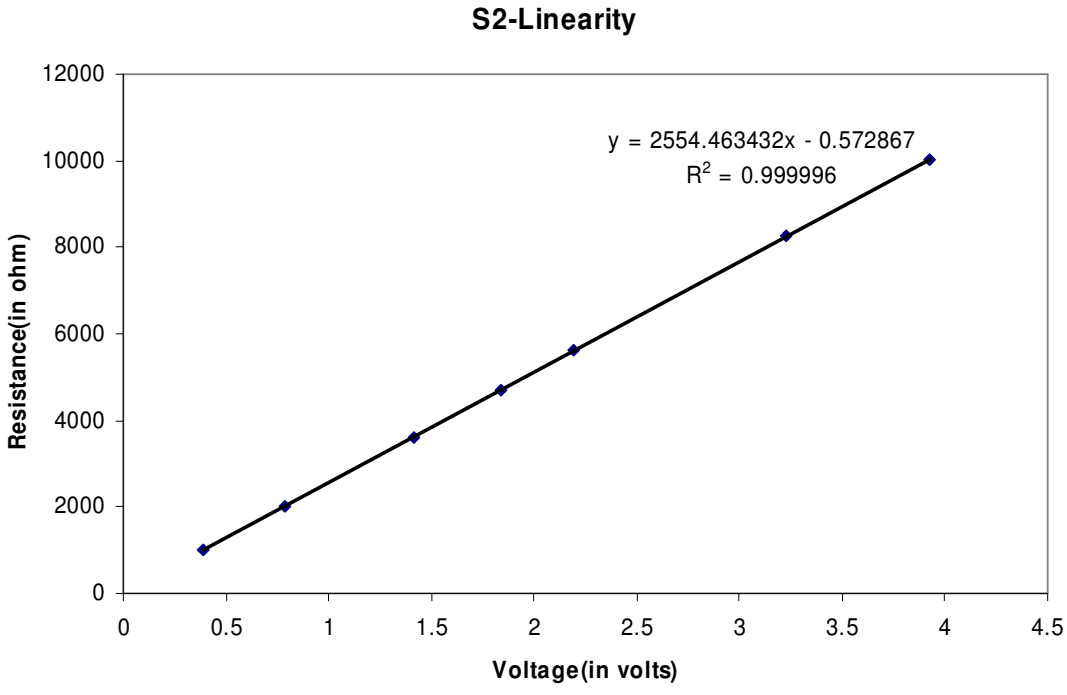

b. Jumper J1 set to S3 with 80 µA excitation

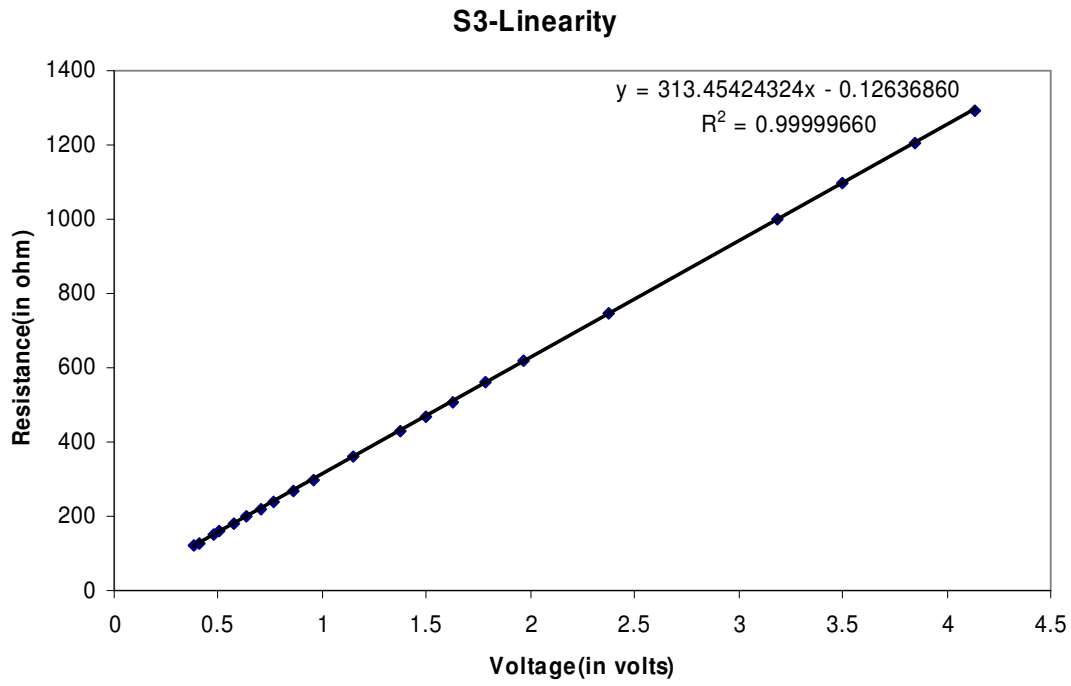

c. Jumper J1 set to S2 with 670 µA excitation

Figure 8-1 Voltage and resistance relationship of conductivity measurement circuit

Figure 8-2a shows the standard deviation of the voltage measurement (repeated 5 times) since it is too small to see in figure 8-1. It is clear that the biggest voltage standard deviation is 164.317µV (occurs at the average voltage point of 3.184V when measured 999.59Ω resistance), which is mainly caused by the circuit noise as well as the reading instrument (DC voltage accuracy is 5V±115µV for Agilent 34410A multi-meter). This voltage standard deviation is converted to a resistance resolution of 0.07Ω (0.007% of 999.59Ω) which is equivalent to the conductivity resolution of 0.0007mS/cm (or 0.7µS/cm) for a cell constant of 10 cm^{-1}.

Figure 8-2b shows the deviation from the linear fit given in figure 8-1. The residual (deviation from linear fit) is within ±0.1%, and the biggest deviation is about 3.8mV (occurs at the average voltage point of 4.1324V when measured 1294 Ω resistor) and will cause an error of 1.192 Ω (0.092% of 1294 Ω) in the calibration if the linear fit is used, which is converted to a conductivity error of 0.0071mS/cm (or 7.1µS/cm) for a cell constant of 10cm^{-1}. The biggest conductivity error caused by linear fit occurs at the average voltage point of 0.4796V when measuring 150.03 Ω resistance; the deviation is 457µV (0.095% of 0.4796V) converted to a conductivity error of 0.0636mS/cm, which is still within the target accuracy of 0.1mS/cm. The deviation from linear fit could be caused by the accumulated nonlinearity of electronic components, stray capacitance,

thermal drift, and measurement errors such as the introduced extra-contacting resistance when measure standard calibration resistors.

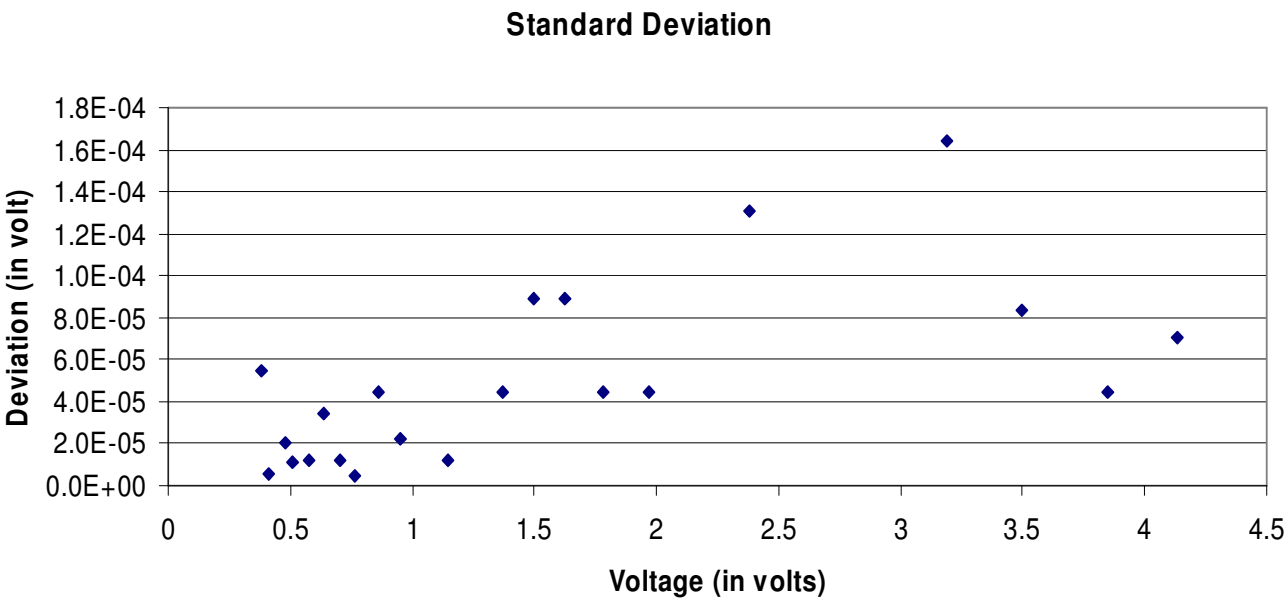

a. Standard deviation of measured voltages

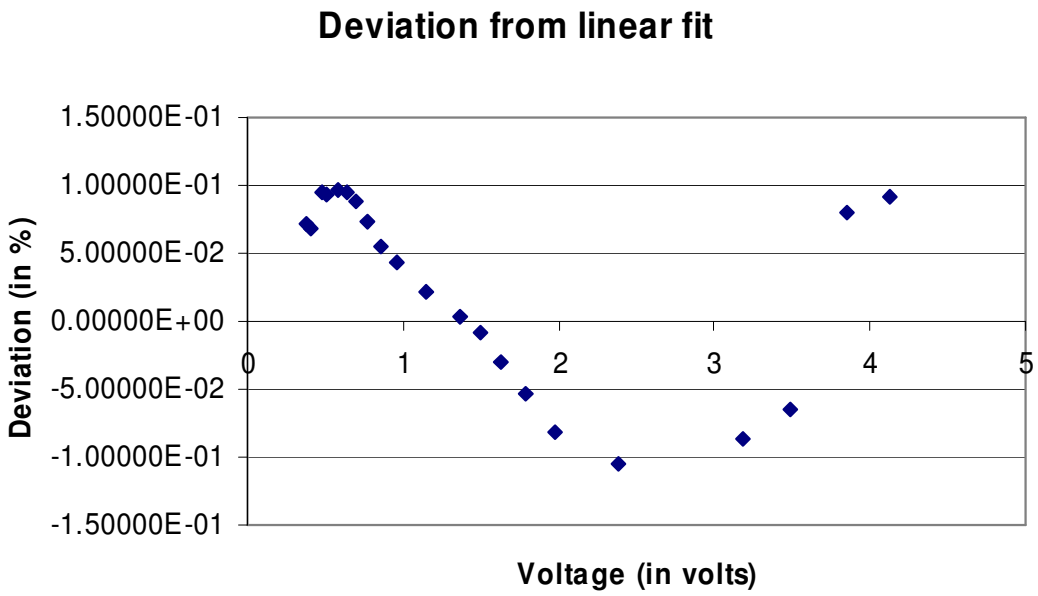

b. Deviation from linear fit in percentage

Figure 8-2 Measurement and calibration deviation of the conductivity sensor circuit (a, b) (Jumper J1 set to S2 with 670 µA excitation)

8.1.2 Four-electrode Conductivity Cell Calibration

A four electrode cell built together with a thermistor is shown in figure 8-3. The four-electrode conductivity cell was built on a PCB. The four planar electrodes were made from platinum foil which was cut into 2mm wide strips and glued on the substrate of the PCB. The electrodes are connected to the copper tracks through via holes and then connected to leads by soldering joints. The side wall and covering lid were made from plastic boards and the channel was formed by bonding them together.

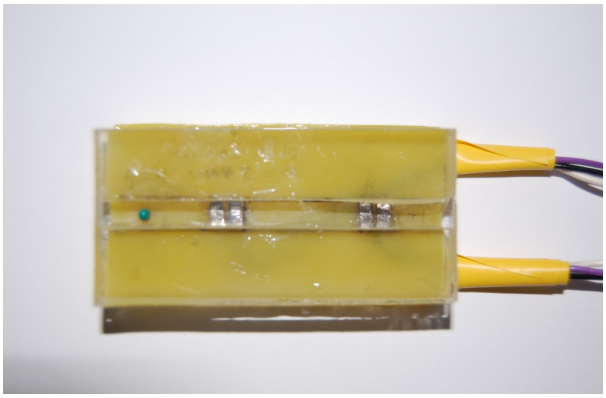

Figure 8-3 Four-electrode conductivity cell, four platinum electrodes together with a thermistor built in an insulated channel with a total dimension of 30x60mm

The cell in figure 8-3 has a total dimension: 30x60mm, Channel size: 5x5mm, Inner electrodes distance: 18mm, Gap between inner and outer electrodes: 1mm. By using conformal mapping method, the calculated cell constant of the conductivity cell is about 9.39/cm.

In order to calibrate the cell constant, an impedance analyser (Alpha-A from Novocontrol Technologies) was used to measure the cell impedance. Three conductivity calibration liquids were used in the experiment, and they were sourced from Hanna Instruments (UK). The cell constant can be calculated by equation 8-1.

$$\kappa = R^{*}\sigma \qquad [8\text{-}1]$$

The test results are shown in Appendix E. The test cell constant ($\boldsymbol{\kappa_T}$) has been compared with the calculated cell constant ($\boldsymbol{\kappa_C}$) and the results are shown in table 8-1.

Table 8-1 Test and calculated cell constant

Channel Dimension (mm)		**Electrodes Dimension (mm)**			**Calculated Cell Constant κ_C (/cm)**	**Test Cell Constant κ_T (/cm)**
Width (W)	**Height (H)**	**Width (W)**	**Gap (G)**	**Length (L_T)**	9.39	9.11
5	5	2	18	5		

Table 8-1 shows the test and calculated cell constants are close, and there are number of possible reason for the difference between them. The first could be the electrode dimension are not exactly those given in table 8-1 since the platinum electrodes were obtained by cutting platinum foil and glued to the PCB board manually, the edge of electrodes and alignment were not necessarily straight lines. The second could be the channel dimension is not exactly the same as the design specification since it was also formed by bonding plastic boards which again were cut by hand. The third reason may be due to the stray capacitance existing between the tracks and connection wires.

8.1.3 Four-electrode Conductivity Sensor Measurement

The conductivity sensor was calibrated in the calibration room of National Oceanography Centre (NOC), Southampton. The electronic circuit board was installed inside a metal box to shield from radio frequency interference, and the four-electrode conductivity cell was connected to the box using a multi-core shielding cable.

The conductivity samples were direct taken from the sea (Solent Sea). In order to make different conductivity, the seawater was diluted by tap water to make low conductivity samples, or added some salt (NaCl) to make high conductivity samples. Five samples with different conductivity were made and they were prepared in five containers. A small pump was dropped in the container to aid water circulation and help conductivity distribute in the container uniformly. A standard laboratory salinity meter (Guideline Portalsal 8410A with an accuracy of ±0.003 Equivalent PSU and a resolution of 0.0003mS/cm @ 15^{o}C) was used as the reference meter, and a precision

multi-meter (Agilent 34410A) was used to record the output voltage of the conductivity sensor.

Although the temperature of the calibration room (air conditioned) was relatively stable, a precision thermometer F25 (with an accuracy of ±0.002°C) was used to measure the actual temperature of samples. Since the temperature in the temperature bath of the salinity meter (Guideline Portalsal 8410A) was slightly different from the sample temperature, software (LAB ASSISTANT V2 from PDMS Ltd.) was used to compensate the difference caused by the temperature. Figure 8-4 shows the experiment setup.

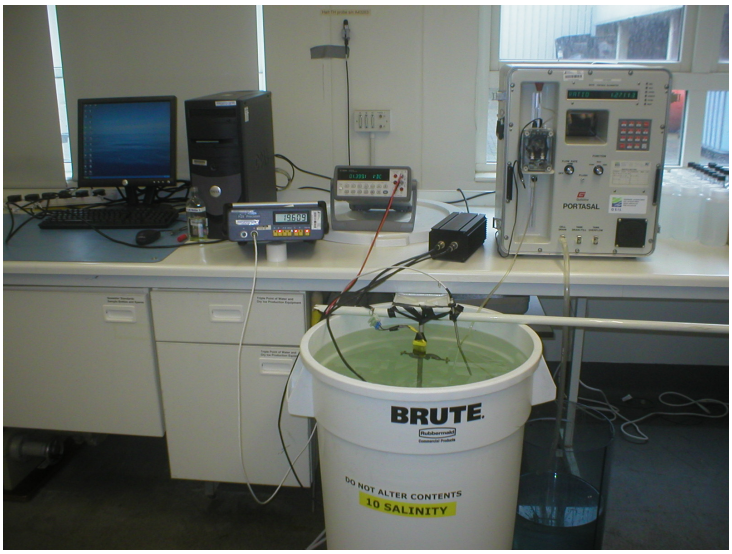

Figure 8-4 Conductivity sensor experiment setup

As shown in figure 8-4, the four-electrode conductivity cell was tied on a stick and dipped into the samples and a precision temperature probe (F25) was also mounted close to the conductivity cell. In order to prevent the current flow outside of the conductivity cell, top end of the cell was sealed with insulation tape and the cell was not totally submerged in the sample but dipped to a marked level (upper end 2 mm above water level). The sample in the container was first measured by the reference salinity meter (Guideline Portalsal 8410A) by sucking up a small mount of sample from the container into its conductivity cell with a built-in temperature bath, and then measured by the conductivity sensor directly dipped into the sample container.

In order to measure the sample accurately, the reference salinity meter and conductivity sensor were flushed by the sample three times before any measurement was made. The output voltage of the conductivity sensor was read five times and the average voltage value was used to calculate the sample resistance. At the same time, the temperature probe was used to measure the actual temperature in the sample container in order to compensate the temperature difference.

Five samples with different conductivities in the range from about 15 to 55 mS/cm were used in the experiment to obtain the calibration curve. In order to see repeatability of the measurement, three runs were carried out within the same day. The five samples were measured in the first and second run in an order from the low conductivity to the high conductivity, but vice versa in the third run. The test results are shown in figure 8-5 and 8-6.

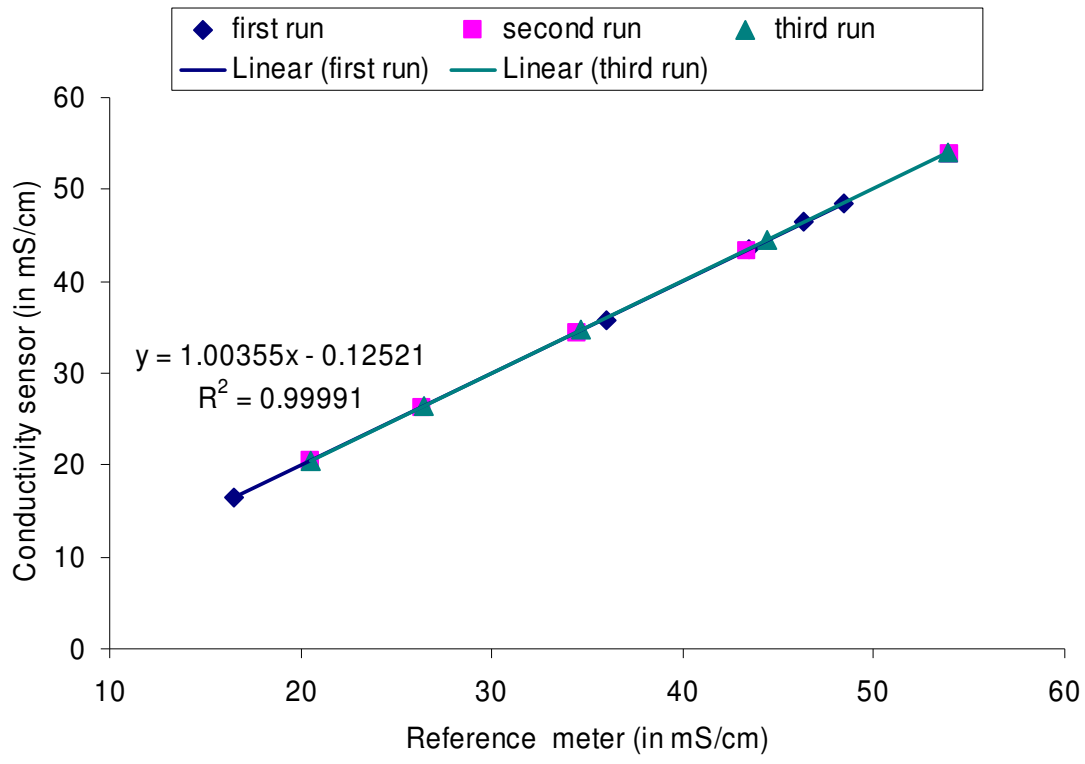

Figure 8-5 Conductivity measurement comparison

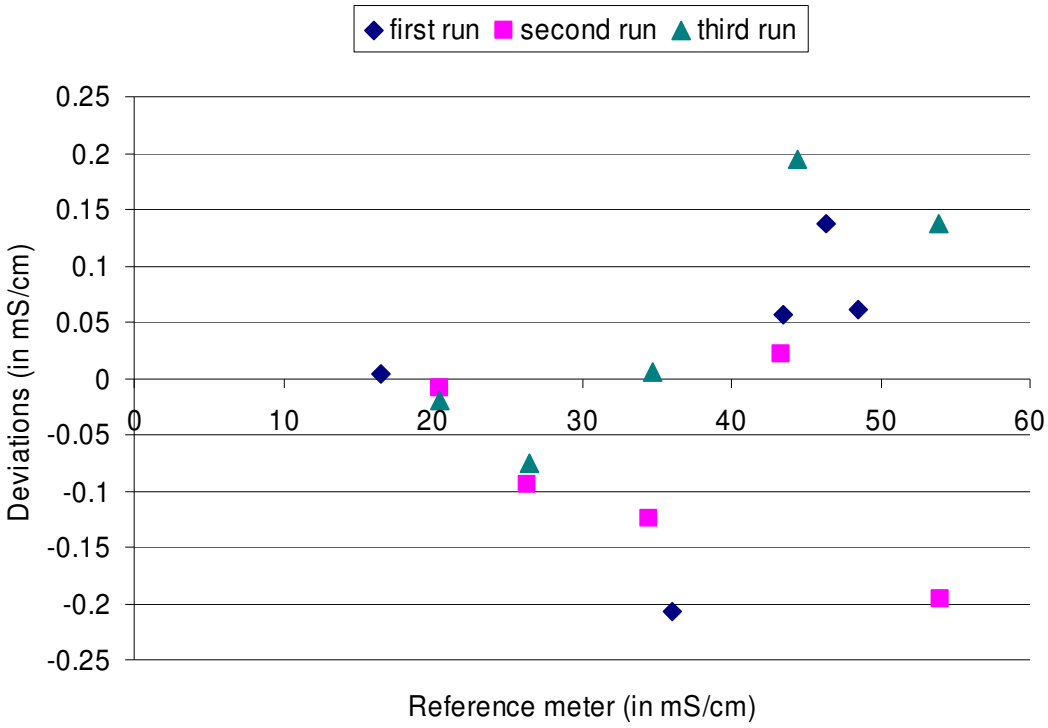

a. Deviation in absolute value

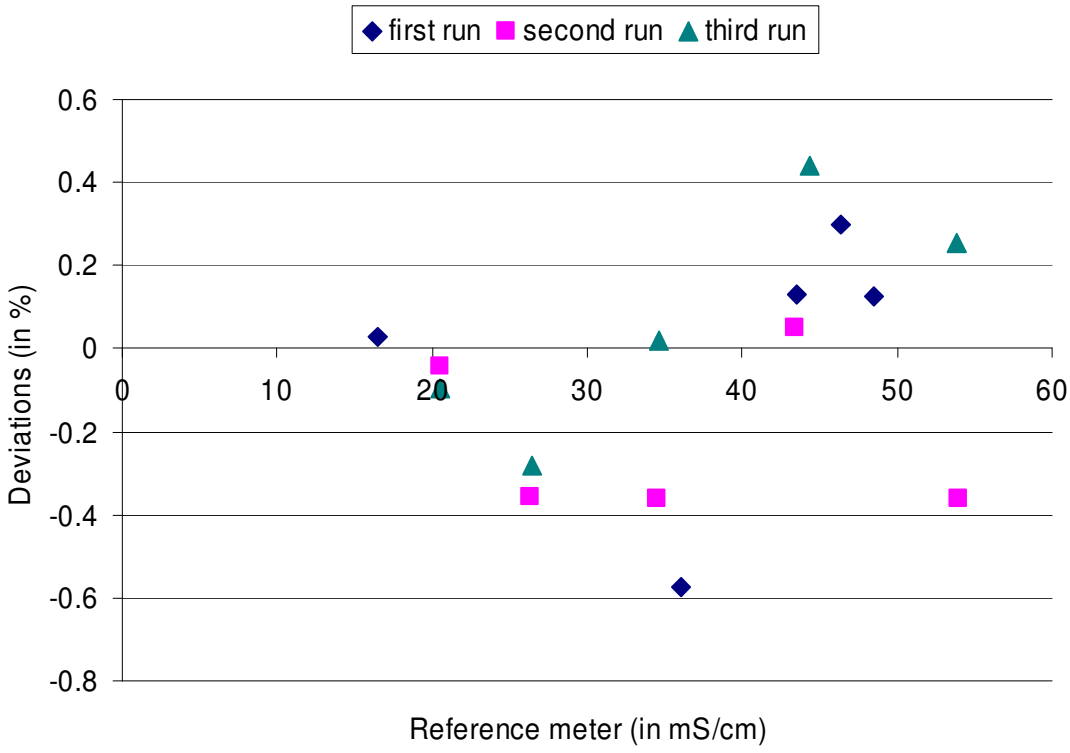

b. Deviation in percentage %

Figure 8-6 Deviation from reference salinity meter (a, b)

Figure 8-5 shows the measurement results of the conductivity sensor compared with the reference salinity meter. In order to analyse the difference between the reference meter and the conductivity sensors, figure 8-6 gives the deviation from the reference salinity meter. From figure 8-6, we can see that the deviation is within ±0.2mS/cm in the range of 15-55mS/cm, and the biggest deviation is about 0.6%.The conductivity resolution is about 0.0053mS/cm, defined by the biggest standard deviation of the measurement at 34 mS/cm (the standard deviation of measured voltage is 54.8μV/√Hz with an average voltage of 0.82479V/√Hz).

8.1.4 Discussion

Figure 8-5 shows there is a good agreement between the conductivity sensor and reference salinity meter, the achieved accuracy (within ±0.2mS/cm and ±0.6% in the range of 15-55mS/cm) is better than the MEMS-based CTD (±1.5% in the range of 0-60mS/cm) reported [205], and also close to the target of ±0.1mS/cm. This proved the designed four-electrode conductivity cells and the circuit work well. However there are small deviations when compared the conductivity sensor with the reference salinity meter. The deviations are caused by the errors and noise sources in the experiment, the sensor and the circuit. The linear fit of circuit could cause a deviation of up to 0.0636mS/cm, and the circuit noise also added a measurement error of 0.7μS/cm (see the discussion in section 8.1.1). Although the thermal noise of conductivity sensor is low (about 4nV for a cell constant of $10cm^{-1}$ and sample conductivity of 10mS/cm), the electrode surface changing with residues of salt, specific ion absorption and chemical corruption could also cause error and uncertainty in the measurement. Other factors in experiment also contributed to measurement error, such as the organic debris, particles and air bubbles in the solution, the temperature variation and the solution evaporation [191].

Temperature is one of the factors which could contribute to the deviation in the experiment. The influence of temperature varies with the concentration. For a solution with high concentration, the variation of conductivity is 2% per degree centigrade. For pure water, the variation can be as high as 4% per degree centigrade. Unlike the salinity meter (Guideline Portalsal 8410A) with a stable temperature bath, the solution in the container was not temperature controlled and the temperature of the solution gradually increased as the reference thermometer indicated. Although the reference temperature

probe was mounted close to the conductivity sensor, there was still small difference in temperature due to the different location and logging time (0.1 degree temperature change will cause 0.2% measurement error of conductivity. The solution evaporation could cause the measurement error, since the same sample was not tested by the reference meter and conductivity sensor at same time (6g water evaporated out of 1kg sample approximately causes 0.6% change of conductivity. The stray capacitance of the electrodes and leads could cause deviation (100 pf stray capacitor will lead to an error of 6.25μS/cm).

The cell leakage current could cause the deviation. When a conductivity sensor is installed in a pumping system, this issue could be minimized or avoided since the inlet and outlet can be separated by a pump or a valve. However, in this experiment, the four-electrode conductivity cell was directly placed in the sample. In order to prevent the current flow outside of the channel, top end of the cell was sealed, but there was still a small leakage current depending on the wet condition of the cell surface. Self heating of the conductivity sensor due to the excitation current may be another reason to generate the temperature variation and thus cause measurement error.

8.2 Temperature Measurement and calibration

There are two procedures to measure temperature using a thermistor. The first procedure is to calibrate the circuit, and the second procedure is to calibrate the thermistor. Finally the sensor output voltage can be mapped to the resistance and then temperature.

8.2.1 Resistance-voltage relationship

The analogue front-end circuit output voltage corresponds to the input resistance of the thermistor. To measure temperature, the Jumper *J6* of PCB is set to *S3* (refer to table 7-1), and *J1* is set to *S4* to select 8μA excitation current. Before using the circuit to measure the thermistor resistance, we need to calibrate the circuit and find out the exact relationship between the input resistance and output voltage. This calibration was achieved by measuring standard resistors. Nine resistors with different value range from 18 kΩ to 100 kΩ were used in the calibration and their resistance values were measured by a precision multi-meter (Agilent 34410A, an accuracy of 100k ±2.5Ω).

Figure 8-7 shows the voltage-resistance value, and the linearity of the circuit is good.

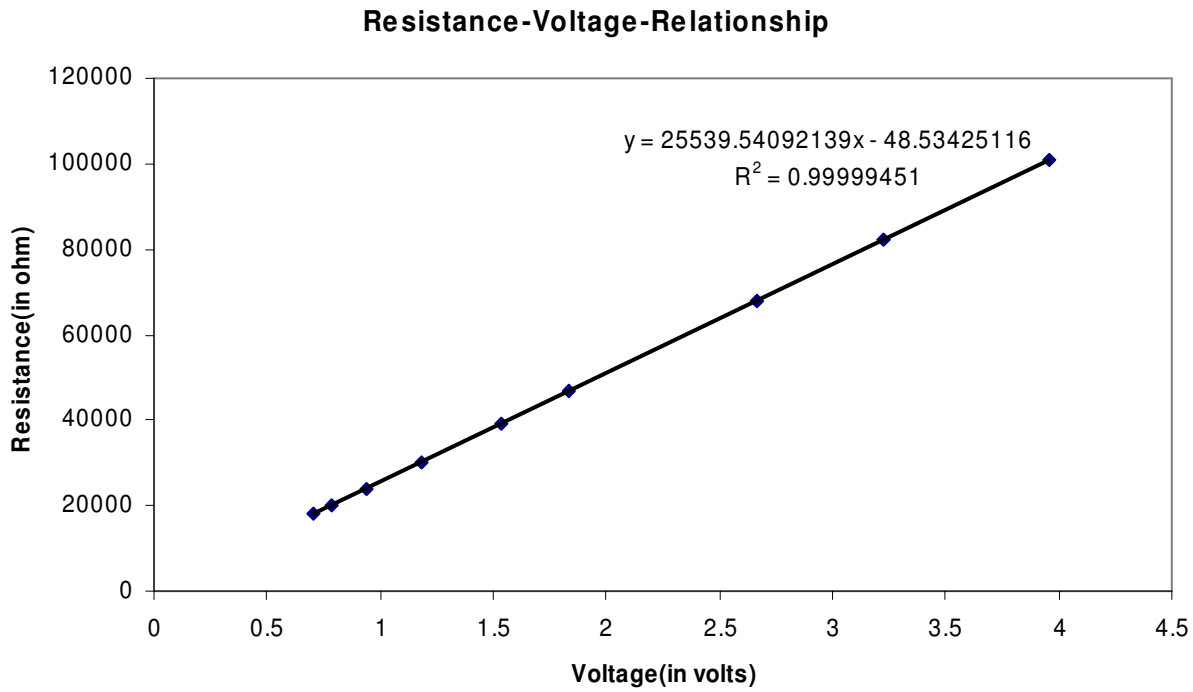

Figure 8-7 Voltage-resistance relationship of temperature sensor

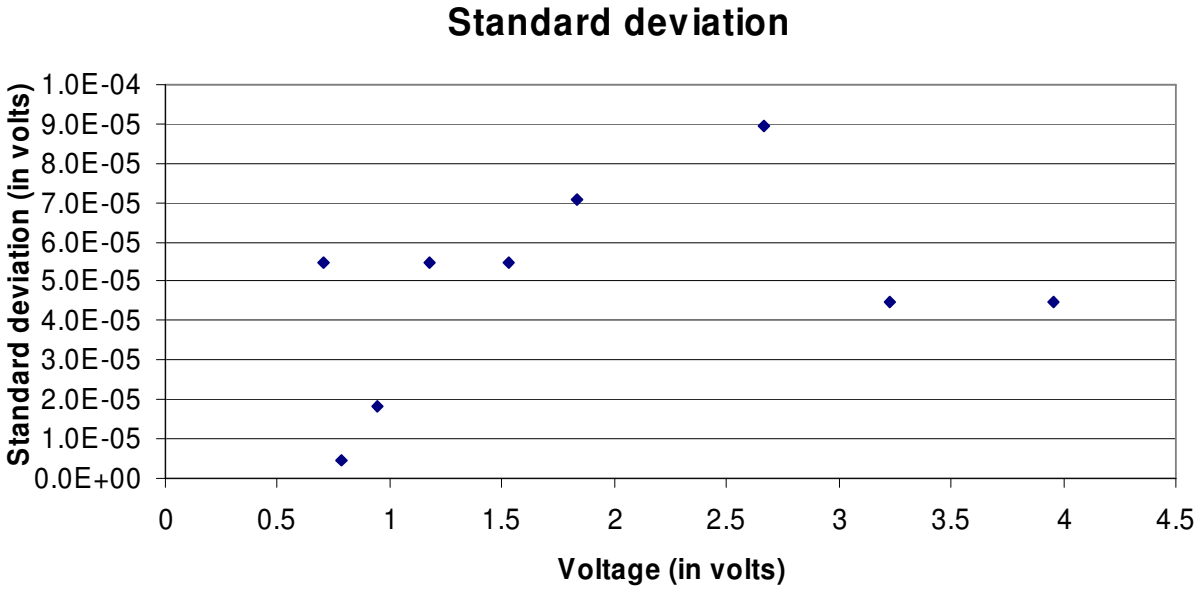

a. Standard deviation of the measured voltages

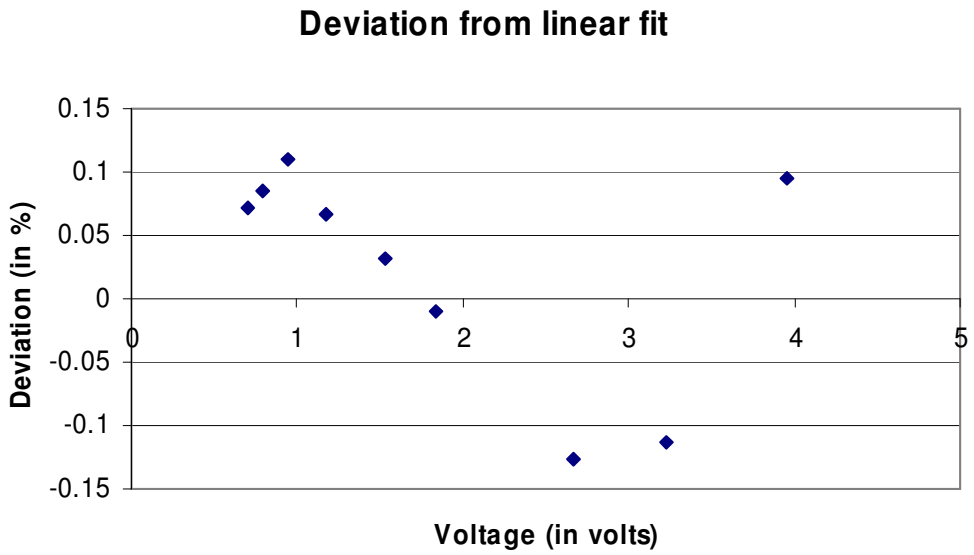

b. Deviation from linear fit in percentage

Figure 8-8 Measurement and calibration deviation of temperature sensor circuit (a, b)

Figure 8-8a shows the standard deviation of the measurement, the biggest voltage standard deviation is 88.443μV by measuring a resistor of 68.09 kΩ with an average output voltage of 2.6648V. This deviation is mainly caused by the circuit noise, and also introduced by the measurement instrument (DC voltage accuracy is 3V±85μV for Agilent 34410A multi-meter). This voltage standard deviation is converted to a resistance resolution of 2.28433 Ω (0.00335% of 68.09 kΩ) which is equivalent to a temperature resolution 0.00066 ^{o}C, and is within the target of 0.01 ^{o}C.

Figure 8-8b shows the residuals from the linear fit given in figure 8-7. The residuals from linear fit is within ±0.15%, and the biggest deviation is about 3.7mV (occurs at the average voltage point of 3.9575V when measured 100942Ω resistance) and will cause an error of 83 Ω in the calibration if the linear fit is used. The deviation from linear fit could be caused by the accumulated nonlinearity of electronic components, stray capacitance, thermal drift, and measurement errors such as the introduced extra-contacting resistance when measure standard calibration resistors.

8.2.2 Thermistor calibration

The three-term Steinhart-Hart equation is the most popular model for thermistor *R-T* characterization [122], The term *C1*, C2 and *C3* are the Steinhart-Hart constants and can be obtained by solving equation 8-2.

$$1/T = C1 + C2 * lnR + C3 * (lnR)^3 \quad [8\text{-}2]$$

For a wide temperature range and higher accuracy, Least-Square-Fit method is used which is given as

$$1/T = A + B\ ln\ R + C\ (ln\ R)^2 + D\ (ln\ R)^3 \quad [8\text{-}3]$$

Least-Squares-Fit includes a square term to reduce error, but requires a greater number of temperature-resistance readings to be taken to adjust the resistance-temperature curve for a good fit.

8.2.3 Stray capacitance

Although AC excitation plus synchronous phase detection (SPD) has advantages over DC excitation in terms of Signal to Noise Ratio (SNR), AC excitation has a drawback that is the additional error introduced by stray capacitance. Since the thermistor is connected to the preamplifier by wires and PCB tracks, the parasitic capacitance of the wires and tracks will cause stray current flow by the side path which leads to measurement error. Transmission line maybe the best model to represent the stray capacitance. However, a simplified model is given by a stray capacitance in parallel with the thermistor.

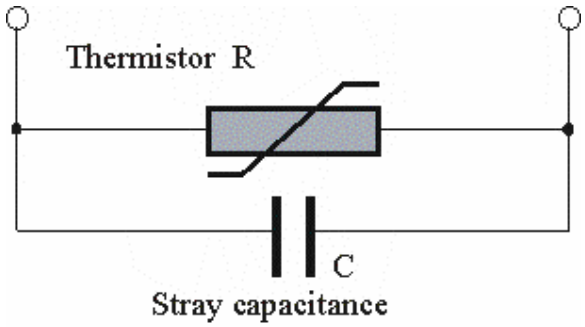

Figure 8-9 Thermistor and stray capacitance model

Figure 8-9 shows that the measurement is actually an impedance (Z) which always includes the reactance of the stray capacitance (C). The impedance (Z) and resistance (R) of the thermistor relationship can be expressed:

$$Z = \frac{R}{1 + j\omega RC} \quad [8\text{-}4]$$

$$Z = \frac{R}{\sqrt{1 + (\omega RC)^2}} * e^{-j\beta} \quad [8\text{-}5]$$

$$\beta = \tan^{-1}((\varpi RC) \qquad [8\text{-}6]$$

$$|Z| = \frac{R}{\sqrt{1+(\varpi RC)^2}} \qquad [8\text{-}7]$$

Thus

$$R = \frac{|Z|}{\sqrt{1-(\varpi C|Z|)^2}} \qquad [8\text{-}8]$$

From equation 8-4, it is clear that the error can be reduced by decreasing the frequency. However, the error introduced by the stray capacitance can be compensated by equation 8-8, and figure 8-10 shows the resistance and the impedance with a stray capacitance of 250pF.

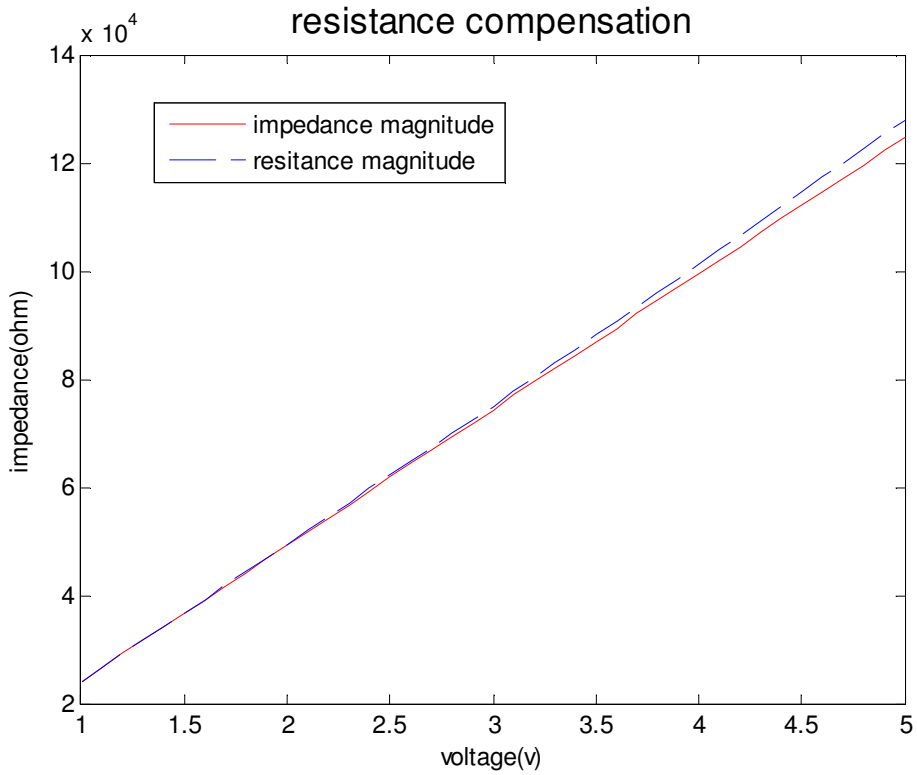

Figure 8-10 Measured impedance and thermistor resistance

8.2.4 Test result

The temperature test was carried out in a temperature bath (Guideline Model 5010 temperature bath with resolution 0.01 ^{o}C, stability ± 0.002 ^{o}, range -9.90 to +65.00 ^{o}C), referred to a precision PRT thermometer (F250 MARKII precision thermometer AΣΛ

with accuracy of 0.002 °C), the experiment setup is shown in figure 8-11. The data was sampled at 7 different temperature points from 1°C to 30°C, and the sensor voltage was measured by a precision multi meter (Agilent 34401A). During the test, the data was sampled only when the bath temperature was stable.

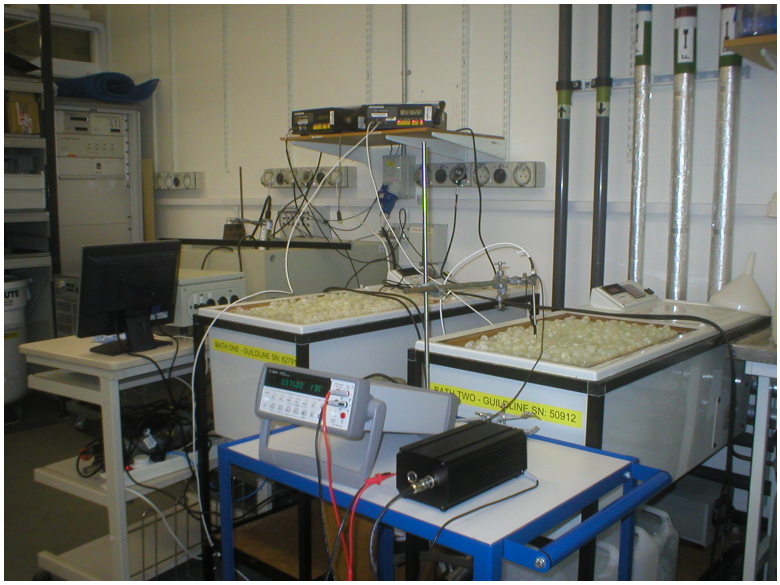

Figure 8-11 Temperature experiment setup

The measured temperature and sensor output voltage relationship is shown in figure 8-12. The resistance corresponds to the output voltage, calculated according to the equation given in figure 8-7 and more precisely compensated by using equation 8-10. The thermistor was calibrated at three different temperature points of 1 °C, 15 °C and 30 °C. The Steinhart-Hart constants for the thermistor (Betatherm 30K6A1B) were obtained by solving equation 8-2. Thus the temperature measured by the thermistor and circuit is given by the following equation:

$$|Z| = 25539.541*V-48.534 \qquad [8\text{-}9]$$

$$R = \frac{|Z|}{\sqrt{1-(\varpi C|Z|)^2}} \qquad [8\text{-}10]$$

$$1/T = 1.18140269*10^{-3} + 1.94389285*10^{-4} * lnR + 1.55983561*10^{-8} * (lnR)^3 \qquad [8\text{-}11]$$

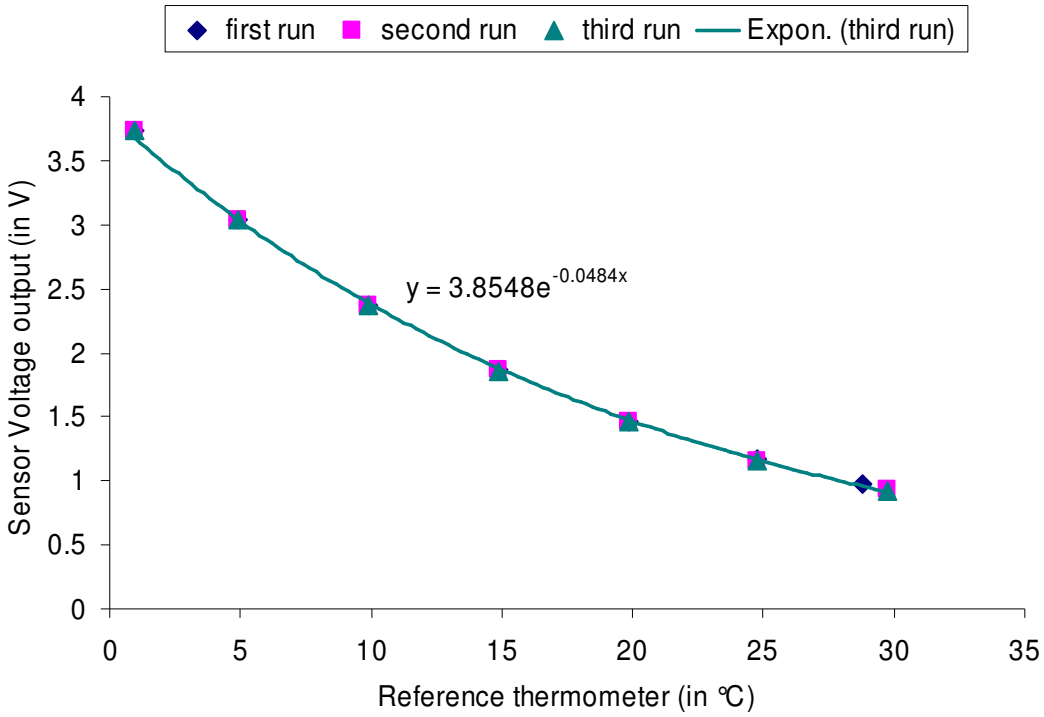

Figure 8-12 Output voltage vs. measured temperature

The temperature measured by the sensor is compared with the reference precision thermometer, and figure 8-13 shows that the test results. The difference of measurement between the sensor and the reference thermometer is shown in figure 8-14.

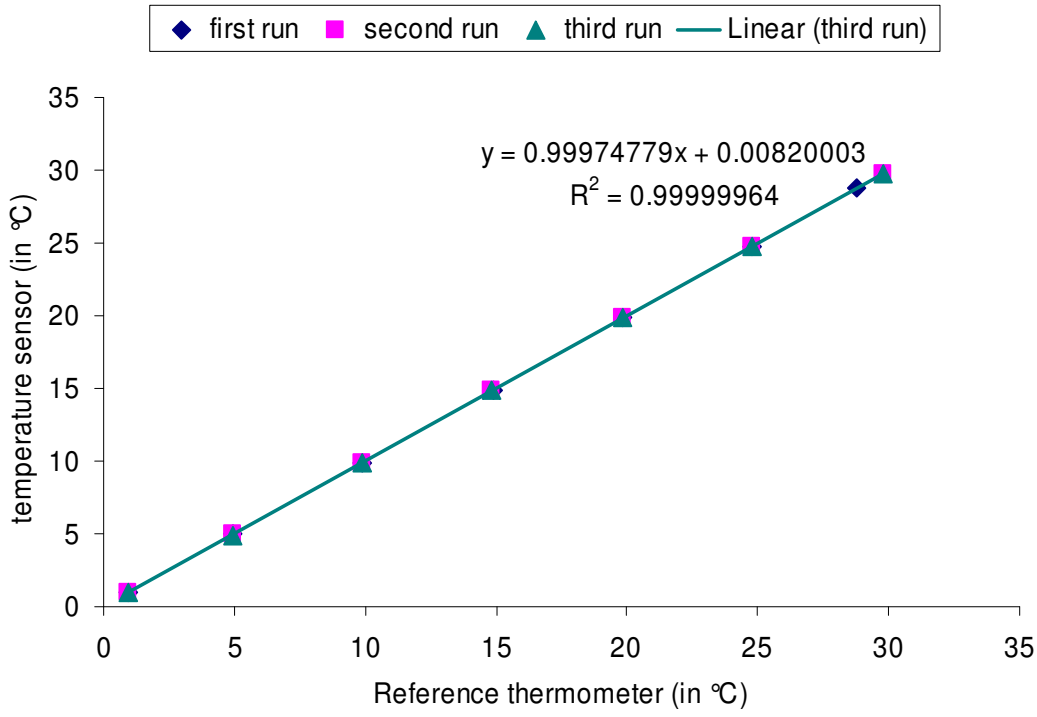

Figure 8-13 Temperature sensor vs. reference thermometer

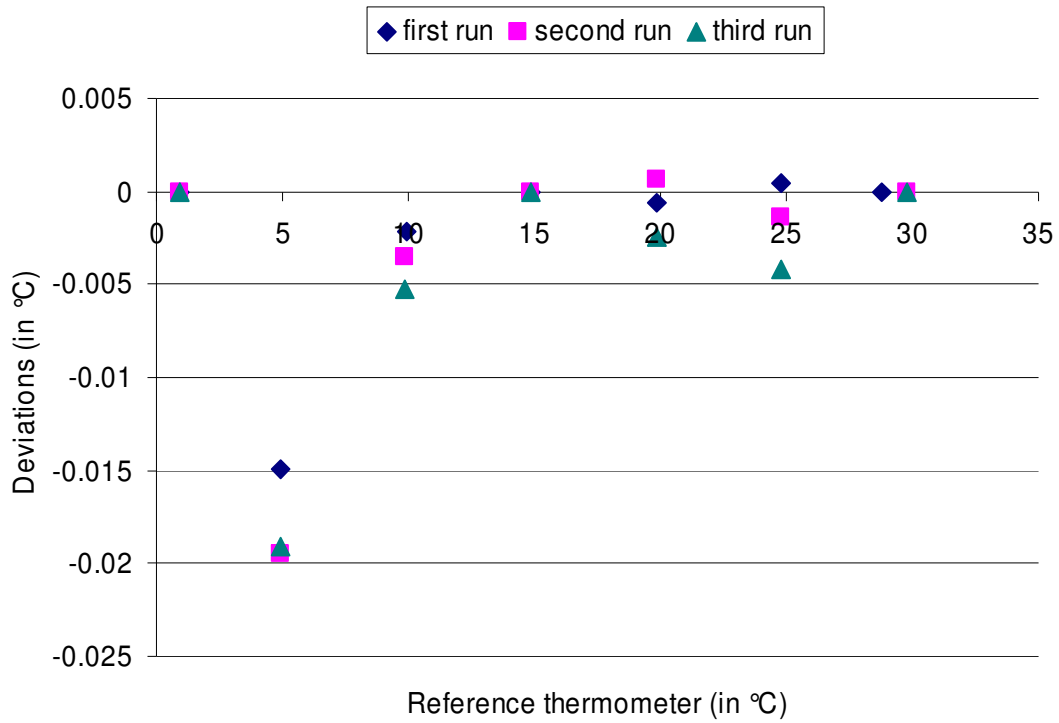

Figure 8-14 Temperature sensor deviation from the reference

From figure 8-14, it is clear that the sensor deviates from the precision reference thermometer in the range of 1 to 30 ^{o}C is almost within ±0.005 ^{o}C except one point of 0.02 ^{o}C at 5 ^{o}C. The possible reasons for the biggest deviation at the particular temperature point of 5 ^{o}C could be caused by the error introduced from linear fit of the circuit (a residual of 10Ω could cause temperature error of about 0.002 ^{o}C at 5 ^{o}C), or the instability of the temperature bath and insufficient mixing resulting in the sensor and reference being at a different temperature, or a defect of the thermistor, or an incorrect calibrated reference thermometer. Therefore the sensor can achieve an accuracy of 0.02 ^{o}C in the measurement range of 1 to 30 ^{o}C. The resolution is about 0.00065 ^{o}C, defined by the biggest standard deviation of temperature at 20 ^{o}C (the standard deviation of measured voltage is 44.7μV/√Hz with an average voltage of 1.46532V/√Hz).

8.2.5 Discussion

The Steinhart-Hart equation is an approximation, and the result depends on the data treatment as well as the calibration. Although self-heating can be minimized by limiting the injected current, the error can not be completely avoided. The dynamic thermal response of the thermistor can also influence the measurement, especially when the thermal dynamics of the monitored environment changes quickly. The thermal mass of the thermistor (Betatherm 30K6A1B has typical 1 second time response in liquids) will determine the maximum sampling rate, thus a thermistor with a small thermal mass and high heat transfer coefficient is desired to get fast response.

The signal conditioning circuit also contributes to errors. An AC excitation is used rather than DC excitation, but the penalty of the AC method is the error introduced by stray capacitance, especially when the resistance of thermistor is high. Data processing can be used to compensate for the stray capacitance and the error can be cancelled providing it is invariant or linearly changing with time between calibrations. Electronic component have thermal effects, and components soldering have thermocouple effects. All of these effects also contribute to the measurement error. Thus optimal design needs to consider the heat dissipation of electronic components, and the PCB board should be mounted in a temperature stable environment.

Calibration is also critical. A good sensor design without a good calibration will not achieve a good result. During the calibration, the thermistor was mounted close to the reference PRT probe. Since the temperature bath has a temperature gradient, there may have been a small temperature difference between the thermistor and reference probe. Although the guideline temperature bath is temperature controlled with a stability $\pm$ 0.002 ^{o}C, there is always a temperature gradient distribution and variation caused by the heat dissipation and generation. Since the heater is located on one side of the bath, it takes time to transport the heat to the whole bath. To reduce errors, each test was carried out at least half hour later after a new temperature setting was made in order to make the bath temperature stable. Although precautions had been taken during the test, there was always a small temperature variation due to the temperature gradient which directly contributes to the measurement error. Reading also could possibly

induce some errors since the test was not automated and the output voltage of the thermistor and the reference temperature were manually recorded at different time which may cause a small temperature variation caused by the limited stability of the bath (± 0.002 ^{o}C).

8.3 Conclusions

A novel four-electrode conductivity cell built on a PCB board with planar electrodes and insulated channel is successfully presented. This conductivity cell together with tailor designed electronics achieved accuracy of ±0.2mS/cm, or 0.6% in the conductivity range of 15-55mS/cm.

An inexpensive thermistor (±0.2°C) combined with bespoke electronics achieved an accuracy of ±0.02°C, just as accurate as an expensive (i.e. tight tolerance) thermistor, in the temperature range of 0-30°C. Compared with other temperature sensors, a thermistor has a narrow measurement range, but it is small, fast and very sensitive and hence suitable for oceanographic instruments.

The tests result shows that the accuracy of design micro CT (Temperature & Conductivity sensors) is close to the target given in table (±0.1mS/cm for conductivity, ±0.01°C for temperature).

Chapter 9 Conclusions

9.1 Conclusion

In this work, low cost optics and conditioning circuits for lock in based detection of the colorimetric method for nitrite detection has been developed, optimized and characterized. This method has been shown to be effective in sea water analysis and could be applied to other colorimetric protocols for different chemical species. The use of a mono-colored LED and integrated photo-detectors makes the optical detector compact.

The interference filters used in the temporary sensor block narrow the bandwidth of the green LED radiation, improves the linearity of the absorbance-concentration curve and thus reduce the deviation from Beer's law.

A successful prototype double beam spectrophotometer has been designed for absorbance measurement of nitride in seawater. Compared with the lab standard spectrophotometers, the designed double beam spectrophotometer is simple and compact. A new phase shifter using PLL technique was realized in the design which is used with lock-in amplifiers with square wave modulation. The signal noise ratio is improved by the lock-in amplifiers used in this design, removing the interference from ambient light as well as the flicker noise produced by the pre-amplifiers. The design also uses a log ratio amplifier to process the reference and sample signal simultaneously and a voltage proportional to the absorbance is the direct output.

During the test, a temporary sensor block with standard cuvette (1cm light path length) was used and the limit detection of nitride in seawater was 0.1μM. The resolution can be further improved if a longer light path is used.

A novel four-electrode conductivity cell built on a PCB board with planar electrodes and insulated channel is successfully presented. This conductivity cell together with tailor designed electronics achieved accuracy of 0.6% in the conductivity range of 15-55mS/cm.

An inexpensive thermistor (±0.2°C) combined with bespoke electronics achieved an accuracy of ±0.02°C, just as accurate as an expensive (i.e. tight tolerance) thermistor, in the temperature range of 0-30°C. Compared with other temperature sensors, a thermistor has a narrow measurement range, but it is small, fast and very sensitive and hence is suitable for oceanographic instruments.

A miniaturized CT (Conductivity & Temperature) system is successfully presented, and potentially can be extended to include ocean depth sensor to be a completed CTD system. Compared with the conventional CTD sensors, the new compact sensor used a planar four-electrode built on PCB incorporating a thermistor which features a small size (30x60mm), low power consumption (175mW), low cost and high accuracy.

A multi-sensor signal conditioning circuit is successfully presented. The circuit design is small (100x65mm) with good performance (SNR improved by 1000, 175mW power consumption) and self-calibration function which is suitable to be used in a multi-sensor system for environmental monitoring.

9.2 Recommendation for future work

A temporary optical sensor block was used in the nitrite experiment since a microfluidics chip was not ready at that time. The recommendation for the microfluidic chips are summarized below:

- In order to improve the resolution, the light path length should be as long as possible. Since the micro channel has a very small size, it is better to use channel section rather than across channel. The ‘U’ and ‘Z’ shape channel

section is the popular technique used in the micro channel to improve the light path length and hence improve the system resolution.

- To prevent deviation from Beer's law, interference filters can be used to narrow the bandwidth of the LED, which reduces deviation and improves the linearity.
- To reduce the temperature influence, the reference and sample photo-detectors should be installed as close as possible with a good thermal coupling.
- Collimation lenses could be used to reduce stray light and improve the linearity of the absorbance-concentration curve.
- Materials used in the microfluidic chip are very important. Black materials reduce reflection and stray light.
- The refractive index of carrier stream should be matched with that of the injected solutions in order to suppress interference from the Shlieren effects.
- Care should be taken to prepare and handle chemical contamination, especially at low concentration.

The designed four-electrode conductivity sensor is best used in a flow system in order to achieve better accuracy. A complete integrated sensor system can be realized when the miniaturized CT system is integrated with the nitrite sensor.

For immersion application, the proposed five-electrode conductivity cell is a good option. Alternatively, a modified four-electrode conductivity cell with extended two end-sections can be used to enable immersion, and to reduce (but not eliminate) proximity effects.

In the test, the measurement error caused by linear fit can be reduced if a lookup table is directly used to map the resistance and voltage. Conductivity accuracy could be improved to 1.4mS/cm if the deviation of 0.0636mS/cm was removed, and temperature accuracy could be improved to 0.006°C if the biggest deviation (3.7mV) had been removed by using look up table.

The multi-sensor signal conditioning circuit can be further improved by the circuit optimization and careful component selection. The circuit can be further simplified by narrowing the conductivity measurement range; the power consumption can be reduced by scaling down the supply voltage. CMOS opamps are also good to

reduce power consumption, but they could lead to a higher noise level since CMOS opamps are noisier than Bipolar and JFET opamps. Last but not least, power consumption can be significantly reduced when sleep mode is used during the interval of data logging. The total size of the PCB board can be further reduced if the components are populated on the double side of the PCB board, and the smallest size can be achieved if the design is realized on an ASIC chip.

References

[1] S.J. Haswell, "Development and Operating Characteristics of Micro Flow Injection Analysis Systems Based on Electroosmotic Flow," *Analyst, January 1997, Vol. 122(1R–10R)*

[2] K. Seiler, Z.H. Fan, K. Fluri, D.J. Harrison, "Electroosmotic Pumping and Valveless Control of Fluid Flow within a Manifold of Capillaries on a Glass Chip," *Anal. Chem. 66 (1994) 3485.*

[3] A. Meulemans, F. Delsenne, J. Chromatogr, "Measurement of nitrite and nitrate levels in biological samples by capillary electrophoresis," *B 660 (1994) 401.*

[4] Manuel Miro , Jose Manuel Estela, Victor Cerda, "Application of flowing stream techniques to water analysis. Part I. Ionic species: dissolved inorganic carbon, nutrients and related compounds," *Talanta 60 (2003) 867_/886.*

[5] L.K. Shpigun, I.Y. Kolotyrkina, Y.A. Zolotov, "Experience with flow-injection analysis in marine chemical research," *Anal. Chim. Acta 261 (1992) 307.*

[6] Blundell, N.J., Worsfold, P.J., Casey, H. and Smith, S. (1995) "The design and performance of a portable, automated flow injection monitor for the in-situ analysis of nutrients in natural waters," *Environ. Int. 21, 205-209.*

[7] T. McCormack, A.R.J. David, P.J. Worsfold, R. Howland, "Flow injection determination of nitrate in estuarine and coastal waters" *Analytical Proceedings 31 (1994) 81.*

[8] A.W. Morris, A.J. Bale, R.J.M. Howland, "Nutrients Distribution in An Estuary: Evidence of Chemical Precipitation of Dissolved Silicate and Phosphate," *Estuarine and Coastal Shelf Science 12 (1981) 205.*

[9] A. Manz, N. Graber, and H. M. Widmer, "Miniaturized total chemical analysis systems: A novel concept for chemical sensing," *Sens. Actuators, vol. B1, pp. 244–248, 1990.*

[10] Alain Poisson, "The Concentration of the KC1 Solution Whose Conductivity is

that of Standard Seawater (35‰) at 15°C", *IEEE Journal of Oceanic Engineering, VOL.OE-5, NO. 1, pp.24-28, January 1980.*

[11] Unesco (1981). "The Practical Salinity Scale 1978 and the International Equation of State of Seawater 1980", *Tech. Pap. Mar. Sci., 36.*

[12] http://www.es.flinders.edu.au/~mattom/IntroOc/lecture03.html

[13] J. Alonsochamarro, J. Bartroli, C. Jimenez, "Nitrate ion-selective electrode as reference electrode for flow-injection analysis", *Anal. Chim. Acta. 261 (1992) 419-423.*

[14] M.J. Rocheleau, W.C. Purdy, "Ion-selective electrode with fixed quaternary phosphonium ion-sensing species", *Analyst 117 (1992) 177-179.*

[15] R. Lumpp, J. Reichert, H.I. Ache, "An optical sensor for the detection of nitrate"**,** *Sensors and Actuators B 7 (1992) 473-475.*

[16] P.C. Hauser, S.S.S. Tan, "All-solid-state instrument for fluorescence-based fibre-optic chemical sensors"**,** *Analyst 118 (1993) 991-995.*

[17] G.J. Mohr, B. Kovacs, O.S. Wolfbeis, "Optical sensors for a wide pH range based on azo dyes immobilized on a novel support", *Anal. Chim. Acta 292, 41-48 (1994).*

[18] J.F. Van Staden, T.A. van der Merwe, Mikrochim, "On-line monitoring of nitrite in fertilizer process streams, natural and waste water effluents with sequential injection analysis", *Microchimica Acta 129 (1998) 33.*

[19]Anne Daniel, Dominique Birot, Michel Lehaitre, Jacques Poncin, "Characterization and reduction of interferences in flow-injection analysis for the in situ determination of nitrate and nitrite in sea water", *Analytica Chimica Acta 308 (1995) 413-424.*

[20]Murad I.H. Helaleh, Takashi Korenaga, "Sensitive Spectrophotometric Determination of Nitrite in Human Saliva and Rain Water and of Nitrogen Dioxide in the Atmosphere," *AOAC International, volume 84, Issue 1, January 2001, P53-58.*

[21] Lourdes Arce, Petr Kuban, Angel Rios, Miguel Valcarcel, Bo Karlberg, "On-line ion-exchange preconcentration in a flow injection system coupled to capillary electrophoresis for the direct determination of UV absorbing anions," *Analytica Chimica Acta 390 (1999) 39-44.*

[22] Dimitrios Tsikas, Jürgen C. Frölich, "Determination of nitrite as pentafluorobenzyl derivative by RP-HPLC and UV detection with and without ion-pair extraction,"

Analytical and Bioanalytical Chemistry, Volume 344, Number 6 (1992), 256-260 Springer.

[23] Miles S. Finch, David J. Hydes, Charles H. Clayson, Bernhard Weigl, John Dakin, Pat Gwilliam, "A low power ultra violet spectrophotometer for measurement of nitrate in seawater: introduction, calibration and initial sea trials", *Analytica Chimica Acta 377 (1998) 167-177.*

[24] Paolo Andrighetto, Tommaso Carofiglio, Roberto Fornasier, Umberto Tonellato, "A highly sensitive method for the analysis of nitrite ions by capillary zone electrophoresis using water-soluble aminophenylporphyrin derivative as chromogenic reagent", *Electrophoresis 2000, 21, 2384-2389.*

[25] Johnson, K. S., L. J. Coletti (2002), "In situ ultraviolet spectrophotometry for high resolution and long-term monitoring of nitrate, bromide and bisulfide in the ocean", *Deep-Sea Research, Part I: Oceanographic Research Papers 49(7): 1291-1305.*

[26] L. Anderson, Anal. "Simultaneous spectrophotometric determination of nitrite and nitrate by flow injection analysis," *Chim. Acta 110 (1979) 123.*

[27] M. F. Giné, H. Bergamin F, E. A. G. Zagatto and B. F. Reis**,** "Simultaneous determination of nitrate and nitrite by flow injection analysis," *Anal. Chim. Acta 114 (1980) 191.*

[28] Jacobus F. Van Staden, "Automated simultaneous determination of nitrate and nitrite by pre-valve reduction of nitrate in a flow-injection system ," *Anal. Chim. Acta 138 (1982) 403.*

[29] M.J. Ahmed, C.D. Stalikas, S.M. Tzouwara-Karayanni, M.I. Karayannis, "Simultaneous spectrophotometric determination of nitrite and nitrate by flow-injection analysis", *Talanta 43 (1996) 1009.*

[30] B.C. Erickson, B.R. Kowalski, **"**Applications of a versatile injection valve for flow injection analysis," *Anal. Chem. 59 (1987) 1246-1248.*

[31] B. Bermudez, A. Rios, M.D. Luque de Castro, M. Valcarcel, "Configuration with internally coupled valves to overcome shortcomings in the simultaneous determination of nitrite and nitrate by flow-injection analysis," *Talanta 35 (1988) 810-812.*

[32] A. Kojlo, E. Gorodkiewicz, "Simultaneous spectrophotometric determination of nitrite and nitrate in a flow-injection system," *Anal. Chim. Acta 302 (1995) 283.*

[33] M.J. Ahmed, C.D. Stalikas, S.M. Tzouwara-Karayanni, M.I. Karayannis, "Simultaneous spectrophotometric determination of nitrite and nitrate by flow-injection analysis," *Talanta 43 (1996) 1009.*

[34] A. Cerda, R. Forteza, V. Cerda, M.T. Oms, "Sequential injection sandwich technique for the simultaneous determination of nitrate and nitrite," *Anal. Chim. Acta 371 (1998) 63.*

[35] G.F. Wang, M. Satake, K. Horita, "Spectrophotometric determination of nitrate and nitrite in water and some fruit samples using column preconcentration," *Talanta 46 (1998) 671.*

[36]K.V.H. Sastry, R.P. Moudgal, J. Mohan, J.S. Tyagi, G.S. Rao, "Spectrophotometric Determination of Serum Nitrite and Nitrate by Copper–Cadmium Alloy**,"** *Anal. Biochem. 306 (2002) 79.*

[37]M. Trojanovic, "Flow Injection Analysis: Instrumentation and Applications," *World Scientific, London, 2000.*

[38] L.T. Skeegs, "An automatemethod for colorimetric analysis", *Am. J. Clin. Pathol. 28 (1957) 311-322.*

[39] J. Ruzicka, E.H. Hansen, "Flow injection analyses : Part I. A new concept of fast continuous flow analysis," *Anal. Chim. Acta 1975, 78, 145.*

[40] http://taylorandfrancis.metapress.com

[41] J. Ruzicka, G. D. Marshall, "Sequential injection: a new concept for chemical sensors, process analysis and laboratory assays," *Anal. Chim. Acta 1990, 237(2), 329-343.*

[42] http://www.dekker.com

[43] H. M. Widmer, "Trends in industrial analytical chemistry," *Trends Anal. Chem.,* vol. 2, pp. viii–x, 1983.

[44] D. R. Reyes, D. Iossifidis, P. A. Auroux, A. Manz, "Micro total analysis systems. 1. Introduction, theory, and technology", *Anal. Chem. 2002, 74, 2623-2636.*

[45] P. A. Auroux, D. Iossifidis, D. R. Reyes and A. Manz, "Micro total analysis systems. 2. Analytical standard operations and applications", *Anal. Chem. 74, 2637-2652 (2002)*

[46] H. Baltes, O. Band et al., "Advanced Micro&Nanosystem Volume1: Enabling Technology for MEMS and Nanodevices", *Wiley-VCH Verlag GmbH&Co. KGaA, P319-355.*

[47] J. Ruzicka, E.H. Hansen, "Flow Injection Analysis", *John Wiley & Sons: New York, 1981.*

[48] Trojanowicz, M. "Flow Injection Analysis Instrumentation and Applications", *World Scientific: Singapore, 2000.*

[49] R.M. Tiggelaar et al. "Analysis systems for the detection of ammonia based on micromachined components modular hybrid versus monolithic integrated approach", Sensors and Actuators B 92 (2003) 25–36.

[50] Zhi Xu, David W. Larsen, "Development of Ultra-Low-Noise Spectrophotometry for analytical Application," *Anal. Chem. 2005, 77, 6463-6468.*

[51] Philip C. D. Hobbs, "Ultrasensitive laser measurements without tears," *Applied Opticals 36(4), pp. 903-920, February 1, 1997.*

[52] Wensheng Yao, Robert H . Byrne, Robert D. Waterbury, "Determination of Nanomolar Concentrations of Nitrite and Nitrate in Natural Waters Using Long Path Length Absorbance Spectroscopy," *Environ. Sci. Technol. 1998, 32, 2646-2649.*

[53] J. M. Ruano, V. Benoit, J. S. Aitchison, and J. M. Cooper, "Flame hydrolysis deposition of glass on silicon for the integration of optical and microfluidics devices", *Anal. Chem. 72, 1093–1097 (2000).*

[54] G. Pandraud, T. M. Koster, C. Gui, M. Dijkstra, A. van den Berg, and P. V. Lambeck, "Evanescent wave sensing: new features for detection in small volumes," *Sens. Actuators A 85, 158–162 (2000).*

[55] K. B. Mogensen, N. J. Petersen, J. Hubner, and J. P. Kutter, "Monolithic integration of optical waveguides for absorbance detection in microfabricated electrophoresis devices," *Electrophoresis 22, 3930–3938 (2001).*

[56] D. Sobek, S. D. Senturia, and M. K. Gray, "Microfabricated fused silica flow chambers for flow cytometry," *in Proceedings of the Solid-State Sensor and Actuator Workshop _Transducer Research Foundation, Cleveland, Ohio, 1994, pp. 260–263.*

[57] Z. Liang, N. Chiem, G. Ocvirk, T. Tang, K. Fluri, and D. J. Harrison, "Microfabrication of planar absorbance and fluorescence cell for integrated capillary electrophoresis devices," *Anal. Chem. 68, 1040–1046 _1996.*

[58] L. Cui, T. Zhang, and H. Morgan, "Optical particle detection integrated in a dielectrophoretic lab-on-a-chip," *J. Micromech. Microeng. 12, 7–12 _2002.*

[59] http://en.wikipedia.org/wiki/LED

[60] http://www.toyoda-gosei.com/led/products/pdf/E1L31_xxxxx_JEA.pdf

[61] http://www.taosinc.com/images/product/document/TSLx257-E13.PDF

[64] S. Okamura and M. Maruyama, "Improvement on the sensitivity of electro-optical system for electric field strength measurements," *Trans. Inst. Electron. Commun. Eng Jpn. E 65, 702(1982)*

[65] Philip C. D. Hobbs, "Building Electro-Optical Systems: Making It All Work," *John Wiley & Sons, Inc, 2000, p.349.*

[66]http://www.dssc.ece.cmu.edu/news_events/seminars/lunch05/headsmedia /021505.pdf

[67] http://www.bentham.co.uk/pdf/Lock-in%20amplifier%20tutorial.pdf

[68] http://www.analog.com/UploadedFiles/Data_Sheets/106127811AD630_e.pdf

[69] http://www.national.com/pf/LM/LM565.html

[70] H. Golnabi, A. Ashrafi, "Phase-shift generation and monitoring by a simple circuit," *Rev. Sci. Instrum. 67 (5), May 1996.*

[71] http://www.thenewports.net/~jonathan/braulab/log100.pdf

[72] Douglas A. Skoog, F. James Holler, Timothy A. Nieman, "Principles of Instrumental Analysis," Fifth Edition, Saunders College Publishing, 1998.

[73] Tovar A., Moreno C., Manuel-Vez M. P., Garca-Vargas M, "A simple automated method for the speciation of dissolved inorganic nitrogen in seawater," *Analytica Chimica Acta, 2002. 469(2): pp. 235-242.*

[74] W. Bolton, "Measurement and Instrumentation Systems," *Newnes, 1996, p.27.*

[75] Hywel Morgan, Nicolas Green, "AC Electrokinetics: colloids and nanoparticles", *Research Studies Press LTD., England (2003).*

[76] http://ieeexplore.ieee.org/iel5/9636/30473/01405784.pdf?arnumber=1405784

[77] M. Whitfield, D. Jagner, "Marine Electrochemistry: A Practical Introduction", *John Wiley & Sons, Ltd, 1981, pp.164.*

[78] A. L. Bradshaw, K. E. Schleicher, "Electrical Conductivity of Seawater", *IEEE Journal of Oceanic Engineering, VOL. OE-5, NO. 1, January 1980.*

[79] M J Tucker, "Measurement in oceanography", *1971 J. Phys. E: Sci. Instrum. 4 405-413*.

[80] Peter K. Weyl, "On the Change in Eletrical Conductance of Seawater with temperature*", Limnology and Oceanography, Vol. 9, No. 1, pp.75-78, Jan., 1964.*

[81] Stanford H. Smith, "Temperature Correction in Conductivity Measurements", *Limnology and Oceanography, Vol. 7, No. 3. , Jul., 1962, pp.330-334.*

[82] Thomas M. Dauphine, John Ancsin, H. Peter Klein, M. John Phillips, "The Electrical Conductivity of Weight Diluted and Concentrated Standard Seawater as a Function of Salinity and Temperature", *IEEE Journal of Oceanic Engineering, VOL.OE-5, NO. 1, January 1980, pp.28-41.*

[83] Alain Poisson, "Conductivity/Salinity/Temperature Relationship of Diluted and Concentrated Standard Seawater", *IEEE Journal of Oceanic Engineering, VOL.OE-5, NO. 1, January 1980, pp.41-50.*

[84] http://en.wikipedia.org/wiki/Friedrich_Kohlrausch

[85] http://www.uibk.ac.at/exphys/museum/en/electr_3.html

[86] N. L. Brown, B. H. Hamon, "An inductive salinometer", *Deep Sea Res.,Volume 8, Issue 1, June 1961, Pages 65-70.*

[87] N.L. Brown, "A precision CTD microprofiler", *Proc. IEEE Oceans '74 Conference, vol.2 no.2, pp. 270-278, 1974.*

[88] H. P. Schwan, "Alternating Current Electrode Polarization", *Biophysik 3, 181—201 (1966).*

[89] T. M. Dauphinee and H. P. Klein, "A new automated laboratory salinometer," *Sea Tech., vol. 16, pp. 23-25, Mar. 1975.*

[90] http://www.seabird.com/technical_references/condpaper.htm

[91] B. Gas, M. Demjanenko, J. Vacik, "High-Frequency Contactless Conductivity Detection in Isotachophoresis", *Journal of Chromatography, 1980, 192, 253–257.*

[92] R. M. Guijt, E.Baltussen, G. Steen, H. Frank, H. Billiet, T. Schalkhammer, F. Laugere, M. Vellekoop, A. Berthold, L. Sarro, G. Dedem, "Capillary electrophoresis with on-chip four-electrode capacitively coupled conductivity detection for application in bioanalysis", *Electrophoresis 2001, 22, 2537–2541.*

[93] J. G. Alves Brito-Neto, J. A. Fracassi da Silva, Lucas Blanes, C. L. do Lago, "Understanding Capacitively Coupled Contactless Conductivity Detection in Capillary and Microchip Electrophoresis. Part1. Fundamentals", *Electroanalysis 2005, 17, No. 13*

[94] P. Kuban, P. C. Hauser, "Fundamental aspects of contactless conductivity detection for capillary electrophoresis.Part I: Frequency behavior and cell geometry", *Electrophoresis 2004, 25, 3387–3397.*

[95] F. Laugere, G. W. Lubking, J. Bastemeijier, M. J. Vellkoo, " Design of an electronic interface for capacitively coupled four-electrode conductivity detection in capillary electrophoresis microchip", *Sensors and Actuators B 83(2002) 104-108.*

[96] C.Y. Lee, C. M. Chen, G. L. Chang, C. H. Lin, L. M. Fu, "Fabrication and characterization of semicircular detection electrodes for contactless conductivity detector-CE microchips", *Electrophoresis 2006, 27, 5043–5050.*

[97] J. Tanyanyiwa, P. C. Hauser, "High-Voltage Capacitively Coupled Contactless Conductivity Detection for Microchip Capillary Electrophoresis", *Analytical Chemistry, Vol. 74, No. 24, December 15, 2002.*

[98] J. Wang, G. Chen, A. Muck, "Movable Contactless-Conductivity Detector for Microchip Capillary Electrophoresis", *Analytical Chemistry, Vol. 75, No. 17, September 1, 2003 4475.*

[99] M. Pumera, J. Wang, F. Opekar, I. Jelinek, J. Feldman, H. Lowe, S. Hardt, "Contactless Conductivity Detector for Microchip Capillary Electrophoresis", *Anal. Chem. 2002, 74, 1968-1971.*

[100] L. Wang, C. G. Fu, "Miniaturized Capillary Electrophoresis System with Contactless Conductivity Detection and Flow Injection Sample Introduction", *Instrumention Science & Technology Vol. 32, No. 3, pp. 303–309, 2004.*

[101] E. M. Abad-Villar, P. Kuban, P.C. Hauser, "Determination of biochemical species on electrophoresis chips with an external contactless conductivity detector", *Electrophoresis 2005, 26, 3609–3614.*

[102] P. Kuban, P. C. Hauser, "Fundamental aspects of contactless conductivity detection for capillary electrophoresis. Part II: Signal-to-noise ratio and stray capacitance", *Electrophoresis 2004, 25, 3398–3405.*

[103] J. Lichtenberg, N. F. Rooij, E. Verpoorte, " A microchip electrophoresis system with integrated in-plane electrodes for contactless conductivity detection", *Electrophoresis 2002, 23, 3769–3780.*

[104] F. Laugere, R. M. Guijt, J. Bastemeijer, G. Steen, A. Berthold, E. Baltussen, P. Sarro, G. Dedem, M. Vellekoop, A. Bossche, "On-Chip Contactless Four-Electrode Conductivity Detection for Capillary Electrophoresis Devices", *Anal. Chem. 2003, 75, 306-312.*

[105] http://www.noc.soton.ac.uk/JRD/SCHOOL/002/mt002b_2.php#s3

[106] http://www.omega.com/temperature/Z/pdf/z021-032.pdf

[107] http://www.zone.ni.com/devzone/cda/tut/p/id/4237

[108] Ernest O. Doebelin, "Measurement Systems: Application and Design", *McGraw-Hill, 4th, 1990.*

[109] http://www.cornerstonesensors.com/AboutWhat.asp

[110] H. Van Haren, R. Groenewegen, M. Laan, B. Koster, "A Fast and Accurate Thermistor String", *Journal of Atmospheric and Oceanic Technology, VOL. 18, February, 2001.*

[111] http://www.seabird.com/products/spec_sheets/3Sdata.htm

[112] Bard, A.J. and Faulkner, L.R., "Electrochemical methods", *John Wiley & Sons, Inc., New York (2001).*

[113] A. C. Fisher, "Electrode Dynamics", *Oxford University Press, New York (1998).*

[114] J.O'M. Bockris and A.K.N. Reddy, "Modern Electrochemistry : an introduction to an interdisciplinary area" , *Plenum Press, New York (1970).*

[115] Lyklema J 1995 Fundamentals of Interface and Colloid Science vol 2, ch 3 (London: Academic) pp 1–232.

[116] O. Teschke, E. F. de Souza, "Dielectric exchange: The key repulsive or attractive transient forces between atomic force microscope tips and charged surfaces", *Appl. Phys. Lett., Vol. 74, No. 12, 22 March 1999.*

[117] Hans G. L. Coster, Terry C. Chilcott, Adelle C.F. Coster, "Impedance spectroscopy of interfaces, membranes and ultrastructures", *Bioelectrochemistry and Bioenergetics 40 (1996) 79-98.*

[118] J. Lyklema, H.P. van Leeuwen, M. Minor, "DLVO-theory, a dynamic re-interpretation", *Adu. Colloid Interface Sci. 83 (1999) 33-69.*

[119] Barry W. Ninham, "Surface Forces — The Last 30 Å", *Pure & Appl. Chem., Vol.53, pp.2135—2147.*

[120] Hans G. L. Coster, Terry C. Chilcott, Adelle C.F. Coster, "Impedance spectroscopy of interfaces, membranes and ultrastructures", *Bioelectrochemistry and Bioenergetics 40 (1996) 79-98.*

[121] E. T. McAdams, J. Jossinet, " Physical interpretation of Schwan's limit voltage of linearity", *Med.& Biol. Eng. & Comput., 1994, 32, 126-30.*

[122] E. T. McAdams, J. Jossinet, "Nonlinear transient response of electrode-electrolyte interfaces", *Medical & Biological Engineering & Computing 2000, Vol. 38.*

[123] Yu Feldman, E Polygalov, I Ermolina, Yu Polevaya, B Tsentsiper, "Electrode polarization correction in time domain dielectric spectroscopy", *Meas. Sci. Technol. 12 (2001) 1355–1364.*

[124] Vetter, K.J., "Electrochemical kinetics: theoretical and experimental aspects", *Academic Press, New York (1967).*

[125] R. S. C. Cobbold, “Transducers for biomedical measurements: principles and applications”, *Wiley, New York (1974).*

[126] K. Najaf, K. D. Wise, “An implantable multi-electrode array with on-chip signal processing”, *IEEE J. Solid-State Circuits, 21(6):1035-1044 (1986).*

[127] Robert C. Weast, “CRC handbook of chemistry and physics”, *CRC Press, Boca Raton, Florida , 1987.*

[128] L. A. Geddes, K. S. Foster, J. Reilly, W. D. Voorhees, J. D. Bourland, T. Ragheb, N. E. Fearnot, “The rectification properties of an electrode-electrolyte interface operated at high sinusoidal current density,” *IEEE Transactions on Biomedical Engineering, BME-34(9):669-672, Sept. (1987).*

[129] H. P. Schwan, “Linear and nonlinear electrode polarization and biological materials”, *Annals of Biomedical Engineering, 20:269-288 (1992).*

[130] M. Moussavi, H. P. Schwan, H. H. Sun, “Harmonic distortion caused by electrode polarization”, *Medical and Biological Computing, 121-125, March (1994).*

[131] E.T. McAdams, J. Jossinet, “A physical interpretation of Schwan's limit current of linearity”, *Annals of Biomedical Engineering, Volume 20, No. 3, May, 1992.*

[132] J. Weiman and J. Mahler, “An Analysis of Electrical Properties of Metal Electrodes”, *Med. Electron, Biol. Engng. Vol. 2, pp. 299-310. Pergamon Press, 1964.*

[133] H. P. Schwan, “Electrode polarization impedance and measurements in biological materials”, *Annals of the New York Academy of Sciences, 148(1):191-209, Feb. (1968).*

[134] R. A. Robinson, R. H. Stokes, “Electrolytic Solutions”, *Buttenvorths, London, 1959 3rd Ed.*

[135] Clifford D. Ferris, “Introduction to Bioelectrodes”, *Plenum Press, New York (1974).*

[136] V.S. Muralidharan, “Warburg impedance –basics revisited”, *Anti-Corrosion Methods and Materials, Volume 44 · Number 1 · 1997 · pp. 26–29.*

[137] Gesteland, R.C., Howland, B., Lettvin, J.Y. and Pitts, W.H., “Comments on Microelectrodes,” *Proceedingsof the IRE, 47:1856-1862 (1959).*

[138] Arjang Hassibi, Reza Navid, Robert W. Dutton, and Thomas H. Lee, “Comprehensive study of noise processes in electrode electrolyte interfaces”, *Journal of Applied Physics, July 15, 2004, Volume 96, Issue 2, pp. 1074-1082.*

[139] Arthur M. Pederson, Michael C. Gregg, "Development of a Small In-Situ Conductivity Instrument", *IEEE Journal on Oceanic Engineering, VOL. OE-4, NO. 3, July 1979.*

[140] B. V. Hamo, "A portable temperature-chlorinity bridge for estuarine investigations and sea water analysis", *Journal of Scientific Instruments, VOL. 33, September 1956, pp. 329-334.*

[141] D. A. Robinson, "The electrical properties of metal microelectrodes", *Proceedings of the IEEE, 56(6):1065-1071 (1968).*

[142] Sascha K. Hooker, Ian L. Boyd, "Salinity sensors on seals: use of marine predators to carry CTD data loggers", *Deep-Sea Research I 50 (2003) 927–939.*

[143] R.G. Jones, "Measurements of the electrical conductivity of water", *IEE Proc.-Sci. Meas. Technol. Vol. 149, No. 6, November 2002.*

[144] P. H. Daum, D. F. Nelson, "Bipolar Current Method for Determination of Solution Resistance", *Analytical Chemistry, VOL. 45, NO. 3, March 1973.*

[145] R. Hayakawa, H. Kanda, M. Sakamoto, Y. Wada, "New Apparatus Measuring the Complex Dielectric Constant of a Highly Conductive Material", *1975 Japan. J. Appl. Phys. 14 12.*

[146] H. Nakamura, Y. Husimi, A. Wada, "Time domain measurement of dielectric spectra of aqueous polyelectrolyte solutions at low frequencies", *1981 Japan J. Appl. Phys. 524.*

[147] T. M. Dauphinee and H. P. Klein, "A new automated laboratory salinometer," *Sea Tech., vol. 16, pp. 23-25, Mar. 1975.*

[148] http://metrohm.co.uk/elcat_e_10_basic_cond.pdf

[149]http://www.iccontrols.com/files/4-1.pdf

[150] Kenneth D. Hill, Donald J. Woods, "The Dynamic Response of the Two-Electrode Conductivity Cell", *IEEE Journal of Oceanic Enginerring, VOL. 13. NO. 3. July 1988.*

[151]S. L. Schiefelbein, N. A. Fried, K. G. Rhoads, D. R. Sadoway, " A High-accuracy, Calibration-free Technique for Measuring the Electrical Conductivity of Liquids", *Review of Scientific Instruments, VOL. 69, NO. 9, September 1998.*

[152] http://www.coas.oregonstate.edu/research/po/research/microsoar/conduct.html

[153]http://www.coleparmer.co.uk/techinfo/techinfo.asp?htmlfile=Conductivity.htm &ID=78

[154] F. Fernandez E., J. S. Meraz M., L. F. Magana, "The Electric Resistance in Electrolytic Solutions", *Revista Mexicana De Fisca 49 (5) 397-400.*

[155] W. Olthuis, W. Streekstra, P. Bergveld, "Theoretical and experimental determination of cell constants of planar-interdigitated electrolyte conductivity sensors", *Sensors and Actuators B 24-25 (1995) 252-256.*

[156] Jongin Hong, Dae Sung Yoon, Sung Kwan Kim, Tae Song Kim, Sanghyo Kim, Eugene Y. Pak, Kwangsoo No, "AC frequency characteristics of coplanar impedance sensors as design parameters", *Lab Chip, 2005, 5, 270–279.*

[157] A.V. Mamshev, K. Sudara-Rajan, F. Yang, Y. Q. DU, M. Zahn, "Interdigital Sensors and Transducers", *Proceedings of the IEEE, VOL. 92, NO. 5, May 2004.*

[158] H. Tang, Y. F. Gao, "An Impedance Microsensor With Coplanar Electrodes and Vertical Sensing Apertures", *IEEE Sensors Journal, VOL. 5, NO. 6, December 2005.*

[159] B. Timmer, W. Sparreboom, W. Olthuis, P. Bergveld, A. van den Berg, "Optimization of an electrolyte conductivity detector for measuring low ion concentration", *Lab chip, 2002, 2, 121-124.*

[160] H. Zhou, R. D. Tilton, L. R. White, "The role of electrode impedance and electrode geometry in the design of microelectrode systems", *Journal of Colloid and Interface Science 297 (2006) 819–831.*

[161] P. Jacobs, A. Varlan, W. Sansen, "Design optimisation of planar electrolytic conductivity sensors", *Medical & Biological Engineering & computing, November 1995.*

[162] P. Bruschi, A. Nannini, F. Pieri, G. Raffa, B. Vigna, S. Zerbini., "Electrostatic analysis of a comb-finger actuator with Schwarz-Christoffel conformal mapping", *Sensors and Actuators A, 2004, 113, pp.106-117.*

[163] Markovic M., Jufer M. and Perriard, Y., "Analyzing an electromechanical actuator by Schwarz-Christoffel mapping*", IEEE T. on Magnetics, 2004, 40, pp.1858-1863.*

[164] Collin R. E., "Field theory of guided waves", *McGraw-Hill Book Company, Inc. New York, 1960.*

[165] Carlsson E. and Gevorgian S., "Conformal mapping of the field and charge distributions in multilayered substrate CPWs", *IEEE Transactions on Microwave Theory and Techniques, VOL. 47, NO. 8, August 1999.*

[166] Gevorgian S., Berg H., Jacobsson H. and Lewin T., "Application notes - basic parameters of coplanar-strip waveguides on multilayer dielectric/semiconductor substrates, Part 1: high permittivity superstrates", *IEEE, Microwave Magazine, 2003, 4, pp.60- 70.*

[167] E. Spillera, A. Schöllb, R. Alexyb, K. Kümmererb and G.A. Urbana, "A sensitive microsystem as biosensor for cell growth monitoring and antibiotic testing", *Sensors and Actuators A: Physical Volumes 130-131, 14 August 2006, Pages 312-321.*

[168] W. R. Smythe, "Static and Dynamic Electricity", *New York, McGrawHill, 1950.*

[169] E. Chen, Y. Chou, "Charactoristics of Coplanar Transmission Lines on Multilayer Substrates: Modeling and Experiments*", IEEE Transactions on Microwave Theory and Techniques, VOL. 45, NO. 6, June 1997.*

[170] Linderholm P. and Renaud Ph., "Comment on "AC frequency characteristics of coplanar impedance sensors as design parameters" by Jongin Hong, Dae Sung Yoon, Sung Kwan Kim, Tae Song Kim, Sanghyo Kim, Eugene Y. Pak and Kwangsoo No", *Lab Chip, 2005, 5, 270, Lab Chip, 2005, 5, pp.1416-1417.*

[171] Demierre N., Braschler T. Linderholm P., Seger U., Lintel H. V. and Renaud Ph.,"Characterization and optimization of liquid electrodes for lateral dielectrophoresis", *Lab Chip, 2007, 7, pp.355-365.*

[172] T. Sun, N.G. Green, S. Gawad, H. Morgan, "Analytical Electric Field and Sensitivity Analysis For two Microfluidic Impedance Cytometer Design", *IET Nanobiotechnology, 1(5). Pp. 69-79.*

[173] Henry P. Hall, "How Electronics Changed Impedance Measurements", *IMTC 2004 lnslrumentation and Measurements Technology Conference, Como. Italy, 18-20 May 2004.*

[174]http://www.coas.oregonstate.edu/research/po/research/microsoar/conduct.html

[175] Peter Hawkins, "A low-powered resistance and conductivity measuring circuit for use with remote transducers", *Meas. Sci. Technol. 1 (1990) 845-847.*

[176] Louis A. Rosenthal, "Conductivity Measurement Method by Means of Multivibrator Frequency Control", *Ind. Eng. Chem., Fundam., Vol. 16, No. 4, 1977 483.*

[177] A. M. Pederson, "A small in-situ conductivity instrument," *in Proc. OCEANS 73-Conf. on Engineering in the Ocean Environment (Seattle, WA, Sept. 25-28, 1973), pp. 68-75.*

[178] A. M. Pederson, M. C. Gregg, “Development of a small in-situ conductivity instrument”, *IEEE J. Oceanic Eng., VOL. OE-4, PP: 69-75, 1979.*

[179] Neil L. Brown, “A High Performance Micro-Power CTD Sensor”, *OCEAN’ 94. ‘Ocean Engineering for Today’s Technology and Tomorrow’s Preservation.’ Proceedings, 13-16 Sep 1994, IEEE, Vol. 1, PP: I/385-I/390.*

[180] Raymond W. Schmitt, Robert A. Petitt, “A fast response, stable CTD for gliders and AUVs”, *IEEE Conference Proceeding, Oceans 2006, September 2006.*

[181] J.P. Vessey, T.H. Williams, “Built-in test and the Oceanographic sensor”, *OCEANS '94. 'Oceans Engineering for Today's Technology and Tomorrow's Preservation.' Proceedings, 1994 IEEE, Vol. 2, PP: II/368-II/371.*

[182] http://www.analog.com/UploadedFiles/Data_Sheets/AD829.pdf

[183] http://www.analog.com/productSelection/pdf/AD8610_20_c.pdf

[184] http://www.analog.com/UploadedFiles/Data_Sheets/AD8033_8034.pdf

[185] http://www.analog.com/UploadedFiles/Data_Sheets/AD8065_8066.pdf

[186] http://literature.agilent.com/litweb/pdf/5968-7181E.pdf

[187] http://www.analog.com/UploadedFiles/Data_Sheets/AD8033_8034.pdf

[188] http://www.falmouth.com/papers/mctd.html

[189] http://www.betatherm.com/news/db/pdf/1107969301.pdf

[190]http://www.linear.com/pc/downloadDocument.do?navId=H0,C1,C1154,C1004,C1012,P1225,D2649

[191] Rubina H. Shreiner, “Stability of Standard Electrolytic Conductivity Solutions in Glass Containers”, *Journal of Research of the National Institute of Standards and Technology, Volume 107, Number 5, September–October 2002.*

[192]Steinhart, J.S. and S.R. Hart (1968), "Calibration Curves for Thermistors", *Deep-Sea Research, Vol 15, 497.*

[200] http://www.microchip.com/downloads/en/DeviceDoc/40192c.pdf

[201] http://www.analog.com/static/imported-files/data_sheets/AD8610_8620.pdf

[202] http://www.datasheetcatalog.org/datasheet/maxim/MAX4680-MAX4700.pdf

[203] A. Hyldgard, I. Olafsdottir, M. Olesen, T. Hedegaard, O. Hansen, E.V. Thomsen, “FISH & CHIPS: Four Electrode Conductivity / Salinity Sensor on a Silicon Multi-Sensor Chip for Fisheries Research**”,** *Sensors, IEEE, Oct. 30 2005, Page(s):1124 – 1127.*

[204] D. Fries, H. Broadbent, G. Steimle, S. Ivanov, A. Cardenas-Valencia, J. Fu, T. Weller, S. Natarajan, L. Guerra, "PCB MEMS for environmental sensing systems", *Industrial Electronics Society, 2005. IECON 2005. 31st Annual Conference of IEEE.*

[205]Heather A Broadbent, Stanislav Z Ivanov, David P Fries, "A miniature, low cost CTD system for coastal salinity measurements", *2007 Meas. Sci. Technol. 18 3295-3302*.

[206] www.generaloceabics.com/genocean/mk3c.htm

[207] www.seabird.com/pdf_documents/manuals/9plus_012.pdf

[208] http://www.valeport.co.uk/ctd_and_multi-parameter.aspx#miniCTD

[209] (http://www.cefastechnology.co.uk/g5/G5tag.pdf)

[210]http://www.star-oddi.com/Temperature_Recorder/Data_Storage_Tags/ conductivity Salinity_recorder/

[211] http:// www.seabird.com

[212] http://www.falmouth.com

[213] K. Grasshoff, K. Kremling., M. Ehrhardt, "Methods of Seawater Analysis", *Wiley-VCH, 1999, 3rd, revised and extended edition: 159-228.*

[214] A.R.J. David, T. McCormack, A. W. Morris, P. J. Worsfold, "A submersible flow injection-based sensor for the determination of total oxidised nitrogen in coastal waters", *Analytica Chimica Acta 361 (1998) 63-72.*

[215] M. Bowden, M. Sequeria, J. P. Krog, P. Gravesen, D. Diamond, " A prototype industrial sensing system for phosphorus based on micro system technology", *Analyst, 2002, 127, 1-4.*

[216] F. A. J. Amstrong, "The determination of silicate in seawater", *Journal of the marine biological association of the United Kingdom, Vol. 30, No. 1, 1951.*

[217] JOHN H. YOE, A LETCHER. JONES, "Colorimetric Determination of Iron with Disodium-1,2-dihydroxybenzene-3,5-disulfonate", *Ind. Eng. Chem. Anal. Ed., 1944, 16 (2), pp 111–115.*

[218] Leanne J. Mallini and Alan M. Shiller, "Determination of Dissolved Manganese in Seawater by Flow Injection Analysis with Colorimetric Detection", *Limnology and Oceanography, Vol. 38, No. 6 (Sep., 1993), pp. 1290-1295.*

[219] RNC Daykin and SJ Haswell, "Development of a micro flow injection manifold for the determination of orthophosphate", *Anal. Chim. Acta 313 (1995) 155.*

[220] M. O'Toole, D. Diamond, "Absorbance Based Light Emitting Diode Optical Sensors and Sensing Devices", *Sensors 2008, 8, 2453-2479.*

[221] Frank B. Myers, Luke P. Lee, "Innovations in optical microfluidic technologies for point-of-care diagnostics", *Lab Chip, 2008, 8, 2015 – 2031.*

[222] K. S. Ryu, K. Shaikh, E. Goluch, Z. Fan, C. Liu, "Micro magnetic stir-bar mixer with parylene microfluidic channels", *Lap Chip 2004 4 608-613.*

[223] Z.Yang Z., S. Matsumoto, R. Maeda, "Active micromixer for microfluidic systems using lead-zironate-titanate (PZT)-generated ultrasonic vibration", *Electrophoresis 2000, 21: 116-119.*

[224] J. B. Knight, A. Vishwanath, J. P. Brody, R. H. Austin, "Hydrodynamic focusing on a silicon chip: mixing nanoliters in microseconds", *Phy. Rev. Lett., 1998, 80: 3863-3866.*

[225] A. D. Stroock, S. K. W. Dertinger, A. Ajdari, H. A. Stone, G. M. Witesides, "Chaotic mixer for microchannels", *Science, 2002, 295: 647-651.*

[226] F. Schönfeld, V. Hessel and C. Hofmann, "An optimised split-and-recombine micro-mixer with uniform 'chaotic' mixing", *Lab Chip, 2004, 4, 65 – 69.*

[227] http://www.wetlabs.com/products/cycle/cycleposter.pdf

[228] Eric T. Steimle, Eric A. Kaltenbacher, Robert H. Byrne, "In situ nitrite measurements using a compact spectrophotometric analysis system", *Marine Chemistry 77 (2002) 255– 262.*

[229]Mims III, F.M. "Sun photometer with light emitting diode as spectrally selective detectors", *Applied Optics 1992, 31, 6965-6967.*

[230] K. T. Lau, S. Baldwin, M. O'Toole, R. Shepherd, W. J. Yerazunis, S. Izuo, S. Ueyama, D. Diamond, "A low-cost optical sensing device based on paired emitter-detector light emitting diodes", *Analytica Chimica Acta 2006, 557, 111-116.*

[231] M.O'Toole, R. Shepherd, K. T. Lau, D Diamond, " Detection of nitrite by flow injection analysis using a novel paired emitter-detector diode (PEDD) as a photometric detectr", *In: Advanced Environmental, Chemical, and Biological Sensing Technologies V , 10 September 2007, Boston, MA, USA* .

[232] A. Hyldgard, D. Mortensen, K. Birkelund, O. Hansen, E.V. Thomsen, "Autonomous multi-sensor micro-system for measurement of ocean water salinity", Sensors and Actuators A 147 (2008) 474–484.

Appendix A: *Matlab script*

1. Matlab Script for SCM mapping of planar electrodes

```
%SCM mapping with finite hight
clear all
W=1000e-6;                          % width of the electrode
H=1000e-6;                           % height of the channel
D=10000e-6;                            % gap between two coplanar
electrodes
LT=10000e-6;                           % LENGTH OF ELECTRODE
k=tanh(pi*D/(4*h))/tanh(pi*(D+2*W)/(4*H));
kv=k^2;
kt=1-kv;
EP=ellipke(kv)
ET=ellipke(kt)
fc=(2*EP)/ET  % cell constant(2 dimension)
a=fc/(100*LT)%cell constant(3 dimension in /cm)


%SCM mapping for cell with infinite hight
clear all
w=500e-6;                          % width of the electrode
% h=infinite-open;                          % height of the channel
D=500e-6;                            % gap between two coplanar
electrodes
LT=2000e-6;                           % LENGTH OF ELECTRODE
k=1/(1+2*w/D);  %modulus
kv=k^2;
kt=1-kv;
EP=ellipke(kv)
ET=ellipke(kt)
fc=(2*EP)/ET  % cell constant(2 dimension)
a=fc/(100*LT)%cell constant(3 dimension in /cm)
```

2. Matlab Script for Four-electrode cell constant

```
%Matlab scrip for 4-ELECTRODE SCM mapping with finite hight
clear all
W=2000e-6;                          % width of the electrode
H=5000e-6;                           % height of the channel
G=20000e-6;                                  % gap between two coplanar
electrodes
LT=5000e-6;                           % LENGTH OF ELECTRODE
k=tanh(pi*G/(4*H))/tanh(pi*(G+2*W)/(4*H));
kv=k^2;
kt=1-kv;
EP=ellipke(kv)
ET=ellipke(kt)
```

```
fc=(2*EP)/ET  % cell constant(2 dimension)
a=fc/(100*LT)%cell constant(3 dimension in /cm)
a=10.1915
```

3. Matlab Script for Five-electrode cell constant

```
%Matlab scrip for 5-electrode SCM mapping with finite hight
clear all
W=2000e-6;                          % width of the electrode
H=2500e-6;                           % height of the channel
G=5000e-6;                         % gap between two coplanar electrodes
LT=3000e-6;                           % LENGTH OF ELECTRODE
k=tanh(pi*G/(4*H))/tanh(pi*(G+2*W)/(4*H));
kv=k^2;
kt=1-kv;
EP=ellipke(kv)
ET=ellipke(kt)
fc=(2*EP)/ET  % cell constant(2 dimension)
a=fc/(100*LT)%cell constant(3 dimension in /cm)
a=9.7866
```

4. Matlab Script for conductivity cell frequency response

```
%a script for the frequency response of conductivity cell
%with a cell constant of 10/cm^2
%sea water conductivity range from 60mS to 0.1mS

clear all
f=logspace(-2,10,100); w=2*pi*f;
%A=1000um*1000um   (A=electrode area)
A=100e-8; k=1000 % k=cell constant 1/m^2
D=k*A   %D= electrode distance
e0=8.854e-12; e=67*e0 %dielectric constant
cp=e*A/D  %parrallel stray capacitance
cs=5*e0*A/(3e-10)%stern layer capacitance,assume permitivity e=5xe0,
                 % thickness l=3e-10
%for NaCl solution with 60mS
c1=0.687     %equivalent concentration
d1=(1.764e-11)*sqrt(298/c1)%thickness of diffusion layer
cd1=e*A/d1                 %diffusion capacitance
cds1=cd1*cs/(cd1+cs)       %double layer cap
R1=1/0.06*(k/100)          %solution resistance
t1=R1*cp
X1=R1./(i.*t1.*w+1.); Y1=1./(i*cds1.*w)
Z1=X1+1/2.*Y1
mag1=abs(Z1)
ang1=angle(Z1)*180/pi
%for NaCl solution with 30mS
c2=0.318
d2=(1.764e-11)*sqrt(298/c2)
cd2=e*A/d2
```

```
cds2=cd2*cs/(cd2+cs)
R2=1/0.03*(k/100)
t2=R2*cp
X2=R2./(i.*t2.*w+1.); Y2=1./(i.*cds2.*w)
Z2=X2+1/2.*Y2
mag2=abs(Z2)
ang2=angle(Z2)*180/pi
%for NaCl solution with 10mS
c3=0.095
d3=(1.764e-11)*sqrt(298/c3)
cd3=e*A/d3
cds3=cd3*cs/(cd3+cs)
R3=1/0.01*(k/100)
t3=R3*cp
X3=R3./(i.*t3.*w+1.); Y3=1./(i.*cds3.*w)
Z3=X3+1/2.*Y3
mag3=abs(Z3)
ang3=angle(Z3)*180/pi
%for NaCl solution with 1mS
c4=0.0084
d4=(1.764e-11)*sqrt(298/c4)
cd4=e*A/d4
cds4=cd4*cs/(cd4+cs)
R4=1/0.001*(k/100)
t4=R4*cp
X4=R4./(i.*t4.*w+1.); Y4=1./(i.*cds4.*w)
Z4=X4+1/2.*Y4
mag4=abs(Z4)
ang4=angle(Z4)*180/pi
%for NaCl solution with 0.1mS
c5=0.00084
d5=(1.764e-11)*sqrt(298/c5)
cd5=e*A/d5
cds5=cd5*cs/(cd5+cs)
R5=1/0.0001*(k/100)
t5=R5*cp
X5=R5./(i.*t5.*w+1.); Y5=1./(i.*cds5.*w)
Z5=X5+1/2.*Y5
mag5=abs(Z5)
ang5=angle(Z5)*180/pi
%plot frequency response
loglog(f,mag1); hold on
loglog(f,mag2,'c')
loglog(f,mag3,'r')
loglog(f,mag4,'m')
loglog(f,mag5,'g')
grid on
xlabel('Frequency(in Hz)')
ylabel('Log magnitude(ohms)')
title('Frequency response(1000umX1000um electrode)')
legend('60mS/cm','30mS/cm','10mS/cm','1mS/cm','0.1mS/cm')
```

Appendix B：*Flow chart*

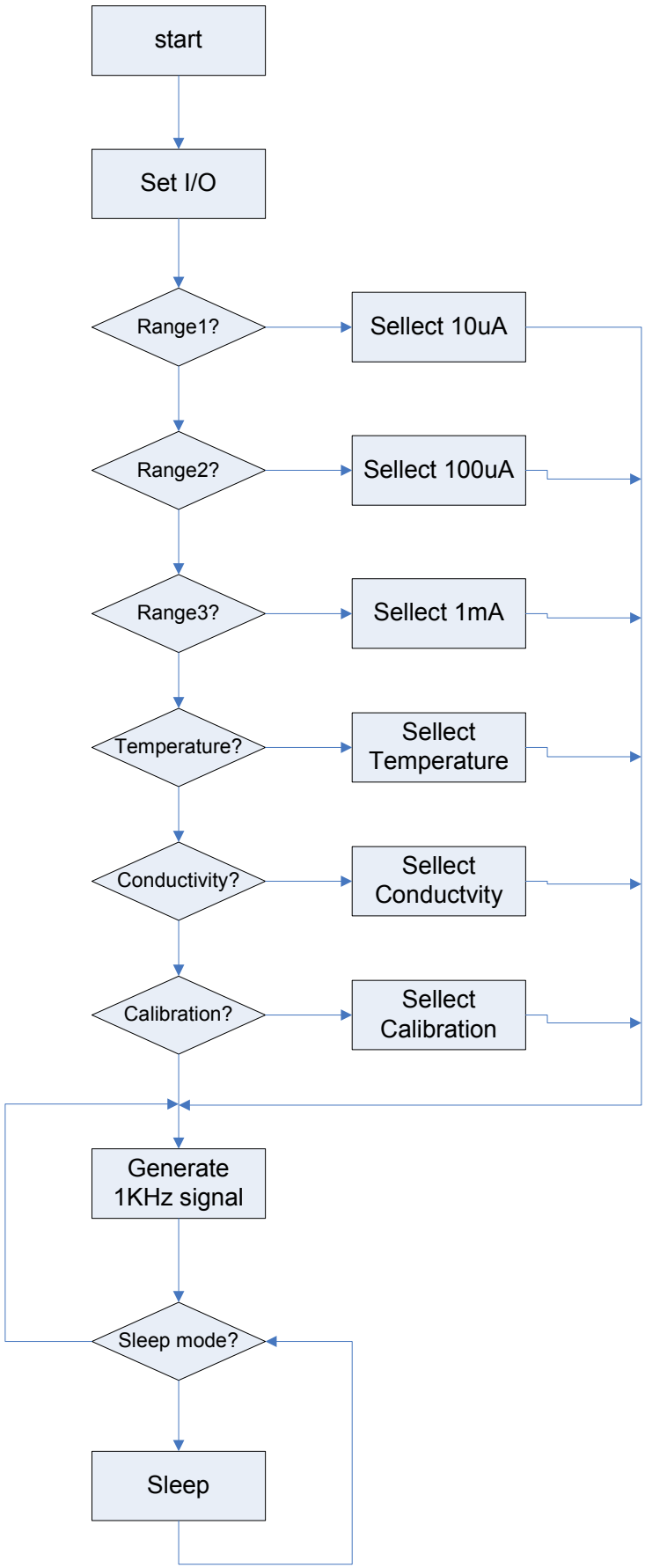
start
Set I/O
Range1?
Sellect 10uA
Range2?
Sellect 100uA
Range3?
Sellect 1mA
Temperature?
Sellect Temperature
Conductivity?
Sellect Conductvity
Calibration?
Sellect Calibration
Generate 1KHz signal
Sleep mode?
Sleep

Appendix C: *Assembly code*

CODE LIST:

```
;*****************************************************************
;   This file is a basic code template for object module code     *
;   generation on the PIC16F505. This file contains the           *
;   basic code building blocks to build upon.
;*****************************************************************
;                                                                 *
;   Filename:           ocean-sensor.asm                          *
;   Date: 29/09/2007                                            *
;   File Version:V1.0                                           *
;   Author:Weidong Gong                                         *
;   Company:University of Southampton                           *
;                                                                 *
;*****************************************************************
;                                                                 *
;   Files required: p16F505.inc                                   *
;                                                                 *
;*****************************************************************
    list      p=16F505          ; list directive to define processor
    #include <p16F505.inc>      ; processor specific variable definitions
    __CONFIG   _MCLRE_OFF & _CP_OFF & _WDT_ON & _LP_OSC
; '__CONFIG' directive is used to embed configuration word within .asm file.
; The lables following the directive are located in the respective .inc file.
; See respective data sheet for additional information on configuration word.

;***** VARIABLE DEFINITIONS
        UDATA
temp      RES    1          ;example variable definition
```

```
;*****************************************************************
****
RESET_VECTOR          CODE   0x3FF      ; processor reset vector
; Internal RC calibration value is placed at location 0x3FF by Microchip
; as a movlw k, where the k is a literal value.
MAIN       CODE    0x000
     movwf   OSCCAL           ; update register with factory cal value
;*****set up the port*****
INITIAL
       bcf     STATUS, PA0       ; switch to page0
   banksel PORTB             ; bank select
   movlw    b'01001111'        ; prescale 1:128 for timer0, internal 1/4 rise up trigger,
wake-up on Pin change bit
   option
   movlw   b'00101011'       ; set data direction bits
   tris    PORTB             ; and load to PortB
   movlw   b'00000011'       ; set data direction bits
   tris    PORTC             ; load to PortC
;*****MAIN PROGRAM*******
start
     nop                   ; example code
     movlw   0x12            ; example code
     movwf   temp            ; example code
   clrf    PORTB
   clrf    PORTC
LOOP
   movlw   PORTB
   btfsc   PORTB,1          ; RB1RB0 INPUT--RC5RC4 OUTPUT
   goto    SET1
   bcf     PORTC,5
   goto    out1
SET1
   bSf     PORTC,5
out1
```

```
   btfsc   PORTB,0
   goto    SET2
   bcf     PORTC,4
   goto    out2
SET2
   bsf     PORTC,4
out2
   btfsc   PORTC,1          ; RC1RC0 INPUT--RC3RC2 OUTPUT
   goto    SET3
   bcf     PORTC,3
   goto    OUT3
SET3
   bsf     PORTC,3
OUT3
   btfsc   PORTC,0
   goto    SET4
   bcf     PORTC,2
   goto    CLOCK
SET4
   bsf     PORTC,2
CLOCK
   bsf     PORTB,2
   clrwdt
   nop
   nop
   bcf     PORTB,2
           btfsc   PORTB,3          ; low sleep mode
           goto    CLOCK            ; high TEST MODE
           bcf     PORTC,4          ; SWITCH OFF POWER
           bcf     PORTC,5
           sleep                    ; sleep mode
   END                      ; directive 'end of program'
```

Appendix D: *Component List*

Double Beam Spectrophotometer PCB Component list

Item	Quantity	Reference	Part
1	12	C1, C2, C3, C4, C11, C15, C16, C17, C24, C25, C28, C37	10u
2	19	C5, C6, C7, C8, C9, C12, C14, C18, C19, C20, C21, C23, C26, C27, C29, C32, C34, C36, C38	0.1u
3	2	C22, C10	1u
4	1	C13	1n
5	1	C30	10n
6	3	C31, C33, C35	0.33u
7	3	J1, J3, J6	CON3
8	2	J4, J2	CON2
9	1	J5	JUMPER3
10	7	POT1, POT2, POT4, POT5, POT6, POT7, POT8	10k
11	4	R8, R9, R16, R18	10k
12	1	POT3	5k
13	4	R4, R5, R12, R14	5k
14	2	R1, R20	68K
15	2	R23, R2	1M
16	8	R3, R6, R7, R11, R13, R27, R28, R30	100k
17	1	R10	0k
18	1	R15	51
19	1	R17	56k
20	2	R26, R19	22k

21	2	R21, R22	27k
22	2	R24, R25	47k
23	2	R29, R31	1k
24	1	SW1	SW DIP-2
25	9	TP1, TP2, TP3, TP4, TP5, TP6, TP7, TP8, TP9	T POINT S
26	1	U1	OP-470/AD
27	1	U2	LM358
28	1	U3	4013
29	1	U4	MAX6120/SOT
30	1	U5	LM565
31	2	U7, U6	AD630/AD
32	1	U8	TS78M06CP/TO252
33	1	U9	TS78M12CP/TO252
34	1	U10	LOG100
35	1	U11	TS79M12/TO252

Multi-sensor signal conditioning PCB Component list

Item	Quantity	Reference	Part
1	15	C1,C2,C3,C4,C5,C14,C17, C20,C21,C23,C25,C27,C31, C32,C33	4.7u
2	17	C6,C7,C8,C9,C10,C13,C18, C19,C22,C24,C26,C28,C34, C35,C36,C38,C40	0.1u
3	1	C11	10u
4	2	C12,C30	1u
5	2	C15,C16	15p
6	1	C29	3.3u
7	2	C37,C39	0.33u
8	2	D1,D2	BAT54/SOT
9	1	J1	JUMPER3
10	1	J2	CON4
11	2	J3,J4	CON2
12	1	J5	CON3
13	1	J6	JUMPER2
14	6	R1,R2,R4,R5,R6,R27	100k
15	10	R3,R8,R10,R11,R12,R13, R18,R23,R26,R28	10k
16	1	R7	39k
17	1	R9	12.5k
18	2	R15,R14	47k
19	3	R16,R22,R25	1k
20	1	R17	270k
21	1	R19	43k
22	1	R20	180k
23	1	R21	120
24	1	R24	240k

25	1	SW1	SW DIP-2
26	3	TP1,TP2,TP3	T POINT S
27	2	U1,U7	AD8620/SO
28	3	U2,U3,U6	ADG1409/SO
29	1	U4	AD8220
30	1	U5	PIC16C505/SO
31	1	U8	MAX4700
32	1	U9	TS78M06CP/TO252
33	1	U10	MC79M06/TO252
34	1	Y1	CRYSTAL 32kHz

Appendix E: *Measurement results of Alpha impedance analyzer*

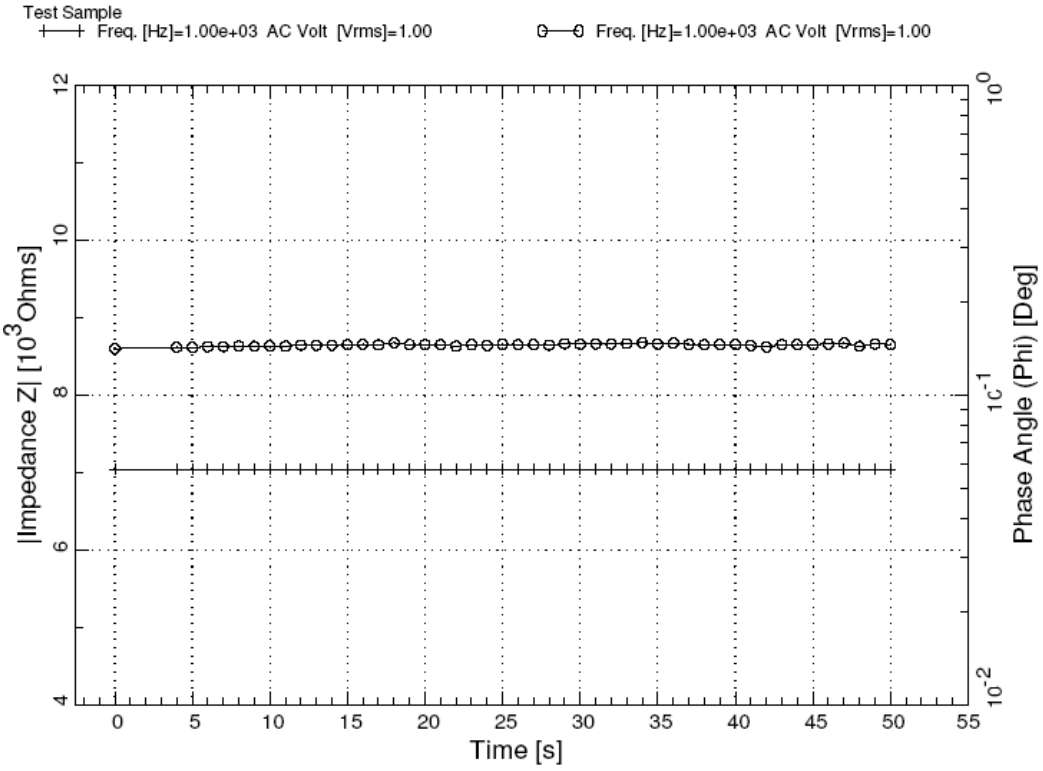

A. Measured by using calibration liquid (Hanna Part No: HI-7031M) 1305µS/cm@ 21°C

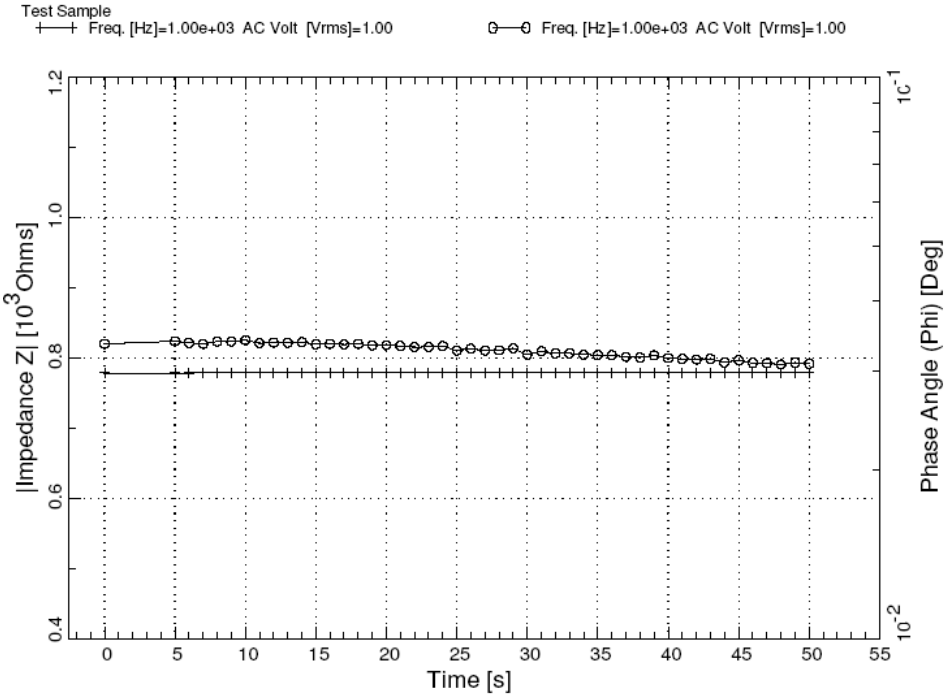

B. Measured by using calibration liquid (Hanna Part No: HI-70030P) 11910 µS/cm @ 21°C

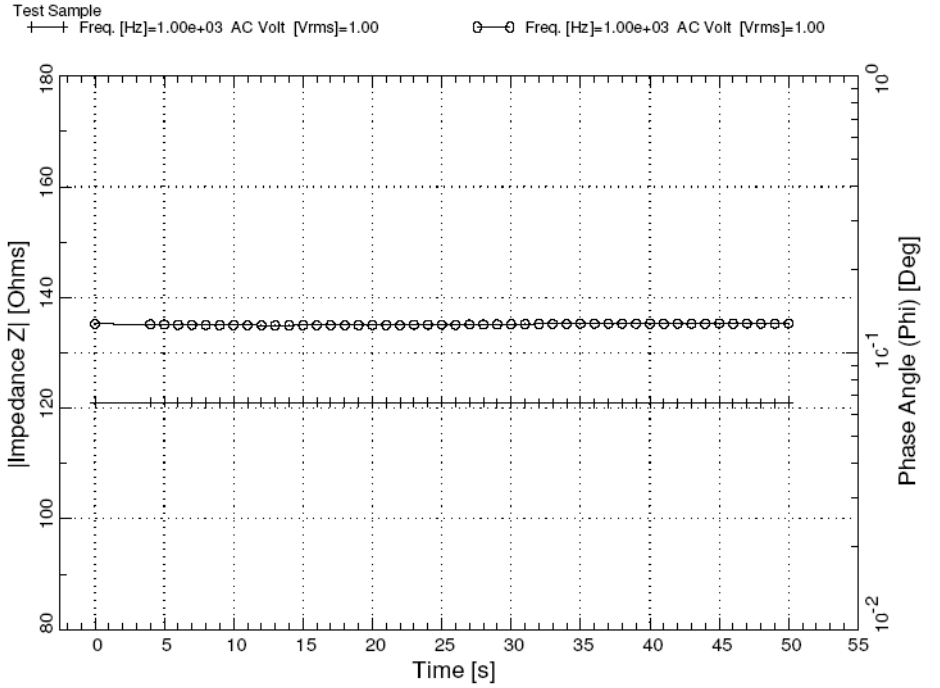

C. Measured by using calibration liquid (Hanna Part No: HI-7034L) 74000 µS/cm @21 °C

Appendix F: *Schematic Diagram*

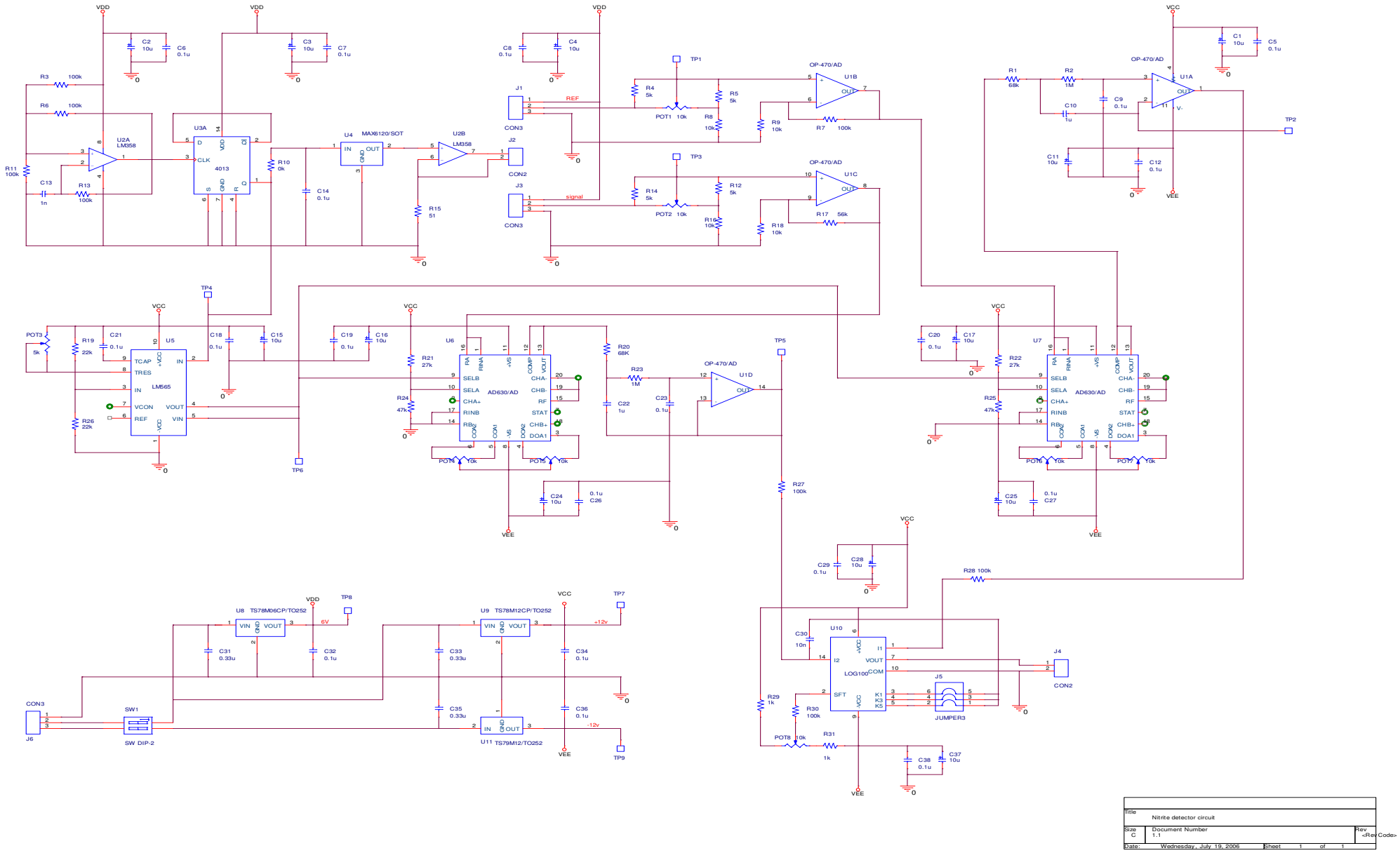

Double Beam Spectrometer Schematic Diagram

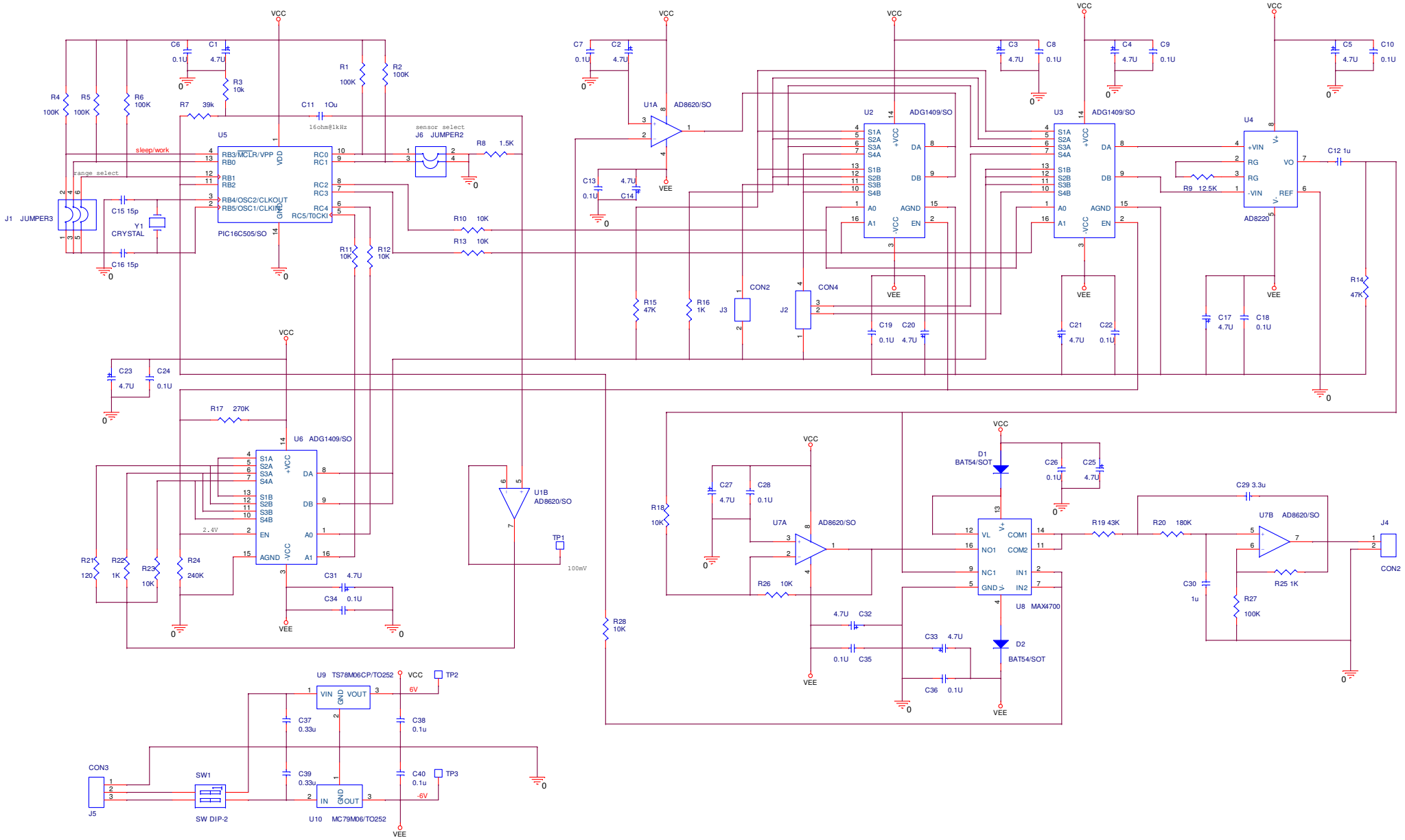

Multi-sensor Signal Conditioning Schematic Diagram